# Design, Development, and Evaluation of a Clinical System for Breast Microwave Imaging.

By

**Mario Alejandro Solis Nepote**

A Thesis submitted to the Faculty of Graduate Studies of
The University of Manitoba
In partial fulfillment of the requirements of the degree of

**Master of Science**

Biomedical Engineering

University of Manitoba

Winnipeg, Manitoba, Canada

# ABSTRACT

Breast Microwave Imaging (BMI) has a promising future for breast cancer detection. The imaging modality is based on the significant dielectric contrast between malignant and benign breast tissue. In radar-based approaches, backscattered signals are collected and reconstructed into images of reflections from the breast tissues to visualize tumors, which are sources of large scatter.

This dissertation presents the research conducted in developing a new clinical radar-based, system for breast microwave imaging. The BMI system features an inspection bed, a rotating radar platform, and the data-acquisition software used to control the system. The system employs a multi-static approach, and an antenna array with four degrees of freedom. The radar platform can be repositioned to reach more than 432 probing points around the breast in a 30-minute scan. The system positioning performance was characterized, resulting in measured accuracies and precisions of 0.25° and 0.05° in the azimuthal plane, and 0.83 mm and 0.20 mm in the vertical plane, respectively. The scan of a heterogeneous phantom resulted in artifact-free images where a 1.5-cm tumor was detected and signal to clutter ratios greater than 20 dB were achieved. Comfort and safety were validated during a phase 0 clinical trial involving 11 asymptomatic volunteers. The system adhered to IEC-6060-1:2005 safety standards and has been licensed as a Class III medical device. Breast phantoms were developed with layers of synthetic skin, morphologically accurate 3D printed materials and dielectrically appropriate tissue surrogates.

The effects of antenna positioning errors in BMI systems were characterized using the developed system and an hemispherical breast phantom. Azimuthal accuracy errors under 2.5° had no impact on the performance of the system. Precision errors greater than 2.5° and 0.05 cm in the azimuthal and vertical directions, respectively, were detrimental to the diagnostic potential of reconstructed images. This work established a set of suitable positioning specifications for BMI systems.

# CONTRIBUTIONS

This thesis presents the design and development a new radar-based, clinical system for breast cancer detection, the characterization of antenna positioning errors in breast microwave imaging systems, and the construction of morphologically and dielectrically accurate breast phantoms. The following contributions were accomplished by the author during his research at the Non-Ionizing Imaging Laboratory at the University of Manitoba

- Design, construction, and integration of a radar-based, modular, multistatic, microwave imaging system for breast cancer detection. The novel design of the system eliminates movement of transmission lines using a rotating-radar platform and efficient air-based antennas. The system development followed a Design for Six-Sigma methodology. Improvements to chest and neck supports were designed and implemented by the summer student Calene Treichel under my supervision. The study of transceiver's performance was conducted in collaboration with Diego Rodriguez, a M.Sc. medical physics student, and Nikita Kopotun, a summer student. The data-acquisition program was developed by a summer student, Valerie Beynon, under my direction.
- Characterization of the positioning performance of the antenna motion-control module as per ISO 230-2(E):2006.
- Development of a photogrammetric algorithm for characterization of the positioning performance of a rotary stage.
- Validation of the diagnostic performance of the BMI system with a heterogeneous, hemispherical breast phantom. The presence and location of tumors in the phantom were successfully assessed using this system.
- Coordination of a phase 0 Clinical trial for comfort and security evaluation of the BMI system. Ethics approval, volunteer recruitment and questionnaire form were completed by Dr. Daniel Flores-Tapia.
- Evaluation of the security performance of the system as per Canadian standards for medical devices. The application for a Class III medical device license was completed by Dr. Daniel Flores-Tapia, a postdoctoral fellow, and Dr. Stephen Pistorius, the principal investigator.
- Development of a skin surrogate for breast phantoms. Characterization of the effects of skin thickness in reconstructed breast microwave images.
- Design and fabrication of transparent, hemispherical containers for breast phantoms. Validation of Cellulose Acetate Butyrate as suitable material for phantom applications.
- Coordination of the development of morphologically accurate breast phantoms using 3D printed adipose and fibroglandular containers from MRI-informed models. The phantoms were developed by a summer student, Tyson Reimer, under my supervision.
- Definition of accuracy and precision specifications of motion-actuators for BMI systems. Induced positioning errors in collected datasets and measured the effects on reconstructed images.
- Finally, it should be noted that the monostatic and multistatic reconstruction algorithms used through this thesis were developed by Dr. Daniel Flores-Tapia.

# LIST OF ACRONYMS

| Acronym | Description |
|---|---|
| BIRR | Breast-imaging rotating radar |
| BMI | Breast microwave imaging |
| DFSS | Design for six-sigma |
| ICOV | Identify – Characterize – Optimize - Validate |
| ABS | Acrylonitrile butadiene styrene |
| VNA | Vector network analyzer |
| CAD | Computer-aided design |
| RAM | Radar absorbent material |
| OI | Object of interest |
| OD | Observation domain |
| IF | Intermediate frequency |
| ROI | Region of interest |
| FWHM | Full-width half-maximum. |
| CAB | Cellulose acetate butyrate |
| ROC | Receiver operating characteristic |
| ICM | Image contrast metrics |
| SCR | Signal-to-clutter ratio |
| TFR | Tumor-to-fibroglandular ratio |
| CNR | Contrast-to-noise ratio |
| CCR | Contrast-to-clutter ratio |
| AUC | Area under the curve (for ROC curves) |
| SD | Standard deviation |
| SE | Standard error of the mean |
| ASP | Single element precision error in the azimuthal plane |
| ASA | Single element accuracy error in the azimuthal plane |
| ARP | Random element precision error in the azimuthal plane |
| ARA | Random element accuracy error in the azimuthal plane |
| AAP | Array precision error in the azimuthal plane |
| AAA | Array accuracy error in the azimuthal plane |
| VAP | Array precision error in the vertical plane |
| VAA | Array accuracy errors in the vertical plane |

# ACKNOWLEDGMENTS

First, I would like to thank my advisor, Dr. Stephen Pistorius, for his endless support, guidance, and encouragement during my studies. I am forever grateful for the many lessons and opportunities that he generously provided me.

I would like to express my appreciation to my colleagues at the Non-Ionizing Imaging Laboratory. Dr. Daniel Flores for his mentorship and for introducing me to microwave imaging research. M.Sc. Diego Rodriguez, for sharing his knowledge in electromagnetic theory, for his assistance during experiments, and for providing me with a renewed motivation to achieve my goals. I also thank my summer students; their diligent work was consequential to the success of this research.

I am grateful to my M.Sc. committee, Dr. Zahra Moussavi, Dr. Bertram Unger, and Dr. Mark G. Torchia, for their exceptional advice and suggestions that improved this work.

I would also like to thank Andrew Pankewycz, as well as Andy Egtberts, Chad Harris and the rest of the Medical Devices workshop at CancerCare Manitoba, for their advice and assistance during the fabrication of the BIRR system.

I would also like to thank the support staff at the Graduate Program in Biomedical Engineering, and at the Department of Physics and Astronomy,

I extend my gratitude to the Canadian Breast Caner Foundation, the Natural Science and Engineering Research Council of Canada, CancerCare Manitoba Research Foundation, and to the University of Manitoba UMGF program, for their financial support.

Last, but certainly not least, I would like to thank all my friends and family, who have been a tremendous source of strength during this journey. Thanks to Taylor Naaykens, who was always ready to share her joy, empathy, and affection, and who, along with her family, was constantly rewarding my efforts. Thanks to my brother and my sister, who will always be an inspiration.

And thanks to my parents, Arturo Solís and Luz María Nepote, for their invaluable support, love, and wisdom. Thanks for being here with me, always.

# TABLE OF CONTENTS

# LIST OF TABLES

# LIST OF FIGURES

# 1 INTRODUCTION TO BREAST MICROWAVE IMAGING SYSTEMS

This chapter starts with an overview of the current challenges of breast cancer diagnosis. Next, microwave imaging is introduced as a promising complementary technology. The next section covers state of the art in clinical breast microwave imaging (BMI) systems. The problem definition will follow. Finally, the chapter conclusions will be presented.

## 1.1 Background and justification

It is estimated that in 2012, the number of breast cancers diagnosed world-wide reached 1.67 million, and it was the most frequent form of cancer for women [1]. With more than 552,000 deaths annual deaths associated with this disease, breast cancer is also the most common cause of cancer death in less developed regions and the second highest in developed regions [1]. For the year 2016, Statistics Canada estimated the occurrence of 25,700 newly diagnosed breast cancers, with nearly 5,000 associated disease-related deaths [2].

Early detection and treatment significantly increase the chances of survival. To this end, frequent mass-screening is recommended. However, the existing methods for breast imaging, X-ray mammography, magnetic resonance imaging, and ultrasound, have limited application as screening tools.

The current gold standard for early-stage breast cancer detection is X-ray mammography, which requires breast compression, involves exposure to ionizing radiation, and suffers from low specificity particularly with dense breast cases [3]. Magnetic resonance procedures are too expensive and time-consuming to be considered as screening candidates. Ultrasound is relatively inexpensive but suffers from low specificity, and its diagnostic outcome is too dependant on the

expertise of the radiologist. Given the limitations of the current imaging technologies, new imaging modalities have been under investigation for breast cancer diagnosis and screening.

For the last 25 years, microwave imaging has been investigated as a complementary modality for breast cancer detection. Compared to the conventional imaging modalities, microwave imaging approaches are cost-effective and do not use ionizing radiation; thus, if their sensitivity is clinically validated, they will become an adjutant tool for mass-screening.

## 1.2 Breast microwave imaging

Biomedical microwave imaging exploits the difference in permittivity and conductivity properties of different tissues. The dielectric properties of a given tissue are correlated to their water content and presence of ionized molecules. Microwave imaging is being investigated for the diagnosis of bone lesions [4], brain hemorrhages [5], liquid in lungs [6], urine volume in the bladder [7], and breast cancer [8]–[11]. This imaging modality is relatively new, and additional biomedical applications might emerge as the technology matures. Some of the current challenges for this technology is the development of custom-hardware for clinical trials and improved reconstruction algorithms [9].

Microwave imaging has promising features for detecting cancerous lesions and is explicitly appealing for inspecting the breast as compared to other body organs. Firstly, the breast volume falls within the penetration range of microwave imaging (i.e., 100 mm); organs like the kidney or liver are consider inaccessible for microwaves [9]. Secondly, the breast can be probed from multiple angles; both backscattered and transmitted reflections can be recorded with an array of antennas surrounding the breast. Unlike the breast, internal organs are surrounded with layers of muscle that result in adverse scatter and signal attenuation. Thirdly, microwave imaging works in the non-ionizing spectrum of radiation, allowing for frequent inspections that might lead to an early diagnosis without the radiation dose associated with exposure to ionizing radiation. Finally, the

difference in dielectric properties between healthy and malignant breast tissues suggest that microwave imaging has the potential of becoming a sensitive tool for breast cancer diagnosis. Due to increased angiogenesis (growth of blood vessels), malignant tumors are associated with higher water concentrations, and thus, greater dielectric properties than normal tissue. This dielectric difference, known as the contrast, is frequency-dependant and decreases with shorter wavelengths. In the range of 0.5 GHz to 20 GHz, ex-vivo measurements have reported dielectric properties of tumors[1] to be six times greater than those of adipose tissue [12]. The contrast between tumors and fibroglandular tissue has been reported to range from 8% to 15% [10], [12], [13]. These values are favorably higher than the 4-10% contrast achieved by X-ray mammography [9], [14].

BMI systems radiate the breast target and record backscatter and transmitted microwave information. The most common imaging modalities are microwave tomography, which creates a map of the electrical properties of the tissues scanned, and radar-based microwave imaging, which produces images focused on the location of strongly scattering objects. Both modalities have been explored with clinical systems.

## 1.3 Tomographic microwave imaging

Microwave tomography is an imaging technique in which the dielectric properties of an object of interest (OI) are inferred from electromagnetic field measurements. During a scan, the OI is successively illuminated by an antenna array, typically, in a circular configuration surrounding the object. Magnitude and phase information from the scattered electromagnetic field are collected by the antenna array. The information is then used to generate 2-D images, or slices, containing information proportional to the real-part and imaginary-part of the complex permittivity of the

[1] A tumor is defined as an abnormal mass of tissue. Not all tumors are malignant (cancerous), however, breast microwave imaging systems are uncapable of discerning between malignant and non-malignant tumors at this stage. Through this thesis, the term tumor is used to describe both conditions.

imaged object. Microwave tomography images have quantitative values associated with the dielectric profile of the OI. [15]

In microwave tomography, nonlinear optimization algorithms are used to solve the inverse scattering problem. An electromagnetic simulation is used as a forward model. The model is iteratively updated to minimize the difference between the solution and the measurement from the antenna array. To reduce computational costs, point sources and point-like responses are assumed in the simulation. The simplifications in the model limit tomography prototypes to the use of monopoles and dipoles. [9].

Current tomographic algorithms are time-consuming and impose a substantial computational cost. Simplifications, such as operating in a single frequency band, are required to reduce the model complexity. Nevertheless, the fidelity of the solution is questionable, and gradient-based optimizations may not converge to a solution [9].

The Electromagnetic Imaging Laboratory at the University of Manitoba has conducted substantial research on tomographic approaches. Their latest prototype features a 3D array of 120 microwave transceivers, and employs water as the immersion medium [16]. A recent studied used radar-based breast measurements to provide a preliminary region estimation to the microwave tomography algorithm, resulting in improved image quality [17].

## 1.4 Radar-based microwave imaging

Radar-based microwave imaging is an application of radar that produces 2D or 3D images of the OI. Radar operates by first transmitting an electromagnetic pulse through an antenna. The microwave signal will then interact with a distant object, reflecting some energy back to the antenna. The reflected signals are analyzed to measure signal strength and travel time. Finally, this information is processed and displayed as an image.

Radar is conventionally used to determine the position and movement of reflective objects. Radar imaging is a modality that aims to form an image of an object by collecting and processing the target backscattering when illuminated with microwave pulses.

Most radar systems use broadband signals centered at a specific frequency. Frequency selection is determined by the application requirements since there is a trade-off between resolution and penetration power. Higher frequencies allow for a finer resolution, at the cost of penetration power. Likewise, low frequencies have deeper penetration but provide less spatial resolution.

Radar-based reconstructions benefit from an increased number of probing locations [9]. When a source of high scattering is present in the target, its interaction with the scattered field component is present in all the collected signals, leading to a coherent addition. The target backscatter is then processed with a reconstruction algorithm. Most algorithms in radar-based approaches are an extension of delay-and-sum beamformer [10]. The image obtained is a reflectivity map, where the brightest spots correspond to areas of greater electromagnetic scattering. In the reconstructed images of radar-based breast microwave systems, high energy regions are associated with the presence of tumors, while low energy regions correspond to adipose or connective tissue.

## 1.5 The need for clinical systems

Early-stage microwave-based breast cancer detection systems have been reported as early as 1978 [18]. To date, most of the published work relies on simulations or phantoms scans to conduct experiments. These approaches are often performed under idealized conditions. Ultimately, the success of this technology is measured during clinical trials. Migrating to patient examinations brings specific challenges, including:

- Accounting for anatomical diversity and isolating the breast for inspection [19]–[21],
- Preventing patient movement while guaranteeing comfort and safety [19], [21],
- Optimizing the size and number of antenna elements [19], [22], [23],
- Eliminating the interference caused by impurities in the propagation path [23],
- Accounting for breast tissue variabilities [23], [24].

The scientific community is interested in developing clinical systems that can address these challenges, while achieving competitive sensitivity and specificity metrics [9].

## 1.6 Literature review—Clinical systems for breast microwave imaging

A few BMI systems have reached the maturity required for clinical trials. The leading research teams that have reported clinical results are the groups from Dartmouth College, The University of Calgary, McGill University, and the University of Bristol. The Non-Ionizing Imaging Laboratory at the University of Manitoba, led by Dr. Pistorius, has developed a promising BMI prototype, and a second-generation system, suitable for clinical examination, is introduced in Chapter 2. The characteristics of the systems for each group are described in the following subsections and are summarized in Table 1.6-1.

Table 1.6-1 State-of-the-art, clinical breast microwave imaging systems.

| | Dartmouth College | University of Bristol | University of Calgary | McGill University | University of Manitoba |
|---|---|---|---|---|---|
| **Prototype name** | | MARIA M4 | TSAR | | BIRR |
| **Clinical evaluations** | 150 symptomatic patients for detection. Eight patients for monitoring | 85 symptomatic patients | One healthy volunteer, Eight symptomatic patients | 13 healthy volunteers. | 11 healthy volunteers |
| **Modality** | Tomographic, multistatic | Radar-based, multistatic | Radar-based, monostatic | Time-domain radar, multistatic | Radar-based mono and multistatic |
| **Operational frequency** | 250 kHz to 3 GHz | 3 GHz to 8 GHz | 50 MHz to 15 GHz | 2 GHz to 4 GHz | 1 GHz to 8 GHz |
| **Key features** | 16 interleaved antennas, immersion tank. | 60 antennas, hemispherical ceramic cup. | One antenna, immersion tank. | 16 antennas, hemispherical cup. | Two antennas, air operation. |
| **Acquisition time** | 5.8 seconds per plane. 2 to 8.7 minutes per breast. | 30 seconds per scan. 1 minute per breast. | 30 minutes. | 70 ps per scan. | 10 minutes per plane. 30 minutes per breast |
| **Trajectories for antenna repositioning** | Elevation | Rotation | Elevation, and rotation. | None. | Elevation, rotation. |
| **Specifications of the motion-control components** | Range of 110 mm Resolution of 0.0254 mm. Speed of 396 mm/s | 15 ° rotation, no details | Mechanical play < 0.1 mm and < 0.1° Displacement error < 0.1 mm and < 0.1° | Antenna spacing of 18°. | Detailed in Chapter 2, section 2.3 |

### 1.6.1 Dartmouth College

In the year 2000, the group from Dartmouth College in New Hampshire, USA, published the first clinical-grade BMI system [25]. In 2007, the group reported 150 patient exams aimed to detect breast malignancies with their system. This study reported a mean increase in contrast (from 150% to 200%) between abnormal (benign and malignant) and normal breast tissue [26]. The system has also been investigated as a chemotherapy monitoring tool with eight patients examined over a period of 6 months [27].

The latest iteration of their system was discussed in [28]. That system uses an immersion tank with glycerin/water coupling mixture, 16 vertical monopole antennas connected to a 16-channel switching matrix and a digital radio-frequency generator with a frequency range of 250 kHz to 3000 MHz. The system is composed of two interleaved sub-arrays of eight antennas each. During a single-plane scan, 240 single-frequency data-points are collected by transmitting through all the elements and using 15 antennas as receivers. The two antenna arrays can be lowered simultaneously to generate 2D coronal slices at each plane. 3D images are acquired by collecting measurements in a cross-plane configuration (i.e., lowering the sub-arrays at independent heights) with acquisitions times of 5.8 s per plane. [28]

A motion-control system allows the two antenna sub-arrays to reach different heights within the illumination tank. The elevation is achieved by four assemblies of a linear actuator driven by a stepper motor.

There are no reported values on the mechanical performance of the microwave imaging system. Although a positioning resolution of 0.0254 mm (0.001 in) is reported in [28], it is not specified how this value was measured. This value matches the expected repeatability of the linear actuator as per the specifications of the manufacturer [29]. For motion-control systems, resolution, and repeatability are not interchangeable terms. Neither value is enough to characterize the

performance of the elevation control system. Factors like mechanical play, sine errors, and differences between the dual assembly can impact the actual positioning resolution, and thus, the performance of the elevation mechanism.

In [28], the Dartmouth group carried on an experiment to evaluate the sensitivity of their microwave imaging system. The experiment evaluated in-plane and cross-plane receiver configuration. During the in-plane evaluation, signal-to-noise ratios increased with frequency as well as the distance between the transmitter and receiving antennas. During the cross-plane configuration, one of the two subarrays was lowered 110 mm in 10 mm decrements. At 1100 MHz, differences of only 10 mm resulted in drops of signal-to-noise ratios of up to 44 dB. When operating at 2300 MHz, signal to noise ratio below 1 dB were measured after only 40 mm of vertical separation. [28]

Reconstructed phantom images corroborated these findings. Three images were reconstructed using data from 30 mm, 40 mm, and 60 mm of separation across the antenna cross-planes. The increase in vertical separation between antennas led to a greater number of artifacts. With distances of 30 mm providing the most accurate estimations for dielectric values (error in conductivity estimates of 0.04 S/m) and spatial accuracy (visual appreciation). There are no reports on the impact of vertical separations smaller than 10 mm. [28]

### 1.6.2 University of Bristol – MARIA M4

The University of Bristol has developed three prototypes for multistatic, radar-based breast imaging [22], [23]. Their last generation system – MARIA M4– has been tested in a clinical setting with 86 symptomatic women obtaining a sensitivity score of 74% (64/86) correspondence with ultrasound examinations [20]. Examination of patients with dense-breast classifications showed a sensitivity of 86 % (36/42) which was better than the score achieved by the original radiologist report (69%) and a second blind review by an experienced radiologist (79%) [20].

The system consists of 60 wide-slot ultra-wideband antennas mounted in a hemispherical cup made of acrylonitrile butadiene styrene (ABS) plastic. A low-loss ceramic cup is fit between the antennas and the breast. To eliminate air gaps between the different materials, a water/oil-based coupling liquid is used. The ceramic cup and coupling liquids have a dielectric constant of 10. A 60-way electromechanical switch connects the antennas to an 8-port, 8 GHz vector network analyzer (VNA). Reconstructed images are formed using a delay-and-sum radar beamformer algorithm. To eliminate unwanted reflections from the skin, a compound differential offset imaging approach is performed where a second scan, collected after rotating the array 15$^{o}$, is used for calibration. Inspections times of 30 seconds per scan are reported in [20].

The rotating mechanism can move the hemispherical cup up to 90$^{o}$ [23]. There are no published values on the specifications of the rotation-control system. Diagnostic sensitivity to the accuracy and repeatability of the cup rotation has not been reported.

### 1.6.3 University of Calgary – TSAR

The research group at the University of Calgary has created and tested a clinical, radar-based system named TSAR. In 2012, the system was validated with phantom scans and one volunteer [30]. In the following year, a pilot clinical studied was carried out with eight patients with known abnormalities [31]. Microwave images were compared against mammograms, magnetic resonance scans and biopsies [31]. Images obtained with the TSAR show responses consistent with the location of malignant lesion for one of three patients with clearly identified cancerous tumors.

The TSAR system consists of single antenna configuration operating in monostatic configuration. The antenna position can be rotated and elevated to reach 200 positions around the breast. The antenna used is a balanced antipodal Vivaldi antenna with increased directivity (BAVA-D) [32]. The antenna is attached to a mechanical arm inside a tank filled with canola oil as

coupling liquid. A laser and a camera are used to obtain the shape of the breast as well as the antenna-to-breast separation. The antenna is connected to a 15 GHz VNA. At each antenna position, microwave pulses are radiated at a frequency band of 50 MHz to 15 GHz. A time-shift and sum beamforming algorithm is used to generate 2-D and 3-D images from the recorded signals [31], [33]. Tank reflections and background noise are reduced by removing the reflections obtained from an identical scan performed in an empty tank; the latter scan is considered a "reference" measurement.

A second-generation system was presented in [19]. This system has two additional degrees of freedom that allow the antennas to be repositioned normal to the contour of the breast and adjust to different breast sizes. To this date, there are no reports on clinical experience with this system.

In [30], the research team at the University of Calgary reported performance values for the elevation and rotation mechanisms. Backlash (mechanical play) and positioning errors were evaluated for each axis. Tolerances of 0.1° and 0.1 mm were defined for each characteristic. Per [30], deviations within these tolerances generate less than 0.6 mm of spatial error in reconstructed images.

For the elevation axis, Bourqui et al. attached a digital caliper to the elevating arm. The maximum displacement error was ± 0.07 mm with an average of 0.04 mm. The direction or the number of iterations required to calculate the displacement errors are not detailed. For backlash, four measurements in each direction are reported, with a maximum of ± 0.03 mm and an average of 0.01 mm after a software compensation. No details are given on the compensation procedure. [30]

Displacement in the azimuth axis was indirectly measured by rotating the system, measuring the length of the arc generated at the outer edge of the tank and calculating the inner angle. Bourqui et al. report that displacements as small as 0.5° can be attained with errors smaller

than the 0.1 ° tolerance. However, no actual values of backlash or displacement error were reported for the azimuth axis. [30]

In [30], the group at the University of Calgary presented the most detailed report of mechanical specifications amongst the current clinical systems. However, several conditions are missing. The range, number of measurement iterations, movement direction and load conditions are not detailed. The paper does not mention the model of the measuring instruments or the uncertainties associated with them.

A sensitivity test was also carried on in [30]. A broadband load was connected instead of the antenna. The magnitude of the reflections and phase delay were measured using 200 successive measurements. Compared to static measurements, repositioning of the load resulted in average sensitivity losses of 10 dB and phase variations of 0.5°. Greater sensitivity losses were measured at higher frequencies. Cable movement was associated with variation in electrical responses. To reduce the detrimental effects of cable movement, a guiding rail was built for the TSAR system. The effects that positioning variations could represent in reconstructed images has not been evaluated in any report.

### 1.6.4 McGill University

In [24] and [34], the research group at McGill University in Montreal, Canada, reported a time-domain, multistatic radar breast imaging system. The system consists of 16 antennas embedded in a ceramic hemispherical cup. The antennas are arranged to obtain cross-polarized and co-polarized information. The system uses a pulse generator to create a 70 ps Gaussian signal with its main frequency content present in the 2 to 4 GHz range. The pulse is transmitted through a single antenna, and after propagating through the breast, the waves are received by the remaining 15 antennas and recorded on an oscilloscope. An electromechanical switch alternates the role of each antenna until all the elements have operated as transmitters and receivers.

Ultrasound gel with a dielectric contrast of 68 is used as coupling liquid. Reconstructed images are obtained using a delay-multiply-and-sum algorithm.

The system has been validated with heterogeneous breast-tissue mimicking phantom [34] as well as volunteers [24]. In 2014, Porter et al. conducted a repeatability trial with 13 volunteers, scanning both breasts with the time-domain system over a period of eight months. By comparing the maximum pixel intensity of reconstructed images, the paper concludes that biological variation over time (approximately one month) has the biggest impact on the information of scans [24]. However, for three volunteers, repositioning scans taken two days apart had similar pixel intensities as monthly scans [24].

The time-domain system from McGill group uses an array of 16 antennas and requires no moving mechanisms. The antenna elements are placed in a radome at 18° intervals. At the time of publication of this thesis, there have been no reports on the tolerances of antenna spacing, or the effects that could result from misalignment.

### 1.6.5 University of Manitoba

The non-ionizing imaging laboratory at the University of Manitoba has published several papers for radar-based breast microwave imaging. A first-generation benchmark system is presented in [35]–[37]. The following chapters in this thesis present a second-generation, clinical grade BMI system.

The first-generation system, shown in Figure 1.6-1, can detect synthetic tumors in simple phantoms. The system used a $560 \times 560 \times 400$ mm$^3$ acrylic tank as an imaging chamber. The tank was used to immerse phantoms in impedance-matching mediums. Cylindrical breast phantoms with a diameter of 13 cm were placed in the middle of the tank. The phantoms mimic the dielectric properties of fat, fibroglandular, and malignant tissue. The lid of the tank featured a circular array of holes through which antennas could be lowered into the imaging chamber. The antennas could

be placed at angular separations of 5°. The distance from the antennas to the center of the tank was fixed at 200 mm. A stepper motor was used to rotate the phantom, allowing multiple radiation positions. [35]

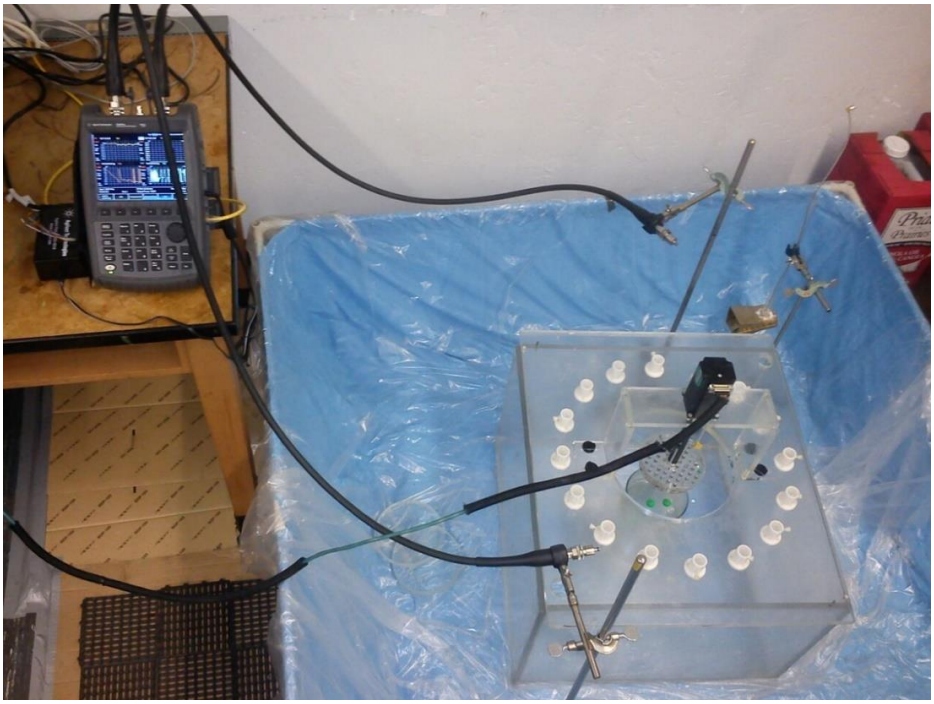

Figure 1.6-1 First-generation microwave imaging system developed at the University of Manitoba. The observation domain was contained in an acrylic tank that could operate in air or with impedance-matching liquids. The position of the antennas was adjusted using a circular array of apertures and fixtures on top of the tank. A two-port VNA was used to generate and record microwave signals. Phase-stable cables transmitted the microwaves to the antennas. A stepper motor above the tank, rotated the phantom contents. [37]

Vivaldi antennas were used in [35], and were later upgraded to custom-made horn antennas [36]. A FieldFox VNA (N9926A, Keysight Technologies, CA, USA), was used to generate and record ultra-wideband pulses centered at 3 GHz and spanning from 20 MHz to 6 GHz [35].

Circular holography was used to reconstruct images from the collected reflections. The algorithm works in the frequency domain and uses a matching filter to compensate for the scan geometry. Monostatic [35] and multistatic [37] configurations have obtained promising results.

The benchtop system provided accurate results for laboratory use. The system could detect the responses from 8-mm-wide inclusions with an average spatial error of 4 ± 2 mm [37]. This

spatial error was below the spatial resolution of the system (8.4 mm)[37]. Complex mechanisms and cable motion were avoided by rotating the scanned object instead of the antenna array. However, this approach would not be feasible for clinical examination.

## 1.7 Problem definition

Despite the positive findings and unique contributions of each research group, there are few details as to the design and manufacturing specifications of the mechanical components of their clinical systems. Moreover, there are no documented results detailing the effects of accuracy and precision of antenna positioning in breast microwave images, nor how antenna positioning errors impact the ability of the microwave system to detect the malignancies inside the breast.

Breast microwave imaging systems benefit from collecting all the scattered reflections from the target. To increase the number of sensing locations, antenna arrays are built. Ideally, the size and crosstalk characteristics of the antenna elements would be the only determining factors for the dimensions of the array. In practice, the size of the array is limited by the number of ports of the microwave component used to record the signals [20], [22], [23]. Employing fast and reliable high-frequency switches can expand the number of antenna elements [28].

An alternative to fixed antenna arrays is the use of a motion-control system to virtually increase the number of antenna elements. The benefits of antenna repositioning include the ability to work with antennas of bigger dimensions, and reduction of cost, hardware, and uncertainties due to antenna variability. Currently, the systems from Dartmouth, Bristol, and Calgary use some form of antenna repositioning.

Repositioning of the antennas is associated with of a loss in the repeatability of the system, and an increase in imaging inspection time because of the movement of the antennas. Fast mechanical actuators can be used to increase speed requirements, and precise mechanical

components can be used reduce positioning errors. However, the cost and complexity of the systems increase with high-performance actuators.

Tolerances for the mechanical performance of a system guide its manufacturing phase. Selection of motion-control components is based on their mechanical performance. The criteria for their evaluation include accuracy, precision, minimal incremental motion, travel length, backlash, maximum carrying capacity, and speed. Performance experiments that adhere to international standards, like ASME B5.57 and ISO-230-2, allow for fair comparison of the capabilities of numerically controlled equipment [38].

To the best of the author's knowledge, design tolerances for antenna-repositioning components have never been thoroughly documented. The only example in literature belongs to the clinical system in [30], where the University of Calgary reported tolerances for the accuracy and backlash of the rotating and elevating components of their system. These design specifications were not justified [30].

Two BMI research groups have performed basic characterization of the mechanical actuators in their systems due to the lack of a detailed manufacturer's specification report for these components. The University of Calgary conducted a characterization of the vertical and azimuthal movement performance of their system [30]. This report was limited to the backlash and the positioning error on the vertical axis. The group from Dartmouth College reported resolution and speed parameters, but did not detail how these values were measured [28]. These shallow reports are insufficient to adequately describe the operation of a motion-control system.

Antenna positioning errors can affect the diagnostic performance of a breast microwave imaging system. Sensitivity analysis performed by the University of Calgary and Dartmouth College hint that errors in the placement of the antennas result in higher noise levels [28], [30]. No studies have been reported on the direct impact that positioning errors might have in the final reconstructed images.

Phantoms, synthetic materials that mimic the specific properties of real tissue, are used to test and improve breast microwave imaging systems. Reconstructed images of phantom scans can be used to determine the diagnostic capabilities of a system. Thus, by using phantoms, the effects of antenna positioning variation can be associated with the diagnostic capabilities of a breast microwave imaging system.

### 1.7.1 Problem statement

In Canada, breast cancer is the most frequent form of cancer diagnosed in women [2]. Microwave imaging has the potential to become a safe, comfortable, and accurate coadjutant technology for breast cancer diagnosis. During a scan, the breast is illuminated from a large number of antenna positions. However, the effects of antenna positional deviations in reconstructed images have not been thoroughly studied, and there are no suggested tolerances for the motion-control components.

### 1.7.2 Thesis objectives

**The main objective of this thesis is the definition of mechanical tolerances for breast microwave imaging systems, specifically, the required precision and accuracy of antenna positioning**. This study is needed to understand the impact of positioning deviations and determine tolerances for future prototypes and clinical systems.

To this end, a clinical-grade breast microwave imaging system was developed, and its antenna positioning performance was thoroughly characterized (Chapter 2). A set of minimal and ideal positioning tolerances were obtained by inducing antenna positioning deviations in phantom scans and measuring the impact on the quality of reconstructed images (Chapter 3). Finally, advanced phantoms that mimic the dielectric and anatomical properties of breast tissue were developed to validate this and further BMI systems (Chapter 4).

## 1.8 Chapter conclusions

The current chapter discussed the state-of-the-art in microwave imaging systems. Breast microwave imaging has many obstacles to overcome in order to become a standard technology for breast cancer diagnosis, one of which is defining the diagnostic effects of erroneous positioning performance from the motion-control components of the systems.

The following chapter will cover the design and development of a novel BMI system with an extensive characterization of the antenna positioning performance of the system.

# 2 DESIGN, DEVELOPMENT, AND VALIDATION OF A BREAST-IMAGING ROTATING-RADAR SYSTEM — BIRR

The previous chapter summarized the challenges reported with current breast microwave imaging systems, emphasizing the lack of characterization in the re-positioning of antenna motion-control component. Breast microwave imaging technology has not matured enough for clinical practice, and BMI systems are not commercially available. To complete the research goals of this thesis, a new clinical system had to be designed and constructed. This chapter presents author's work in designing, developing, and validating the breast-imaging rotating-radar (BIRR) system. The first section of this chapter describes the methodology followed to develop a new clinical BMI system. Next, the system product requirements, design concepts and construction process are discussed. Then, the manufactured system is presented, and each component is described. The last section of this chapter details the experiments conducted to validate the system as a suitable device for clinical examinations.

## 2.1 Product development methodology

A Design for Six-Sigma (DFSS) methodology was implemented through the development of the new clinical microwave imaging system. Design methodologies are followed in industry to expedite the production of high-quality, reliable, and economical products [39]. The design and construction of the clinical microwave imaging system followed the ICOV process from DFSS. The acronym ICOV stands for the four main stages of a new product development: Identify, Characterize, Optimize, Verify/ Validate (Figure 2.1-1) [40].

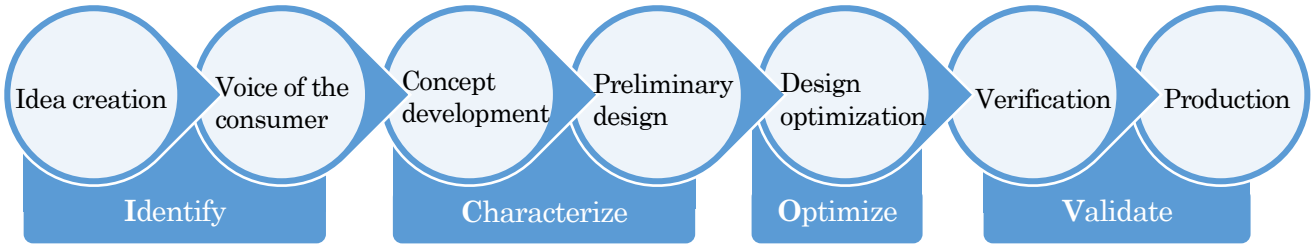

Figure 2.1-1 The ICOV process, from DFSS, was followed during the creation of the BIRR system.

The identification phase involved understanding the principles of the technology, establishing critical product and user requirements, as well as customer needs. During this stage, the benchtop microwave imaging prototype available at the University of Manitoba was studied (previously detailed in Section 1.6.5). Microwave-based breast scanning devices reported in the literature were reviewed as a benchmark. A panel of experts was assembled to provide feedback on the design and construction process. The panel consisted of Dr. Flores-Tapia (Microwave Imaging), Chad Harris, Andy Egtberts, and Andrew Pankewycz (Design and Manufacturing). An expert on medical imaging, Dr. Stephen Pistorius, was established as the customer. The end-user was established as the average Canadian women above age 40. During this phase, project goals, product challenges (Section 2.2.1) and product specifications (Section 2.2.2) were determined.

The design of the BMI device was created during the characterization phase. Preliminary design concepts were created in aims to meet product requirements (Section 2.2.3). Operation, manufacturability, and potential risks were evaluated using drafts, computer-aided design (CAD) models, and simulations. CAD models were also used to adjust the design to meet anthropometric dimensions. The system design undertook a first-pass refinement process, where the panel of experts reviewed each design concept until a satisfactory design was achieved. At the end of the characterization phase, the design concept was sent to manufacturing. Mechanical drawings (Appendix 7.6) and a design specification document were created to facilitate the system construction. Gannt charts were used to schedule and track project development.

At the optimization stage, the end-user (represented by 11 female volunteers) evaluated the product. User feedback was used to perform modifications to the system (Section 2.4.3). The head and chest support sections of the inspection bed were re-designed to improve the comfort during clinical examinations.

The validation phase took place after manufacturing and integrating the product. The system was evaluated in accordance with the product specifications established in Section 2.2.2, internal customer wants, and Canadian safety standards for medical devices.

## 2.2 Design and construction process

The design phase of the BIRR took place from May 2013 to February 2014. First, design constraints were identified, and a list of specifications was created. Next, preliminary concepts were created to solve the defined requirements. Design concepts were reviewed and refined through meetings with the panel of experts and with the customer. The system manufacture took place between November 2013 and July 2014.

### 2.2.1 Definition of product challenges

Two groups of challenges were identified when designing a system for active microwave scanning of the breast. The first obstacles were associated with human anatomy and the location of breast tumors. The second set of challenges arose from the operation of radar-based systems.

#### 2.2.1.1 Body and breast dimensions

A breast microwave imaging system must comply with the weights, body dimensions and breast dimensions of women past the age of 30. According to measurement surveys, the average height of a Canadian woman is 162.7 cm (SD 5.6 cm), and the average weight is 69.8 kg (SD 23.2 kg) [41], [42]. To accommodate for 95% of the expected population ($\bar{x} + 2\sigma$), the system had to be designed to support women with heights of 174.0 cm and weights of 116.2 kg

The system must also accommodate most breast dimensions. S.Y. Huang et al. analyzed 216 CT breast scans of North American women between the ages of 35 to 82 [43]. Measurements of breast diameters at the chest wall ranged from 6 cm to 18 cm with a mean ± SD of 12.1 cm ± 2.1 cm. Breast length, measured from the chest wall to the nipple, ranged from 1 cm to 13 cm with a mean ± SD of 8.1 cm ± 2.4 cm. Figure 2.2-1 shows the cumulative distribution of breast dimensions. While inspecting all breast dimensions would be ideal, higher values can greatly increase the size of an imaging chamber. To account for 95% of expected breast cases, the system was designed to scan breast with a diameter as big as 16.4 cm and lengths of up to 12.8 cm.

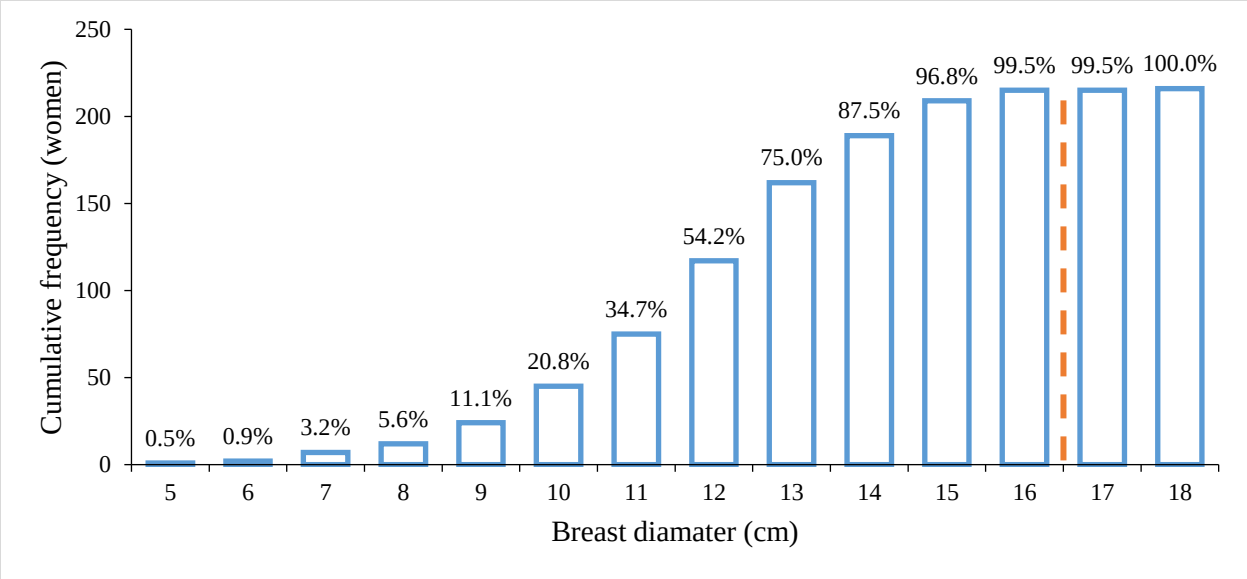


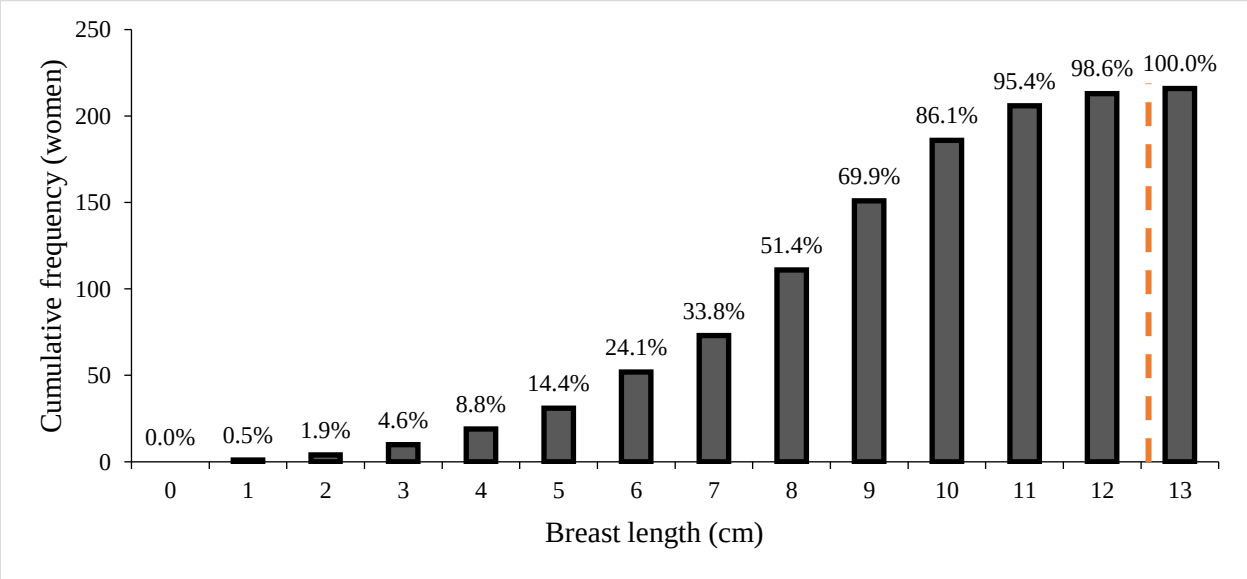


Figure 2.2-1 Cumulative frequency of breast diameter and length from CT scans of North America woman between ages 35 to 82. The diameter was measured at the chest wall. Length measured from the chest wall to the nipple. Dashed lines indicate the 95 % upper bound. (n = 216) [43]

#### 2.2.1.2 Tumor locations

Tumors are located with significantly higher incidence in the upper-outer quadrant of the breast (51% to 58%) [44], [45]. The other quadrants and the nipple complex account for 42% to 49% of the remaining cases. The intended imaging system had to radiate the entirety of breast volume with particular consideration for the upper-outer quadrant. To properly recover the scatter from tumors within the breast, sensors should surround the breast along a 360-degree arc, and along the extent of the breast length in the sagittal direction.

#### 2.2.1.3 Patient movement during scan

Image blur introduced by patient motion is a common source of image quality degradation in medical imaging [14]. Breast movement during microwave scan has been attributed as a source of artifacts [46]. The design needed to isolate and immobilize the breast, without compromising comfort.

#### 2.2.1.4 Inspection time

A time limit of 30 minutes per-breast scan was established in discussion with the panel of experts. This specification represents a compromise between opposing criteria. Reconstruction algorithms benefit from an increased number of probing locations [47]. It is desired to illuminate the breast from as many locations as possible, in both coronal and sagittal directions, which in turn increase the inspection time. Nevertheless, shorter scans are preferred to reduce the potential of patient movement and limit the exposure to microwave radiation.

#### 2.2.1.5 Noise generated by cable movement

Transmission line movement is associated with noise spikes through two different phenomena. Deformation of the dielectric materials can generate electrical potentials due to the piezoelectric effect [48]. Electrostatic discharges can also occur due to the movement of the

dielectric material against the conductors [48]. The final design had to propose a solution that minimized cable movement.

#### 2.2.1.6 Unwanted scatter

The region covered by the measurement points is defined as the observation domain (OD) [49]. It can be assumed that the OD contains the object of interest and the space between the measurement points. Reconstruction procedures assume all measured signals radiate from the OI. Highly scattering surfaces within the OD can alter the propagation path and intensity of backscatter microwaves, increasing background noise as well as the number of artifacts. For this reason, metallic parts, which have high scattering properties, could not be used near the observation domain.

#### 2.2.1.7 Background interference

Electromagnetic interference is associated with unwanted signals entering the OD. Sources of interference can be transmission lines or devices operating in the same frequency range as the imaging system. Scattering surfaces outside the OD can also generate interference if the incident waves propagate past the scanning region. Thus, the observation domain had to be isolated for the frequency range of the system, preventing electromagnetic waves from escaping or entering the scan region.

#### 2.2.1.8 Transceiver characteristics

Antenna selection is a critical element of a successful imaging system. Radiation pattern and penetration power are highly dependent on the antenna model. Additionally, transceiver dimensions and cross-talk characteristics can limit the number of elements of an array. The selection of a suitable antenna model for this design followed an extensive characterization study further explained in [36], [50]–[52]. In order to use and test more than one type of antenna, the system required a versatile design for the antenna array.

The system frequency is also a critical selection. Frequencies above 10 GHz can provide subcentimeter resolution [9]. However, lower frequency values have a greater penetration power and result in less signal attenuation [9]. The use of ultrawideband signals between 1 GHz and 8 GHz provides a good balance between penetration depth and resolution [53].

#### 2.2.1.9 Signal measurement configurations

The selection of hardware and reconstruction algorithms is highly dependent on the configuration used to transmit and measure the signals radiated to the breast. Monostatic configurations rely on a single antenna simultaneously operating as a transmitter and a receiver. To collect the backscatter reflections from all the possible scatters in the breast, monostatic configurations require antenna repositioning. Multistatic approaches use a single element to illuminate the breast, and additional neighboring antennas to measure the transmitted signal. Compared to multistatic approaches, monostatic measurements are associated with greater scatter energy [37]. Multistatic measurements demand complex equipment, as well as highly populated antenna arrays, but have an increased ability to collect the scatter from otherwise obscured targets [37]. Further studies are required to validate multistatic algorithms. Therefore, an ideal system could work in monostatic and multistatic configurations.

### 2.2.2 Product specifications

Based on the previously discussed challenges, a successful design was required to achieve the following tasks:

- Radiate microwaves towards breast targets and measure the backscatter and transmitted signals in a span of 360 degrees.
- Support safely and comfortably, the weight of a body of up to 125 kg and a height of up to 174 cm during a 30-minute scan.
- Provide the space to inspect breasts with diameters of up to 16.4 cm and lengths of up to 12.8 cm.
- Prevent breast motion and deformation of the RF transmission lines.
- Avoid highly reflective surfaces near the observation domain.
- Operate in monostatic and multistatic configurations, using an ultrawideband frequency of 1 GHz to 8 GHz.
- Provide versatility for antenna selection.

### 2.2.3 Product concepts

Design concepts were created with the intention of satisfying the previously defined specifications. Each concept was reviewed by the panel of experts, where areas of improvement were identified. The final design concept was refined to meet all requirements and obtain approval from the panel of experts and the consumer. Two preliminary concepts are described in the following sections.

#### 2.2.3.1 Preliminary concept #1

The first concept design was an adaptation of the benchtop system for clinical use. Two opposing actuator-tire couples provided axial rotation of the entire device around a patient breast. The system was intended to be used in conjunction with a patient bed. An aperture in the middle of the bed would allow for a single breast to be lowered into the scanning chamber underneath. A cylindrical tank sat atop the device. The tank could be filled with impedance-matching liquids. The antenna array was routed through sealed openings at the bottom of the tank. To eliminate cable

movement, the microwave equipment placed underneath the tank would rotate along the axis of the entire device. A CAD render of the design is presented in Figure 2.2-2.

Figure 2.2-2 CAD render of discarded BMI concept #1 Microwave equipment sits below round tank for impedance matching liquids. The device rotated on its vertical axis under an inspection bed (not shown in this figure).

The concept was dismissed due to the unreliability of the rotation mechanism. Individual motor control would provide advanced maneuverability. However, this came at the cost of accuracy. Differences between motor speeds and torques would have resulted in inaccurate rotation. Antenna height could not be adjusted during a scan; only single plane measurements could be collected. Leaks were a significant concern since the impedance-matching liquid could fall directly into the equipment underneath.

#### 2.2.3.2 Preliminary concept #2

The next design concept provided a three-dimensional data acquisition solution. A scissor lift mechanism controlled the height of the entire antenna array during a scan. The scissor lift mechanism consists of a platform suspended by two pairs of supports linked in a crisscross pattern. The platform is elevated when pressure is applied to a piston at the base of the mechanism.

Pressure is controlled through a worm gear that shortens the distance between the bases of the supports. Compared to other elevation mechanisms, scissor lifts have a greater travel range and can be collapsed to minimize its volumetric footprint.

Like the previous concept, the microwave electronic equipment rotated in unison with the antenna array. A rotary mechanism was used to reposition the radar module in the azimuthal direction. Using a single motor to drive the rotating mechanism reduced the complexity and risk of positioning inaccuracy. To ease movement of the entire radar module, a pallet was placed at the bottom of the rotating platform. Using a small forklift, the pallet could be lifted to move the radar module from underneath the inspection bed.

The design concept no longer used a tank with matching liquid. Instead, antennas with good performance in air were selected [36]. A circular chamber of radar absorbing material (RAM) isolated the antenna array and scanned object. Before a scan, the antenna array could be configured to adjust to the dimensions of the breast. Radial distance and angular separation of each transceiver element could be modified using a slotted tabletop. Holders were designed to keep the antennas secured and provide tilt adjustment.

Like previous concepts, microwave equipment was placed underneath the inspection elements. An instrument rack housed the equipment. The height of shelves could be adapted to different equipment, avoiding re-manufacturing if the hardware was replaced or updated. The rack was placed above the rotary mechanism to reduce motion-induced noise on transmission lines.

This concept provided a satisfactory solution to most of the design requirements. However, the design of the inspection bed had not been addressed. Furthermore, the dimensions of the radar equipment were excessively large for a clinical system.

Figure 2.2-3 shows a side-view of the design concept with preliminary dimensions.

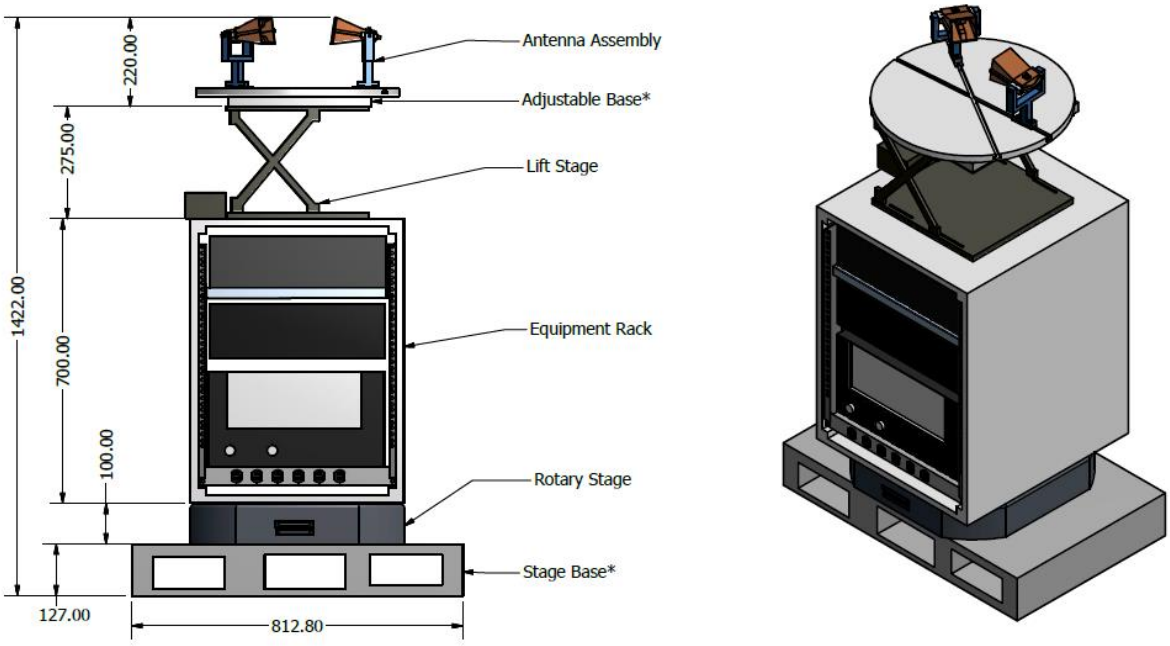


Figure 2.2-3 Design concept #2 featuring a radar module with lift and rotary stages. The motion-control stages allow three-dimensional scanning trajectories

#### 2.2.3.3 BIRR design concept

The final design of the BIRR system provides an improved version over the previous concept with particular attention to modularity, which reduces complexity and increases the reliability of products [54]. As will be explained further in Section 2.3, components can be easily replaced or removed.

In the BIRR design, the woman lies prone on top of an inspection bed. The inspection bed is designed to provide a cushioned support for the user. During a clinical examination, the subject places one breast through a 17-cm-wide aperture in the middle of the bed. The aperture connects to the radar scanning chamber below the bed frame. Gravity is used to elongate the breast, making it accessible for microwave illumination. Support of the head weight is provided by a massage-style headrest, a sturdy canvas sheet for the chest region, and cushioned layer on top of plywood for the abdomen and lower section of the body. The canvas material was selected to reduce the separation

between antennas and the body of the patient. To reduce target motion, breast casts can be placed between the antennas and the breast aperture in the bed.

Underneath the bed, a rotating-radar module is housed. The radar module can support multiple antennas operating in monostatic, or multistatic configuration. During a scan, motion-control mechanisms (i.e. rotary and lift stages) provide computer-controlled rotation and elevation of antennas. Individual tilt, radial distance and angular separation for each array element can be adjusted with the antenna holding mechanism. The radar module sits above a low-profile platform which allows the removal of the radar module from underneath the bed.

The system frame was made of extruded aluminum profiles. An rack below the bottom part of the inspection bed can be used to store equipment and tools. The inspection bed can be extended with an additional frame at the foot of the bed. The additional frame was designed to contain a secondary diagnostic system. This design feature provided the option of performing clinical examinations of a single volunteer with two diagnostic devices.

A CAD model was created to define the final dimensions of the design (see Figure 2.2-4). Individual components were modeled and assembled in Autodesk Inventor 2013 (Autodesk Inc, CA, US). A CAD model of a woman was used for dimensional reference. During this stage, static stress analysis of the bed frame was performed to guarantee structural support. Using a simulated weight of 130 kg, the frame obtained a safety factor of 12, which surpassed the recommended value of 8 for suspended loads in a medical device (CAN/CSA- C22.2 No.601.1-M90) [55].

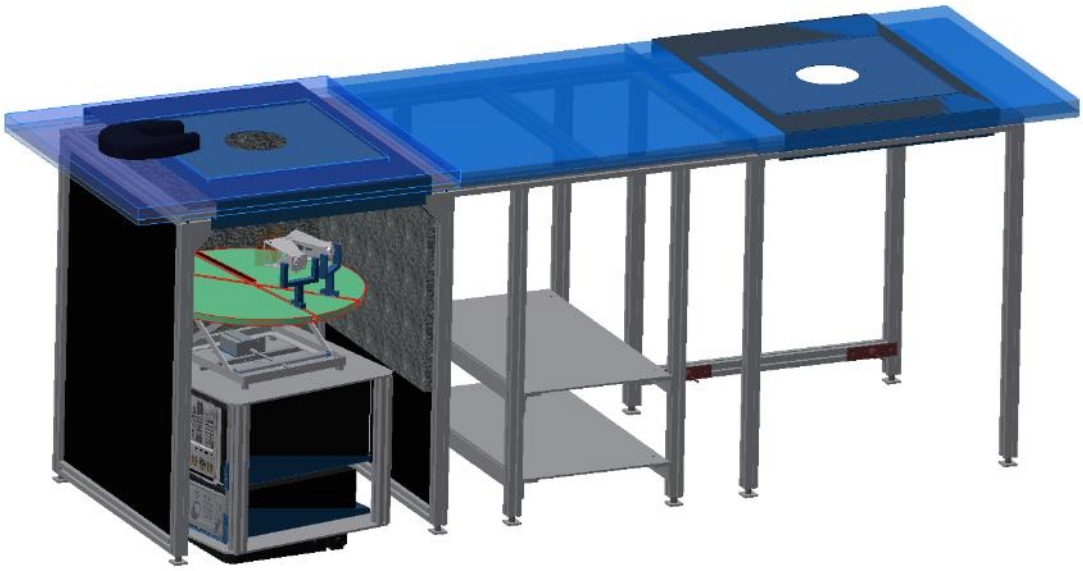

Figure 2.2-4 CAD render of the BIRR design concept, a breast-imaging rotating-radar system.

The panel of experts approved the final design in February 2014, leading the way for system manufacture.

### 2.2.4 System manufacture and integration

System manufacture began with the sourcing of components. Commercial devices often provide better performance, are more reliable than built-in solutions [54]. Thus, purchasing off-the-shelf equipment was given preference over manufacturing custom items. The availability of commercial products expedited the project development.

When commercial products did not meet design expectations, custom solutions were manufactured at the Medical Devices workshop in CancerCare Manitoba. Detailed technical drawings were given to the workshop to assist construction. A design specification document was also prepared for ease of manufacture. The document provided a high-level description of the system structure, requirements, and expected performance.

Manufacture of the system was closely monitored. Monthly meetings at the workshop were held to provide direction. Gannt charts were used to coordinate and track project tasks. The final

components were delivered to the Non-Ionizing Imaging Laboratory at the University of Manitoba on June 2014. The integration of the workstation and graphical user interface marked the end of the manufacturing phase (November 2013 to July 2014). Figure 2.2-5 and Figure 2.2-6 show photos of the fully integrated BIRR system.

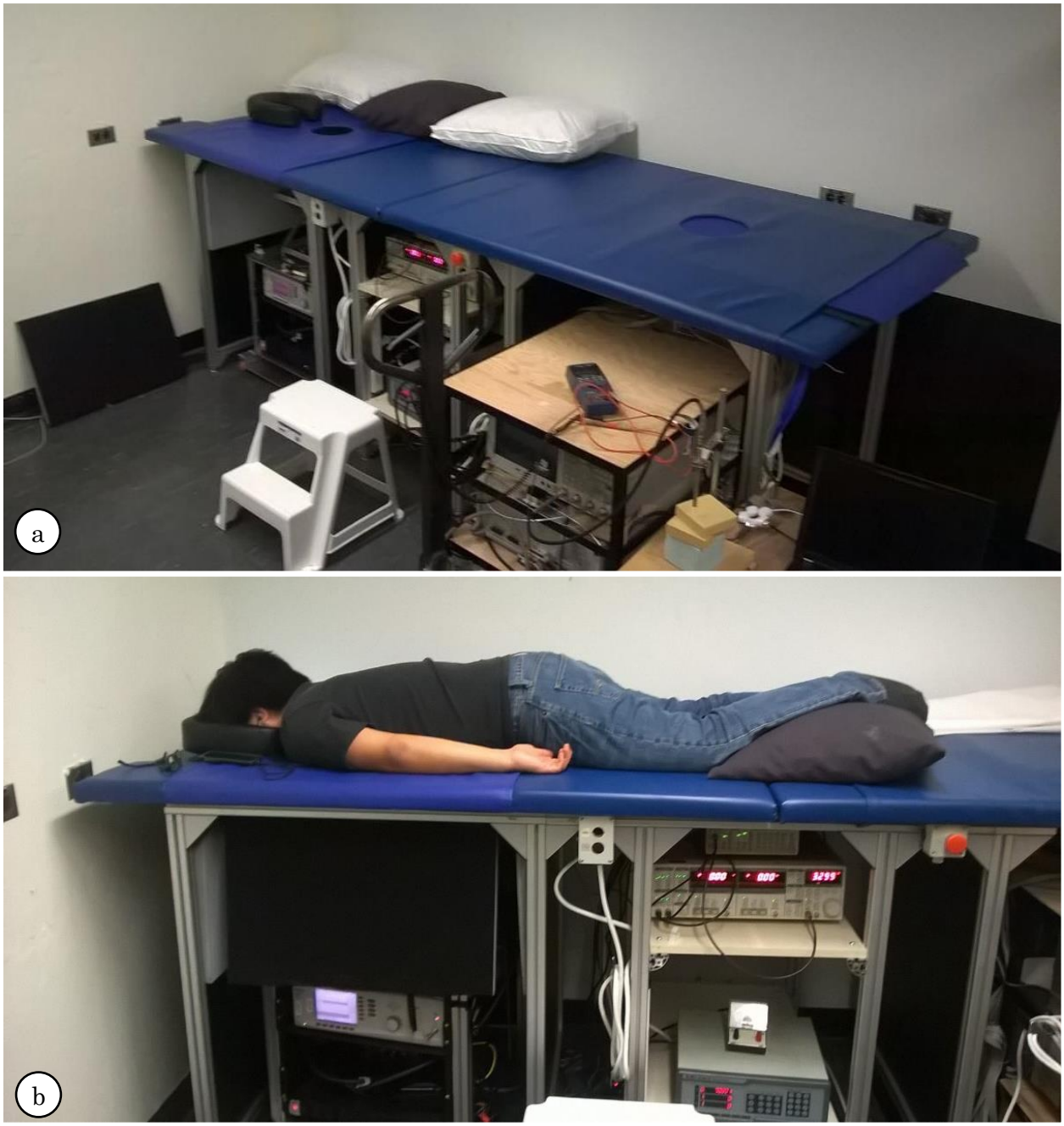


Figure 2.2-5 Photos of the manufactured BIRR system. a) Integrated system with a bed extension. A microwave tomographic system is installed to the right of the BIRR [16]. B) A volunteer demonstrates the position of the body during an inspection.

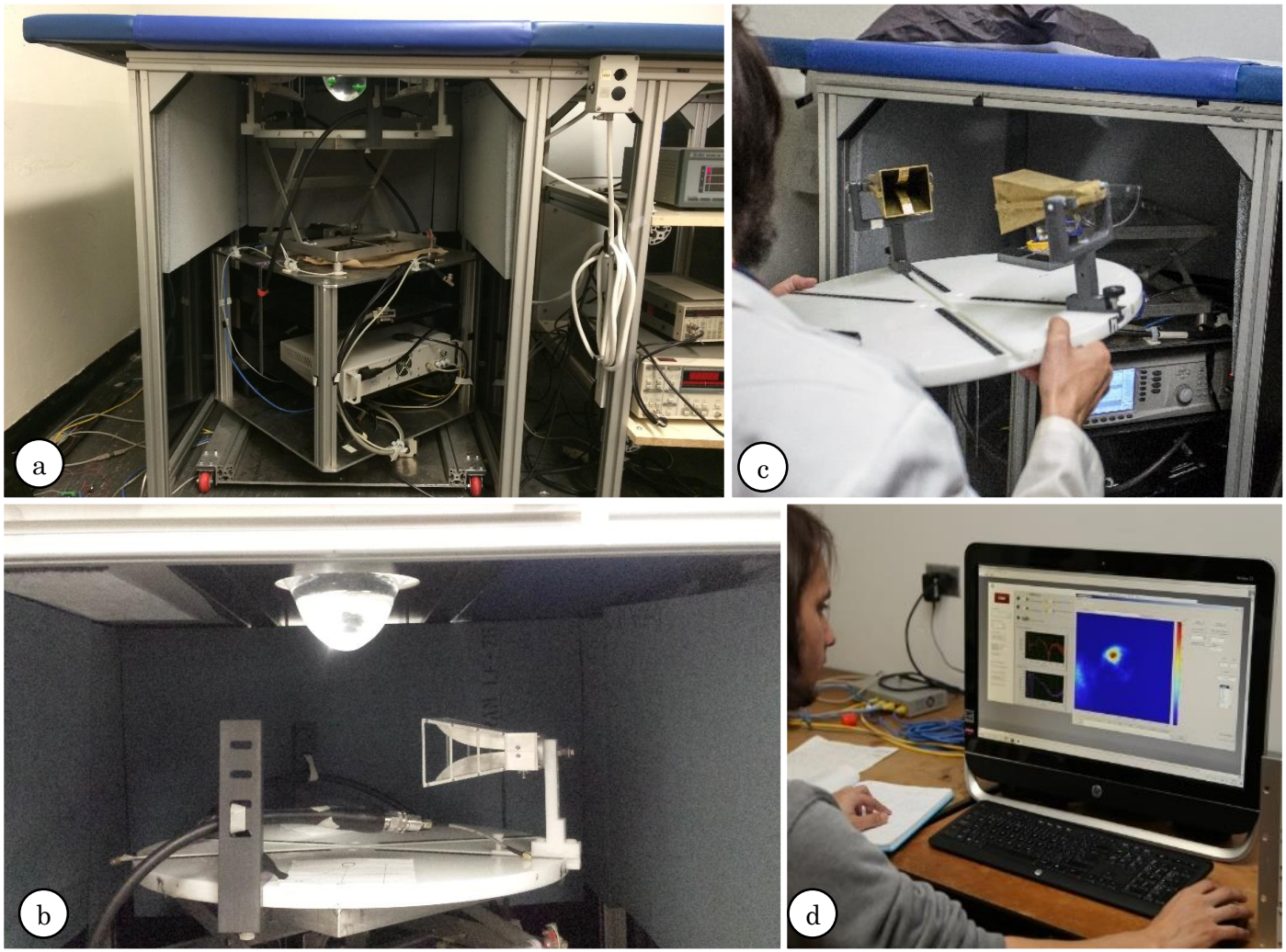


Figure 2.2-6 Integrated components of the BIRR system. a) Radar platform b) Imaging chamber with a single LB-20200-SF horn antenna in monostatic configuration. A hemispherical phantom is pendant through the breast aperture. The collapsed lift stage provides enough room to connect and calibrate RF cables. Radar absorbent material covers the chamber. c) Tabletop replacement with custom-made horn antennas in monostatic configuration. The modular approach of the BIRR permits modifications of the antenna configuration within minutes d) Workstation with the dedicated graphic user interface.

## 2.3 System components and materials

The BIRR system is divided into four subcategories: inspection bed, radar module, security devices and the control workstation. Figure 2.3-1 shows the schematic of the system. The following section will describe the characteristics of each component.

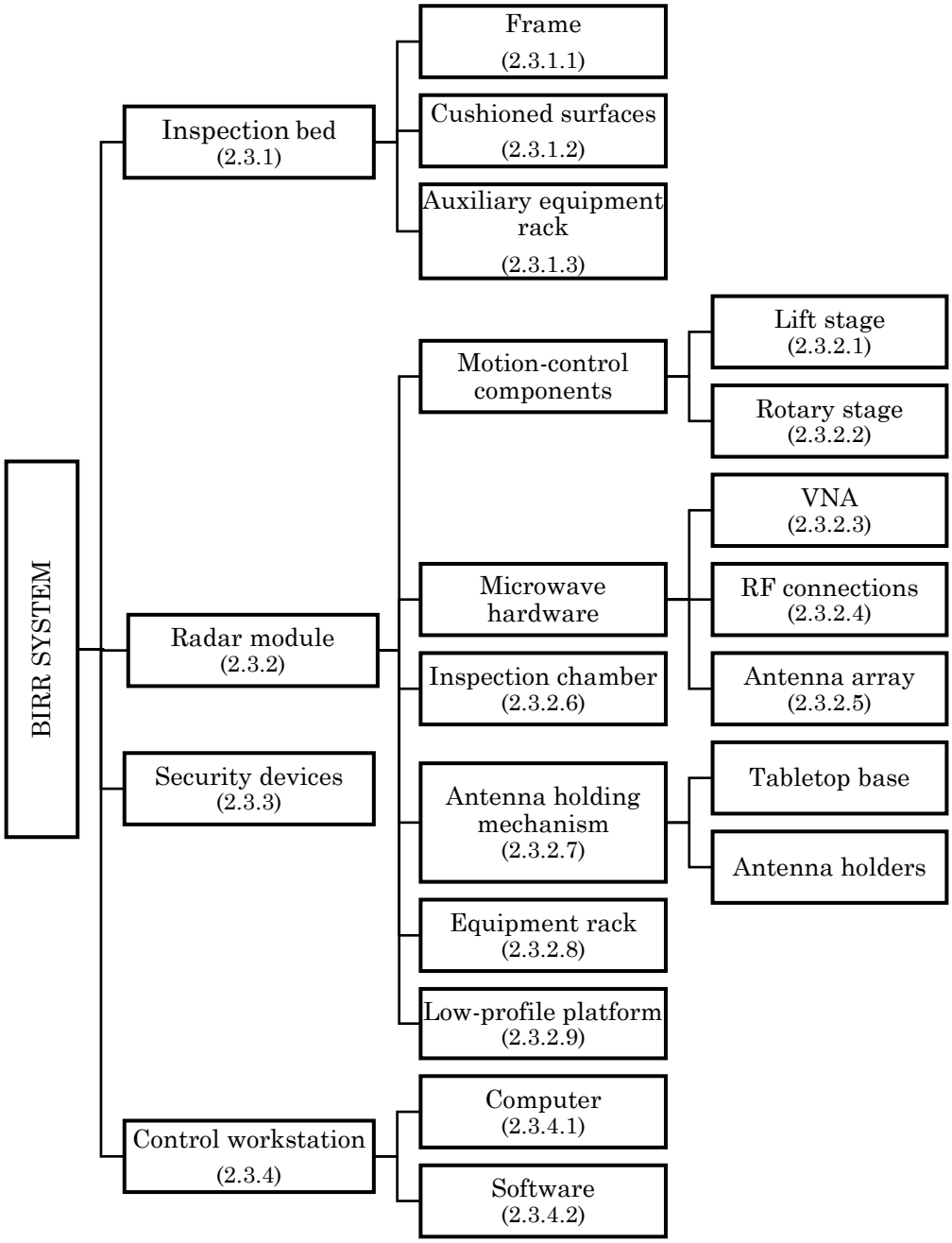


Figure 2.3-1 Schematic of the modules in the BIRR system.

### 2.3.1 Inspection bed

The inspection bed is designed to support a woman in the prone position during the scan. An aperture of 17 cm in the middle of the bed allows for one breast to fall into the radar device beneath the bed. The bed is 102 cm wide, 191 cm long and 102 cm tall. The bed was designed to be 3 cm wider than a standard twin size bed [56]. The radar equipment determined the height of the bed. Three main components form the inspection bed: Frame, cushioned surfaces, and an auxiliary equipment rack.

#### 2.3.1.1 Frame

The frame provides the structural support to the system. The material used for the frame is a commercial extruded aluminum profile (Profile 8, item America LLC, Hagerstown, MD, USA). The profile has a cross section of 4 × 4 cm, a minimum tensile strength of 245 $N/mm^2$ and a density of 2.7 $kg/dm^3$ [57]. The commercial profile was selected for its versatility and ease of assembly. Instead of welding points, the aluminum beams are fastened together, which allows to detach the beams and perform cost-effective adjustments. The versatility of the frame assembly was useful for centering the radar module to the breast aperture, adjusting the position of the docking mechanism in the low-profile platform (Section 2.3.2.9), and for the optimization based on user feedback (Section 2.4.3).

#### 2.3.1.2 Cushioned surfaces

The body of the user rests on 1-cm-thick plywood planks covered with a 2-cm-layer of high-density foam. A high-strength canvas material supports the chest region above the radar equipment. An ABS plate below the canvas provides additional support. The combination of ABS and canvas material covers only 2 cm of the breast length. A massage-style headrest supports the weight of the user's head. The headrest is not attached to the bed; it slides on the bed surface to adapt to the physical proportions of different users.

All the surfaces on the bed can be cleaned with common detergents. During clinical trials, medical-grade crepe paper was placed on top of the bed and discarded after each use.

As it will be explained further in Section 2.4.3, chest and head support sections were optimized to improve the comfort of the inspection bed.

#### 2.3.1.3 Auxiliary equipment rack

An equipment rack sits underneath the middle section of the inspection bed. The rack is meant to store all calibration tools along with any equipment that is not required to rotate with the rotary stage (i.e., rotary stage driver).

### 2.3.2 Radar module

The radar module is composed of the data-acquisition components: lift stage, rotary stage, microwave equipment, inspection chamber, equipment rack and a low-profile platform. The radar module is centered underneath the breast aperture of the inspection bed.

#### 2.3.2.1 Lift stage

The purpose of the lift stage is to elevate the antenna array, increasing the volume of the breast interrogated during a scan. The lift stage simultaneously elevates all antenna elements and their respective support structures and cable connections. The lift stage is composed of a scissor lift mechanism driven by a stepper motor.

As previously mentioned, employing a scissor lift has several advantages compared to the other elevation mechanism. Scissor lifts have a small vertical footprint when collapsed, but can provide a long travel range. Additionally, motors, gears, and actuators are located underneath the platform on top of the lift stage; this mechanism does not interfere with the OD. Design and manufacture of the scissor lift was commissioned to Andy Egtberts, from the Medical Devices workshop at CancerCare Manitoba. Technical drawings are shared with his permission in Appendix 7.6.

The worm gear in the scissor lift mechanism is driven by a 1.8° bi-polar stepper motor with an integrated driver (Silverpack 23 CE-5718L-01P, Lin Engineering, CA, USA). The lift stage has a greater resolution (worm gear steps to scissor lift height) when the scissor lift is extended. This is an intrinsic characteristic of scissor lifts. A conversion table was obtained to transcode motor steps positions to lift stage heights values (Appendix 7.5). The stepper motor absolute zero position (home position) is calibrated with a limit switch. The switch is placed in the travel path of the scissor lift's piston. When the scissor lift is collapsed, the piston presses against the limit switch and an inbuilt command in the IMC23-L01 resets the microstep counter.

Based on the product specifications established in Section 2.2.2, a set of design requirements were established for the manufacture of the lift stage. A travel range of at least 12.8 cm was required to account for 95% of the possible breast lengths. A load capacity above 6.5 kg was desired to support the weight of the antenna array, cables, and corresponding support mechanisms, and provide a safety factor above 3. In discussion with the panel of experts, the requirements for the accuracy and precision of the lift stage were estimated to be smaller than 2 mm and 1 mm.

The performance of the lift stage was evaluated to validate its compliance to design requirements. Characterization experiments for the range, speed, and load performance of the lift stage are detailed in Appendix 7.5 and summarized in Table 2.3-1. The lift stage meets the initial design requirements.

Table 2.3-1 Lift stage specifications

| Specification | Value |
|---|---|
| Platform surface area | 35 cm × 35 cm |
| Height (collapsed) | 11.2 cm |
| Height (extended) | 27.8 cm |
| Travel range | 16.62 cm ± 0.2 cm |
| Extension time | 121 s ± 0.2 s |
| Load capacity | 8.8 kg ± 0.01 kg |
| Speed (maximum) | 0.28 cm/s ± 0.06 cm/s |
| Speed (minimum) | 0.07 cm/s ± 0.01 cm/s |
| Power | 12 V to 40 V DC |
| Maximum current | 3 $A_{peak}$ |

#### 2.3.2.1.1 Positioning performance of the lift stage

During the design phase, positioning specifications were estimated in discussion with the panel of experts. The design requirements for the lift stage required an accuracy of 2 mm and a repeatability error lower than 1 mm. The positioning performance of the lift stage was studied to determine compliance with these design specifications.

The lift stage was programmed to reach eight target positions $\boldsymbol{P_i}$ along the axis of operation: 10.85, 60.5, 83.8, 95.3, 120.4, 133, 140.3 and 154 mm. Each target position was reached five times in each direction. Using a digital caliper (CP20003, Capri Tools, CA, USA) a total of 80 actual positions $\boldsymbol{P_{ij}}$ were measured. The reported accuracy error on the caliper was 0.01 mm, however, this value was closer to 0.02 mm when validated with a known value. To minimize human error, the ends of the caliper were fixed to the top and base of the scissor lift.

Positional deviations $\boldsymbol{x_{ij}}$ were calculated as the difference between the actual positions and the target positions. Accuracy and repeatability values were obtained following ISO 230-2 [58] definitions reported in Appendix 7.1. A coverage factor of 2 was used to calculate the standard uncertainties and repeatability values (Appendix 7.2). As per ISO 230-9:2005, uncertainties in the measurement of accuracy values originate from alignment errors and errors in the measuring tool [59]. Uncertainties in the measurement of repeatability values originate from environmental variations (e.g. thermal drift) [59]. The results of the lift stage axis performance are summarized in Table 2.3-2. Figure 2.3-2 shows the positioning performance along the travel range of the scissor lift.

Table 2.3-2 Lift stage positioning performance

| Parameter | Equation* | Symbol | Value (mm) | Uncertainty* (mm) |
|---|---|---|---|---|
| **Bi-directional accuracy** | A.18 | $\boldsymbol{A}$ | 2.03 | 0.03 |
| Unidirectional accuracy (Elevation) | A.17 | $a\uparrow$ | 1.08 | 0.03 |
| Unidirectional accuracy (Descent) | A.17 | $a\downarrow$ | 0.83 | 0.03 |
| Bi-directional systematic deviation | A.15 | $E$ | 1.81 | 0.03 |
| Unidirectional systematic deviation (Elevation) | A.14 | $e\uparrow$ | 0.94 | 0.03 |
| Unidirectional systematic deviation (Descent) | A.14 | $e\downarrow$ | 0.71 | 0.03 |
| Range of the mean bi-directional deviation | A.16 | $M$ | 0.34 | 0.03 |
| **Bi-directional repeatability (precision)** | A.13 | $\boldsymbol{R}$ | 1.92 | 0.01 |
| Unidirectional repeatability (Elevation) | A.11 | $r\uparrow$ | 0.24 | 0.01 |
| Unidirectional repeatability (Descent) | A.11 | $r\downarrow$ | 0.20 | 0.01 |
| Maximum reversal of an axis | A.7 | $B$ | 1.81 | 0.01 |
| Mean reversal of an axis | A.8 | $\bar{B}$ | -0.73 | 0.01 |
| Mean axis offset | A.19 | $\bar{\bar{X}}_{off}$ | -0.54 | 0.03 |

**Equations for positioning parameters and uncertainties are defined in Appendix 7.1 and Appendix 7.2*

The lift stage failed to meet the initial design requirements when operated in both directions. The bidirectional accuracy and repeatability of the system are 2.03 ± 0.03 mm and 1.92 ± 0.01 mm respectively. The deviation curve shown in Figure 2.3-2 indicates that accuracy and precision errors are greater at lower heights, and diminish at higher positions. This is attributed to the increase in step resolution as the scissor lift expands.

The high values of the mean reversal ($\bar{B}$) and maximum reversal ($B$) are caused by a combination of backlash and hysteresis. These are the major contributors of deviations in bidirectional calculations. The effects of reversal can be seen in Figure 2.3-2 as the separation between the mean forward and reverse values.

The stage has better performance under unidirectional movement, particularly during the reverse direction (descent). When only operated in descent, the accuracy and repeatability of the stage are 0.83 ± 0.03 mm and 0.20 ± 0.01 mm, respectively. During descent, initial design requirements were met. The implications of this results will be studied in Chapter 3.

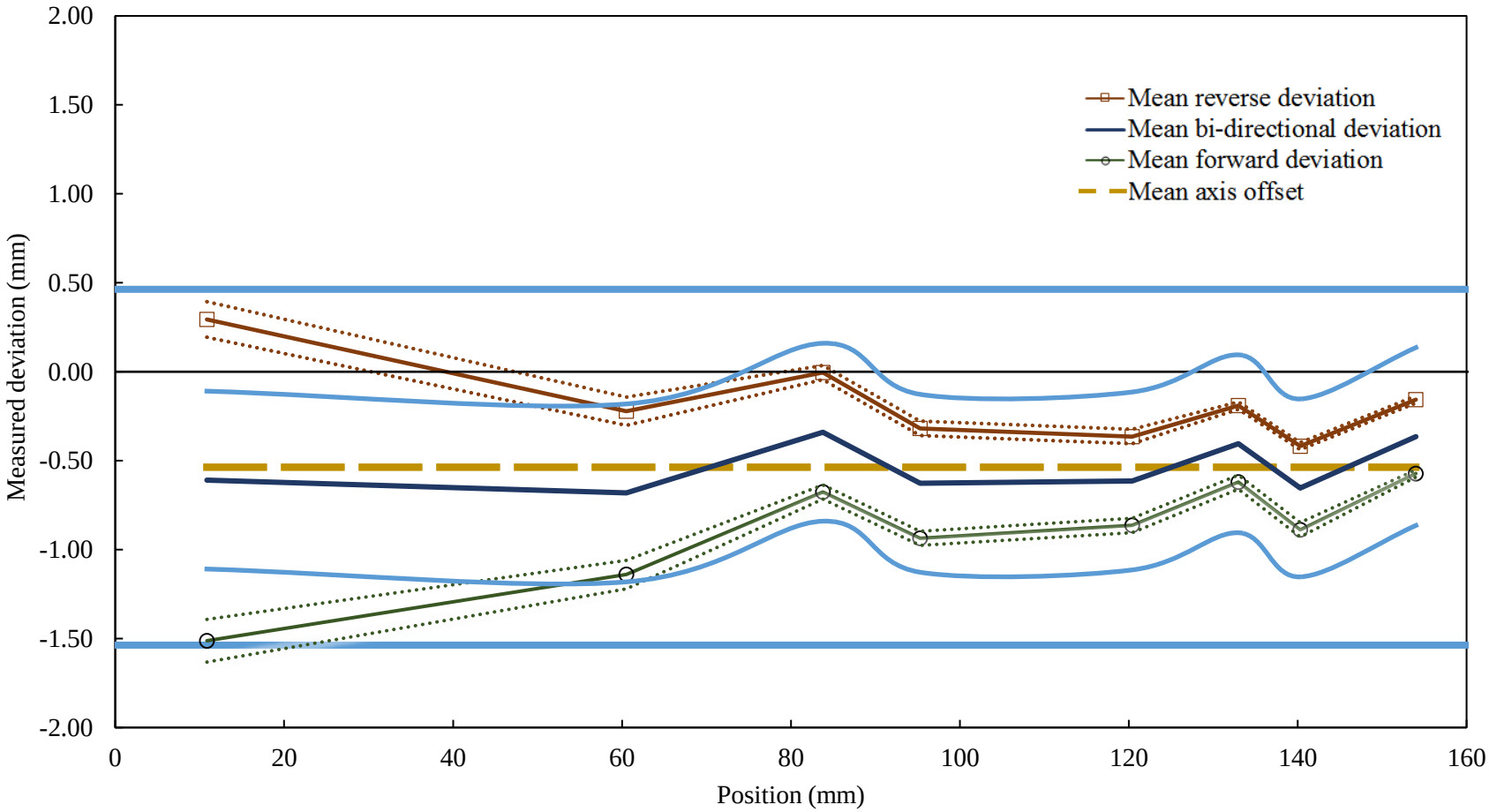


Figure 2.3-2 Plot of positional deviations of the lift stage. A total of eight locations were reached five times in the forward and reverse direction. Positional deviations were calculated by subtracting commanded and measured lift stage heights. Motion-direction affects the rotary stage with a maximum reversal error of 1.81 mm. The measurements were performed from the collapsed (0 mm) position to fully extended (160 mm). A coverage factor of two was used to account for measurement and performance uncertainties. Reversal and repeatability errors decrease at higher lift stage heights, where a greater amount of worm gear steps is required to increase the height of the scissor lift (better resolution). A mean axis offset was calculated at −0.54 mm. Solid blue lines indicate the accuracy design criteria of 2.00 mm and the dashed blue lines show the precision design criteria of 1.00 mm for bidirectional movement.

#### 2.3.2.2 Rotary stage

A motorized rotary stage moves the entire radar module along the azimuth plane relative to the center of the target (RAK350, Zolix Co LTD, Beijing, China). Placing the stage underneath the radar module required a device with a small vertical profile (under10 cm), a wide table surface (greater than 30 cm) for stability, and enough load capacity to support the weight of the radar module (calculated at 60 Kg). The specifications for the rotary stage selected are summarized in Table 2.3-3 [60].

Table 2.3-3 Rotary stage specifications.

| Specification | Value. |
|---|---|
| Table surface diameter | 35.0 cm |
| Width | 37.25 cm |
| Height | 7.35 cm |
| Length | 39.0 cm |
| Load capacity | 100 kg |
| Travel range | 358.2 ° |
| Worm gear ratio | 1: 320 |
| Maximum speed | 11.25 °/s |
| Maximum acceleration | 7.8 °/s$^2$ |
| Power | 120 to 240 $V_{ims}$ at 60 Hz |
| Maximum current | 2.4 $A_{rms}$ |

Movement of the rotary stage is controlled through a worm gear connected to an integrated 1.8° stepper motor and a corresponding stepper motor driver (SC300, Zolix Co LTD, Beijing China). The worm gear ratio of 1:320 allows to move the stage in increments as small as 0.007°. A hard stop serves as a reference home position (i.e., absolute 0º). The stage has an effective range of 357.8°, after which the hard stop engages and prevents reverse movement. During a scan, the radar module is rotated in cycles of forward (clockwise) and reverse (counter clockwise) motion to reduce inspection time and prevent cable torsion.

The stage has an aperture of 15 cm through which the power cables are routed. Routing cables through the axis of rotation eliminates the risk of tangling cables.

#### 2.3.2.2.1 Positioning performance of the rotary stage

During the design phase, positioning specifications were estimated in discussion with the panel of experts. The design requirements for the rotary stage required an accuracy of 2° and a repeatability error lower than 1°. The positioning performance the rotary stage was characterized along its entire travel path.

The rotational movement of the stage was measured using a photogrammetric approach (Figure 2.3-3). The rotary stage was programmed to reach 72 target positions, separated by 5° each. Every target position was reached six times in the forward (clockwise) and reverse (counter-clockwise) direction. A printed image with three circles was used as a marker and placed on top of the rotary stage. The displacement of a marker was captured with a camera placed one meter above the tabletop (Cannon EOS 6Dm, Ōta, Tokyo, Japan). The position of each marker relative to the center of rotation was detected using a MATLAB image-processing program (Figure 2.3-4a).

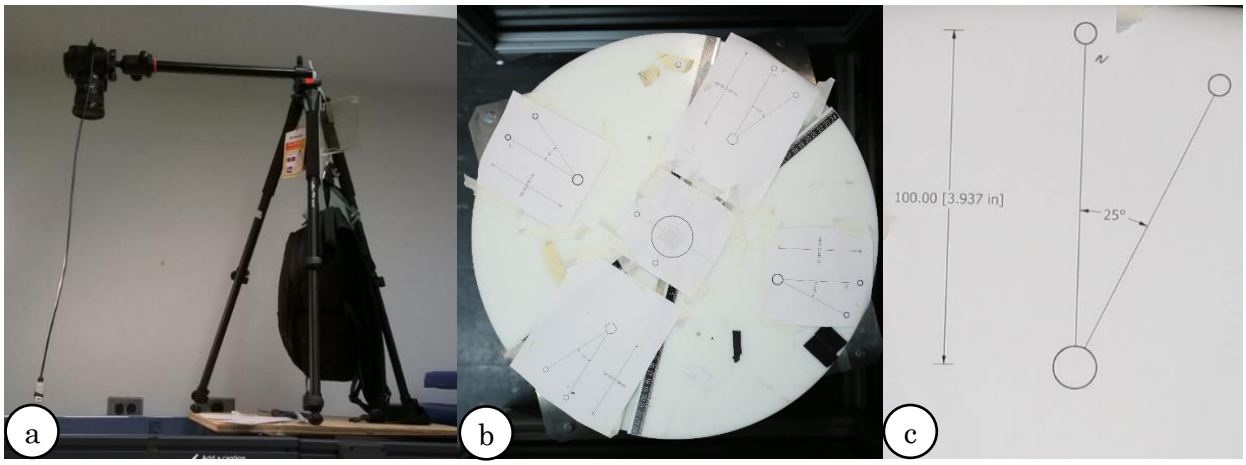


Figure 2.3-3 Photogrammetric evaluation of the rotary stage performance. a) Camera set up to take photos after each movement of the rotary stage b) Printed figures placed on top of the tabletop and used as a tracker. c) The tracker is formed of well-defined circles that were detected by an image-processing algorithm. The reference angle of 25° on the printed figure was used to calibrate each image.

The photos were processed to remove distortions that could induce erroneous measurements. Focal aberrations, such a barrel and pincushion distortions, were removed using a photo-editing software (DxO Optics Pro 11, DxO Labs, Boulogne-Billancourt, France).

Additionally, each photo was calibrated to a reference angle formed by the printed figure (Figure 2.3-4c). Variation in the angle of the printed figure was used to compensate for image distortions.

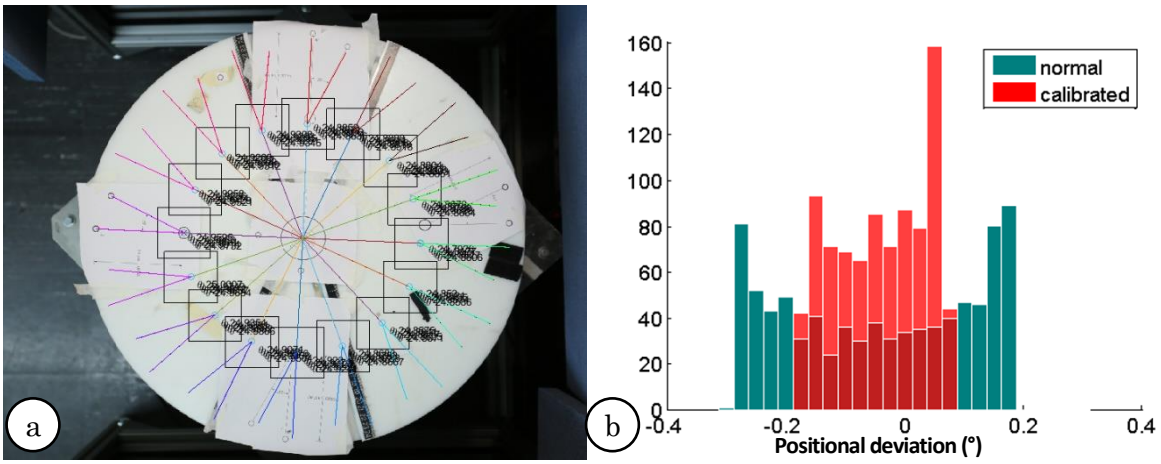


Figure 2.3-4 A MATLAB algorithm was developed to track the position of the markers a) Rotary stage photo with the super-imposed position of 80 trackers. b) Histogram of the measured positional deviations before and after calibration to remove image distortions ($n$ = 864)A total of 864 photos were taken and processed to obtain the position of the marker. Positional deviations were calculated as the difference between the programmed positions and the measured position of the marker. As with the lift stage evaluation, the parameters for accuracy, repeatability of the rotary stage were associated uncertainties were calculated following the industry standard ISO-230-2 [58]. A coverage factor of two was used to obtain an expanded uncertainty (a parameter akin to the standard deviation). As previously explained, uncertainties in the measurement of accuracy values originate from alignment errors and errors in the measuring tool, while uncertainties in the measurement of repeatability values originate from environmental variation [59].

Table 2.3-4 shows that the rotary stage has a bidirectional accuracy of 0.26° ± 0.05°and a repeatability of 0.08° ± 0.01°. Minimal reversal values were detected. The biggest contributor to the accuracy error was the range of the mean deviations: the difference between the highest and lowest points in the bidirectional deviations.

Table 2.3-4 Rotary stage positioning performance.

| Parameter | Equation* | Symbol | Value (°) | Uncertainty (°)* |
|---|---|---|---|---|
| **Bi-directional accuracy** | **A.18** | $\boldsymbol{A}$ | **0.26** | **0.05** |
| Unidirectional accuracy (forward) | A.17 | $a\uparrow$ | 0.26 | 0.05 |
| Unidirectional accuracy (reverse) | A.17 | $a\downarrow$ | 0.25 | 0.05 |
| Bi-directional systematic deviation | A.15 | $E$ | 0.23 | 0.05 |
| Unidirectional systematic deviation (forward) | A.14 | $e\uparrow$ | 0.23 | 0.05 |
| Unidirectional systematic deviation (reverse) | A.14 | $e\downarrow$ | 0.23 | 0.05 |
| Range of the mean bi-directional deviation | A.16 | $M$ | 0.23 | 0.05 |
| **Bi-directional repeatability (precision)** | **A.13** | $\boldsymbol{R}$ | **0.08** | **0.01** |
| Unidirectional repeatability (forward) | A.11 | $r\uparrow$ | 0.07 | 0.01 |
| Unidirectional repeatability (reverse) | A.11 | $r\downarrow$ | 0.05 | 0.01 |
| Maximum reversal value of an axis | A.7 | $B$ | 0.02 | 0.01 |
| Mean reversal value of an axis | A.8 | $\bar{B}$ | -0.01 | 0.01 |
| Mean axis offset | A.19 | $\bar{\bar{X}}_{off}$ | -0.04 | 0.05 |

**Equations for positioning parameters and uncertainties are defined in Appendix 7.1 and Appendix 7.2*

Figure 2.3-5 shows the deviation curve for the rotary stage. The sinusoidal deviation pattern indicates the presence of a non-random error attributed to wobble of the rotary stage, which is the tilting of the axis of rotation relative to its ideal axis. Wobble is linked to imperfections on the bearings. The proximity between curves indicates low reversal and repeatability errors.

The rotary stage meets the design requirements of a repeatability under 0.1°, but fails to meet the design requirement of 0.2° accuracy. The reported manufacturer's specification of repeatability lower than 0.003° was not supported by the characterization study. The greatest effect of this positioning deviation is present at the edge of the circular tabletop (with a radius of 250 mm), where the antennas are supported, a positioning deviation of 0.26° generates a linear error 1.13 mm. The implications of this performance will be studied in Chapter 3 of this thesis.

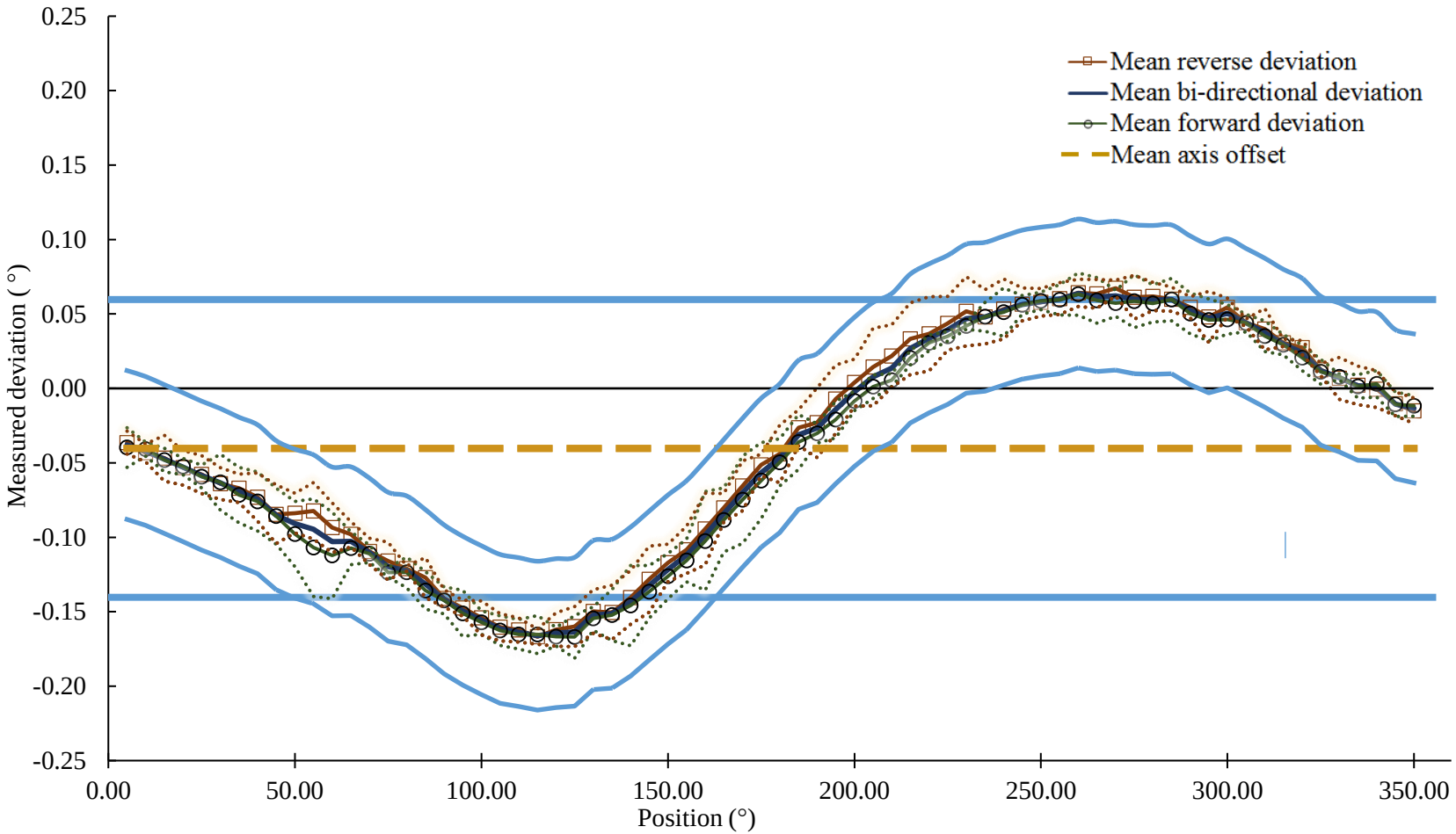


Figure 2.3-5 Plot of positional deviations of the rotary stage. 72 locations were reached six times in the forward and reverse direction. A systematic accuracy error of 0.26 ° is present in the shape of a sinusoidal curve, whit its apex at 115° and 260°. The proximity between forward (clockwise) and reverse (counter-clockwise) curves indicate higher levels of repeatability and minimal presence of reversal (backlash). The stage has a mean positioning axis offset of −0.04 °. Solid blue lines indicate the accuracy design criteria of 0.2° and the dashed blue lines show the precision design criteria of 0.1° for bidirectional movement

#### 2.3.2.3 Vector network analyzer (VNA)

The system used the VNA as the microwave generator and recording device. The VNA model is a two-port Planar 804/1 with a dynamic range of 140 dBm, an output power of 10 dBm (10 mW) and an operating frequency range of 100 kHz to 8 GHz (Planar 804/1, Copper Mountain Technologies, IA, USA). During a scan, measurements were taken at 1001 frequency points over the range of 1 GHz to 8 GHz. To lower the system noise floor, an intermediate frequency (IF) bandwidth of 10 kHz was used. Measurements are performed every 300 ms in a continuous-sweep mode to maintain internal components at a constant temperature.

The Planar 804/1 was controlled through an external computer, where reflection measurements were also stored. The button-panel interface found on most commercial VNAs was unnecessary for the BIRR application. The lack of the button-panel interface reduced the cost, and dimensional footprint of the device and its absence on the Planar 804/1 is a benefit.

Full port VNA calibration was employed to remove imperfections in the reflection measurements. An automatic calibration kit exposed the system to short, open, and load standards (ACM8000T, Copper Mountain Technologies, IA, USA). Using the standards, a correction vector was calculated and applied to each frequency point of the VNA measurement range [61]. The calibration was performed at the end of each cable assembly (2.3.2.4) and the process required 10 minutes per cable assembly. To ensure accuracy and repeatability of measurements, the VNA was calibrated before every use of the BIRR system. In a clinical setting, this calibration can be performed minutes before the subject examination.

#### 2.3.2.4 RF connections

Two cable assemblies carry the ultra-wideband signals between the VNA ports and the antenna array. Each assembly is composed of a 1.5 m long, type-N, phase-stable cable (N9910X-810, Keysight, CA, USA), an N-to-SMA adapter (PE9083, Pasternack Enterprises Inc, CA, USA), and a 1.5 cm long hand-formable SMA-to-SMA cable (CCSMA18-MM-141-3, Crystek Corporation,

FL, USA). The rugged phase-stable cable provides a robust connection to the VNA while reducing the effects of temperature related drifts. The flexible, hand-formable SMA cable at the end of the assembly facilitates the antenna connection and the calibration procedure. Every component of the assembly is rated for a maximum frequency of at least 8 GHz.

#### 2.3.2.5 Antenna array

The system employs two double-ridged horn antennas. The model employed is rated from 2 GHz to 20 GHz with a typical gain of 12 dB (LB-20200, AINFO, Hong Kong, China). The array operates in air to reduce the mechanical complications of impedance-matching liquids. The bandwidth of the antenna covers the range of 2 GHz to 8 GHz shown by J. C. Lin [53] to provide the optimal balance of resolution and attenuation inside body tissues.

Selection of the antenna model was not a trivial task. The author compared the performance of Vivaldi and elliptical monopole antennas, as well as custom-made and commercially-available horn antennas [36], [50], [62]. The results of these studies are summarized by in [52], where it is shown that for the LB-20200 exhibits superior performance in air compared to the antenna models previously mentioned. D. Rodriguez also shows that the LB-20200 exhibits a phase delay which induces an offset $y = p_1 x + p_2$ with values $p_1 = 1.18$ and $p_2 = 14.8$ cm [52].

An array of up to eight simultaneous LB-20200 antennas can be mounted in the BIRR system. This constraint is in part, determined by the antenna dimensions. The antennas are 12.7 cm long, and the bore has a height of 7.8 cm and a width of 10.4 cm. For a 2D circular geometry, the configuration of antenna elements approximates the shape of an equilateral polygon centered on the OI (Figure 2.3-6). Using the width of the horn and the length of each side, the number of antenna elements $n$ can be expressed as shown in Equation 2-1.

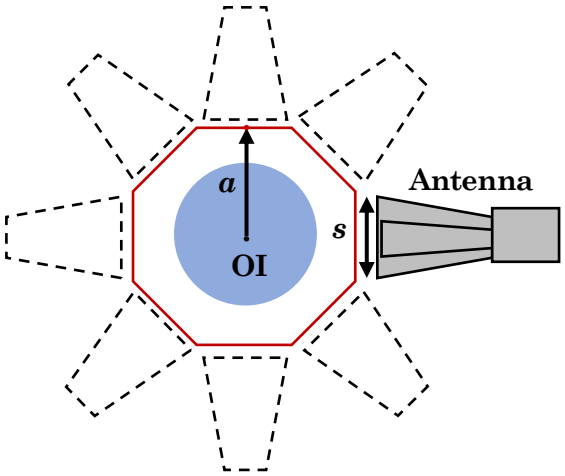


$$n = \frac{\pi}{\tan^{-1}(\frac{s}{2a})} \qquad (2\text{-}1)$$

Figure 2.3-6 Illustration of an array of horn antennas surrounding a circular OI. The configuration resembles the shape of a polygon.The apothem $a$ is the sum of the radius of the target and reactive near field distance. The length of the sides $s$ is given by the width (10.4 cm) of the antenna bore.

Figure 2.3-6 suggests that the number of antenna elements is inversely proportional to their width of the antenna bore, and directly proportional to the apothem of the polygon formed by the antenna array. The apothem is expressed as the distance from the center of the OI to the midpoint of the antenna front edge. As described in 2.3.1.1, the bed aperture is wide enough for targets of up to 8.5 cm in radius. Using the LB-20200, an additional separation of at least 4 cm is required to avoid interference with the reactive near-field region of the antenna. Following equation 2-2, the maximum number of simultaneous antennas elements in the array is close to eight.

$$\frac{\pi}{\tan^{-1}\left(\frac{antenna\ width}{2(r_{breast} + r_{reactive\ zone})}\right)} = \frac{\pi}{\tan^{-1}\left(\frac{10.4\ cm}{2(8.5\ cm + 4\ cm)}\right)} 7.96 \cong 8$$

#### 2.3.2.6 Inspection chamber

The inspection chamber surrounds the OD and prevents contamination due to spurious signals. The chamber is located underneath the inspection bed and encompasses the OI as well as the antenna array. During a scan, the breast is lowered into the chamber through an aperture on

the bed. The antenna elements move inside the chamber as they radiate the breast at different planes and azimuthal positions

To electromagnetically isolate the OI, the four walls surrounding the radar module are covered with radiation-absorbent material (RAM). The length of the RAM panels extends over the inspection chamber even when the lift stage is collapsed. The material reflects less than 17 dB of incident energy between 1 GHz and 20 GHz (Eccosorb AN-75, Emerson & Cuming Microwave Products, MA, USA).

#### 2.3.2.7 Antenna holding mechanism

The position and orientation of antenna elements, relative to the axis of rotation of the radar module, is determined by the antenna holding mechanism. The mechanism is composed of a tabletop base and antenna holders. The mechanism allows for individual antenna tilt, radial distance, and azimuthal angle adjustments. The ensemble lies on top of the lift stage, and it is surrounded by the inspection chamber.

The mechanism can be adapted to fit monostatic or multistatic antenna array configurations. All parts are made with a high-density polyethylene plastic to avoid detrimental interaction with the radiation pattern of the antenna array.

A circular tabletop, made of a single sheet of high-density polyethylene, serves as a base for the antenna array. The base has a radius of 25 cm and a thickness of 2.45 cm. Intersecting grooves cross the center of the tabletop and project to the end to the base. The center of the base aligns with the axis of rotation of the radar module.

For monostatic configurations, the angles between the grooves in the tabletop determine the azimuthal separation of antenna elements. Using a tabletop with a different pattern allows the modification of the azimuthal angle. The tabletop used in this system featured grooves intersecting at 35 degrees and 145 degrees. An additional tabletop was manufactured to have intersecting angles at intervals of 30 degrees. Figure 2.3-7 demonstrates the two tabletops side by side.

Individual antenna elements are supported with custom-made holders. The antenna holders suspend the antennas 11 cm above the tabletop base. The separation allows the system to scan objects of up to 13 cm of length without contacting the tabletop base.

Antenna holders are used to modify the tilt of the antenna elements. The two antenna holders shown in Figure 2.3-8 demonstrate tilt adjustment. The first example has a fixed tilt of 90 degrees. The second antenna holder can be adjusted to cover a range of -35 degrees to 35 degrees.

The base of the antenna holders is designed to slide along the grooves of the tabletop base. A pressure screw keeps the antenna at a fixed distance from the center of the base. Rules engraved parallel to each groove allow for accurate radial adjustment of the antenna elements. Figure 2.3-9 shows the components of the sliding assembly.

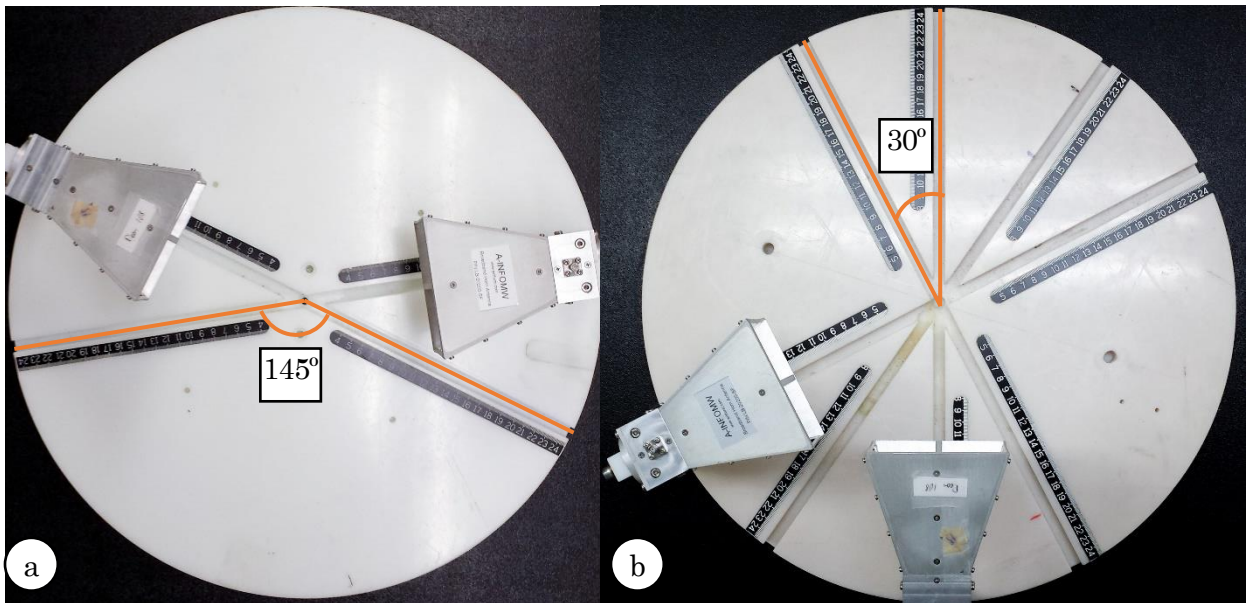


Figure 2.3-7 Tabletop configurations. The azimuthal separation of antenna elements can be adjusted using the grooves in the tabletop base. a) The main tabletop allows configurations of 35, 145 and 180 degrees. b) The secondary base provides, even more, configurations with grooves intersecting at 30, 60, 90, 120, 150 and 180 degrees.

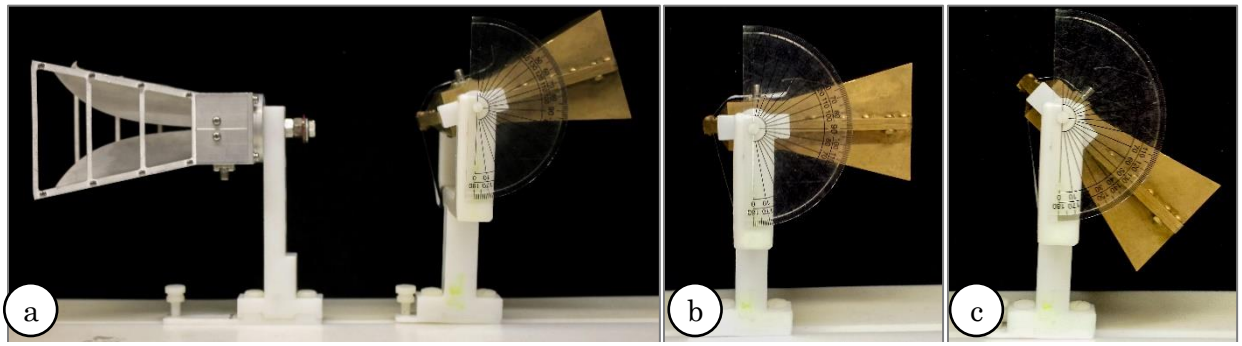

Figure 2.3-8 Two antenna holders for the BIRR with different antenna tilt. a) Right-angle holder and adjustable-tilt holder at 15 degrees. b) Adjustable-tilt holder at 90 degrees. c) Adjustable-tilt holder at −35 degrees.

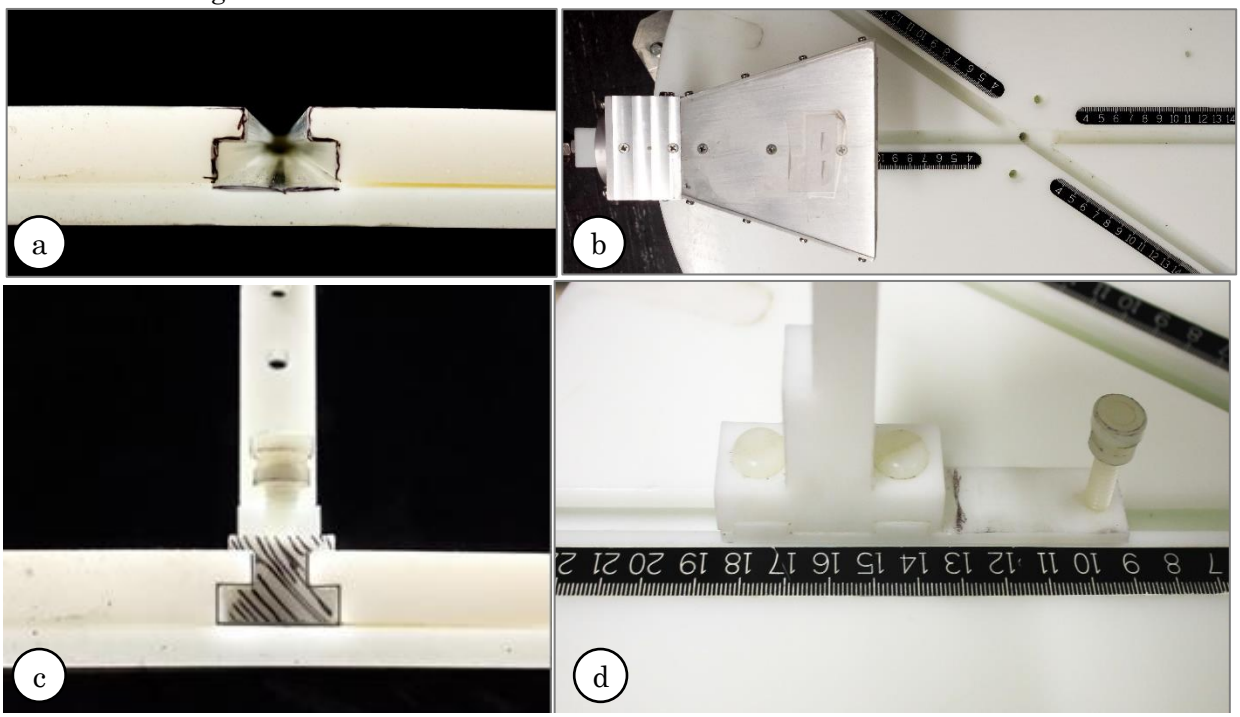

Figure 2.3-9. The slide mechanism used to adjust the radial position of antenna elements. a) T-Shaped groove runs along the tabletop. b) The base of the antenna holder fits the grooves with a clearance of 0.1 mm. c to d) Rules engraved along the grooves are used to adjust the position of the elements accurately. A thumb screw locks the antenna holder in place.

#### 2.3.2.8 Equipment rack

Microwave equipment is mounted within a typical 19-in rack. Items can be directly mounted to the rack or placed on steel shelves. The shelves are 16-gauge steel, with a depth of 36.8 cm and a load capacity of 90 kg. Multiple items can be accommodated along the 76 cm of height of the rack by modifying the number of shelves and the vertical separation between them. The rack was made of four aluminum profiles beams and 0.64-cm-thick aluminum plates at each end. The

structure is 43 cm tall, 56.5 cm wide and 56.5 cm deep. A surge protector (CPS-1215rms, Cyber Power Systems, MN, USA) was placed at the bottom of the rack to powers the microwave equipment. This model features 15-A of output power, surge suppression, and has been designed to filter electromagnetic and radio frequency noise from its cable lines.

The rack was fastened to the top plate of the rotary stage. Cable motion was virtually eliminated by rotating the equipment rack along with the antenna array. To avoid entanglement, power and communication cables from the equipment rack are routed through an opening in the center of the rack bottom plate.

#### 2.3.2.9 Low-profile platform

A custom-made low-profile platform supports the weight of the radar module and enables its transportation. The platform is made with a square 0.64-cm-thick steel plate as a base and two item aluminum beams at each side. An 8-cm-wide aperture in the middle of the plate permits routing of power cables out of the radar module. Four heavy-weight spinning wheels lift the platform only 2 cm from the floor to reduce the vertical footprint of the radar module. The wheels on the platform allow the radar module to be pulled out from under the inspection bed.

A docking mechanism in the platform guarantees precise alignment of the radar module with the breast aperture on the inspection bed. The docking mechanism consist of two anchoring rods and their respective holes. The 0.64-cm-wide, unthreaded holes run parallel to, and through the center of the aluminum beams on each side of the low-profile platform. The holes align with matching rods attached to the bed frame. Nuts on each of the rods adjust the separation between the frame and the radar module. By using two docking assemblies, the radar module was fully constrained. A photo of the docking mechanism is shown in Figure 2.3-10.

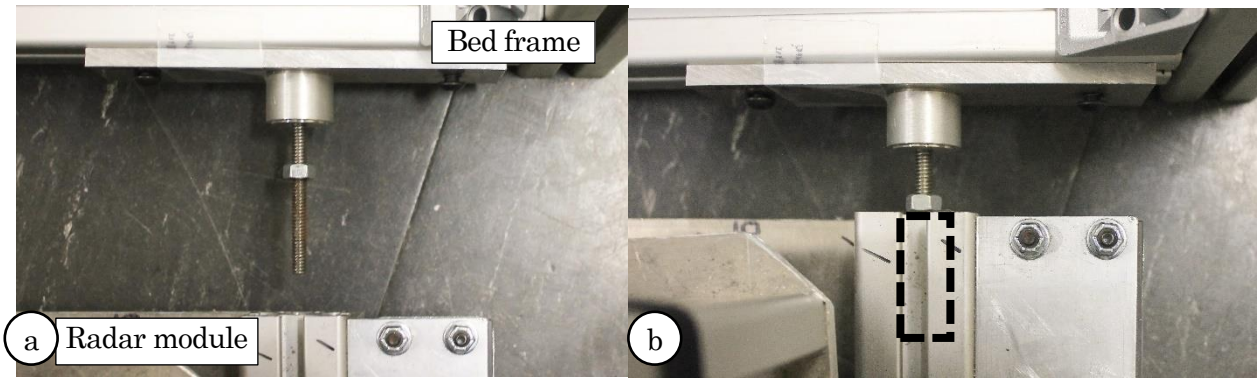

Figure 2.3-10 The docking mechanism aligns the radar module with the frame. a) Rods on the frame align with holes on the beams of the low-profile platform. b) Docked and aligned radar module.

### 2.3.3 Security devices

Four security mechanisms protect the user from injuries in the occurrence of a system malfunction: a limit stop in the lift stage, ground-fault circuit interrupter, power strips with over-voltage protection and manual emergency stops.

#### 2.3.3.1 Lift stage limit stop

A brake on the lift stage prevents the system from pressing the antenna array against the chest of the user. The stop is controlled by a limit-switch connected to the ground line of the lift stage stepper motor. The limit switch is placed past the standard travel path of the scissor lift piston. If the piston travels past a calculated safety distance, it will press the limit switch and interrupt the circuit, effectively shutting down the lift stage.

#### 2.3.3.2 Portable ground fault circuit interrupter

A dedicated, in-line ground circuit interrupter reduces the risk of electric shock. The device interrupts the flow of current in the system at a difference of 4 to 6 milliamps between lines and has a response time of 25 ms (25000 016-6 GFCI, Technology Research LLC, FL, USA).

#### 2.3.3.3 Hospital-grade power strips

The electrical components of the system are connected to two power strips with IEC 60601-1 compliance (PS-415-HGULTRA, Tripp Lite, IL, USA) [63]. Each power strip has four NEMA 5-

15R-HG hospital-grade outlets, safety covers and a built-in 15 A circuit breaker to avoid electrical overloads and shock hazards. The power strips connect to 120 V at 60 Hz AC.

#### 2.3.3.4 Emergency stops

The electrical circuit of the entire system can be manually interrupted with emergency stop switches (A22E-MP-01, Omron Automation and Safety, Kyoto, Japan). The emergency stops are meant to protect the equipment and user in case of a system malfunction. Two switches are installed on the left side of the inspection bed frame, where they are in close proximity to the user, and the assisting staff. When either switch is pressed, current flow is interrupted, halting the scan, movement of any mechanical parts, and microwave radiation. After an emergency shutdown, the VNA requires re-calibration and reconfiguration.

### 2.3.4 Control workstation

The control workstation coordinates the system re-positioning and microwave measurements. This module is divided into the computer, where the microwave measurements are collected, and the program that controls the operation of the system.

#### 2.3.4.1 Computer

The system uses a desktop PC running Windows OS 10, with a 3.6 GHz AMD A6-5400K CPU, and 4 GB of RAM. Communication with the system is carried through USB and LAN protocols.

#### 2.3.4.2 Software

A program was created to control the antenna motion and scatter measurement. At the beginning of a scan, the inspection plane is reached first by extending the scissor lift to a pre-defined vertical height. Then, the rotary stage positions the radar module on the first azimuthal position. Once the radar module has reach a desired location, reflection measurements are collected

with the VNA and stored on the computer. The process is repeated until all the programmed positions are reached.

A graphical user interface is used to initiate the scan process and to configure settings such as the number of scan positions, the speed of the mechanical actuators, VNA parameters and data storing locations. During a clinical examination, an additional graphical user interface is employed to register the name of the patient, and to initiate and stop the scan.

The program was written in C# by a summer student, Valerie Beynon and was developed in the summer of 2014 under the author's supervision. The program runs in any Windows OS.

## 2.4 System validation and results

After finalizing manufacture and integration, the BIRR was validated as a safe and comfortable medical device, fit for clinical examinations. First, the scan times of the system were determined. Next safety experiments evaluated the potential risk to which users of the system were exposed during normal and least-favorable scenarios. We conducted a phase 0 volunteer trial to determine perceived safety and comfort of the system. Next, an experimental setup tested the capability of the system to collect microwave reflections in a three-dimensional space. Finally, the diagnostic capabilities of the system were explored using a synthetic breast phantom and a state-of-the-art reconstruction algorithm.

### 2.4.1 Scan times

The length of a scan with the BIRR system is dependent on the number of antenna positions. During a scan, the antenna array was rotated in intervals from one angular position to the next. Each repositioning interval was composed of a displacement and a static phase. During displacement, the antennas were rotated to the next azimuthal position. The displacement component is dependent on the acceleration and speed of the rotary stage. During the static phase, the system was halted for 1.2 seconds. This dead time was required to account for jitter observed in the antenna array due to inertia. VNA measurement and recording times account for an additional 0.3 seconds in the static phase. Table 2.4-1 summarizes the total scan times for three typical number of probing points.

Table 2.4-1 BIRR scan times for a single azimuthal plane scan

| Antenna positions | Static time (s)* | Displacement time (s)* | Total scan time (s)* |
|---|---|---|---|
| 288 | 432 (46 %) | 511 (54 %) | 943 (100 %) |
| 144 | 216 (37 %) | 369 (63 %) | 585 (100 %) |
| 72 | 108 (28 %) | 282 (72 %) | 390 (100 %) |

**Time measurements accurate to ± 0.3 s*

For a multi-plane scan, the elevation times of the lift stage need to be considered. Due to the nature of the scissor-lift mechanism, movement times increase as the height of the stage increases. From the uppermost position of the lift stage, a 1 cm plane decrease requires 14 s. A movement of 16 cm (the complete travel range of the scissor lift) takes 121 s. Detailed lift stage travel times can be found in Appendix 7.5

Scans with the BIRR system aim to be completed under 30 minutes or 1800 seconds. A combination of three vertical planes with 144 antenna positions each can be completed in 1755 s to 1876 s depending on the vertical separation between planes. This configuration collects a total of 432 measurement points around the target. The number of antenna locations represents more than twice the value of the TSAR system reported in [30]. As mentioned previously, an increased number of probing locations is associated with higher quality images and an increased likelihood of detecting sources of abnormal microwave scattering [47], [52].

It is worth mentioning that scan times are, in part, constrained by the speed of the microwave hardware. Fast, yet reliable microwave equipment could be used to continuously record the scattered signals as the antennas move around the breast. In that case, the speed of the repositioning equipment would constrain the scan speed. The maximum movement velocity of the BIRR system is 11.25 °/s in the azimuthal plane and 0.28 cm/s in the vertical plane. At maximum velocity, the previous 432 measurement points could be collected in approximately 186 seconds or 3.1 minutes.

### 2.4.2 Safety validation

Safety experiments were conducted to obtain a Class III medical device designation from Health Canada. The experiments evaluate the performance of the BIRR under operation or simulated faults following the regulations for Canadian medical devices, the IEC 60601-1 standard [63]. Table 2.4-2 summarizes the results of these experiments.

Table 2.4-2 Summary of safety studies performed with the BIRR

| Experiment | Result | Outcome |
|---|---|---|
| Control-software accidental closing or process crash. | Motion actuators stop. User is at no risk of harm. | Pass |
| Sudden actuator disconnection. | Motion actuators stop. Control-software warns and interrupts scan. User is at no risk of harm. | Pass |
| Levels of RF power delivered. | Maximum specific absorption rate measured at 1.33 W/kg. Measured value is under the limit of 1.6 W/ kg as established by Health Canada [64]. | Pass |
| Chassis and earth leakage current. | Earth leakage current remains under 0.01 mA during normal and single fault operations. | Pass |
| Residual voltage levels. | After 1 s of power interruption, voltage levels are 0.05 mV in line, 0.02 mV in neutral and 0.0 mV in earth pins. | Pass |
| Motor temperature and instrument-frame voltage potential.<br><br>Temperature gradient limit is 50°C for idle condition and 20°C for least favorable conditions.<br><br>Maximum harmless voltage limit was set at 100 mV as per [63] assuming a worst-case-condition of a skin resistance of 1,000 Ω. | During normal conditions, temperature increases up to 5.5°C of the 50°C limit. Maximum voltage between an antenna and the bed frame is 1.0 mV, representing 1% of the harmless voltage limit.<br><br>During least favorable conditions, temperature increases up to 6°C of the 20°C limit. Maximum voltage between an antenna and the bed frame is 0.9 mV, representing 0.9% of the harmless voltage limit.<br><br>During least favorable conditions and increased electric load in room circuitry, temperature increases up to 6°C of the 20°C limit. Maximum voltage between an antenna and the bed frame is 0.9 mV, representing 0.9% of the harmless voltage limit. | Pass |
| Electrical current consumption. | Power levels remain at 110 V ± 0.3 V and 0.5 A ± 0.02 A while idle, and 110 V ± 0.05 V and 2.82 A ± 0.04 A while performing a scan. | Pass |
| Disconnection of power during a scan. | Disconnecting any or multiple of the system cables will alter the results of the scan. However, there is no scenario were the user will be at risk of harm. | Pass |
| Electromagnetic interference between applications in nearby RF spectrum. | No distortion or interference is observed in any device or network. | Pass |
| Emergency button press. | Microwave equipment and motion actuators stop. Control-software warns and interrupts scan. User is at no risk of harm. | Pass |

### 2.4.3 Volunteer evaluation of comfort and safety

A phase 0 clinical trial (Ethics approval: B2012-117, University of Manitoba) was carried between the summer of 2014 and fall 2016. The experiment explored the safety and comfort performance of the BIRR system under a clinical scenario. Eleven asymptomatic volunteers were scanned with the system. A survey was used to collect qualitative perspectives on their experience using the system. The feedback provided by the participants led to the re-design of the head and chest supports to improve ergonomics of the system.

The inclusion criteria for the study required participants to be women above the age of 40, with breast cup of size B, C, or D, to have no breast implants and no history of breast abnormalities in the last two years. Volunteers were expected to be able to lie prone for at least 30 minutes. Participants were recruited through posters and word-of-mouth. Volunteers received a T-shirt, but no monetary compensation was given.

All scan procedures took place at the Non-Ionizing Imaging Laboratory at the University of Manitoba. The BIRR system was disinfected, calibrated, and configured before each scan. Volunteers were briefed on the length and steps of the procedure. A female assistant helped the women to lay prone on the table and center their exposed breast into the bed aperture. Volunteers were instructed to remain as immobile as possible. When the volunteers were ready, the assistant initiated the scan through the user interface.

After completion of the scan, volunteers anonymously filled a survey with their experienced levels of comfort and security (available in appendix 7.3). Personal, non-identifiable information was collected regarding each volunteer age and bra cup size. The assistant registered approximate breast circumference at the base of the breast using a measuring tape.

A total of eleven women participated in the study (see Table 2.4-3). The volunteers were women between the ages of 42 to 52. Self-reported bra size ranged from A to D, while measured breast diameter ranged from 8 cm to 15 cm. Each patient had one breast scanned with the BIRR

system. The scan duration ranged from 20 minutes to 56 minutes, lengthier scans were performed to collect microwave measurements with an increased number of antenna locations. Monostatic and multistatic reflections were collected at different vertical plane levels and azimuthal antenna locations.

Results of the questionnaire indicated an overall approval and sense of security with the system. No volunteer felt unsafe nor demanded to stop the scan. Minor pain was reported from the abdominal and neck areas. There was no report of discomfort or pain from the examined breast during the extent of the scan. The comfort rating of the BIRR system based on the volunteers' response is presented in Figure 2.4-1.

Of the eleven volunteers, four reported no pain or discomfort during or after the procedure. The remaining seven volunteers reported some level of discomfort or pain from the neck, shoulder, and abdominal region. The complete survey results are available in Appendix 7.4.

Results from the survey were used to improve bed frame and support. The first three volunteers reported discomfort localized in the abdominal region. The discomfort originated from the weight of the volunteer body pressing against the edge of the ABS plate under the chest region (see section 2.3.1.2). As an immediate corrective action, the edge of the plate was rounded. In subsequent scans, a 12-mm-thick foam pad was placed between the bed and the abdomen of the participants. Subsequent volunteers reported less discomfort.

Following the volunteer trial, sections of the inspection bed were re-designed to resolve the reported sources of discomfort. Re-designed elements included a sliding head-rest support, a padded cushion with a central orifice for the breast, and a carbon-fiber chest support. With the author's guidance, the new components were designed and implemented by a summer student, Calene Treichel, during the summer of 2015. On Figure 2.4-2 a volunteer is demonstrating the use of the head support and the new padding on the breast area. Technical drawings for the head and chest supports are available in Appendix 7.6

Table 2.4-3 Summary of volunteer information for the phase 0 clinical trial

| Volunteer # | Age | Breast scanned | Breast length (cm ± 0.5 cm) | Breast diameter (cm ± 0.5 cm) | Bra cup size | Scan times (m) | Coronal planes | Total antenna positions |
|---|---|---|---|---|---|---|---|---|
| 1 | 57 | R | – | – | C | 27 | 3 | 432 |
| 2 | 54 | R | 9 | 10.5 | B | 20 | 3 | 144 |
| 3 | 50 | L | 14.5 | 12.6 | C | 28 | * | * |
| 4 | 53 | R | 14 | 12.4 | B-C | 20 | 4 | 180 |
| 5 | 51 | R | 15 | 14.3 | D | 20 | 4 | 180 |
| 6 | 42 | L | 8.5 | 8.9 | D | 22 | * | * |
| 7 | 52 | R | 10.5 | 13.4 | C | 22 | 4 | 360 |
| 8 | 51 | R | 11 | 11.5 | B | 25 | 4 | 288 |
| 9 | 51 | L | 13.5 | 14.3 | C-D | 22 | 3 | 180 |
| 10 | 60 | R | 13 | 14.6 | D | 56 | * | * |
| 11 | 70 | R (twice) | 13 | 12.4 | C | 55 | 3 and 2 | 432 and 288 |

**Volunteers #3, #6, and #10 were not scanned with the radar-system. Nevertheless, they still evaluated the comfort and security of the BIRR system.*

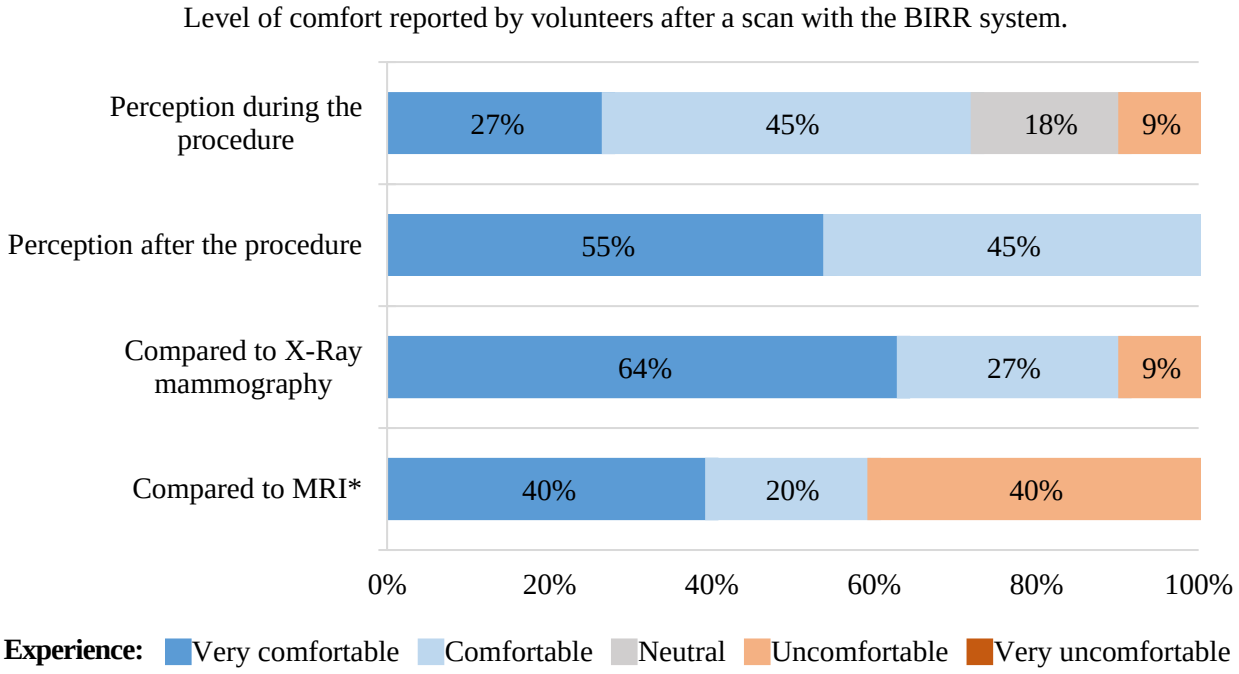


Figure 2.4-1 Post-scan survey of eleven volunteers regarding comfort levels of the BIRR system. All volunteer had undergone an X-ray mammography scan ($n$ = 11). *Only five volunteers had experience with MRI scans ($n$ = 5).

Figure 2.4-2 Volunteer above the BIRR system with the re-designed head and chest supports. A massage-like headrest supports the weight and position of the head. The headrest, in turn, lies on top of on ABS plate with a rectangular slit for air circulation. The chest area is support by a 1-cm thick carbon-fiber support and a custom-made padded cushion, with a central aperture.

### 2.4.4 System resolution

The far-field range resolution of the radar system can be approximated by [65]:

$$\Delta x = \frac{c\tau}{2} = \frac{c}{2B} \tag{2-2}$$

where $B$ is the frequency bandwidth, and $c$ is the speed of light. However, the near-field resolution is dependent on the position of the target as well as the antenna beam-width. The point spread function (PSF) is commonly used to characterize the resolution of an imaging system. By assuming rotational symmetry, the PSF can be calculated as the double derivative of the edge spread function [14].

The edge spread function of the BIRR system was calculated using a metallic plate in the center of the inspection chamber. The LB-20200 antenna was used for this experiment. S11 reflections were recorded with the probe placed 12 cm apart from the plate. Then, the antenna was lowered below the edge of the plate in increments of 1.5 cm. Figure 2.4-3 shows the PSF of the

normalized amplitude reflections. The full-width half maximum value of 48.9 mm suggests a broader resolution than the predicted far-field range resolution of $\frac{c}{2B} = 21.4$ mm.

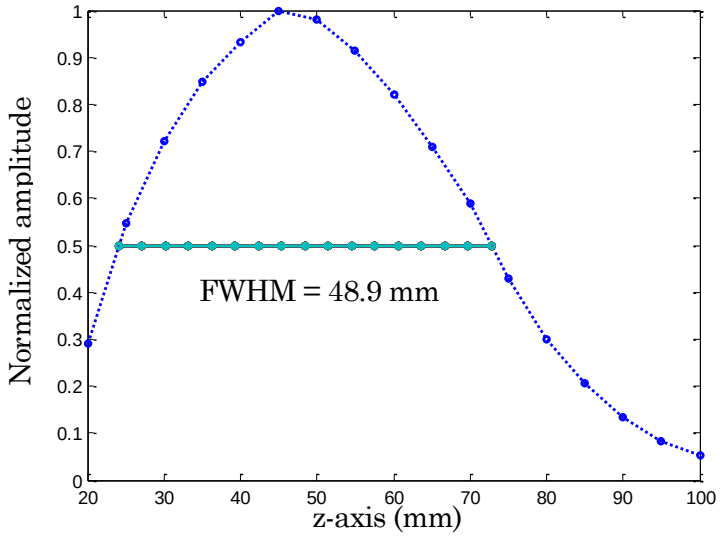


Figure 2.4-3 Point spread curve of the BIRR with the LB-20200 transceiver. The full-width half-maximum value was calculated to be 48.9 mm.

The response of a radar system varies depending on the location of the scatter. The resolution calculated through the PSF analysis represent a worst-case condition since the scatter was placed in the center of the OD.

The BIRR system resolution of 48.9 mm is lower than the typical resolution of MRI (1 mm) or X-ray mammography (0.15 – 1 mm) technologies [9]. However, BMI systems are not expected to surpass the resolution of other imaging modalities. Instead, microwave imaging devices aim to provide physiological information on the health of the tissues inspected.

### 2.4.5 Monostatic and multistatic, three-dimensional scattering measurement.

This section evaluates the ability of the BIRR system to recover useful microwave reflections from a target radiated in a three-dimensional space. Using a highly scattering target, monostatic (the same transceiver emits and collects scattered waves) and multistatic (a different transceiver collects the scattered waves) microwave reflections were recorded while the rotary stage relocated the antenna array around the OI. From the highest position attainable by the lift

stage, antennas were lowered to collect measurements at different vertical planes. S11 and S21 reflections follow the characteristic sinusoidal pattern of a target radiated in a circular scan trajectory.

A cylindrical metallic rod was used as a highly-reflective target. The rod had a diameter of 2 cm and a length of 5 cm. The rod was placed at x = 2.25 cm and y = 2.25 cm. The end of the rod projected for only 1 cm relative to the horizontal plane of the antennas.

S11 and S21 reflections were collected using the VNA equipment described in 2.3.2.3. A bi-static configuration was used with the antennas separated 145°. Antennas were placed at a radial distance of 21 cm from the center of the axis of rotation. The system was configured to collect 72 scan locations, using a sweep frequency of 1 GHz to 8 GHz and 1001 frequency points. Three vertical planes were collected at positions of z = 0 cm, z = −5 cm and z = −10 cm.

The collected S11 and S21 reflections are shown for the time and angular domain in Figure 2.4-4. The sinusoidal response indicates the ability of the system to detect the presence of the metallic object. For the S11 measurements, the strongest reflections were observed at antenna position 59. This position corresponds to the shortest distance between the antenna and the reflective target. The S21 reflections show lower intensity and the sinusoidal shape is hardly distinguishable. However, the response from the reflective target is considerably larger than the background.

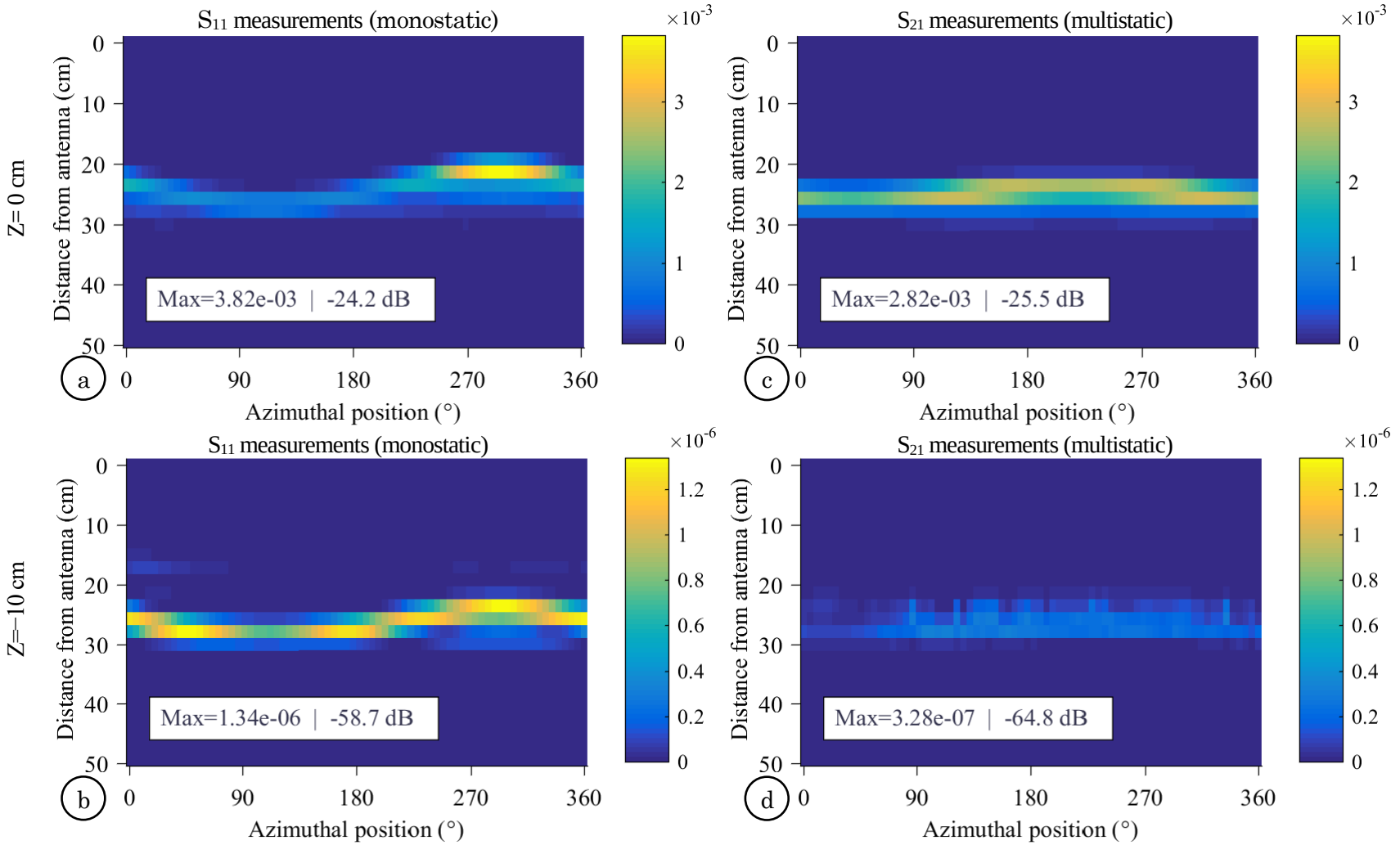


Figure 2.4-4 Time-domain plots of scatter intensity from a BIRR scan of a 2-cm-wide metallic bar. Plots show the power measured at the VNA ports (unitless S-parameter). Images are normalized to the maximum value in the monostatic measurements for each height. a) S11 at lift stage height z f 0 cm. b) S11 after lowering the antennas 10 cm. c) S21 at height z = 0 cm. d) S21 after lowering the antennas 10 cm. Monostatic measurements show a higher intensity than multistatic measurements. Despite lowering the antennas 10 cm, reflections from the metallic bar can still be recovered at a significant ratio above the background values (average <−140 dB).

### 2.4.6 Validation with breast phantom

The efficiency of a microwave imaging system is defined by its ability to resolve the location of tumorous structures as well as their contrast with surrounding tissue. A diseased breast can be partially mimicked using a breast phantom. The following experiment explores the potential diagnostic capabilities of the BIRR system using the known location of tumor inclusions in a breast phantom. Then, time-domain reflection measurements of the phantom and the images generated by a reconstruction algorithm are evaluated.

The experiment was performed using a hemispherical-shaped breast phantom with the electromagnetic properties of breast tissue. Two phantom configurations were used to represent homogenous and heterogeneous conditions. In the first configuration, a 1.5 cm tumor inclusion was immersed in a low-density breast phantom. A heterogeneous condition was tested next by adding a fibroglandular patch of the same size. The size of the inclusions was chosen to approximate the diameter of an invasive breast cancer [66]. Both homogenous and heterogenous conditions were scanned with the BIRR system previously described in this chapter.

Using the VNA measurements and the known location of the targets, time-domain reflections were compared to the expected position of the targets. Next, holographic reconstruction algorithm was used to generate an intensity map of the phantoms cross-section. The spatial deviation of the inclusions compared to their known location was used to evaluate the positioning performance of the system. Finally, the diagnostic potential of the BIRR system was established by calculating the signal to clutter ratio (SCR) and tumor to fibroglandular ratio (TFR) in the reconstructed images.

The phantom was created using a 2-mm-thick hemispherical container made of cellulose acetate butyrate (CAB). The transparent thermoplastic provides convenient moldable capabilities and little electromagnetic interference in the frequency bandwidth of the device [67]. The diameter of the container starts at 15.6 cm and decreases over its 14.4 cm of length. The container was

designed to match the volume of an average breast of cup size D [43]. The large volume of the container represents a challenging scenario due to propagation losses. Manufacturing details of the container are further explained in Section 4.6.

The phantom materials are similar to the one used by Flores et al. [37]. The phantom container was filled with glycerine to emulate low-density tissue (i.e., fat). A mixture of a solidifying powder known as TX-151 (Hydrophilic organic polymer, Oil Center Research Inc, LA, USA), and distilled water was used as a surrogate for fibroglandular breast tissue. A malignant inclusion was fabricated using a glass bulb filled with saline. The dielectric properties of the phantom materials used for this experiment are shown in Table 2.4-4. The reported dielectric properties of the surrogate materials used in this study fall within the measured values corresponding to real breast tissue (further explained in Section 4.4)

Table 2.4-4 Dielectric properties of breast tissue and surrogate materials at 3 GHz.[37]

| **Breast tissue** | $\varepsilon_r$ | $\sigma$ **(S/m)** | **Surrogate material** | $\varepsilon_r$ | $\sigma$ **(S/m)** |
|---|---|---|---|---|---|
| Adipose | 9 | 0.4 | Glycerin | 7.29 | 0.72 |
| Fibroglandular | 25-32 | 1.5 | TX-151 and distilled water | 26-36 | 1.6 |
| Tumor | 55 | 2.1 | Saline | 53 | 1.9 |

For this experiment, the transceiver used was the commercial horn antenna LB-20200 (Detailed in section 2.3.2.5) operating in monostatic configuration. S11 reflections were performed with the Planar 804/1 VNA (Detailed in section 2.3.2.3). Measurements were taken at 1001 frequency points over the range of 1 GHz to 8 GH, with an intermediate frequency (IF) bandwidth of 10 kHz and an output power of 10 dBm.

Each phantom configuration was interrogated at 72 antenna locations with an angular separation of 5 degrees. The distance from the antenna to the edge of the phantom was 4 cm. In the homogeneous configuration, the tumor inclusion was placed at (0, 3.75) cm and had a diameter

of 1.5 cm. For the heterogeneous configuration, a fibroglandular patch with a diameter 1.5 cm was added at (0.75, 3.75) cm. The layout of the phantom is described in Figure 2.4-5, and a photo of the heterogeneous phantom configuration is shown in Figure 2.4-6.

An initial scan of the adipose phantom without inclusions was used as calibration. Background signals from the imaging chamber and the low-density tissue are collected in a reference scan using the same number of antenna positions. The reference measurements are subtracted from the phantom signals.

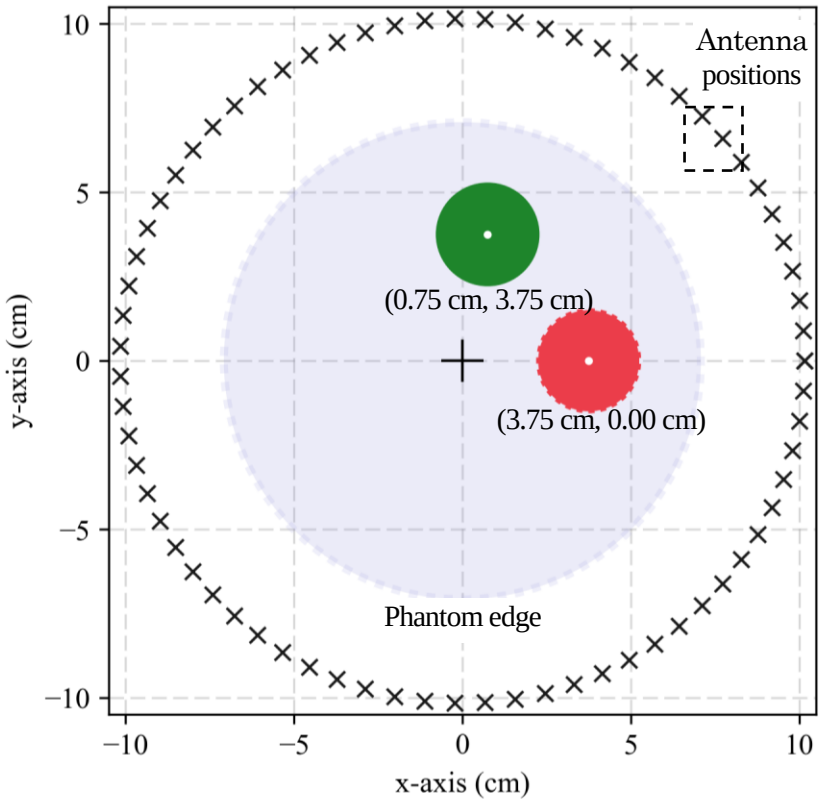


Figure 2.4-5 Breast phantom layout for malignancy sensitivity test. A tumor inclusion (red) with a diameter of 1.5 cm was placed at (0.75, 3.75) cm. For the second scan, a fibroglandular patch (green) of 1.5 cm diameter was added at (3.75, 0.00) cm. The antenna probed the phantom at 72 azimuthal positions (marked with as ×) around the phantom, with an angular separation of 5° and at a radius of 11.1 cm.

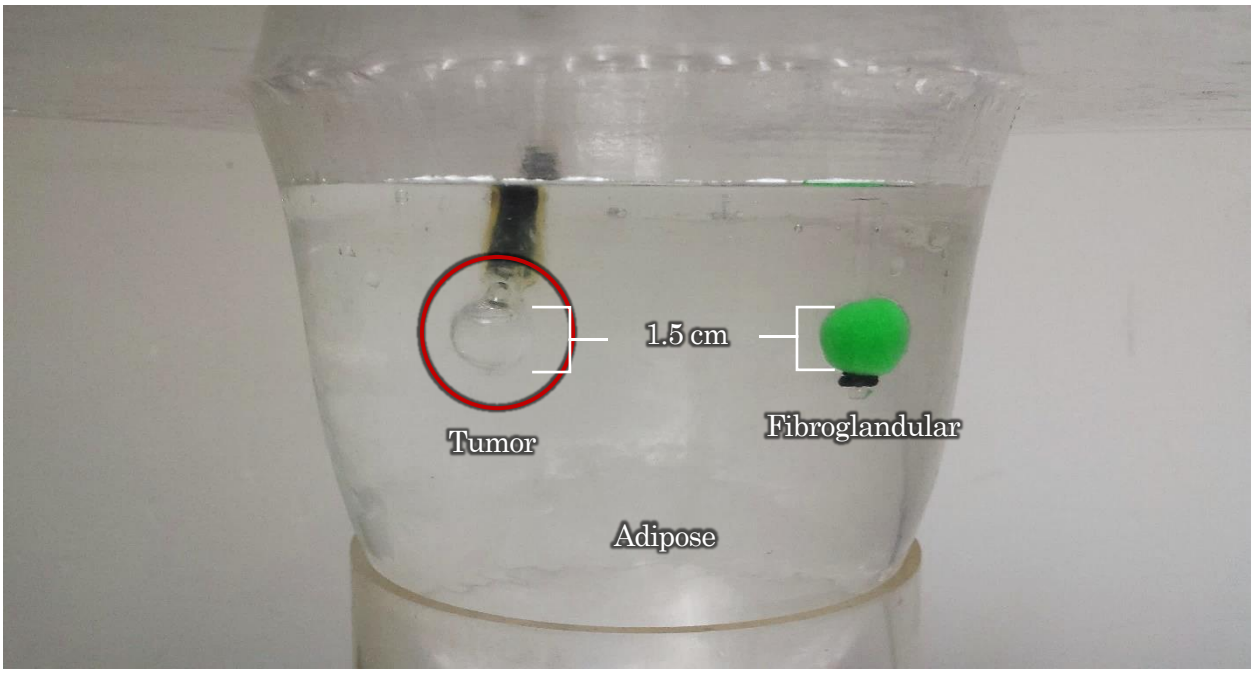

Figure 2.4-6 Heterogeneous phantom used to evaluate the diagnostic performance of the BIRR system. Synthetic tumor and fibroglandular inclusions are immersed in an adipose tissue surrogate. The dimensions of the phantom CAB hemispherical container were derived from CT breast examinations.

The raw data contains the unprocessed time-domain reflections from the phantom at each probing point during the circular scan trajectory. For a circular monostatic signal model, the distance $D$ from the transceiver to the q$^{th}$ targets follows equation 2.4-1.

$$D_q(\theta) = \sqrt{R^2 + r_q^2 - 2Rr_q\cos(\theta - \phi_q)} \qquad (2\text{-}3)$$

Where R is the radius of the scan geometry, $\theta$ is the angular position of the transceiver, and $(r_q, \phi_q)$ are the polar coordinates of the $q^{th}$ scatter. Equation 2-2 was used to relate the time-domain measurements from the VNA into distances [35].

The recorded datasets were converted to a rectangular coordinate system using the circular holography algorithm proposed by Flores-Tapia et al. [35]. For the reconstructed images, the spatial and angular deviation was calculated. In reconstructed images, target coordinates were attributed to the pixel with the highest value. The spatial error was calculated as the difference

between the locations of the targets in the image compared to the known location of the inclusions in the phantom.

To measure the contrast of the tumor inclusion to the adipose tissue, signal (i.e., tumor) to clutter ratio was defined as follows:

$$SCR = 10\log_{10}\frac{(\Gamma_{\max})^2}{\left(\frac{1}{m}\sum_0^m b_i\right)^2} \tag{2-4}$$

Where $\Gamma_{\max}$ is the strongest tumor response in the image and $b$ is the response from the energy-free region (background)

For the heterogeneous phantom, contrast between tumor and dense tissue was calculated as:

$$TFR = 10\log_{10}\frac{(\Gamma_{\max})^2}{(F_{\max})^2} \tag{2-5}$$

Where $F_{\max}$ is the strongest fibroglandular tissue response in the image.

Time-domain reflection measurements from the homogenous phantom are shown in Figure 2.4-7. Due to propagation losses in the adipose medium, only the points closest to the antenna are visible in the image. From the measurements, the strongest reflection at 355° is located at a distance of 25.71 cm. The expected travel path of the tumor inclusion is marked with a red line. From equation 2-3, the shortest distance to the antenna is located at the azimuthal position 0° at a distance of 22.33 cm. It is noted that the time delay introduced by the LB20200 antenna generates an offset of 14.96 cm [68].

The raw data (i.e., S11 measurements) for the heterogeneous phantom scan are shown in Figure 2.4-8. Compared to the homogeneous case, the heterogeneous raw data shows an additional scatter spot with reduced intensity. The apex of this spot is located at 23.57 cm and 270°. The shortest distance from the travel path of the fibroglandular inclusion is 22.26 cm, at 280°. The

expected travel path for the tumor inclusion is identical to the homogeneous case. The strongest reflection is measured at the angular position 0°, at a distance of 27.86 cm.

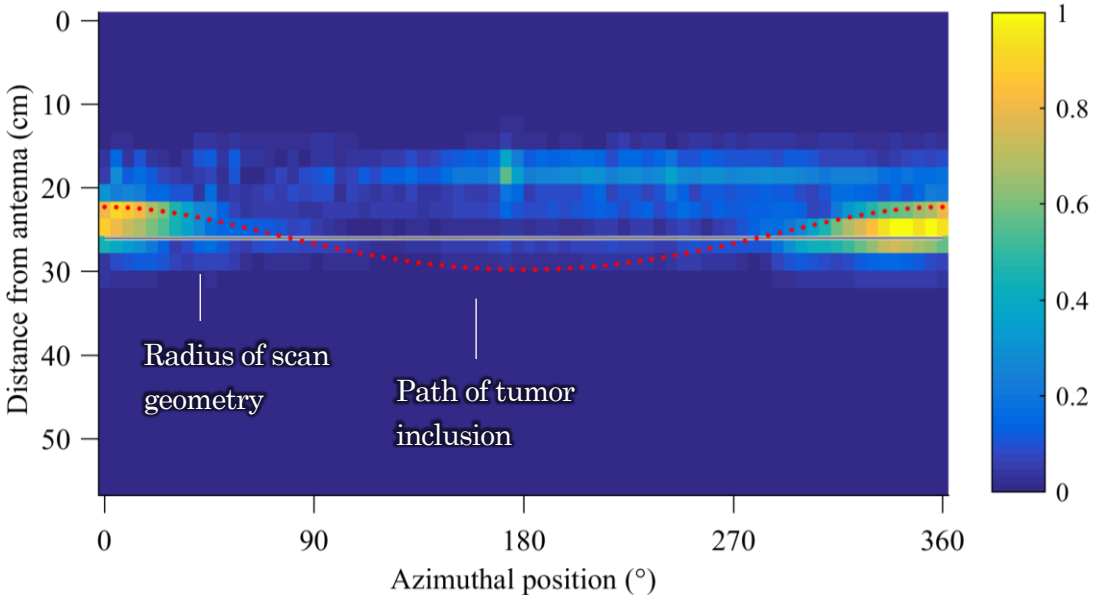


Figure 2.4-7 S11 measurements from the homogeneous phantom with a tumor inclusion. The image is normalized to the maximum value in the image. The dotted red line marks the tumor calculated response as the antennas rotate around the phantom. The energy reflected increases as the separation between antenna and target decreases.

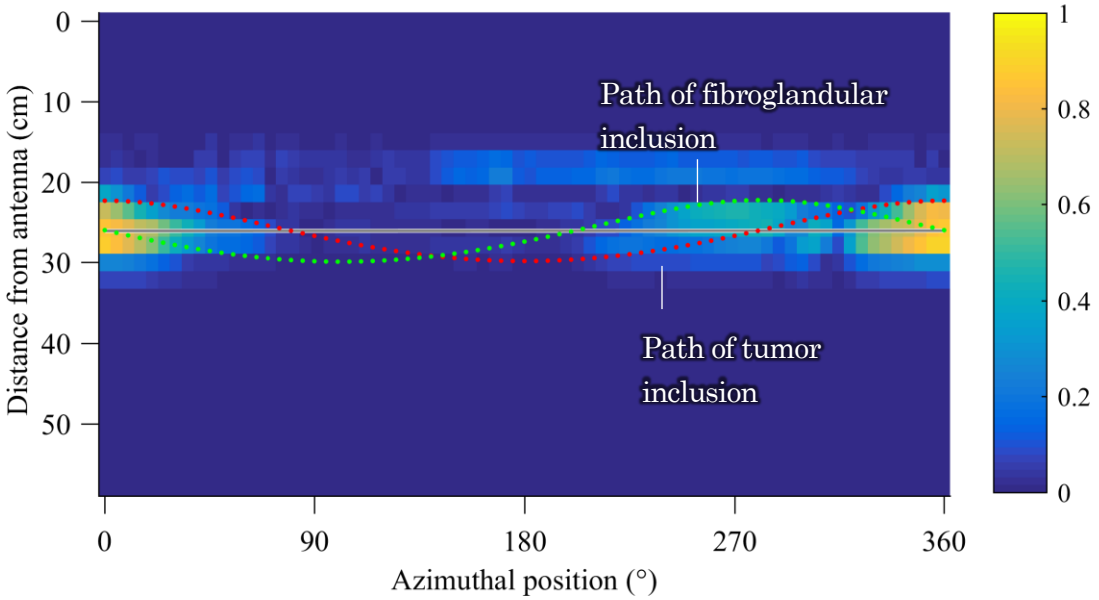


Figure 2.4-8 S11 measurements from the heterogeneous phantom with tumor and fibroglandular inclusions. The expected position of the tumor and the fibroglandular patch is marked with a red and green line respectively. The plot is normalized to the maximum intensity of the homogeneous condition (Figure 2.4-7)

The responses from individual inclusions inside the phantom can be seen in both time-domain plots in Figure 2.4-7 and Figure 2.4-8. A sinusoidal graph representing the projection of the inclusions as the antenna rotates around the target was super-imposed onto the plots. The calculated target path overlaps with the responses in the raw data. Notably, areas of high intensity coincide with the locations where the antennas are closest to the inclusions.

Reconstructed images for both phantom configurations are shown in Figure 2.4-9. The image resolution is 0.7 cm for every bin. In both images, the strongest reflection appears at (3.67, 0) cm. The image for the second experiment contains an additional response at (0, 5.14) cm. The angular separation between responses is 90°. Table 2.4-5 shows a summary of positional deviations and contrast metrics for the two reconstructed images. Reconstructed images show a close spatial agreement with the known location of the tumor and fibroglandular inclusions. Small positional deviations on the fibroglandular target can be attributed to placement uncertainties (0.3 cm) and low resolution in the reconstructed image (0.7 cm). Overall, the study indicates good spatial agreement between the inclusions and the responses in the reconstructed image.

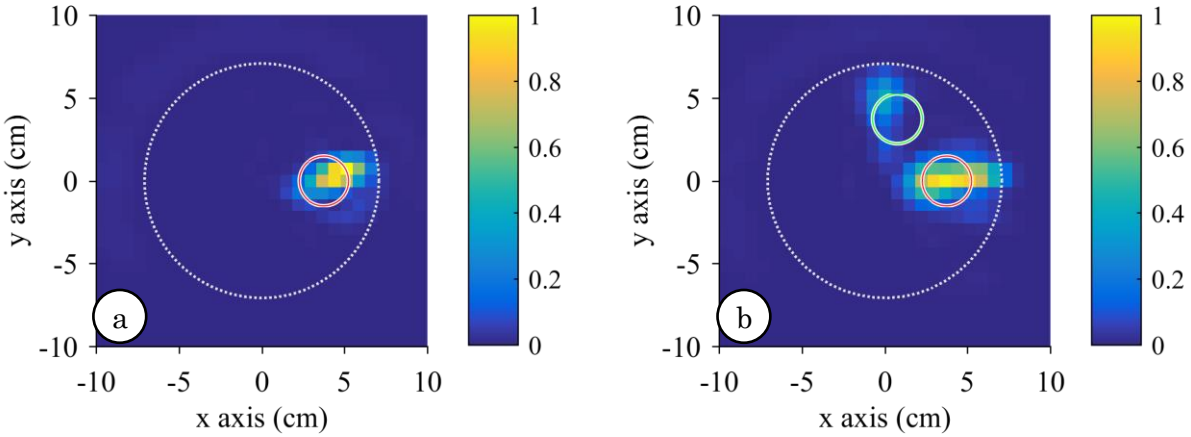


Figure 2.4-9 Reconstructed images of breast phantom scanned with the BIRR system. a) With tumor target. b) With tumor and fibroglandular target. Expected locations of the inclusions are encircled green (fibroglandular) and red (tumor). The edge of the phantom container (ROI) is marked with a gray line. Both images are normalized to the maximum response from image a)

Table 2.4-5 Summary of contrast metrics and spatial error based on reconstructed images from homogeneous and heterogeneous phantoms.

| Phantom | SCR (dB) | TFR (dB) | Inclusion | Spatial error (± 0.3 cm) | Angular error (± 4.6°) |
|---|---|---|---|---|---|
| Homogeneous phantom | 20.9 | NA | Tumor | 0.1 cm | 0.0° |
| Heterogeneous phantom | 22.0 | 2.9 | Tumor | 0.1 cm | 0.0° |
| | | | Fibro | 1.6 cm | 11.3° |

## 2.5 Chapter conclusions

This chapter introduced the BIRR as a new clinical system for breast cancer detection. First, the design and construction process were explained. The operation and characteristic of every system component were detailed. At the end of this chapter, the BIRR was evaluated for safety, comfort, and performance.

The BIRR features a modular design with convenient air-based operation. The antenna array can be adjusted with four degrees of freedom for monostatic and multistatic operation. Components can be replaced or updated without affecting the functionality of the system. The absence of an impedance-matching-liquid reduces the mechanical complexity of the system without hindering its sensing capabilities.

The BIRR system has proven to be a safe and comfortable medical device. Experiments performed in accordance with IEC-6060-1:2005 indicated that even during least favorable conditions, the user would not be at risk of harm. Feedback collected during a phase 0 clinical trial indicated a general sense of comfort and security by volunteers. Based on end-user recommendations, head and chest support structures were redesigned to increase the comfort during clinical examinations.

A dielectrically-accurate phantom validated the diagnostic performance of the BIRR system. The phantom partially mimicked a diseased breast, with a malignancy of 1.5 cm, in inhomogeneous and heterogeneous tissue conditions. Measurements were processed with a

reconstruction algorithm, and the resulting images were clear and free of artifacts. The presence of the mimicked malignant inclusions was easily spotted. In both homogenous and heterogeneous conditions, tumor responses showed a high contrast to surrounding background achieving signal-to-clutter ratios above 20 dB for both conditions. These results are higher[1] than the signal-to-clutter value of 15.0 dB achieved by the first-generation system of Flores et al. [37], higher than the signal-to-noise ratio of 17.63 dB reported for the clinical system in Kurrant et al. [69], and substantially higher than the signal-to-clutter value of 8.2 dB reported in Klemm et al. [22]. The contrast between the tumor and fibroglandular inclusions was approximately 3:1, which is in agreement with the dielectric contrast between of malignant and dense tissue [12].

The BIRR system meets the product requirements established in Section 2.2.2 and has been proven fit for clinical examinations. Results indicate that the system can collect the microwave responses of both simple, highly reflective targets as well as complex, heterogeneous breast phantoms. Paired with a state-of-the-art reconstruction algorithm, the BIRR system detected a 1.5-cm-wide tumor lesion inside a heterogeneous breast phantom. The BIRR system has the potential to become a regular adjunct device for breast cancer detection.

Systematic positioning errors were detected during the characterization of the lift stage and rotary stage components. These positioning errors translate to an inaccurate and imprecise antenna placement. Positioning performance can be improved by integrating encoders, closed-loop correction algorithms or better positioning stages. However, there is no standard to guide the selection of such equipment. As it was discussed in Chapter 1, it is not yet understood how positioning errors affect the diagnostic value of reconstructed images. The following chapter will answer to that gap in knowledge.

[1] Differences between the metrics and phantoms employed by different research groups make it impossible to directly compare the performance of clinical BMI systems.

# 3 DEFINITION OF ANTENNA POSITIONING SPECIFICATIONS FOR BREAST MICROWAVE IMAGING SYSTEMS

The primary aim of this thesis was to establish antenna positioning tolerances for Breast Microwave Imaging (BMI) systems. A series of experiments were conducted to evaluate the effects of induced positioning errors on reconstructed images of breast phantom scans. These experiments employed the BIRR system described in Chapter 2, as well as the breast phantoms used in Section 2.4.6. This combination provided a reliable representation of the effects of positioning errors during a clinical examination. Accuracy and precision errors were induced in the vertical and azimuthal planes, which are the principal directions in which BMI systems probe their targets. Reconstructed images of the scans with induced positioning errors were compared against control error-free scans.

This chapter describes the system and phantom configuration used for these experiments, as well as the technique used to generate datasets with controlled positioning errors. The reconstructed images of error-induced datasets are shown, followed by the results of Image Contrast Metrics (ICM), Receiver Operating Characteristic (ROC) curves, spatial error, and a set of suitable diagnostic criteria. Finally, in section 3.4 the results are discussed, and the chapter ends with the recommendation of positioning specifications for future systems BMI systems.

## 3.1 Methods and materials

As previously mentioned, this study was performed with the clinical BMI system built by our group at the University of Manitoba. The details of the system components can be found in Section 2.3 of this thesis. The positioning performance of the lift and rotary stage was monitored to minimize inaccuracies. A digital caliper was attached to the scissor lift to reduce positioning errors to an uncertainty of ± 0.002 cm. The rotary stage positions were validated using the graded scale

on the chassis of the stage with a resolution of 0.1°. Cushioned surfaces were removed from the bed to preserve the location of the phantom across scans.

For this experiment, the phantom described in Section 2.3.6 was used. The phantom container has a symmetric, hemispherical shape with a maximum diameter of 15.6 cm and length of 14.4 cm. For the azimuthal plane analysis, the phantom was scanned at a level where the diameter of the phantom was 14.3 cm. For the vertical plane analysis, the phantom was scanned at three planes with vertical separation of 3.5 cm. The top section had a diameter of 15.1 cm, the middle section had a diameter of 14.3 cm, and the bottom section was 12.1 cm.

The phantom contained material representing fibroglandular and malignant (tumor) breast tissue inclusions. Both inclusions had a spherical shape and a diameter of 1.5 cm. The inclusions were surrounded with low density (fat-like) material. The dielectric properties of the materials are identical to the ones previously presented in Table 2.8-3. The position of targets inside the phantom was kept constant through all the scans, with a placement uncertainty of ± 0.3 cm. The inclusions were also aligned to the horizontal plane of the antennas. Figure 3.1-1 shows a coronal diagram of phantom configuration used for the middle section scan.

The antenna used for the study was the LB-20200 (see 2.6.2.5) operating in monostatic configuration. The antenna tilt and orientation were secured using the fixed 90° holder described in Section 2.3.2.7. Through all the scans, the antenna was kept at 4.0 ± 0.1 cm from the edge of the phantom, to eliminate changes in the signal propagation path. As with previous experiments, no liquid was used to match the impedance of antenna and phantom. The phantom was illuminated with a continuous stepped-frequency sweep from 1 GHz to 8 GHz, at 1001 frequency points and with an output power of 10 dBm.

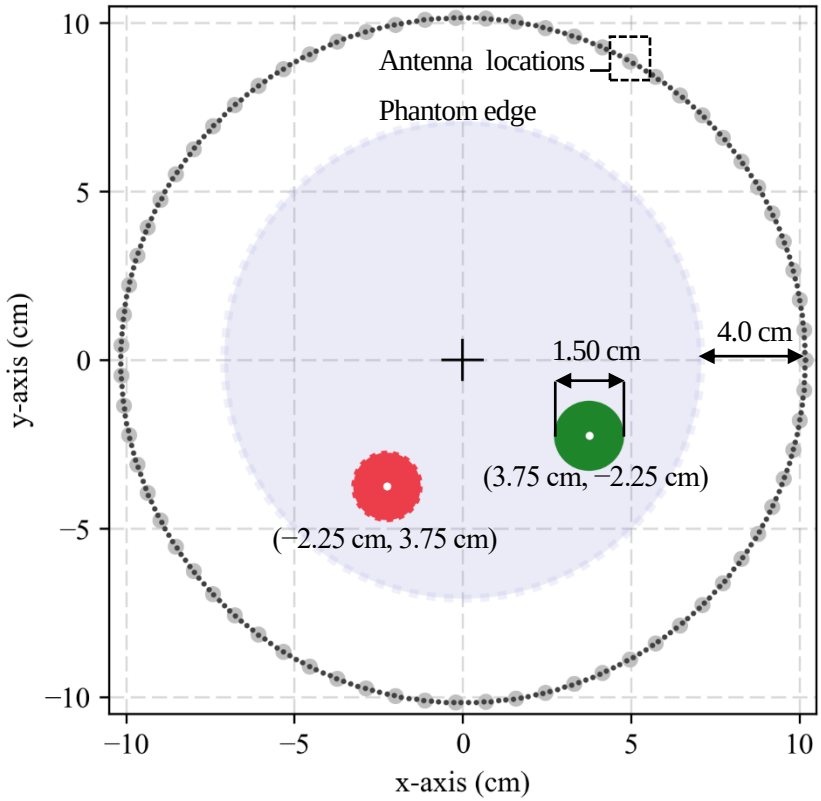


Figure 3.1-1 Phantom layout for precision and accuracy experiments. Tumor (red) and fibroglandular (green) spherical inclusions with 1.5 cm diameter, submerged into a fat surrogate (gray). Small black dots represent antenna probing points during a 288-location scan. Bigger, gray dots represent the antenna locations used for the 72-location datasets.

Up-sampled datasets were recorded by probing the breast phantom above the minimum sampling locations required to obtain suitable reconstructed images [52], [70]. For the azimuthal direction study, the phantom was probed at 288 antenna positions uniformly spaced at 1.25°. The scan was performed three times for repeatability. Up-sampled measurements in the vertical direction were collected by lowering the position of the lift stage in increments of 0.05 cm, 0.10 cm, and 0.20 cm. At each level, a horizontal-plane scan was performed with 72 antenna positions and it was repeated two times. To measure the effects of the hemispherical geometry of the breast, up-sampled vertical datasets were collected at three different height sections of the breast phantom (top, middle, and bottom). Up-sampled azimuthal datasets were collected in the middle section

only. In total, the phantom was illuminated from 1,581 different antenna locations. Table 3.1-1 summarizes the number of probing points for each phantom scan $p_n$.

Table 3.1-1 Antenna positioning scheme for phantom and calibration scans.

| **Relative z level (± 0.003 cm)** | **Antenna locations in the azimuth plane** | | | | | | | | |
|---|---|---|---|---|---|---|---|---|---|
| | **Top section** | | | **Middle section** | | | **Bottom section** | | |
| | $p_1$ | $p_2$ | $p_3$ | $p_1$ | $p_2$ | $p_3$ | $p_1$ | $p_2$ | $p_3$ |
| 0.00 cm | 72 | 72 | — | 288 | 288 | 288 | 72 | 72 | — |
| -0.05 cm | 72 | 72 | — | 72 | 72 | — | 72 | 72 | — |
| -0.10 cm | 72 | 72 | — | 72 | 72 | — | 72 | 72 | — |
| -0.20 cm | 72 | 72 | — | 72 | 72 | — | 72 | 72 | — |

A second, inclusion-free scan was performed to calibrate unwanted reflections in the chamber. The same antenna positioning scheme of Table 3.1-1 was repeated without the tumor and fibroglandular inclusions present in the phantom. The calibration scan contained reflections from the imaging chamber, the phantom wall, and the adipose surrogate.

Error-free datasets were generated by subtracting the corresponding calibration measurements from the phantom measurements. The reconstructed images of these datasets were used as control (see Figure 3.1-1). Reconstructed images were normalized to a maximum scan value. The scan-maximum value was calculated as the average maximum response from control images, plus three standard deviations.

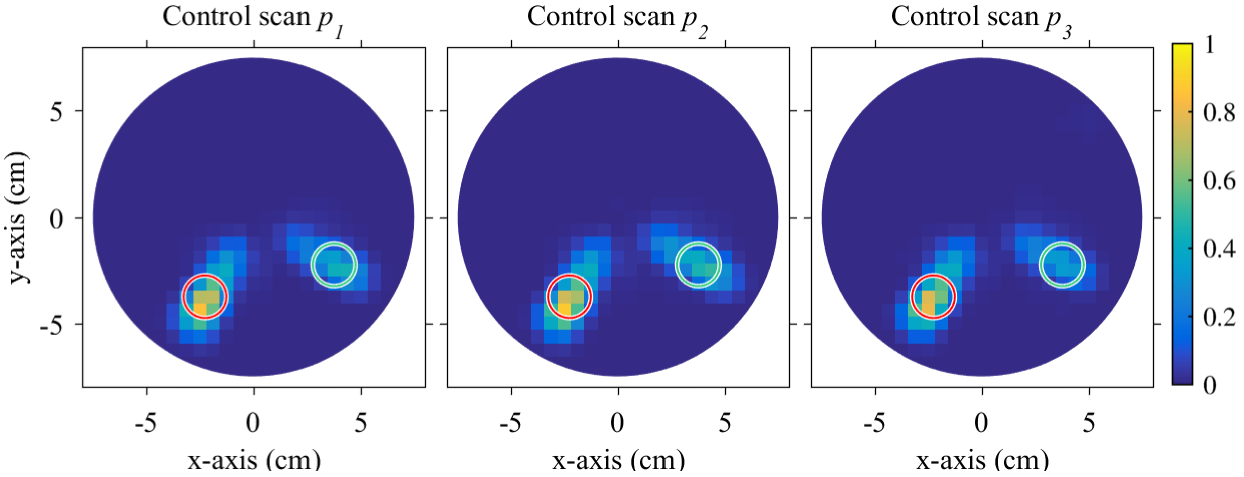


Figure 3.1-2 Reconstructed images of control phantom scans. Measurements performed at the middle section of the phantom. Images are normalized to the maximum scan value. Red and green circles indicate the known-location of the tumor and fibroglandular targets.

Datasets with imprecise antenna placement errors were generated by pairing phantom scan measurements with an incorrect calibration measurement. For the azimuthal plane, both phantom and calibration datasets were down-sampled to scans with 72 antenna locations. Next, the measurements from the original up-sampled datasets were used to pair the phantoms scan with a measurement taken at an antenna angle offset from the calibration scan. The collection of 288 antenna positions enabled mismatched offsets of 1.25°, 2.5°, 5° and 15° to be taken.

The same technique was used to generate datasets with precision errors in the vertical plane: the phantom scans were calibrated using the scans collected at a lower vertical level. Datasets with vertical offsets were generated at 0.05 cm, 0.10 cm, and 0.20 cm.

To generate datasets with accuracy errors, the offset was induced in both calibration and phantom scans. In the azimuthal plane, accuracy offsets were generated with values of 1.25°, 2.5°, 5° and 15°. In the vertical plane, the offsets induced had a value of 0.05 cm, 0.10 cm, and 0.20 cm.

In the azimuthal plane, three erroneous conditions were recreated by modifying the type of distribution and the number of antenna locations where an error was induced: single element, random element, and the entire array conditions. The single element conditions were generated with only one antenna location affected. The offset was induced at the probing point located closest to the tumor inclusion (at 240°) to represent the worst possible condition. For the entire array dataset, all the antenna locations had an induced error. Finally, for the random error cases, the antenna positions followed a uniform random distribution with ranges as big as −15° to 15° (see Figure 3.1-3). Figure 3.1-4 depicts the position of antennas during ideal (control) cases, and the representation of each erroneous case is illustrated in Figure 3.1-5. Finally, Table 3.1-2 shows the classification of induced antenna positioning errors for each case in the azimuthal and vertical plane.

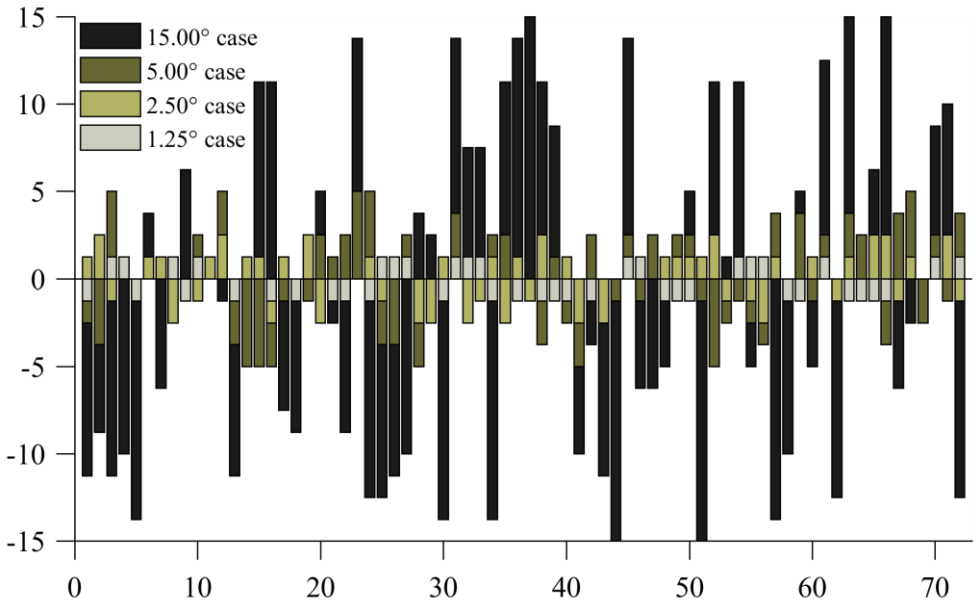


Figure 3.1-3 Positioning curve of 72 antenna locations with the uniform random distribution used for this experiment. E1) 43 probing points have an offset in the range of −1.25° to 1.25°. E2) 59 probing points have an offset ranging from −2.5° to 2.5°. E4) 63 probing points have an offset ranging from −5° to 5°. E12) 69 probing points have an offset ranging from −15° to 15°.

Table 3.1-2 Classification of induced positioning errors

| | **AZIMUTHAL PLANE** | | | **VERTICAL PLANE** |
|---|---|---|---|---|
| | **Single element** At only one antenna location | **Random element** At a fraction of antenna locations | **Array** At all antenna locations | |
| **PRECISION** Introduced on calibration scan | Single element precision error (ASP) | Random element precision error (ARP) | Array precision error (AAP) | Array precision errors (VAP) |
| **ACCURACY** Introduced on calibration and phantom scans | Single element accuracy error (ASA) | Random element accuracy error (ARA) | Array accuracy error (AAA) | Array accuracy errors (VAA) |

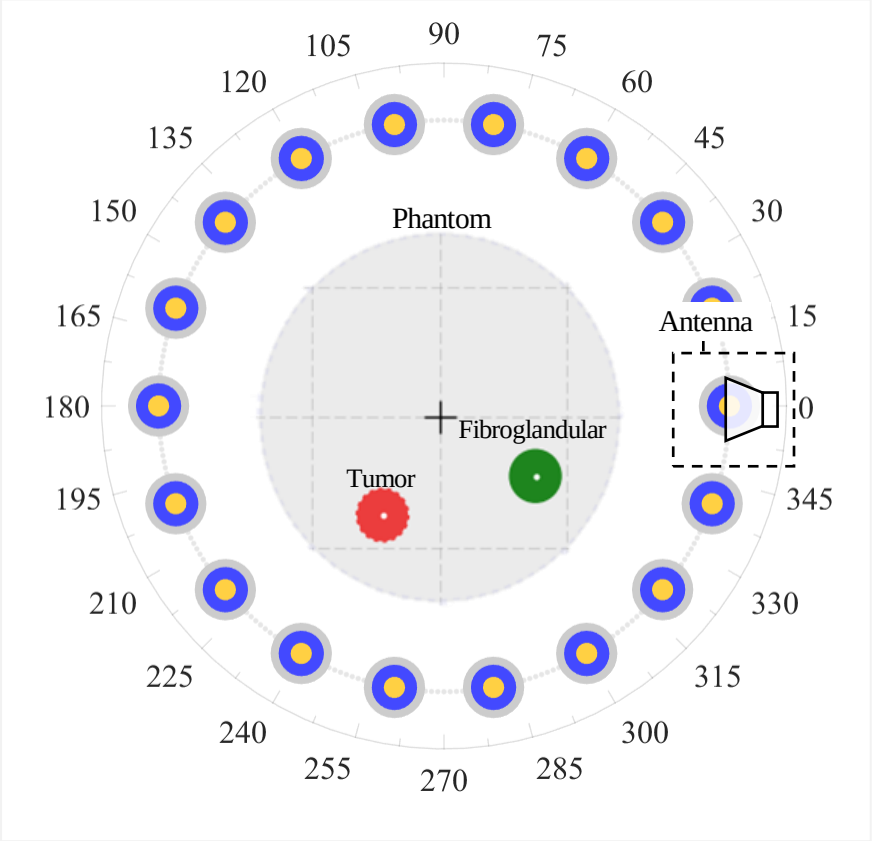


Figure 3.1-4 Illustration of antenna positioning for control scans. Grey circles indicate the ideal antenna position. Blue and yellow circles show the actual location of the antennas during calibration and the phantom scan respectively. During an ideal operation, all circles align perfectly. Red and green circles illustrate tumor and fibroglandular inclusions.

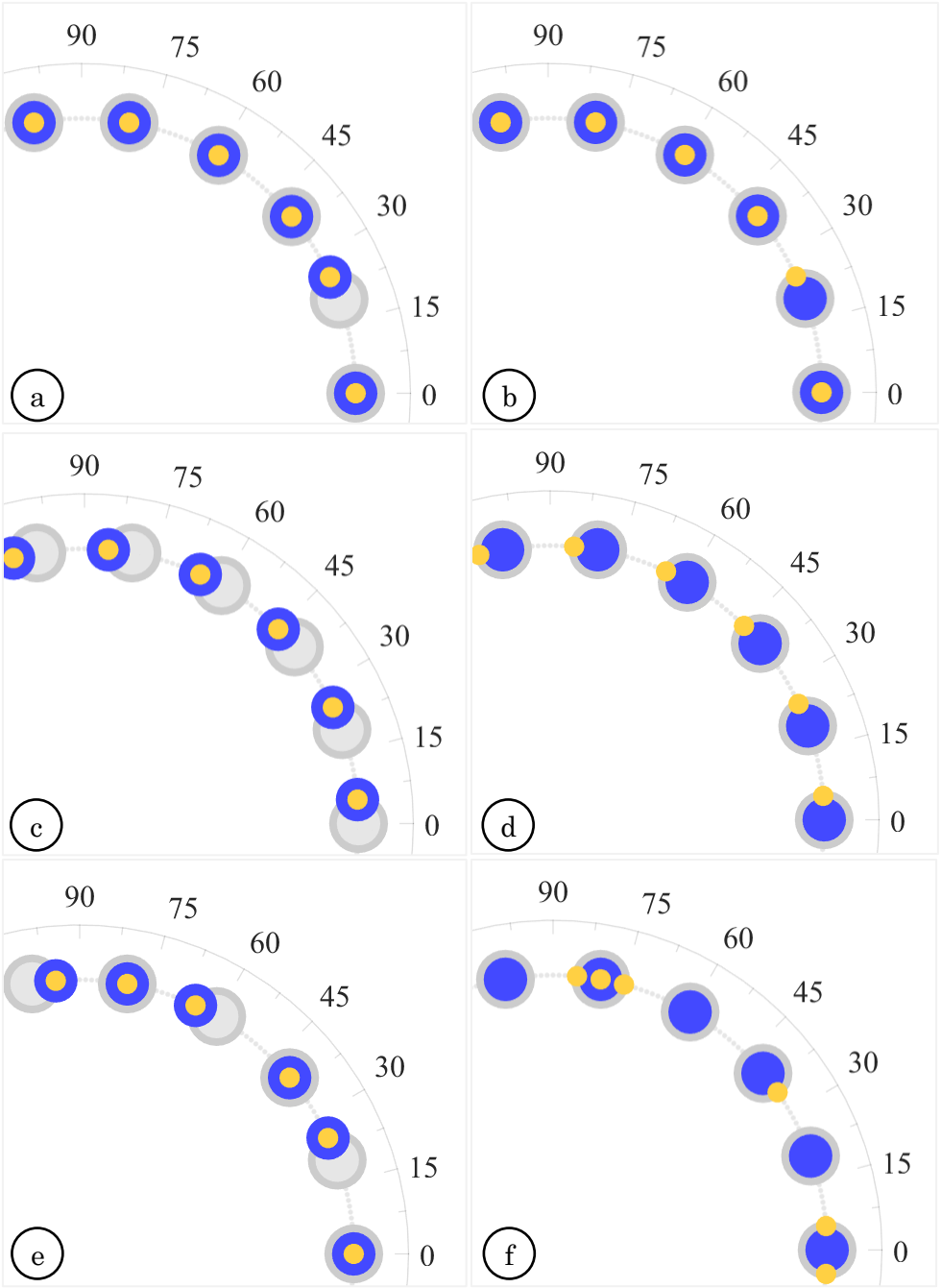


Figure 3.1-5 Illustrations of induced positioning errors in the azimuth plane. Gray circles indicate the ideal antenna position. Blue and yellow circles show the actual location of the antennas during calibration and the phantom scan respectively. a) Single element accuracy error; both phantom and calibration scan have an induced 5° antenna offset of at l = 20°. b) Single element precision error; the phantom scan has induced offset of 5° at l = 20°. c) Array accuracy error; all antenna elements in both scans have an induced offset of 5°. d) Array precision error; all the antenna elements in the phantom scan have an induced offset of 5°. e) Random accuracy error; positioning errors in both scans follow a uniform distribution. The error distribution is identical in both scans. f) Random precision error, the induced error distribution is only present in the phantom scan.

All datasets were processed with the holographic reconstruction algorithm discussed in Flores-Tapia et al. [37]. The algorithm generated an intensity map for each dataset. The resolution of the images, bound by Equation 2-2, was 0.6 cm per pixel. A circular ROI was delimited by the diameter of the breast phantom. Based on the known location of the inclusions, images were segmented into tumor, fibroglandular, and clutter (background) regions. The size and shape of the inclusion regions were derived from the FWHM of a high-scattering cylindrical object of the same diameter as the inclusions.

Image contrast metrics (ICM) were used to compare the intensity of the targets inside the breast phantom. Three contrast metrics were used for this study: Signal to clutter ratio (SCR), tumor to fibroglandular ratio (TFR) and contrast to clutter ratio (CCR). For these experiments, SCR and TFR were calculated as follow:

$$SCR = 20\log\left(\frac{\bar{\Gamma}}{\bar{\Psi}}\right) \qquad TFR = 20\log\left(\frac{\bar{\Gamma}}{\bar{P}}\right)$$

Where $\bar{\Gamma}$ is the average intensity of the tumor region, $\bar{\Psi}$ is the average intensity of the background clutter (within the ROI), and $\bar{P}$ is the average intensity of the fibroglandular region. Contrast to clutter region was defined as:

$$CCR = 10\log\left(\frac{\bar{\Gamma}^2 - \bar{P}^2}{\bar{\Psi}^2}\right)$$

These metrics are similar to those employed in previous BMI studies [22], [31], [37], [71].

A threshold for signal and clutter intensity was determined using a ROC analysis. First, the reflections from tumor, fibroglandular and background regions of three control scans were combined. Then, fibroglandular-region values were treated as diseased and were compared to the background (normal condition). The resulting ROC curve served to establish a cut-off point (calculated using the maximum Youden index and cost-effective criterion) between the low-intensity background noise and the rest of the responses in the image. Values below the cut-off

threshold were removed from subsequent ROC analysis, as they resulted in ROC curves which were biased to the 0,1 corner.

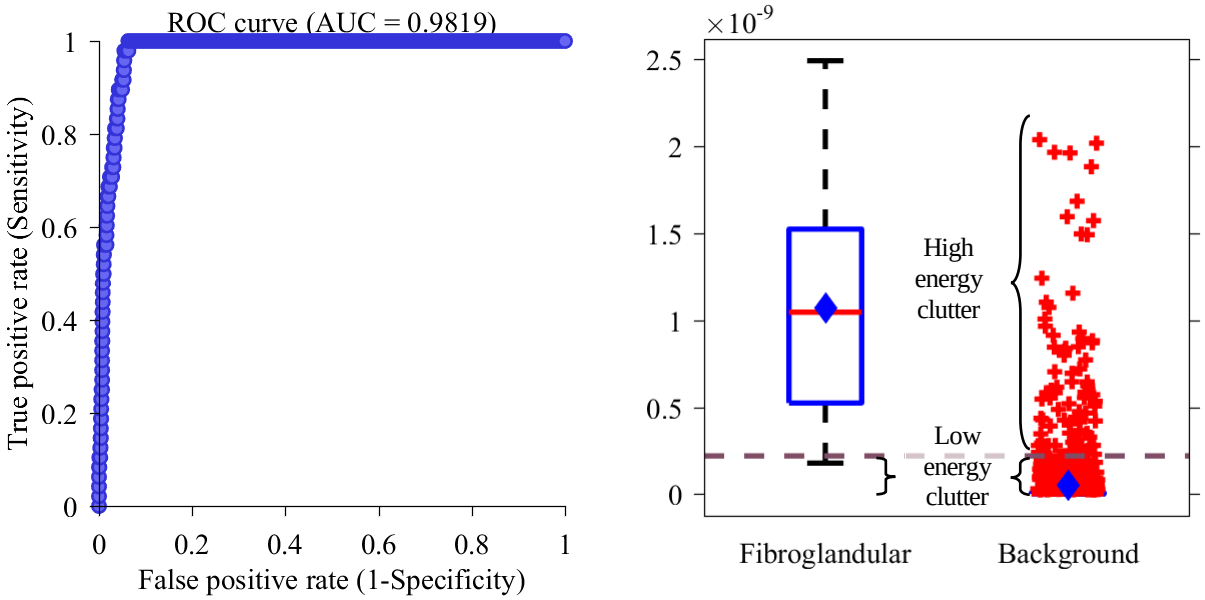


Figure 3.1-6 ROC analysis of fibroglandular vs. background regions in reconstructed images. a) ROC of the regions. The high contrast between the fibroglandular region (positive, $n = 16$) and the background region (negative, $n = 1649$) results in an almost-ideal curve (AUC = 0.981, SE = 0.025). b) Box-plot of fibroglandular and background regions with a cost-effective cut-off point. The dotted horizontal line marks the cut-off point for the low-intensity background noise. Values above the threshold are classified as clutter, fibroglandular or tumor regions.

ROC curves were generated for control and erroneous cases following a similar principle. Tumor-regions (diseased condition) were compared against fibroglandular and background regions above the low-intensity threshold (normal condition). For each ROC, the Area Under the Curve (AUC) and corresponding Standard Error of the mean (SE) were calculated following the methodology of Henley and McNeil [72]. Finally, the AUC of error-induced dataset were compared against control values using a unpaired Chi-square test with one degree of freedom [73].

A tumor diagnostic test was established using three criteria: presence, location, and dissimilarity. The tumor-presence criterion required that three or more adjacent pixels surpassed a threshold value. The threshold value was obtained from control scans and was established as two standard deviations above the mean value of the maximum fibroglandular responses. The location

criterion was met when the pixel with the highest intensity in the image was located inside the tumor-region. Since tumors are expected to provide the greatest amount of energy scatter, a strong response outside the tumor-region indicates the presence of an artifact or a substantial spatial error. Finally, the dissimilarity criterion compared the response contained within the tumor region against the responses from fibroglandular and clutter regions. The regions were compared using the non-parametric two-sample Kolmogorov-Smirnov test (k-s test) at the 95% confidence level. The criterion was considered satisfactory if the tumor distribution was significantly different than fibroglandular and clutter distributions. A diagnosis was considered correct if a reconstructed image passed all three criteria. Reconstructed control images satisfactory passed these diagnostic criteria.

In addition to the location criterion, spatial error was quantified in the reconstructed images. The spatial error was defined as the difference between the location of the maximum-intensity pixel in the image and the known location of the tumor. Within control images, a spatial uncertainty of 0.7 cm was attributed to the resolution of reconstructed images and phantom placement uncertainties.

## 3.2 Results from antenna positioning errors in the azimuthal direction

The following section analyses the reconstructed images of BMI scans with induced positioning errors in the azimuth direction. This study reports the effects of accuracy and precision errors at single, random, and array-wise antenna locations.

### 3.2.1 Single element accuracy error (ASA)

Single element accuracy errors had a minimal impact on the quality of breast microwave images. As Figure 3.2-1 shows, reconstructed images of error-induced datasets are free of artifacts, target shift or intensity loss even with an error of 15°. The images do experience a drop in the contrast of targets at values higher than 5° as indicated in Figure 3.2-2. SCR and CCR values at

15° are significantly lower than control images (unpaired one-tailed t-test, $p < 0.01$). The diagnostic outcome and spatial accuracy remained unaffected for all offset cases under 15° (see Table 3.2-1). At the 15° case, the ASA offset induces a slight improvement of the spatial error, however, compared to the resolution of the reconstructed image the change is negligible. The ROC curves of error-induced images overlap with the control images, and there are no significant differences in the AUC (see Figure 3.2-3 and Table 3.2-2).

In summary, single element accuracy errors in the azimuthal plane have no major impact on the diagnostic outcome of the system. Despite the statistically significant contrast change between signal and background intensity at the 15° case, all other metrics are unaffected.

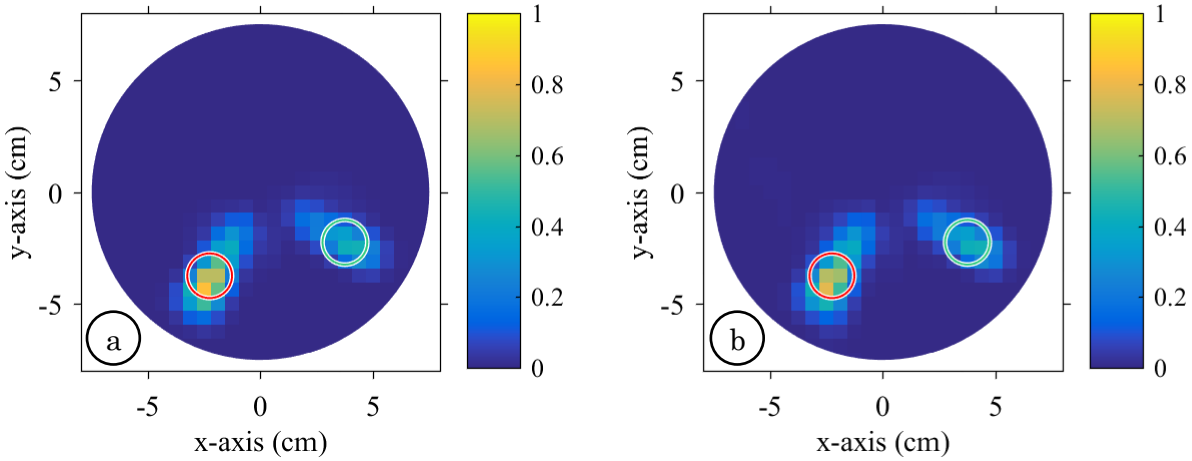


Figure 3.2-1 Reconstructed images of phantom scans with a single element accuracy error in the azimuthal plane. Images are normalized to the maximum scan value. Red and green circles indicate the known location of tumor and fibroglandular targets respectively. Error induced at the 48$^{th}$ antenna location (240°) with an offset of a) 1.25° and b) 15°. Despite the induced antenna positioning errors, there are no signs of image degradation.

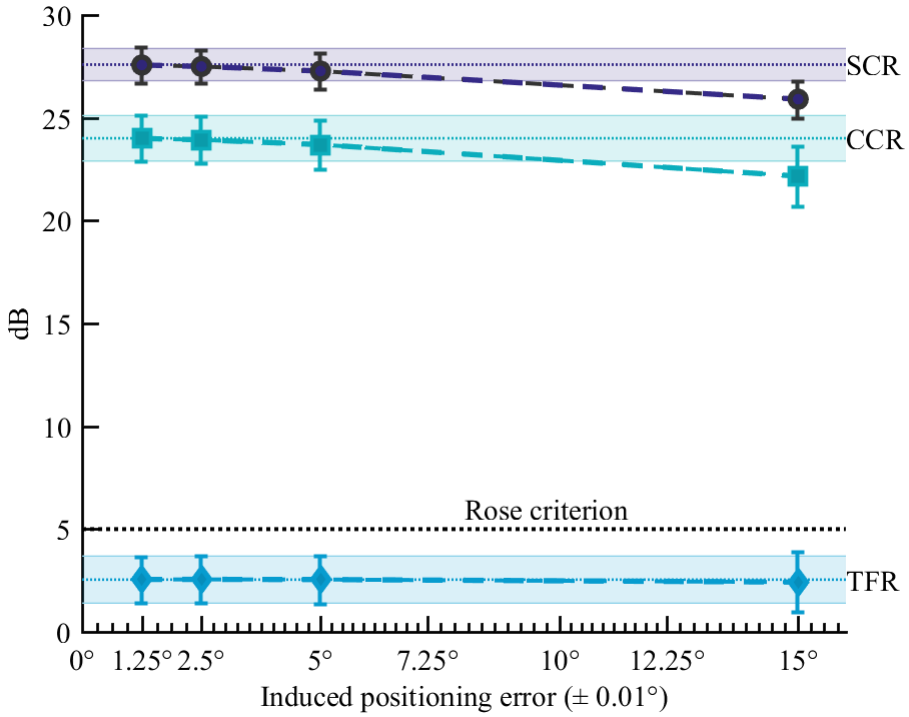


Figure 3.2-2 Plots of SCR, TFR, and CCR of reconstructed images with induced cases of a single element accuracy error in the azimuthal plane. Shaded areas indicate average metric value in control scans with 95% confidence interval ($n$ = 3). Error bars indicate the SE per error case ($n$ = 3). The contrast metrics remain unaffected by single element accuracy errors of up to 5°. In the 15° case, SCR and CCR are significantly lower than control values.

Table 3.2-1 Results of presence, location, and dissimilarity criteria of reconstructed images with induced cases of a single element accuracy error in the azimuthal plane.

| Case | Tumor presence | Tumor spatial error (cm) | Tumor dissimilarity to other regions (k-s test < 0.05) | **Diagnosis**. |
|---|---|---|---|---|
| Control | True | 0.7 ± 0.7 | Significant | Correct |
| 1.25° | True | 0.7 ± 0.7 | Significant | Correct |
| 2.50° | True | 0.7 ± 0.7 | Significant | Correct |
| 5.00° | True | 0.7 ± 0.7 | Significant | Correct |
| 15.00° | True | 0.5 ± 0.9 | Significant | Correct |

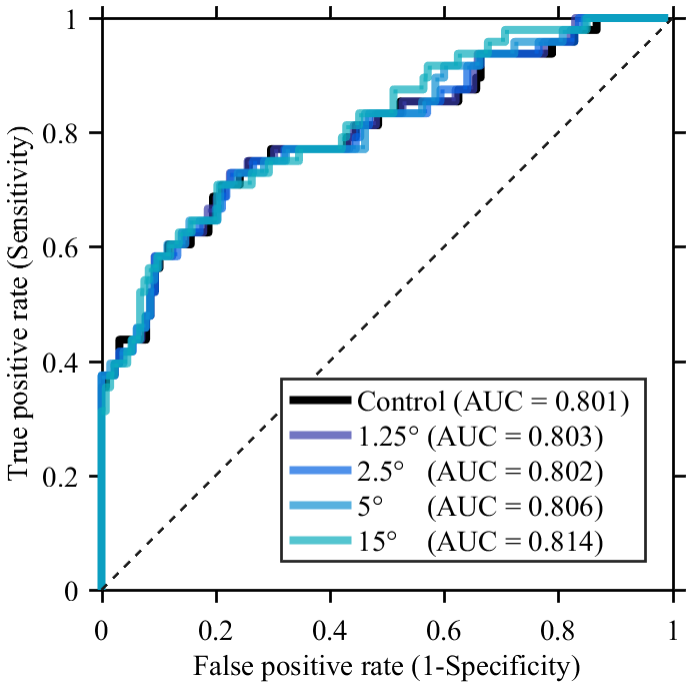


Figure 3.2-3 ROC curves of reconstructed images with accuracy errors induced in a single element in the azimuthal plane. ROC curves for all error cases overlap with the curves of control cases.

Table 3.2-2 Difference in AUC of control cases vs. single element accuracy error cases in the azimuthal plane

| **Case** | **AUC difference to control scan** | **SE** | **Outcome** ($X^2$, df = 1, $p < 0.05$) |
|---|---|---|---|
| Control | 0.000 | 0.041 | – |
| 1.25° | 0.002 | 0.041 | No significant difference |
| 2.50° | 0.001 | 0.041 | No significant difference |
| 5.00° | 0.005 | 0.041 | No significant difference |
| 15.00° | 0.013 | 0.040 | No significant difference |

### 3.2.2 Single element precision error (ASP)

Single element precision errors had a minimal impact on the quality of breast microwave images. As shown in Figure 3.2-4, precision errors of up to 15° have no noticeable effect on reconstructed images. Images are clear, without artifacts or target-shift. Figure 3.2-5 shows contrast metrics within the confidence interval of control scans up to 5° of error. A 15° precision error causes a significant drop in SCR and CCR (unpaired one-tailed t-test, $p < 0.05$). For all the single element precision error cases, the diagnostic outcome and spatial accuracy remained unaffected (see Table 3.2-3). ROC curves of error-induced images overlap with the control curve, and AUC differences are not statistically significant (see Figure 3.2-3 and Table 3.2-2).

Precision errors smaller than 15° affecting a single probing point in the azimuthal plane have no significant impact on the diagnostic outcome of the BMI system. Despite the statistically significant contrast change between signal and background in the 15° case, all other metrics remain unaffected, and the tumor inclusion can be easily resolved in the generated images.

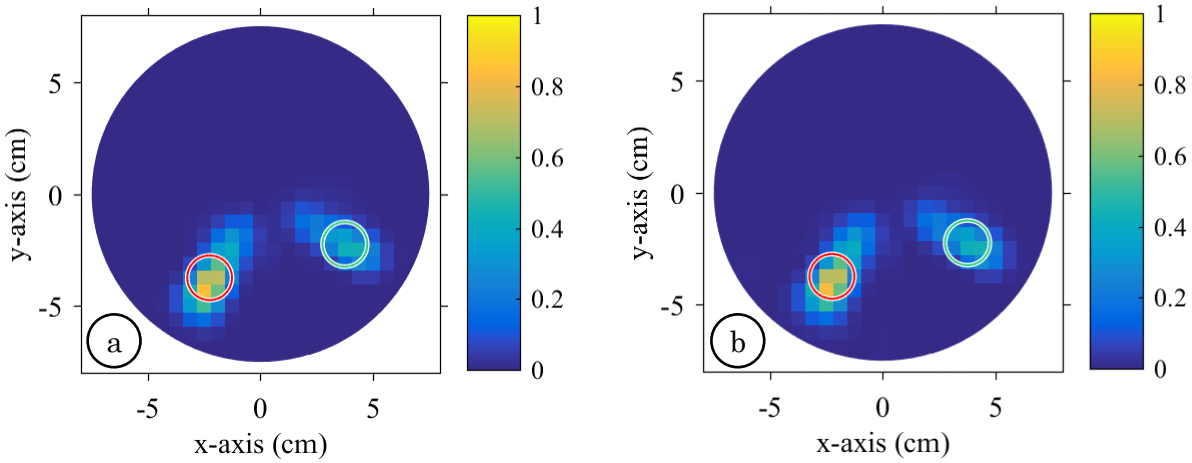


Figure 3.2-4 Reconstructed images of phantom scans with a single element precision error in the azimuthal plane.Images are normalized to the maximum scan value. Red and green circles indicate the known location of tumor and fibroglandular targets respectively. Error induced at the 48th antenna location (240°) with an offset of a) 1.25° and b) 15°. Despite the induced errors, there are no visible signs of image degradation.

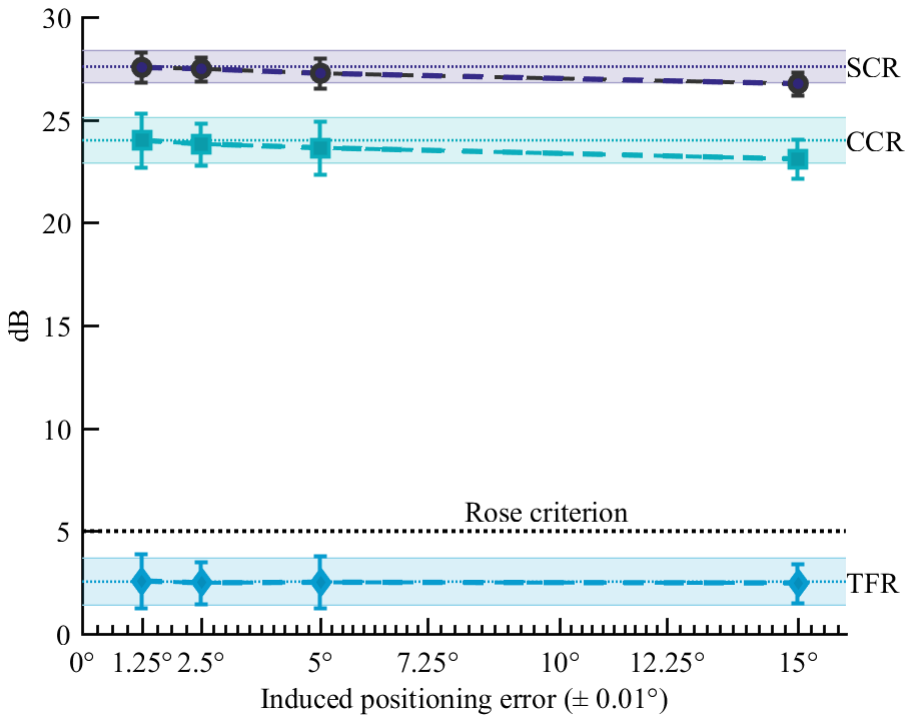


Figure 3.2-5 Plots of SCR, TFR, and CCR of reconstructed images with induced cases of a single element precision error in the azimuthal plane. Shaded areas indicate average metric value in control scans with 95% confidence interval ($n$ = 3). Error bars indicate the SE per error case ($n$ = 3). The contrast metrics remain unaffected by single element precision errors of up to 5°. In the 15° case SCR and CCR are significantly lower than control values.

Table 3.2-3 Results of presence, location, and dissimilarity criteria of reconstructed images with induced cases of a single element precision error in the azimuthal plane.

| Case | Tumor presence | Tumor spatial error (cm) | Tumor dissimilarity to other regions (k-s test > 0.05) | **Diagnosis**. |
|---|---|---|---|---|
| Control | True | 0.7 ± 0.7 | Significant | Correct |
| 1.25° | True | 0.7 ± 0.7 | Significant | Correct |
| 2.50° | True | 0.7 ± 0.7 | Significant | Correct |
| 5.00° | True | 0.7 ± 0.7 | Significant | Correct |
| 15.00° | True | 0.7 ± 0.7 | Significant | Correct |

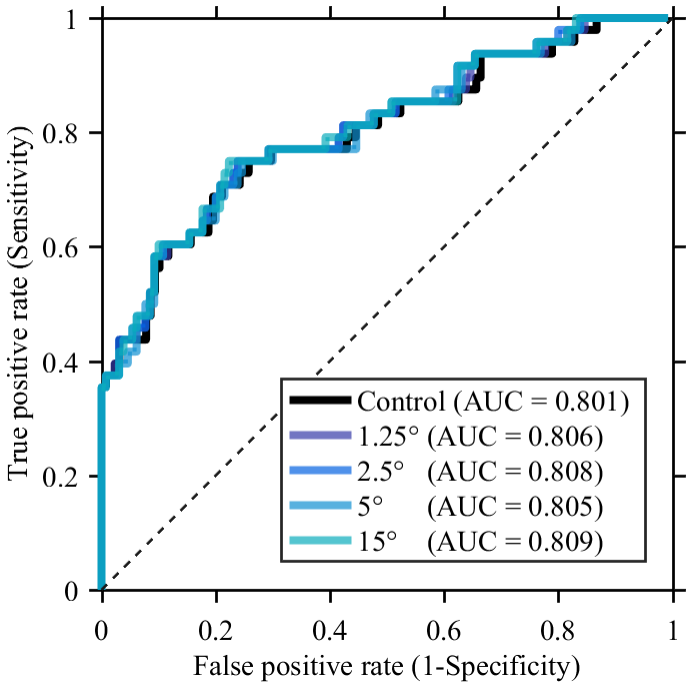


Figure 3.2-6 ROC curves of three reconstructed images with accuracy errors induced in a single element in the azimuthal plane. ROC curves for all error cases overlap with the curves of control cases.

Table 3.2-4 Difference in AUC of control cases vs. single element precision errors in the azimuthal plane.

| **Case** | **AUC difference to control** | **SE** | **Outcome ($X^2$, df = 1, $p < 0.05$)** |
|---|---|---|---|
| Control | 0.000 | 0.041 | – |
| 1.25° | 0.005 | 0.041 | No significant difference |
| 2.50° | 0.007 | 0.041 | No significant difference |
| 5.00° | 0.004 | 0.041 | No significant difference |
| 15.00° | 0.008 | 0.040 | No significant difference |

### 3.2.3 Random element accuracy error (ARA)

The system is immune to low-magnitude random accuracy errors, but high values reduce the visibility of targets. Reconstructed images with this type of error exhibit no noticeable change up to offsets of 2.5°. Figure 3.2-7a) shows a small decrease in target intensity for the 5° case. At the 15° case shown in Figure 3.2-7b), the intensity of both targets has dropped by almost an order of magnitude and the targets exhibit a diffused cross-section. Errors below 2.5° do not result in a significant contrast change between targets as shown in Figure 3.2-8. SCR and CCR fall below control values after errors greater than 5°. Average TFR remains close to control values for all cases, but the 15° case has a greater SE. As shown in Table 3.2-5, random accuracy errors below 5° do no alter the ability of the system to detect the tumor responses. In the 15° case, the diffuse reflections from the target are below the tumor-threshold criteria, rendering an incorrect diagnostic (i.e., false negative).

The induced random accuracy had an interesting effect on the ROC curve analysis (see Figure 3.2-9 and Table 3.2-6). The ROC curve and the AUC significantly improve for the 15° case despite the evident image degradation. This behavior is observed because the tumor pixel values are above the rest in the image. The remaining contrast, combined with an increase in clutter yield the apparent better performance.

Random accuracy errors greater than 5° have a significant effect on the reconstructed images by reducing the target intensity. Distributions with errors as large as 15° obscure the presence of the malignant tissue.

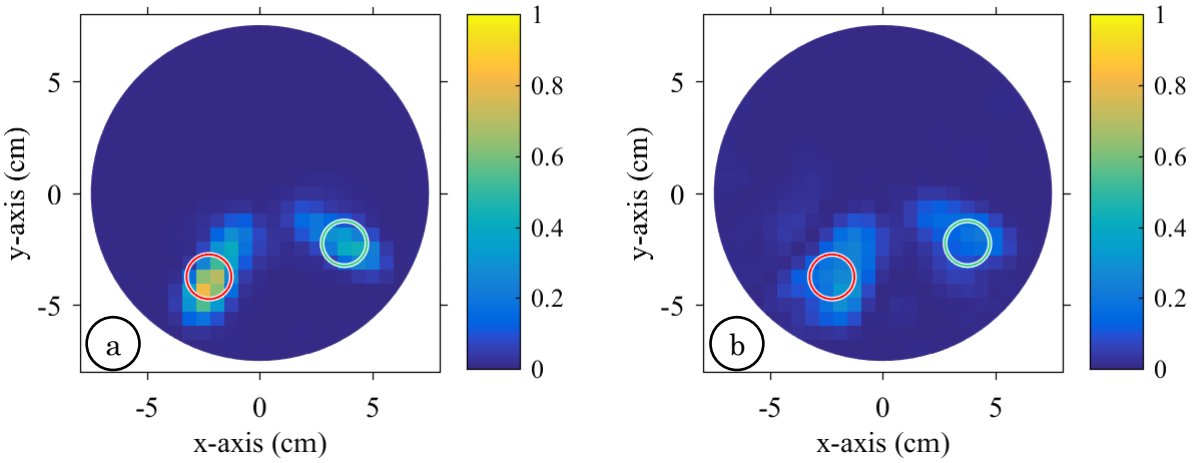


Figure 3.2-7 Reconstructed images of phantom scans with a random accuracy error in the azimuthal plane. Images are normalized to the maximum scan value. Red and green circles indicate the known location of tumor and fibroglandular targets respectively. a) Offsets induced in the range of -5° to 5°, in multiples of 1.25°. b) Offsets ranged from -15° to 15°. Image a) shows no visible signs of image degradation. The targets in b) have noticeable intensity reduction and a bigger cross section.

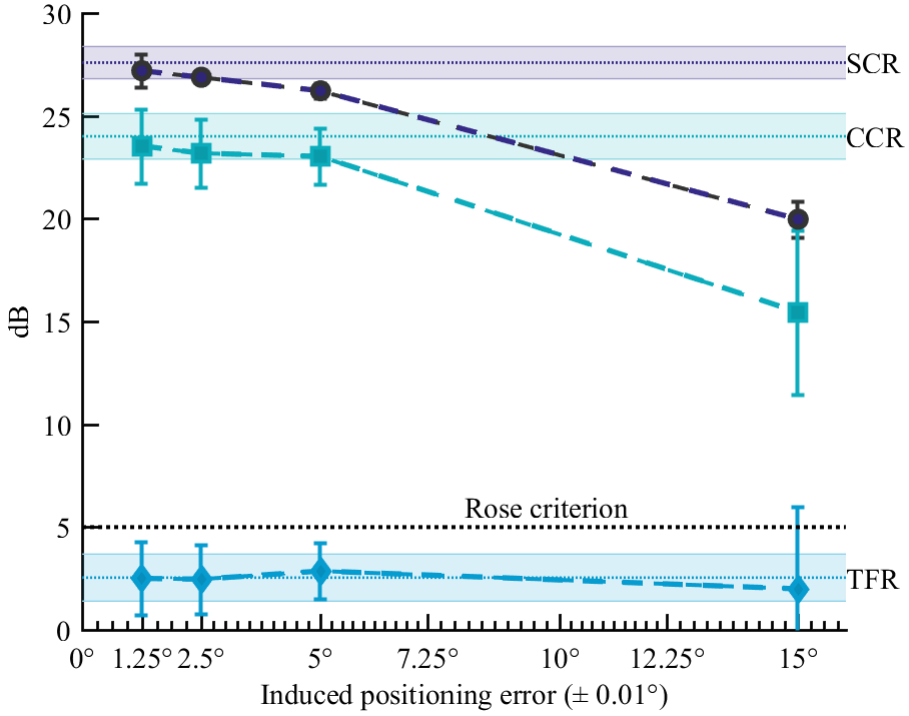


Figure 3.2-8 Plots of SCR, TFR, and CCR of reconstructed images with induced random accuracy errors in the azimuthal plane. Shaded areas indicate average metric value in control scans with 95% confidence interval ($n$ = 3). Error bars indicate the SE per error cases ($n$ = 3). At the 5° case the SCR and CCR are significantly lower than control scans, and the difference increases considerably at the 15° case. TFR values remain within the confidence intervals of control scans. TFR and CCR have an increased SE in the 15° case.

Table 3.2-5 Results of presence, location, and dissimilarity criteria of reconstructed images with induced random accuracy errors in the azimuthal plane.

| Case | Tumor presence | Tumor spatial error (cm) | Tumor dissimilarity to other regions (k-s test > 0.05) | **Diagnosis**. |
|---|---|---|---|---|
| Control | True | 0.7 ± 0.7 | Significant | Correct |
| 1.25° | True | 0.7 ± 0.7 | Significant | Correct |
| 2.50° | True | 0.7 ± 0.7 | Significant | Correct |
| 5.00° | True | 0.7 ± 0.7 | Significant | Correct |
| 15.00° | False | NA | Significant | Incorrect |

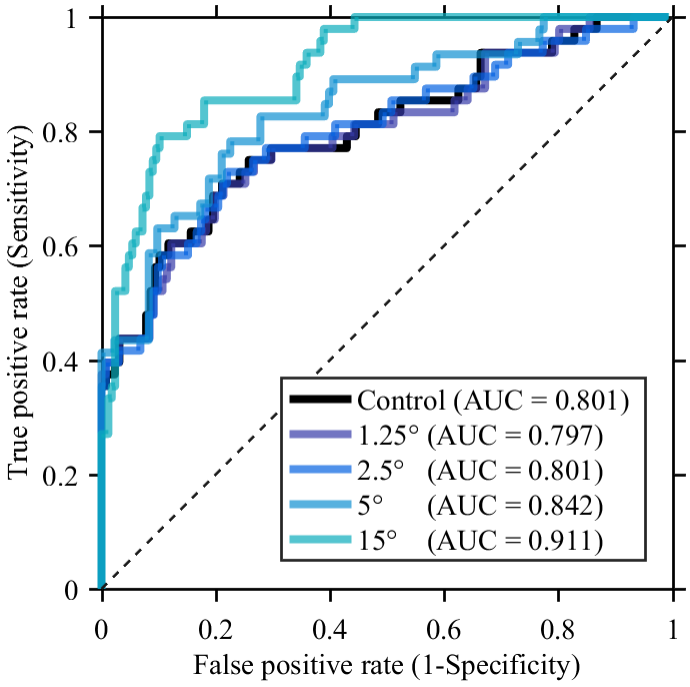


Figure 3.2-9 ROC curves of three reconstructed images with random accuracy errors induced in the azimuthal plane. Curves for the 1.25° and 2.5° cases follow the control scan curve closely. The 5° and 15° cases have a greater AUC and their ROC yields toward the false positive region combined with a positive shift towards the true positive rate.

Table 3.2-6 Difference in AUC of control cases vs. random accuracy errors in the azimuthal plane.

| Case | AUC difference to control | SE | **Outcome** ($X^2$, df = 1, p < 0.05) |
|---|---|---|---|
| Control | 0.000 | 0.041 | – |
| 1.25° | -0.004 | 0.041 | No significant difference |
| 2.50° | 0.000 | 0.041 | No significant difference |
| 5.00° | 0.041 | 0.038 | No significant difference |
| 15.00° | 0.110 | 0.029 | The AUC are different |

### 3.2.4 Random element precision error (ARP)

Phantom scans with high-magnitude random precision errors result in reconstructed images with artifacts and reduced target intensity (see Figure 3.2-10). Low-intensity artifacts are visible in reconstructed images with offsets in the range of -5° to 5°. In the 15° case, the inclusions in the phantom are no longer identifiable as the target response decreases and the intensity of the artifacts increases. The contrast metric plot seen in Figure 3.2-11 shows that error cases as small as 1.25° decrease the SCR and CCR below the confidence intervals of control scans. In the 15° case, the reflections from the fibroglandular region surpass the tumor response, and the TFR becomes negative. For the same case, the SCR drops below half its original value, and the CCR falls close to the rose criterion. The 15° was the only case with an incorrect diagnosis (see Table 3.2-7). For this case only, one of the three scans contained reflections above the tumor-threshold, and the reflection corresponded to an artifact (see Figure 3.2-12). Finally, the ROC curve for the 15° case is skewed to the right, with an increased false positive rate but a greater sensitivity.

In summary, random precision errors with values as low as 1.25° have a statistically significant effect on reconstructed images, reducing SCR and CCR. Artifacts and reduced target intensity are associated with 5° and 15° cases.

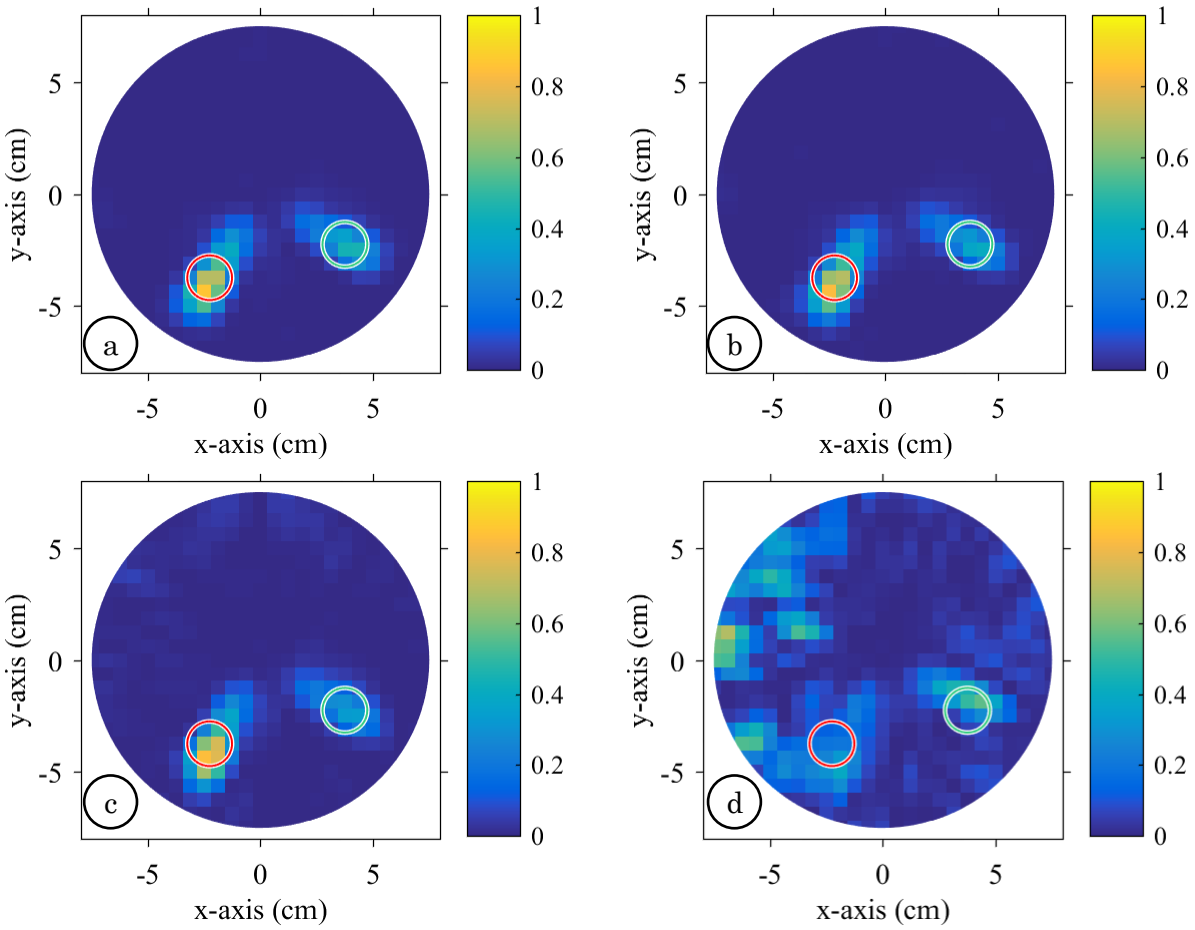


Figure 3.2-10 Reconstructed images of phantom scans with induced with random precision errors in the azimuthal plane. Images are normalized to the maximum scan value. Red and green circles indicate the known location of the tumor and fibroglandular targets, respectively. a) Offsets in the range of -1.25° to 1.25°, in multiples of 1.25°. b) Offsets in the range of -2.5° to 2.5°. c) Offsets in the range of -5° and 5° c) Offsets range from -15° to 15°. Image a) shows no visible signs of image degradation. A minimal change in intensity is perceptible in c). Low-intensity artifacts are present in c). Image d) is saturated with artifacts. Targets show a decreased intensity and can no longer be resolved amidst the surrounding clutter.

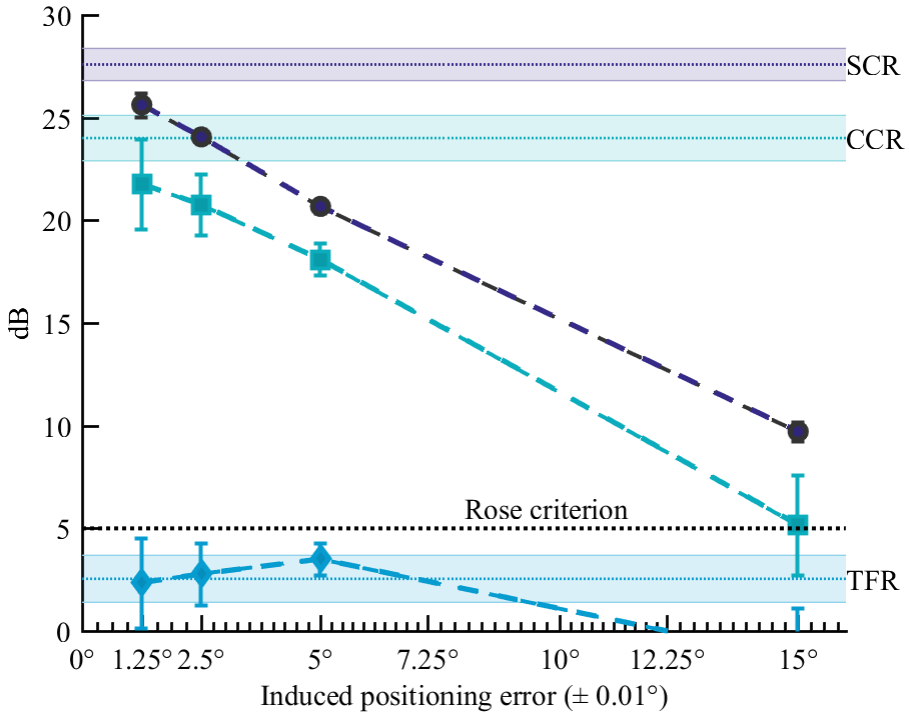


Figure 3.2-11 Plots of SCR, TFR, and CCR of reconstructed images with induced cases of random precision errors in the azimuthal plane. Shaded areas indicate average metric value in control scans with 95% confidence interval ($n$ = 3). Error bars indicate the SE per error cases ($n$ = 3). SCR and CCR metrics significantly drop after the 1.25° case and consistently decays as the magnitude of the errors increases. The TFR remain within the confidence bounds up until the 5° case, where it reaches values significantly greater than those of the controls. At the 15° case, TFR drops to negative values while the CCR decays to values close to the rose criterion.

Table 3.2-7 Results of presence, location, and dissimilarity criteria of reconstructed images with induced cases of random precision errors in the azimuthal plane.

| Case | Tumor presence | Tumor spatial error (cm) | Tumor dissimilarity to other regions (k-s test > 0.05) | **Diagnosis**. |
|---|---|---|---|---|
| Control | True | 0.7 ± 0.7 | Significant | Correct |
| 1.25° | True | 0.7 ± 0.7 | Significant | Correct |
| 2.50° | True | 0.7 ± 0.7 | Significant | Correct |
| 5.00° | True | 0.7 ± 0.7 | Significant | Correct |
| 15.00° | Outside region (1/3) False (2/3) | 6.8 ± 0.7 | Significant | Incorrect |

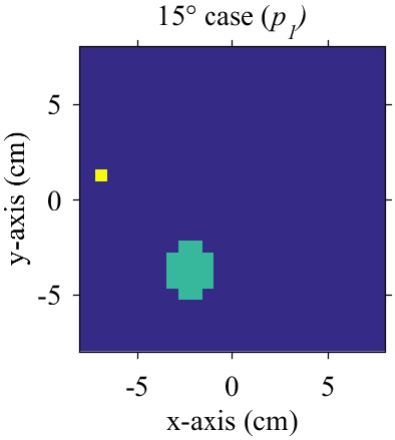


Figure 3.2-12 Location of the maximum value in reconstructed images with random precision errors in the azimuthal plane. At the 15° case, only one scan ($p_1$) the maximum value (yellow) is above the tumor-threshold criterion, and it is located outside the tumor region (green).

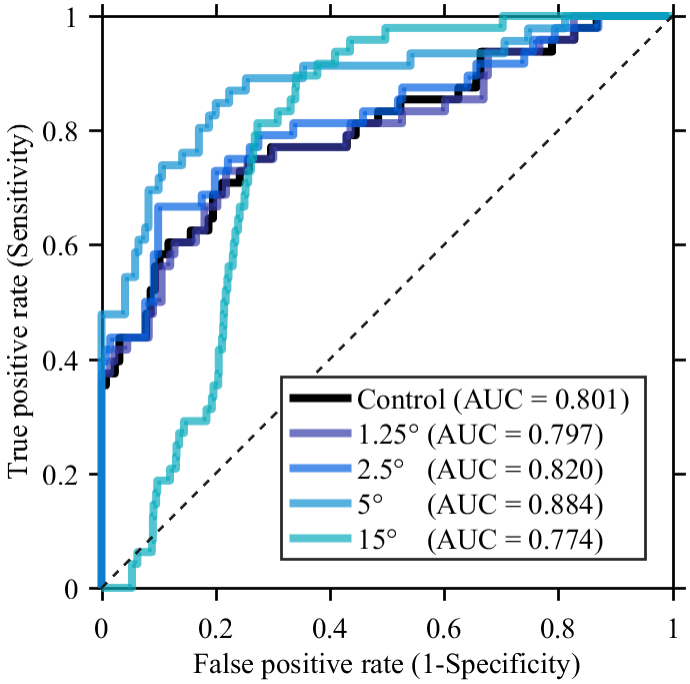


Figure 3.2-13 ROC curves of three reconstructed images with random precision errors induced in the azimuthal plane. ROC and corresponding AUC of error cases below 2.5° remain close to control scans values. The 5° case exhibits a slightly better ROC curve and AUC values. The 15° case has a remarkably different ROC curve, skewed towards the false positive rate albeit better sensitivity scores.

Table 3.2-8 Difference in AUC of control cases vs. random precision errors in the azimuthal plane.

| Case | AUC difference to control | SE | **Outcome** ($X^2$, df = 1, $p < 0.05$) |
|---|---|---|---|
| Control | 0.000 | 0.041 | – |
| 1.25° | -0.004 | 0.041 | No significant difference |
| 2.50° | 0.019 | 0.040 | No significant difference |
| 5.00° | 0.083 | 0.033 | No significant difference |
| 15.00° | -0.027 | 0.040 | No significant difference |

### 3.2.5 Array accuracy error (AAA)

The presence of array accuracy errors resulted in a shift in the location of the target responses. Compared to control images, a small change in the location of the targets can be seen in Figure 3.2-14a. Figure 3.2-14b shows that an accuracy error of 15° results in target reflections outside their expected location based on prior knowledge. No other changes are perceptible in the reconstructed images. The three contrast metrics remain within the confidence intervals of control scans for the 1.25°, 2.5°, and 5° cases (see Figure 3.2-15). At 15°, the SCR and CCR experience a statistically significant drop (unpaired one-tailed t-test, $p < 0.01$). Table 3.2-9 shows that presence and dissimilarity diagnostic criteria remain unchanged for all error cases. Tumor location criteria are met despite the shift in the location of tumor-like responses (i.e., above tumor-threshold value) since the responses remain within the tumor region (see Figure 3.2-16). A decrease in the AUC of ROC is observed in Figure 3.2-17 for errors greater than 1.25°. However, the change in AUC is not significantly different to control values (see Table 3.2-10).

Entire array accuracy errors greater than 5° generate a significant drop in contrast metrics, an increase in the spatial error of images, and a small change in the ROC curves. However, the changes are associated with reflections moving outside the boundaries of the target regions established for control scans. Reconstructed images are free of artifacts or intensity losses, and the tumor response can be distinguished from fibroglandular and background reflections.

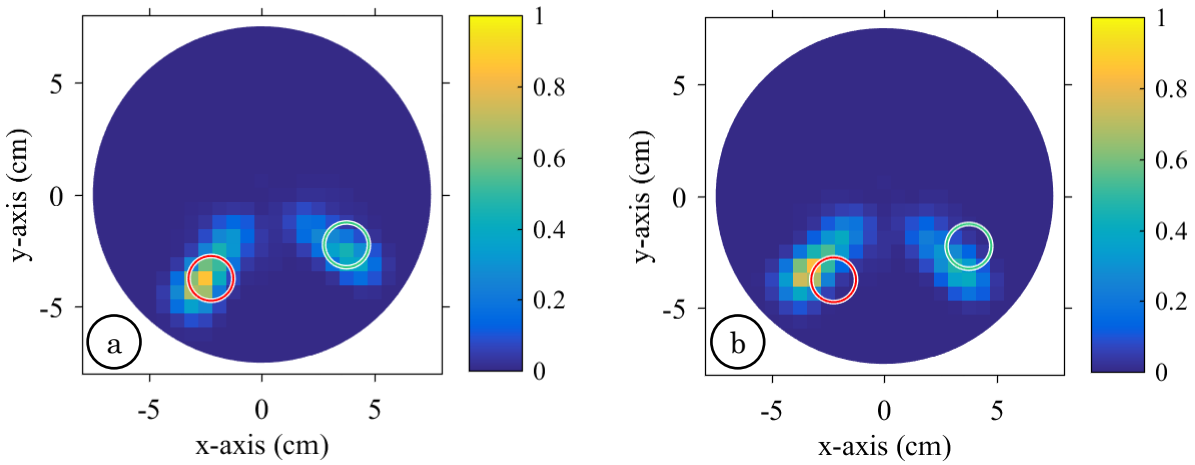


Figure 3.2-14 Reconstructed images of phantom scans with an entire array accuracy error in the azimuthal plane. Images are normalized to the maximum scan value. Red and green circles indicate the known location of tumor and fibroglandular targets respectively. Offset induced uniformly among all probing points with a value of a) 5° and b) 15°. The responses inside the phantom experience an angular shift, proportional to the induced antenna offset. The images have no artifacts, and the intensity of the targets remains unaffected.

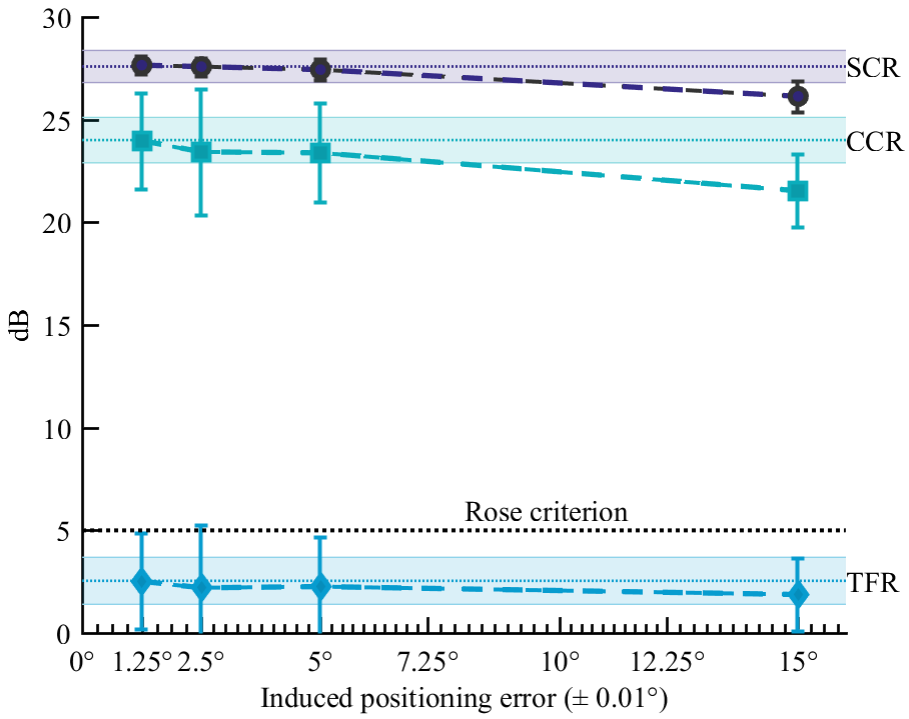


Figure 3.2-15 Plot of SCR, TFR, and CCR of reconstructed images with entire array errors in the azimuthal plane. Shaded areas indicate average metric value in control scans with 95% confidence interval (n = 3). Error bars indicate the SE per error case (n = 3). SCR remains within the confidence intervals of control scans for errors smaller than 5°. The 15° accuracy error case results in a significant drop in SCR and CCR compared to control scans. The SE of CCR and TFR metrics is greater than that of the control values.

Table 3.2-9 Results of presence, location, and dissimilarity criteria of reconstructed images with entire array accuracy errors in the azimuthal plane.

| Case | Tumor presence | Tumor spatial error (cm) | Tumor dissimilarity to other regions (k-s test > 0.05) | **Diagnosis**. |
|---|---|---|---|---|
| Control | True | 0.7 ± 0.7 | Significant | Correct |
| 1.25° | True | 0.5 ± 0.9 | Significant | Correct |
| 2.50° | True | 0.3 ± 0.7 | Significant | Correct |
| 5.00° | True | 0.3 ± 0.7 | Significant | Correct |
| 15.00° | True | 1.1 ± 0.7 | Significant | Correct |

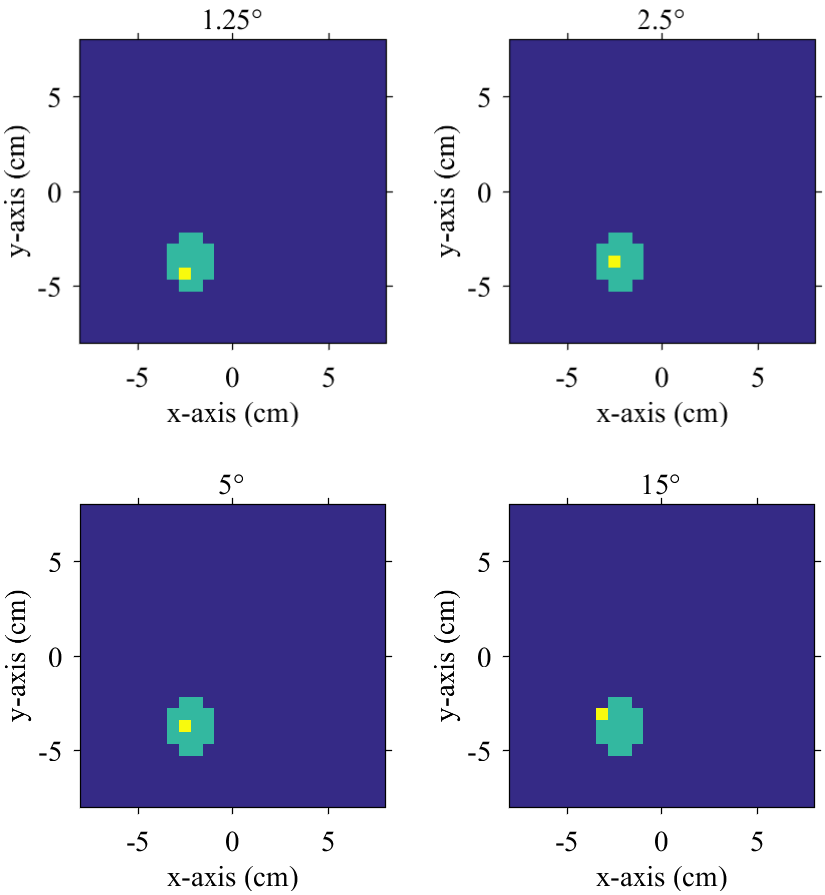


Figure 3.2-16 Location of the maximum value in reconstructed images with entire array accuracy errors in the azimuthal plane. As the error increases, the position of maximum values (yellow) shifts towards the middle-left area on the image. For all values of accuracy error, the maximums remain within the tumor region (green).

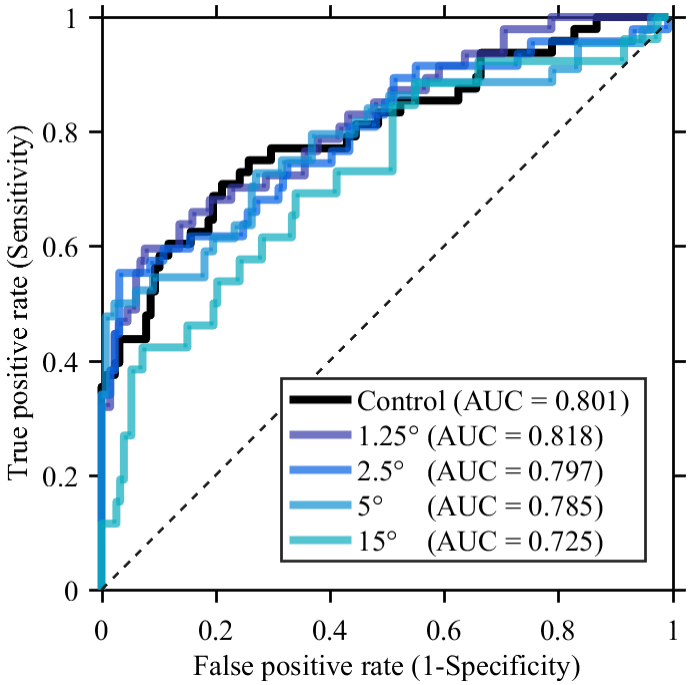


Figure 3.2-17 ROC curves of three reconstructed images with entire array accuracy errors induced in the azimuthal plane. The induced errors result in slightly different ROC, with a tendency towards a lower AUC.

Table 3.2-10 Difference in the AUC of control cases vs. cases with entire array accuracy errors in the azimuthal plane.

| Case | AUC difference to control | SE | **Outcome** (**$X^2$, df = 1, p < 0.05**) |
|---|---|---|---|
| Control | 0.000 | 0.041 | – |
| 1.25° | 0.017 | 0.040 | No significant difference |
| 2.50° | 0.004 | 0.042 | No significant difference |
| 5.00° | 0.016 | 0.044 | No significant difference |
| 15.00° | 0.076 | 0.059 | No significant difference |

### 3.2.6 Array precision error (AAP)

The presence of precision errors in the entire azimuthal plane has a detrimental effect on the quality of reconstructed images and their diagnostic outcome. Figure 3.2-19 shows that an array-wide precision error of 2.5° generates artifacts in the reconstructed images. The intensity and size of the artifacts increases relative to the magnitude of the induced errors. Additionally, the induced errors modify the intensity of targets. Errors as small as 1.25° can significantly decrease the contrast between targets and the background. At 5°, the intensity of the fibroglandular region is greater than the tumor region, the TFR become negative, and the CCR falls to values close to the rose criterion. Table 3.2-11 show that the induced errors greater than 1.25° obstruct the ability of the system to detect tumor responses. In the 5° and 15° cases, the strongest responses in the image are located outside the tumor region with a spatial error of 4.3 cm (± 3.4 cm) and 5.5 cm (± 0.3 cm) (Figure 3.2-20). In the 2.5° and 5° cases, the difference between the tumor and fibroglandular responses was not significant (k-s test < 0.05). These type of precision errors also affect the AUC with a significant difference at the 15° case (see Figure 3.2-21 and Table 3.2-12).

In summary, precision errors affecting the entire antenna array result in artifacts and decreased contrast between targets. The magnitude of the artifacts is not detrimental to the image quality at precision errors below 1.25°. However, they have a statistically significant effect in contrast metrics. Reconstructed images with array precision errors greater than 2.5° will result in low-quality images and an incorrect diagnosis.

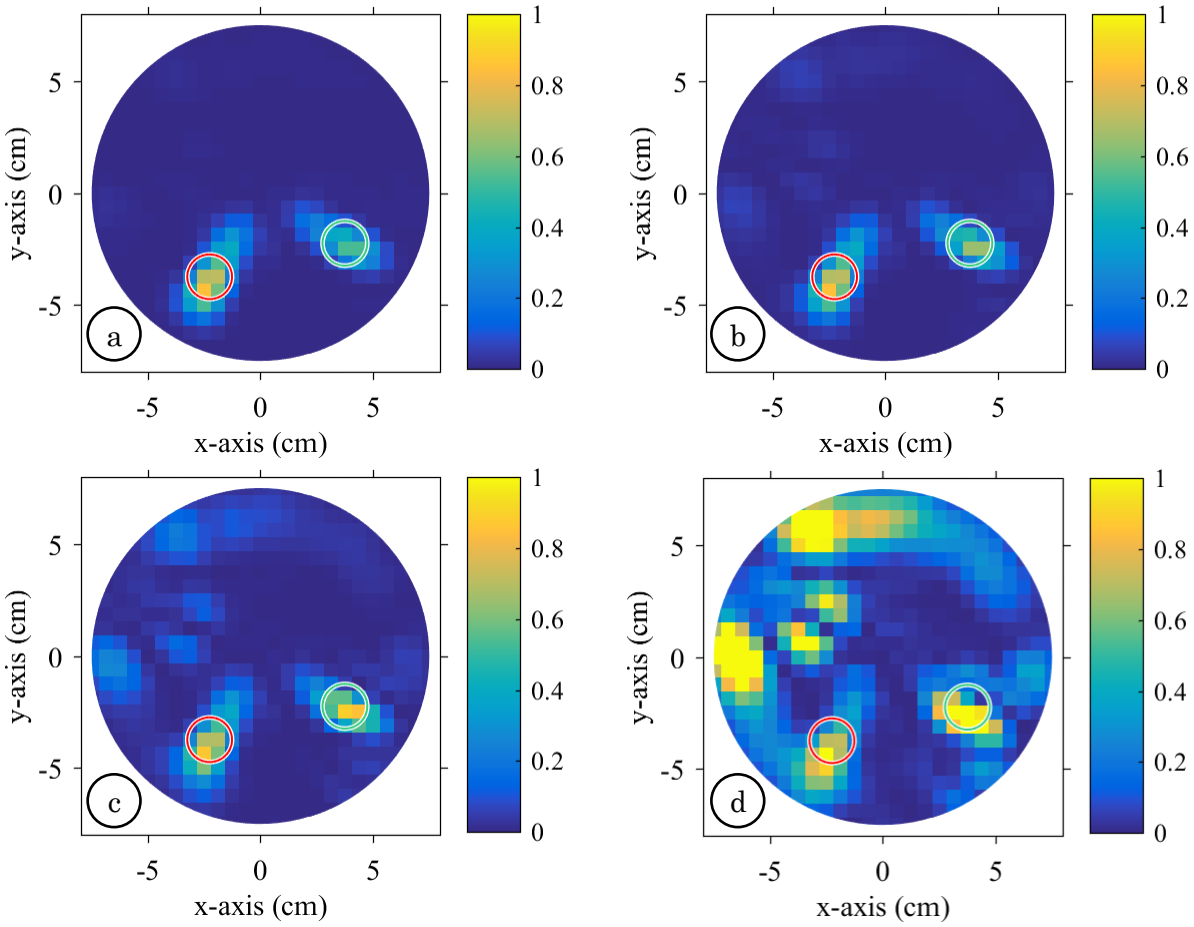


Figure 3.2-18 Reconstructed images of phantom scans with an entire array precision error in the azimuthal plane. Images are normalized to the maximum scan value. Red and green circles indicate the known location of tumor and fibroglandular targets respectively. The figures show an offset value of a) 1.25° b) 2.5° c) 5° and d) 15°. Low-intensity artifacts become visible at 2.5° and increase in size and intensity for images with greater errors. At 5°, the fibroglandular target has reached a similar intensity level than the tumor target. At 15°, artifacts have a higher intensity than a tumor or fibroglandular targets.

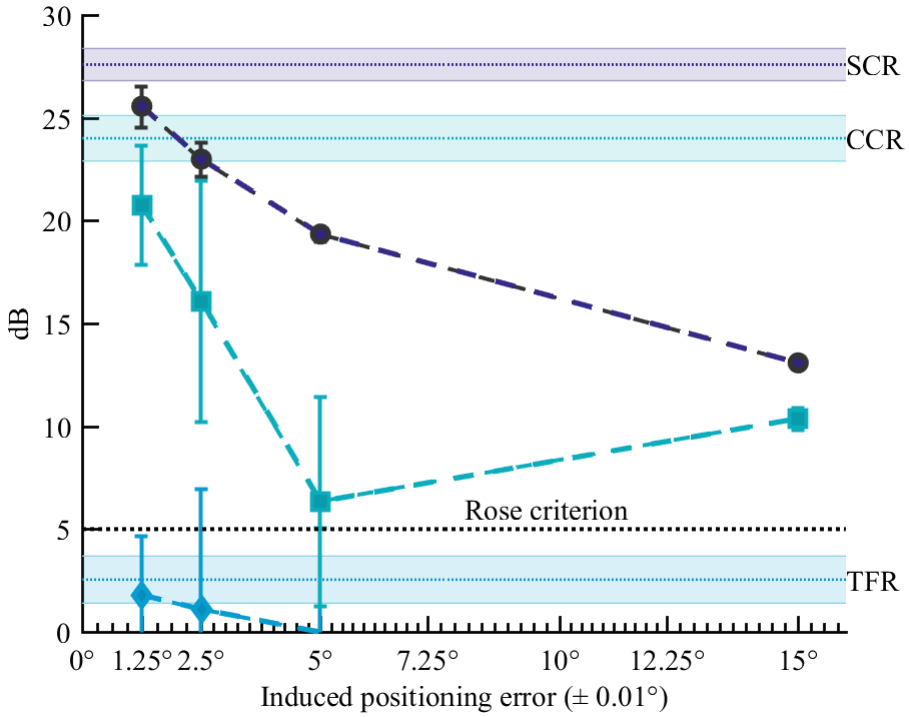


Figure 3.2-19 Plots of SCR, TFR, and CCR of reconstructed images with entire array precision errors in the azimuthal plane. Shaded areas indicate average metric value in control scans with 95% confidence interval ($n$ = 3). Error bars indicate the SE per error case ($n$ = 3). All metrics experience a drop in magnitude proportional to the induced error. At the 1.25° error case, SCR and CCR are significantly below control values. At 2.5° TFR is significantly lower than control values. After 5° of induced error, the fibroglandular region intensity is greater than the tumor region, and the TFR becomes negative. The average CCR at 5° is 75% lower compared to control values, with the SE crossing below the rose criterion. For the 15° case, the CCR recover in magnitude, but the SCR decrease to nearly half of its original value. Greater SE are obtained with the TFR and CCR metrics.

Table 3.2-11 Results of presence, location, and dissimilarity criteria of reconstructed images with entire array precision errors in the azimuthal plane.

| Case | Tumor presence | Tumor spatial error (cm) | Tumor dissimilarity to other regions (k-s test > 0.05) | **Diagnosis**. |
|---|---|---|---|---|
| Control | True | 0.7 ± 0.7 | Significant | Correct |
| 1.25° | True | 0.7 ± 0.7 | Significant | Correct |
| 2.50° | True | 0.7 ± 0.7 | Not significant | Incorrect |
| 5.00° | Outside region | 4.3 ± 3.8 | Not significant | Incorrect |
| 15.00° | Outside region | 5.5 ± 0.7 | Significant | Incorrect |

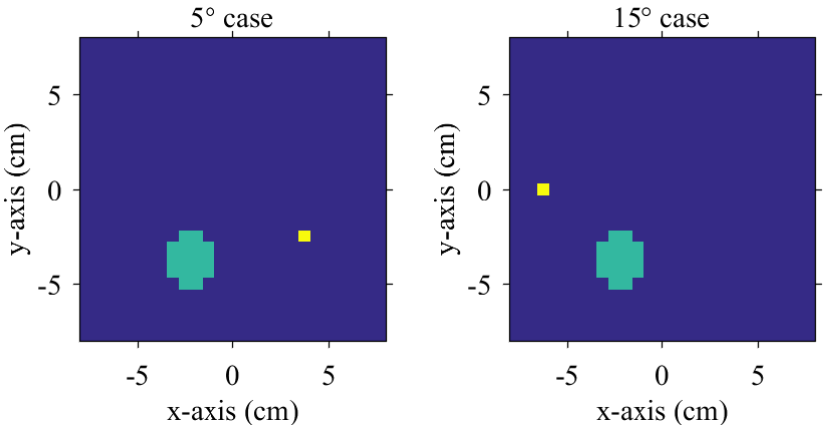


Figure 3.2-20 Location of the maximum value in reconstructed images with an entire array precision error in the azimuthal plane. For the 5° and 15° error cases, the highest intensity pixel in the image (yellow) was located outside the expected tumor region (green).

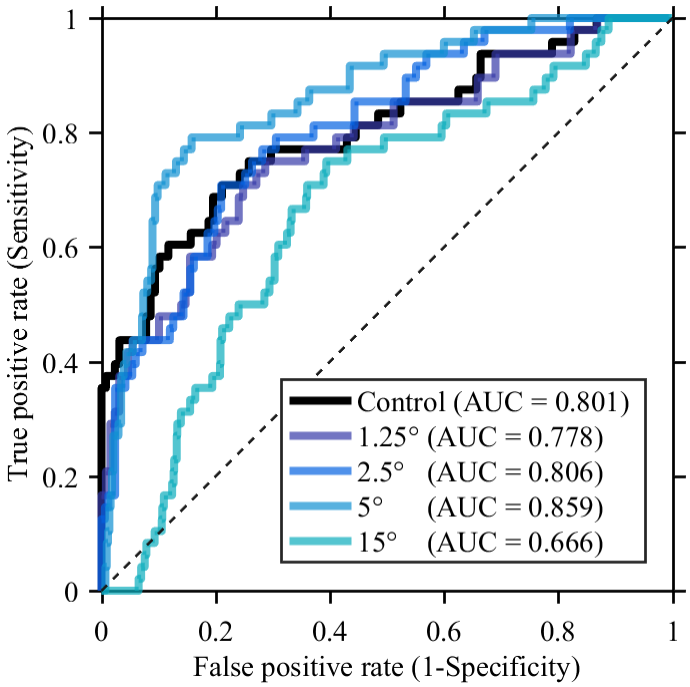


Figure 3.2-21 ROC curves of three reconstructed images with entire array precision errors in the azimuthal plane. The ROC from error-cases differs from the control case with a shift towards the false positive rate. The 5° error case has a slightly bigger AUC with a positive shift in the ROC towards the true positive rate. The ROC and corresponding AUC significantly deteriorate for the 15° case.

Table 3.2-12 Difference in AUC of control cases vs. entire array precision errors in the azimuthal plane.

| Case | AUC difference to control | SE | **Outcome** ($X^2$, df = 1, $p < 0.05$) |
|---|---|---|---|
| Control | 0.000 | 0.041 | – |
| 1.25° | -0.023 | 0.043 | No significant difference |
| 2.50° | 0.005 | 0.040 | No significant difference |
| 5.00° | 0.058 | 0.035 | No significant difference |
| 15.00° | -0.135 | 0.044 | The AUC are different |

## 3.3 Results from antenna positioning errors in the vertical direction

Accuracy and precision errors in the vertical direction were induced in datasets collected at three sections of the breast phantom: top (closer to the chest wall), medium, and bottom (closer to the nipple). Preliminary analysis of the reconstructed images showed that the uppermost level contained the worst conditions of image degradation. The breast diameter is greater closer the chest wall. The increased propagation losses result in a lower response from the structures inside the breast. Thus, noise and artifacts had a greater impact on the quality of images collected in the top section of the phantom. The following in-depth analysis presented is for the top section case.

### 3.3.1 Array accuracy errors (VAA)

Accuracy errors in the vertical plane significantly change the contrast of reconstructed images but do not deteriorate the quality of reconstructed images. Figure 3.3-1 shows a fluctuation in the intensity of targets as the accuracy errors increase. The Figure 3.3-2 shows an improvement in the CCR and TFR for the 0.05 cm case. The 0.10 cm case exhibits a drop in SCR and CCR below control values while TFR returns to control scans. Finally, the three metrics return to control-like values for the 0.20 cm case. The induced accuracy errors have no impact on the diagnostic criteria (see Table 3.3-1) and do not significantly alter the ROC curve (see Figure 3.3-3 and Table 3.3-2).

The improvement on the ROC curve and contrast metrics at 0.05° indicates a better alignment between the horizontal antenna plane and the equator of the inclusion targets. The small differences are attributed to human error in the placement of the targets (± 0.3 cm).

Vertical accuracy errors as big as 0.20 cm do not adversely affect the reconstructed images. A significant change in the contrast of the targets occurs with errors as small as 0.05 cm. However, the change does not impact the ability of the system to resolve the presence and location of the malignant inclusion.

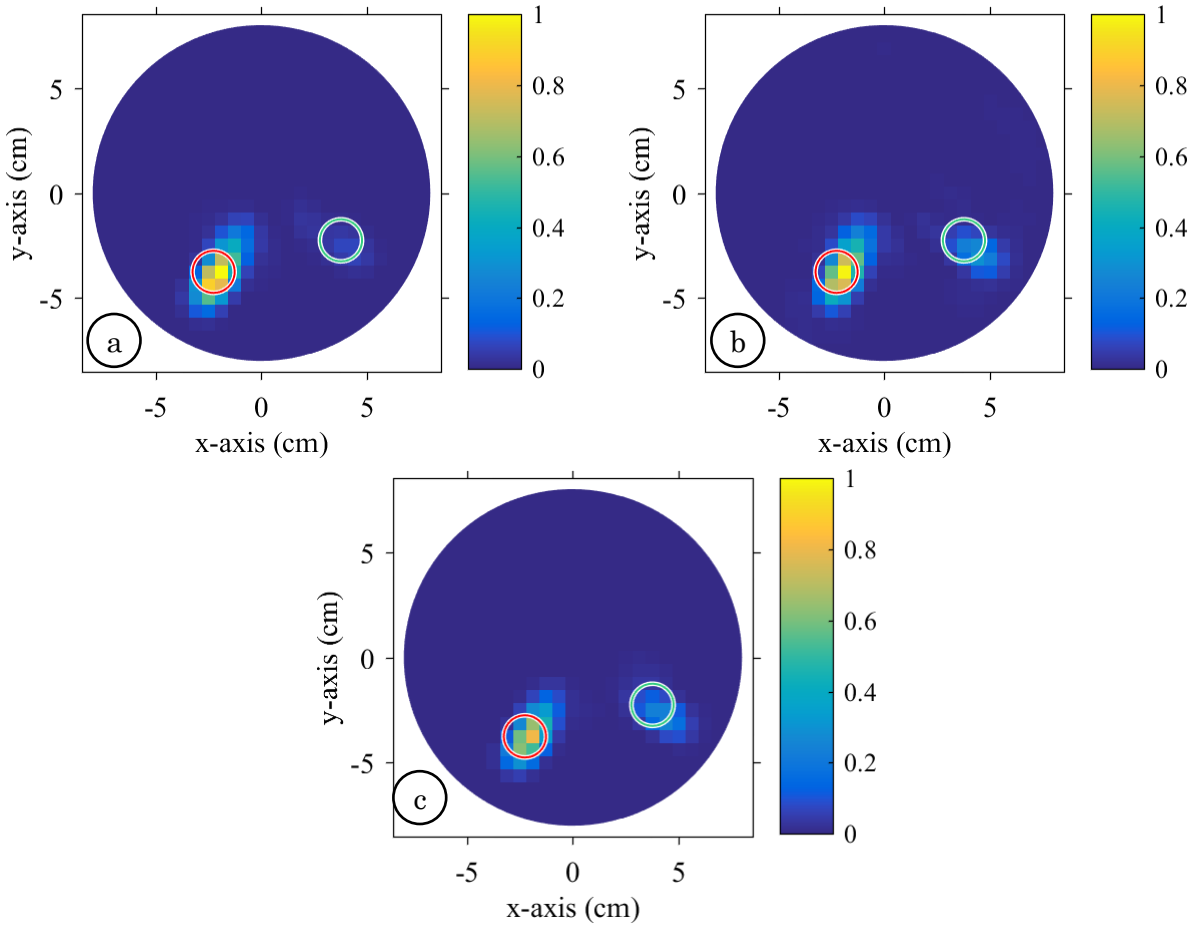


Figure 3.3-1 Reconstructed images of phantom scans with induced accuracy errors in the vertical plane. Images are normalized to the maximum scan value. Red and green circles indicate the known location of the tumor and fibroglandular targets, respectively. The vertical offset is a) 0.05 cm, b) 0.10 cm, and c) 0.20 cm. The fibroglandular response in the 0.05 cm case is almost indistinguishable from background. The tumor target exhibits an intensity close to the scan maximum in the 0.05 cm and 0.10 cm cases. In the 0.20 cm case, both targets exhibit control-like intensities.

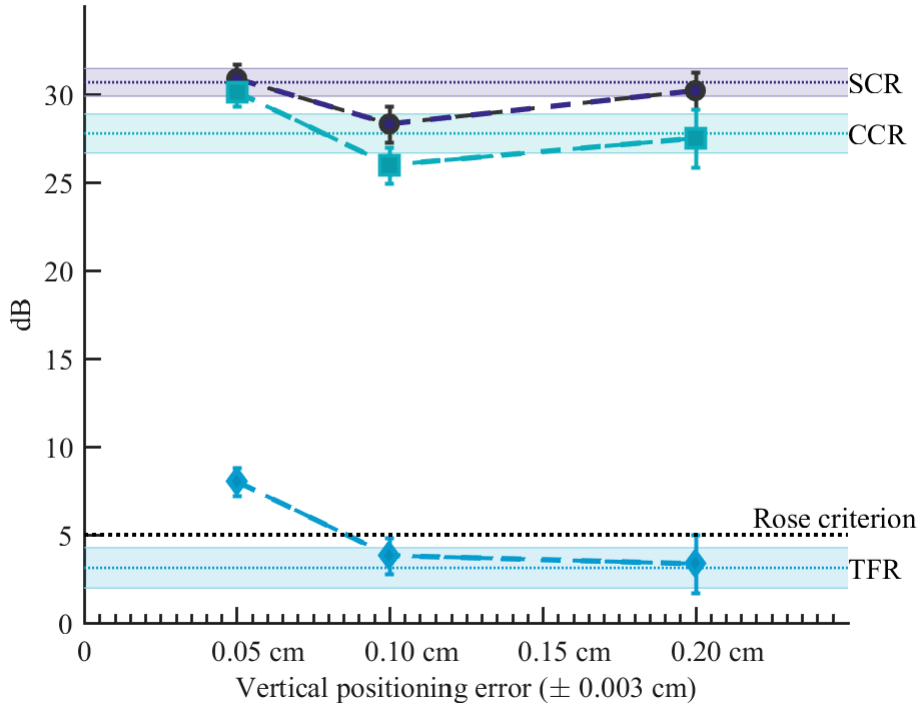


Figure 3.3-2 Plots of SCR, TFR, and CCR of reconstructed images with induced cases of accuracy errors in the azimuthal plane. Shaded areas indicate average metric value in control scans with 95% confidence interval ($n$ = 2). Error bars indicate the SE per error cases ($n$ = 2). For the 0.05 cm case, CCR and TFR values are significantly higher than control scans. SCR and CCR decay below control values in the 0.10 cm case. For the 0.20 cm case, the three metrics exhibit values close to those of control scans.

Table 3.3-1 Results of presence, location, and dissimilarity criteria of reconstructed images with induced cases of accuracy error in the vertical plane

| Case | Tumor presence | Tumor spatial error (cm) | Tumor dissimilarity to other regions (k-s test > 0.05) | **Diagnosis**. |
|---|---|---|---|---|
| Control | True | 0.4 ± 0.7 | Significant | Correct |
| 0.05 cm | True | 0.4 ± 0.7 | Significant | Correct |
| 0.10 cm | True | 0.4 ± 0.7 | Significant | Correct |
| 0.20 cm | True | 0.4 ± 0.7 | Significant | Correct |

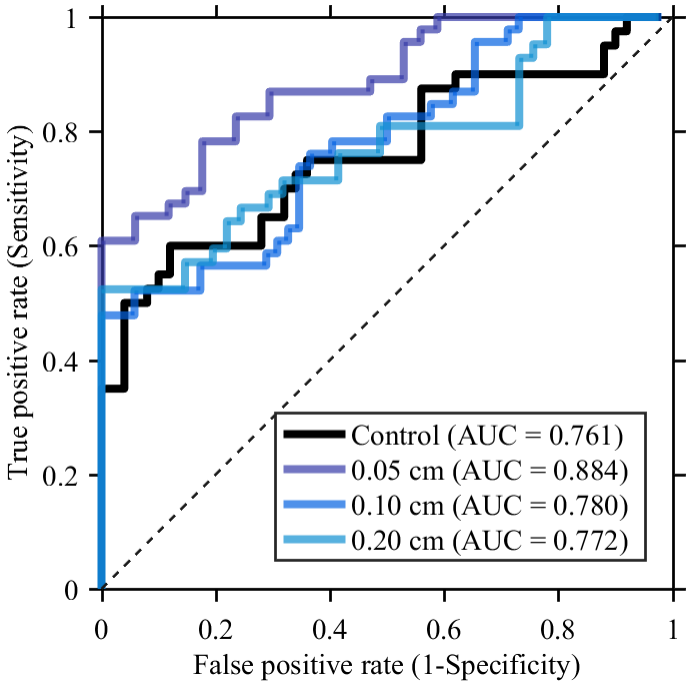


Figure 3.3-3 ROC curves of two reconstructed images with accuracy errors induced in the vertical plane. The curve and AUC for the 0.05 cm exhibit a positive increase compared to control values. The 0.10 cm and 0.20 cm curves overlap with the control curve and show minimal changes in AUC.

Table 3.3-2 Difference in AUC of control cases vs. cases with induced accuracy errors in the vertical plane.

| Case | AUC difference to control | SE | **Outcome** ($X^2$, df = 1, $p < 0.05$) |
|---|---|---|---|
| Control | 0.000 | 0.052 | – |
| 0.05 cm | 0.123 | 0.037 | No significant difference |
| 0.10 cm | 0.019 | 0.048 | No significant difference |
| 0.20 cm | 0.011 | 0.052 | No significant difference |

### 3.3.2 Array precision errors (VAP)

In the vertical plane, precision errors severely impact the quality and diagnostic potential of reconstructed images. The reconstructed images shown in Figure 3.3-4 exhibit ring-shaped artifacts that obscure the response of the tumor and fibroglandular inclusions. Error as small as 0.05 cm produce artifacts in the images with higher intensity than the fibroglandular region. In the 0.1 cm case, the response from the tumor is hardly distinguishable due to the overwhelming presence of artifacts. The ring artifacts are associated with the incorrect calibration of the air-adipose tissue interface. The poor quality of the images is reflected in the ICM plot shown in Figure 3.3-5. An induced error of 0.05 cm halves the values of SCR and CCR with the ladder falling to negative values at 0.20 cm. The contrast between tumor and fibroglandular regions significantly increases in the 0.05 cm case but drops below control values at 0.10 cm. Table 3.3-3 presents a positive diagnosis in the 0.05 cm case despite the presence of artifacts. In the 0.10 cm case, the system is capable of detecting tumor-responses in the corresponding region, however, the distribution of the tumor response is no longer different to clutter (k-s test > 0.05), In the 0.15 cm case, the maximum value in the image is no longer detected within the tumor region (see Figure 3.3-6). The ROC curves for the 0.10 cm and 0.20 cm cases approach the random guess line, with significantly lower AUC ($X^2$, $p < 0.05$).

Precision errors in the vertical plane generate characteristic ring-shaped artifacts that significantly impact the performance of the BMI system. Errors as small as 0.05 cm have detrimental effects on the quality images with low contrast metrics and the fibroglandular response obscured by artifacts. Errors of 0.10 cm are highly detrimental and result in reconstructed images where the tumor response can no longer be resolved amidst the overwhelming intensity of artifacts.

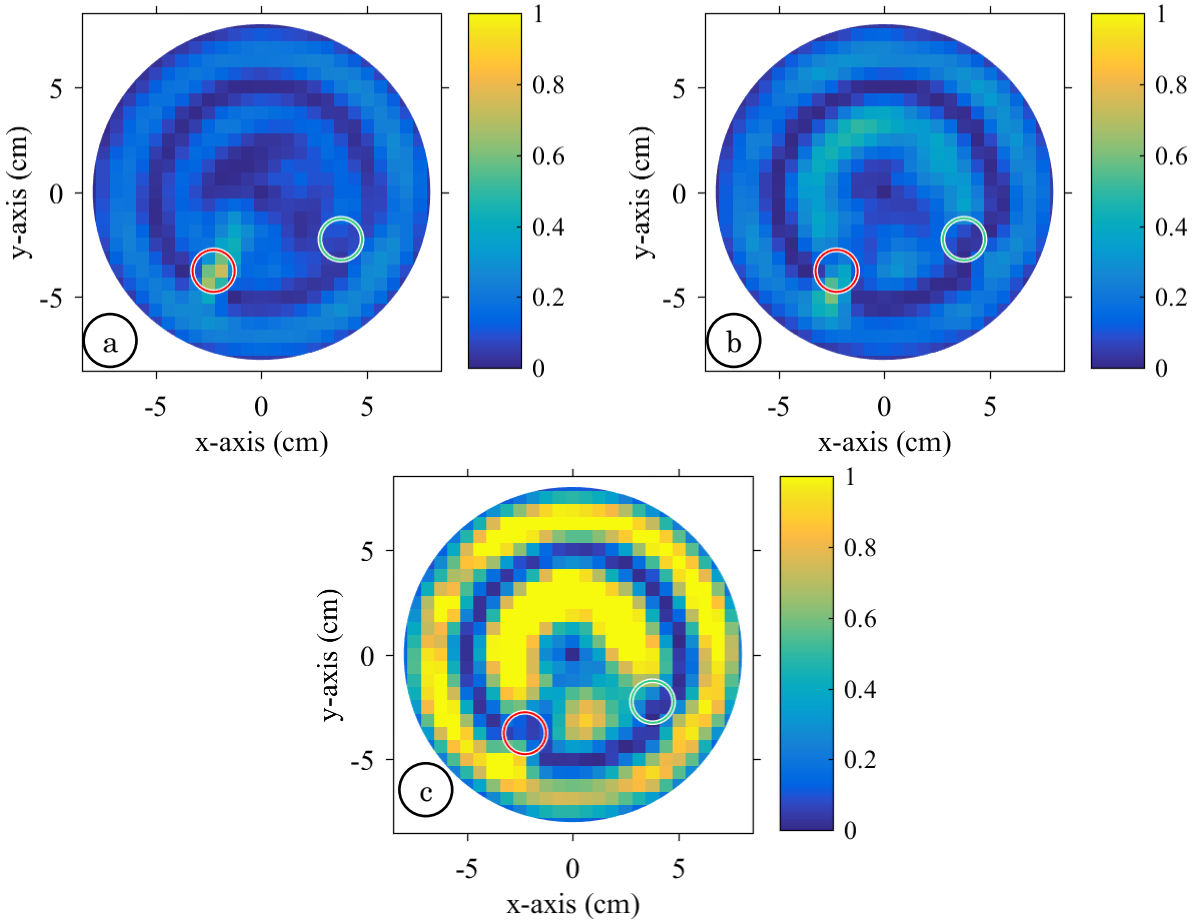


Figure 3.3-4. Reconstructed images of phantom scans with induced precision errors in the vertical plane. Images are normalized to the maximum scan value. Red and green circles indicate the known location of the tumor and fibroglandular targets, respectively. Each image shows the effect of an induced vertical offset of a) 0.05 cm, b) 0.10 cm, and c) 0.20 cm. Two concentric ring-shaped artifacts are present in the three images. The intensity of the artifacts increases in proportion to the induced offset. At 0.5 cm, the artifact intensity is similar to the fibroglandular target, and the inclusion is no longer discernable. At 0.20 cm, the ring artifacts have a higher intensity than the tumor, and the inclusion can no longer be detected. The source of the artifacts is associated with an incorrect calibration of the air-adipose tissue interface.

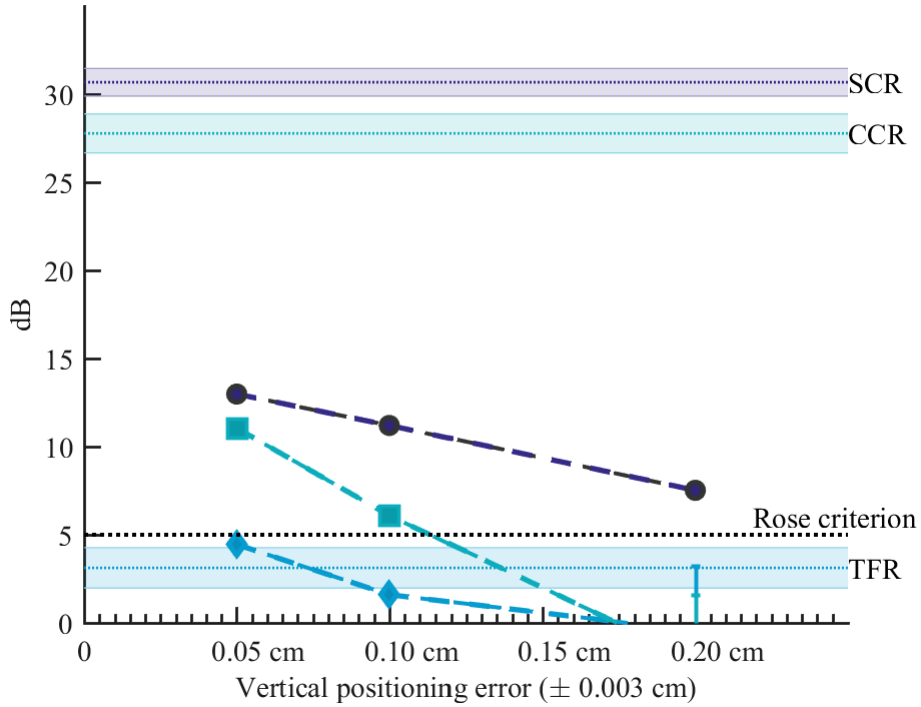


Figure 3.3-5 Plots of SCR, TFR, and CCR of reconstructed images with induced cases of a single element precision error in the azimuthal plane. Shaded areas indicate average metric value in control scans with 95% confidence interval ($n$ = 2). Error bars indicate the SE per error cases ($n$ = 2). The values of SCR and CCR are halved at just 0.5 cm of precision error and fall below the confidence intervals of control scans. For the same error case, TFR value is significantly higher than control values. At the 0.10 cm case, the TFR significantly drops below the control scans. In the 0.20 cm case, CCR and TFR metrics drop to negative values.

Table 3.3-3 Results of presence, location, and dissimilarity criteria of reconstructed images with induced precision errors in the vertical plane.

| Case | Tumor presence | Tumor spatial error (cm) | Tumor dissimilarity to other regions (k-s test < 0.05) | **Diagnosis**. |
|---|---|---|---|---|
| Control | True | 0.4 ± 0.7 | Significant | Correct |
| 0.05 cm | True | 0.4 ± 0.7 | Significant | Correct |
| 0.10 cm | True | 1.3 ± 0.7 | Not significant | Incorrect |
| 0.20 cm | True | 7.1 ± 0.7 | Not significant | Incorrect |

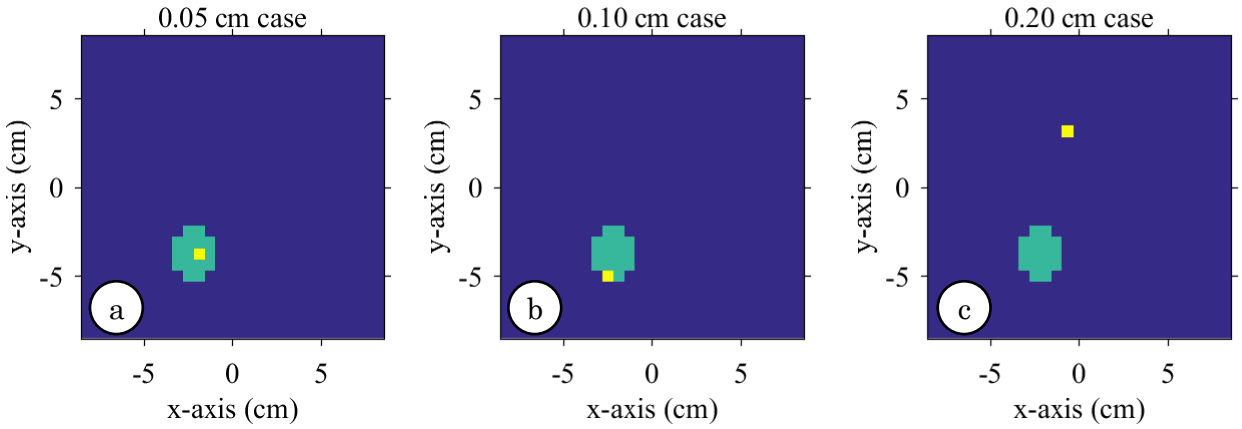


Figure 3.3-6 Location of the maximum value in reconstructed images with precision errors in the vertical plane a) In the 0.05 cm case, the highest intensity pixel (yellow) is located inside the tumor region (green). b) At 0.10 cm, the pixel location shifted towards the bottom-left corner of the image but remains within the tumor region. c) At an error of 0.10 cm, the maximum tumor-like response in image falls outside the tumor region.

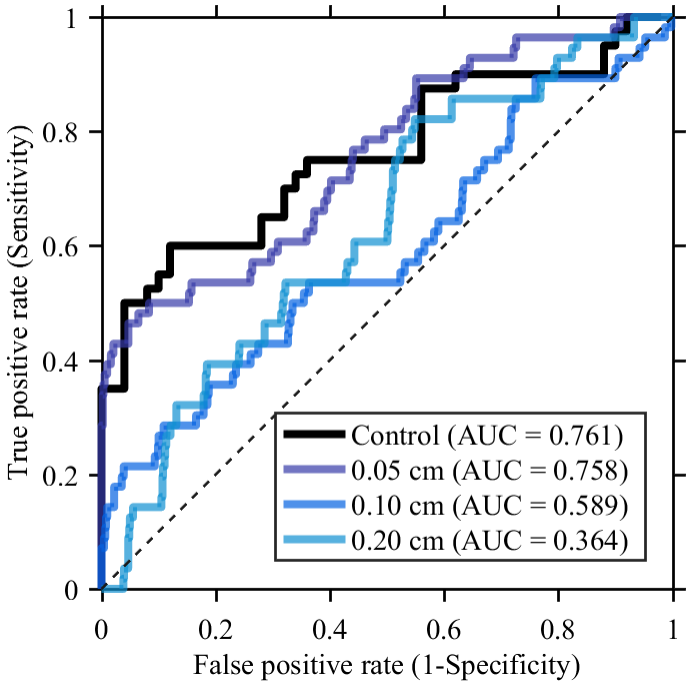


Figure 3.3-7 ROC curves of two reconstructed images with precision errors induced in the vertical plane The 0.05 cm ROC curve overlaps with the control curve. The 0.10 cm and 0.20 cm curves fall close to the random guess line and have significantly lower AUC.

Table 3.3-4 Difference in AUC of control cases vs. cases with precision errors induced in the vertical plane

| Case | AUC difference to control | SE | **Outcome** ($X^2$, df = 1, $p < 0.05$) |
|---|---|---|---|
| Control | 0.000 | 0.052 | – |
| 0.05 cm | -0.003 | 0.038 | No significant difference |
| 0.10 cm | -0.172 | 0.041 | The AUC are different |
| 0.20 cm | -0.397 | 0.034 | The AUC are different |

## 3.4 Chapter discussion and conclusion

This study set out to assess the impact of antenna positioning errors in breast microwave imaging systems. This is the first study, to our knowledge, to examine the repercussions of specific positioning errors in reconstructed images. The results are summarized in Table 3.4-1 and Table 3.4-2. The impact on the system was considered null, if changes in contrast metrics, ROC curve or reconstructed images were not significantly different to control scans. The outcome was considered only significant when the value of a contrast metric was significantly different to control values, but inclusions could still be resolved within reconstructed images. An impact was considered detrimental when noise or artifacts were visible on reconstructed images; contrast metrics were within 2/3 of the control values. Finally, an error was classified as highly detrimental when the value of a contrast metric was reduced by more than half, the diagnostic of a tumor lesion based on prior knowledge was incorrect, the ROC curve was significantly lower than control cases, or inclusions in reconstructed images could no longer be resolved from the background.

Table 3.4-1 Summary of the impact of **precision** errors

| **Outcome** | **Azimuthal plane** | | | **Vertical plane** |
|---|---|---|---|---|
| | Single element error (ASP) | Random error (ARP) | Array error (AAP) | Array error (VAP) |
| Null | 5.00° | 0.00° | 0.00° | 0.00 cm |
| Significant | 15.00° | 1.25° | 1.25° | – |
| Detrimental | Not observed | 5.00° | 2.50° | 0.05 cm |
| Highly detrimental | Not observed | 15.00° | 5.00° | 0.10 cm |

Table 3.4-2 Summary of the impact of **accuracy** errors

| **Outcome** | **Azimuthal plane** | | | **Vertical plane** |
|---|---|---|---|---|
| | Single element error (ASA) | Random error (ARA) | Array error (AAA) | Array error (VAA) |
| Null | 5.00° | 2.50° | 5.00° | 0.00 cm |
| Significant | 15.00° | 5.00° | 15.00° | 0.05 cm |
| Detrimental | Not observed | – | Not observed | Not observed |
| Highly detrimental | Not observed | 15.00° | Not observed | Not observed |

Some important observations are noted and summarized below:

- **Several positioning errors do not affect the reconstructed images.**
  All azimuthal accuracy errors below 2.5°, as well as azimuthal single element precision errors under 5°, have no impact on the outcome of the scans.
- **Specific positioning errors have a detrimental effect in the reconstructed images.**
  Azimuthal precision errors greater than 2.50° and vertical precision errors greater than 0.05 cm render the collected information useless.
- **The system is more robust to accuracy errors than precision errors.**
  Accuracy errors as big as 5° in the azimuthal plane and 0.20 cm in the vertical plane have an insignificant effect on the scan outcome. Detrimental effects of accuracy errors were only perceived when induced in a uniform random distribution over 95% of the probing points. On the other hand, precision errors of the same magnitude as accuracy errors significantly affect the scan outcome. Image degradation is observed at precision errors as small as 2.5° in the azimuthal plane and 0.05 cm in the vertical plane. These findings point to the need for equipment with excellent positioning precision for future and current BMI systems.
- **Detrimental effects are proportional to the number probing locations.**
  A precision error of 5° is inconsequential when present in a single probing point. However, when an error of the same magnitude is present in the entire array (or in a fraction of the array as in 3.2.4), the resulting outcome is highly detrimental. A similar conclusion can be obtained using the accuracy results. Thus, positioning errors distributed among several probing elements are more concerning than errors of bigger magnitude but localized among few positions.

  This finding raises the importance of characterizing the positioning performance of the motion actuators in BMI systems. Often, equipment is obtained based solely on the specifications of accuracy and repeatability (i.e., precision) given by the manufacturer of the product. However, a single-value metric cannot adequately describe the operation of a linear system over its axes.

A thorough examination of the positioning performance on each axis, like the one performed in this thesis, is necessary to understand the magnitude and extent of positioning errors.

- **Array-wise accuracy errors can be corrected with a shift on the location of the scanned object.**

  The results of the azimuthal accuracy errors present in section 3.2.3 show an angular shift on the phantom contents. The shift is relative to the magnitude of the error. The effects of the positioning error can be corrected by rotating the reconstructed image in the opposite direction. When correcting for the known angle, reconstructed images, contrast metrics and spatial error values return to control image values (see Figure 3.4-1 and Table 3.4-3). If the degree of azimuthal accuracy error is unknown, (such as for an existing BMI system that has not been fully characterized), the shift can be quantified using a calibration scan with high scattering objects placed at a known distance from each other and at a known angular distance from the antenna array. The azimuthal accuracy error can be calibrated by either correcting the order of pre-processed antenna measurements or by using image rotation algorithms. The former is advised over the latter as rotation algorithms require interpolation and are bound to lose information.

  A shift in the position of the target can also be perceived in the vertical accuracy errors. The contrast improvement in ICM (Figure 3.3-2) at 0.05 cm, is likely caused by a better alignment between the horizontal antenna plane and the equator of the tumor inclusion. As the distance between the antenna and tumor increases, the TFR returns to contrast values. Additional variations in the intensity of the fibroglandular target could be attributed to placement uncertainties (in the range of 0.3 cm).

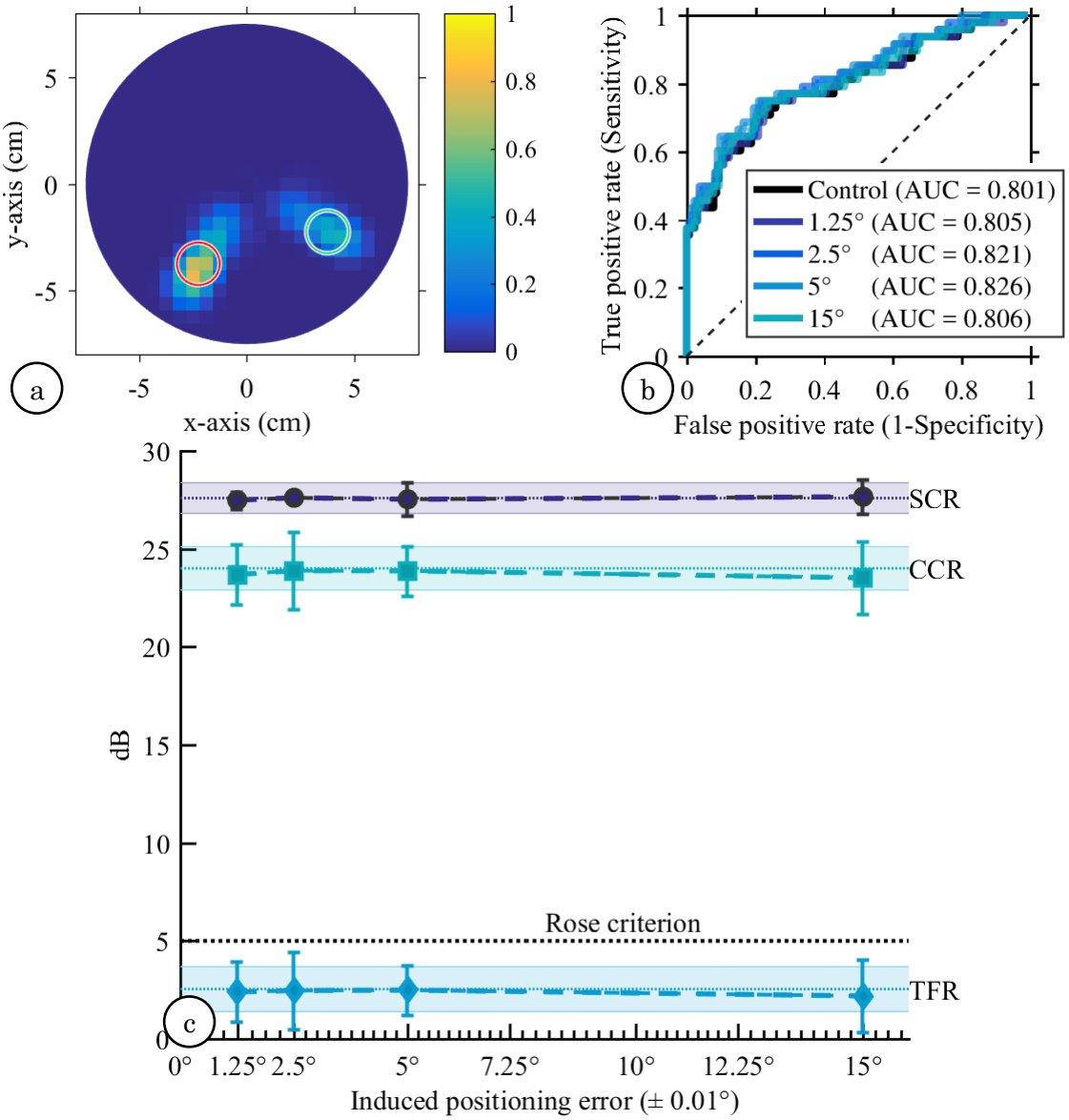


Figure 3.4-1 Reconstructed image, ROC curves and ICM plot for scans with a post-reconstruction angular shift correction for entire array accuracy errors a) Reconstructed image from Figure 3.2-14c rotated 15° to correct the angular shift. High-scattering regions in the image align with the known location of the targets (red and green circles). The image is normalized to the maximum scan value. b) ROC curves and corresponding AUC regain control-like values. c) ICM plot reveals control-like metrics even for the 15° case

Table 3.4-3 Diagnosis test and spatial error of images with an array accuracy error in the azimuthal plane after correction for the angular shift.

| Case | Tumor presence (above threshold) | Spatial error magnitude (cm) | Uncertainty (cm) | Difference to other regions | Diagnosis |
|---|---|---|---|---|---|
| Control | True | 0.7 | 0.3 | Significant | Correct |
| 1.25° | True | 0.7 | 0.3 | Significant | Correct |
| 2.50° | True | 0.7 | 0.3 | Significant | Correct |
| 5.00° | True | 0.5 | 0.5 | Significant | Correct |

### 3.4.1 Positioning specifications for BMI systems

Based on the results discussed in this chapter, the following specifications for BMI systems are presented.

Table 3.4-4 Minimal antenna positioning specifications for breast microwave imaging systems

| | Azimuthal direction* | Vertical direction |
|---|---|---|
| **Accuracy** | 2.50° | 0.20 cm§ |
| **Precision** | 1.25° | Better than 0.05 cm† |

Table 3.4-5 Ideal antenna positioning specifications for breast microwave imaging systems

| | Azimuthal direction* | Vertical direction |
|---|---|---|
| **Accuracy** | Better than 1.25° | Better than 0.05 cm |
| **Precision** | Better than 1.25° | Considerably better than 0.05 cm† |

* The specification can be relaxed if positioning inaccuracies are present in only a fraction of the total number of angular positions.

† Values close to 0.05 cm greatly impact the performance of BMI systems. Future research should concentrate in determining a tolerance threshold.

§ Values greater than 0.20 cm are acceptable. Further investigation could determine the value where vertical accuracy errors becomes detrimental to the diagnostic outcome.

### 3.4.2 BIRR performance according to established specifications

The specifications established in the previous section provide an insight into the performance of the BIRR system. Table 3.4-6 summarizes the positioning performance of the vertical and rotary stages of the system (previously detailed in section 2.3.2.1 and 2.3.2.2).

Table 3.4-6 Positioning performance of the BIRR system.

| | Azimuthal direction | | Vertical direction | |
|---|---|---|---|---|
| | Unidirectional* | Bidirectional | Unidirectional* | Bidirectional |
| **Accuracy** | 0.25° ± 0.05° | 0.26° ± 0.05° | 0.083 cm ± 0.003 cm* | 0.203 cm ± 0.003 cm |
| **Precision** | 0.05° ± 0.01° | 0.08° ± 0.01° | 0.020 cm ± 0.002 cm | 0.192 cm ± 0.001 cm |

*Unidirectional axis movement with the best positioning performance for each stage: Counter-clockwise for the rotary stage and descent for the lift stage.

The BIRR system meets the ideal criteria for the azimuthal positioning requirements presented in section 3.4.1. Both bidirectional and unidirectional movement are within tolerances. This means that during regular operation, the present positioning errors in the rotary stage do not have a significant impact on the quality of the images generated.

The lift stage of the BIRR system meets the minimum requirements in the vertical direction when employing unidirectional movement. Bidirectional movement of the stage falls out of these specifications due to the combinations of backlash and hysteresis. These results imply that, during a scan, the BIRR system must be moved in a single vertical direction (descent). Since unidirectional movement is more efficient than bi-directional, there are no repercussions to limiting operation to the former.

In conclusion, this study has established antenna positioning specifications for BMI systems. The positioning performance of the BIRR system is fit for clinical use, and its positioning errors previously calculated are not a source of image degradation.

# 4 DEVELOPMENT OF BREAST PHANTOMS FOR MICROWAVE IMAGING

## 4.1 Introduction

In biomedical applications, a phantom is a synthetic material, or model, that emulates one or several properties of a human body part [9]. In the case of breast microwave imaging, phantoms mimic the dielectric properties of benign and malignant breast tissue. Breast phantoms provide a reliable, repetitive, and low-cost alternative to clinical experimentation. This chapter presents the work conducted to develop an advanced, dielectrically, and anatomically accurate breast phantom.

This chapter begins with a description of the breast anatomy, the characteristics of breast cancer and the dielectric properties of both tissues. The first section of this chapter covers the development of a skin surrogate as well as the effects of skin thickness.[1] In the next section, an array of hemispherical and transparent phantoms was developed based on CT breast scans.[2] Finally, the third section of this chapter covers the development of an array of 3D-printed breast phantoms that accurately represent the diverse size and density of the breast.[3]

---

This chapter is based on the following submitted work:

[1] M. Solis Nepote, D. Rodriguez Herrera, J. Sacristan, D. Flores-Tapia, and S. Pistorius, "Evaluation of the skin thickness effects in Breast Microwave Radar images," in *2014 IEEE Antennas and Propagation Society International Symposium (APSURSI)*, 2014, pp. 516–517.[74]

[2] M. Solis Nepote, D. Flores-Tapia and S. Pistorius, "Initial Results on Cellulose Acetate Butyrate Vessels for Breast Microwave Radar Imaging", in *Canadian-American-Mexican Graduate Student Physics Conference*, Waterloo, Ontario, 2013, pp. 32-33.[67]

[3] D. Rodriguez Herrera, D. R. Herrera, T. Reimer, M. Solis Nepote, and S. Pistorius, "Manufacture and testing of anthropomorphic 3D-printed breast phantoms using a microwave radar algorithm optimized for propagation speed," in *2017 11th European Conference on Antennas and Propagation (EUCAP)*, 2017, pp. 3480–3484. [68]

## 4.2 Breast anatomy

Breasts are paired structures whose major function is to provide nutrition for infants through milk production. In females, breasts grow after puberty under the influence of hormones. The breast structure is found anterior to the pectoralis major and serratus anterior muscles. It is attached to the muscles by a layer of fascia composed of dense, irregular connective tissue. [75], [76]

Within each breast, there is a mammary gland whose function is to synthesize and secrete milk during pregnancy and lactation. The mammary gland consists of 15 to 20 lobes located around the nipple. Each lobe is composed of smaller compartments called lobules. These lobules contain clusters of milk-secreting glands called alveoli. During lactation, milk is synthesized in the alveoli and passed through epithelial tubes (mammary ducts) into the lactiferous sinuses, where milk is stored before being drained into the lactiferous ducts. The lactiferous ducts converge and emerge through closely spaced openings in the nipple. [76], [77]

A network of lymph vessels connects the breast to the lymphatic system. The lymph vessels drain lymph fluid (i.e. white blood cells, cell by-products, and waste material) away from the breast. The main lymph nodes in the breast structure are found under the arm (axillary nodes), around the collarbone (supraclavicular and infraclavicular), and inside the chest (internal mammary lymph node). [75]

Adipose tissue surrounds the mammary glands, giving volume and shape to the breast. Strands of connective tissue called suspensory ligaments (or Cooper's ligaments), run between the skin and fascia. These ligaments help maintain the structure and position of the tissues inside the breast. [75], [76]

The skin surrounding the breast is part of the integumentary system and is composed of three heterogeneous layers: the epidermis, the dermis, and the hypodermis. The thickness of the

skin surrounding the breast can range from 0.83 mm to 2.4 mm, with an average thickness of 1.55 mm ± 0.25 mm [78].The areola is a pigmented area of skin surrounding the nipple; it contains sebaceous and Montgomery's glands which lubricate the skin [76].

Breast size and shape vary across individuals, but breasts are generally tear-shaped. Breast size is predominantly determined by the genetic predisposition to the relative amount of adipose tissue within the breast. Adipose tissue typically accounts for one-third of the breast mass [75]. In North American women the median breast diameter at the chest wall is 12 cm ± 1 cm and the median length from chest wall to nipple is 6 cm ± 1cm [43]. Breast size can be affected by body fat percentage and by hormonal changes (e.g. menstruation, pregnancy, lactation, menopause) [75]. The relative amount of adipose tissue in the breast is unique to an individual woman, and as women age, the suspensory ligaments became loose and are often replaced by adipose tissue [76].

In radiology, breast density describes the ratio of dense tissue to adipose tissue [9]. Breast density is a semi-quantitative classification conventionally performed by a radiologist through visual assessment [79], [80]. The fifth edition of the American College of Radiology's Breast Imaging Reporting and Data System (BI-RADS), defines four categories for breast composition. These categories are: almost entirely fatty (class I), scattered areas of fibroglandular density (class II), heterogeneously dense (class III), and extremely dense (class IV) [81]. Categories III and IV lower the sensitivity of mammography.

## 4.3 Breast cancer

Cancers are pathologies defined by an abnormal, uncontrolled growth of cells that can invade other tissues [82]. In the breast, cancer typically develops as adenocarcinomas (i.e., from glandular structures in the epithelial tissue) [83]. The most frequent types of invasive breast cancer are invasive (or infiltrating) ductal carcinoma (comprising 70-80% of all cases) and, invasive lobular

carcinoma (5-15%). [84], [85]. Pre-invasive forms of breast cancer include ductal carcinoma *in situ* and lobular carcinoma *in situ* [83]–[85].

Breast cancer size, shape, and location varies among cases. A study of 1,894 Canadian patients reported a mean tumor size of 2.0 cm, with 24.1%, 38.3%, and 37.6% of tumors between 0.01 cm to 1.0 cm, 1.1 cm to 2.0 cm, and 2.1 to 5.0 cm, respectively [66]. That same study indicates that larger tumors correlated with a decrease in 15-year survival rate [66]. Breast tumors are predominately found in the upper-outer quadrant of the breast (see Section 2.2.1.1).

## 4.4 Dielectric properties of breast tissues

Permittivity ($\varepsilon$) is a complex value that describes the interaction of a material with an electric field. The permittivity of a material is often expressed as a ratio relative to the permittivity of vacuum. Thus:

$$\varepsilon = \varepsilon' + \varepsilon'' = \varepsilon_0(\varepsilon_r' - j\varepsilon_r'')$$

Where $\varepsilon_0 = 8.85 \times 10^{-12}$ F m$^{-1}$ is the permittivity of free space. The real part of the relative permittivity ($\varepsilon_r'$) is a measure of how much energy, from an external electric field, is stored in a material. The imaginary part of permittivity ($\varepsilon_r''$) is called the loss factor, it combines the dielectric loss ($\varepsilon_{rd}''$) and the conductivity ($\sigma$), and can be expressed as:

$$\varepsilon_r'' = \varepsilon_{rd}'' + \frac{\sigma}{\omega\varepsilon_0}$$

Conductivity can be expressed as:

$$\sigma = \omega\varepsilon_0\varepsilon' \tan\delta$$

Where the loss tangent ($\tan\delta$) is a ratio of the energy lost to the energy stored.

$$\tan\delta = \frac{\varepsilon_r''}{\varepsilon_r'} = \frac{\text{Energy lost per cycle}}{\text{Energy stored per cycle}}$$

The dielectric properties of materials are commonly described using the real part of the relative permittivity ($\varepsilon_r$) and conductivity values ($\sigma$). [86], [87]

Several studies have consistently reported a large contrast between the dielectric properties of malignant tumours and normal breast tissue in the microwave spectrum [9], [11]. Traditionally, in microwave imaging approaches, these breast tissues are classified into four main categories: tumor, skin, adipose (i.e., fat), and fibroglandular tissue. The fibroglandular group incorporates mammary glands, lobules, milk ducts, lymph nodes, connective, and supportive ligaments. Dielectric measurements in biological tissue differ mainly due different concentrations of water and ions and are frequency-dependent. [88]. In 2012, Sugitani et al. conducted dielectric measurements on 35 breast cancer patients [12], [89]. Ex-vivo tissue was measured in the 0.5 GHz to 20 GHz range using an open-ended coaxial probe [12]. These measurements were suitable for the measuring bandwidth of the BIRR system, and are represented in Figure 4.4-1. Measured median values at of permittivity and conductivity at 3 and 6 GHz are shown in Table 2.4-4 and Table 4.4-1, respectively. At 6 GHz, the relative permittivity of cancer tissue was approximately 4 times bigger than adipose tissue [12]. The contrast between cancer and fibroglandular tissue was approximately 1.5 [12]. In-vivo measurements reported in Halter et al. [90] show a similar contrast between tumor and normal tissue, albeit, the measured permittivity and conductivity values were higher.

Table 4.4-1 Dielectric measurements for excised breast tissue in the 6 GHz range ($n$ = 35).[12]

| **Tissue** | $\boldsymbol{\varepsilon_r}$ | $\boldsymbol{\sigma}$ **(S/m)** |
|---|---|---|
| Cancer | 35 to 65 | 5 to 8 |
| Fibroglandular | 15 to 50 | 2 to 7 |
| Adipose | 0.8 to 25 | 0.5 to 3.5 |

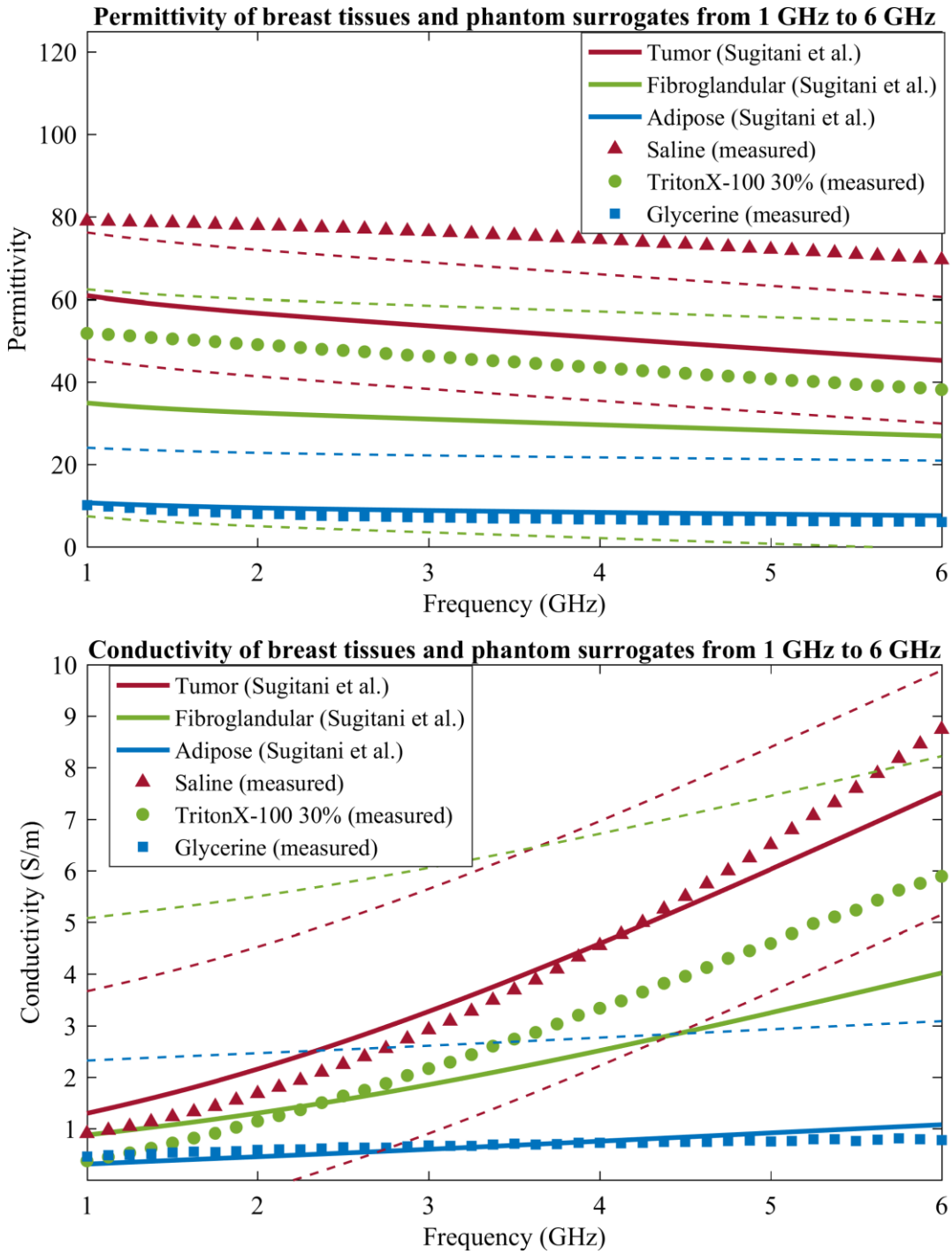


Figure 4.4-1 Two-pole Cole-Cole permittivity and conductivity models of excised breast tissue in the 1 – 6 GHz range [12], [89]. Tumors (red line) have a characteristic higher permittivity and conductivity than fibroglandular (blue line) and adipose (green line) tissue. Dotted lines indicate three SD from measurements of breast tissue at 6 GH. Dielectric measurements of surrogate materials used in breast phantoms are shown as: saline (red triangle), triton X-100 at 3:10 concentration (green circles), and glycerine (blue squares). Measurement uncertainties in the surrogate materials are smaller than their corresponding symbol.

## 4.5 A skin surrogate with uniform thickness

The relative high reflections produced by the skin interface represent a considerable challenge for BMI systems. In the frequency of operation of the BIRR system (i.e., 1 GHz to 8 GHz), the skin has a relative permittivity of around 30 and a conductivity of around 3 S/m, which reduces the penetration power of the microwaves [9]. Various techniques have been used to minimize the dominant reflections of skin including impedance-coupling materials [20], [27], [30] and laser-guided time domain windowing [91]. Previous experiments have tested BMI prototypes and algorithms using phantoms with synthetic skin surrogates. However, phantom skin thickness has been tested with a constant skin of 2 mm [23], [92] or 2.5 mm [34]. Based upon the observation that breast skin thickness ranges from 0.8 mm to 2.6 mm and because the skin dielectric properties dominate the dielectric properties seen in real tissue, an analysis of skin thickness on BMI systems was performed to develop a more accurate understanding of the effects of skin thickness in reconstructed images.

For this experiment, a cylindrical phantom similar to the one in [35] was used. The acrylic container had a diameter of 13 cm and a height of 35 cm. The container was filled with an adipose surrogate, as well as two fibroglandular inclusions and a 1 cm tumor inclusion. The dielectric properties of breast tissue and the surrogate materials used for this experiment are present in Table 2.4-4.

A skin surrogate was created using a solidifying polymer know as TX-151 (Oil Center Research International, Lafayette. LA, USA). The powder was mixed with distilled water in a 1:3 ratio to emulate skin dielectric properties [21], [23]. After partial solidification, the mixture was compressed against two plates to produce 1 mm ± 0.05 mm thick sheets.

The benchtop microwave imaging prototype described in Section 1.6.5 was used to illuminate the phantom with a stepped-frequency continuous sweep at 144 antenna locations. The

transceivers used were two custom-made double-ridged horn antennas [36] operating in air, in a multistatic configuration and with an angular separation of 135°.

Reflection measurements were collected with the phantom covered in layers of skin. The surrogate skin sheets were wrapped around the exterior of the acrylic container and held together with elastic bands. A total of three skin layers were wrapped around the phantom, and two scans were collected for each layer. At each skin layer, a second scan of the phantom without inclusions was collected for calibration. A photo of the experimental setup is shown in Figure 4.5-1. Imaging scans were reconstructed using the multistatic reconstruction algorithm discussed in [37]. Equations 2-4 and 2-5 were used to calculate SCR and TFR for each image. An additional metric, the contrast to noise ratio (CNR), was calculated as:

$$CNR = 10\log_{10}\left(\frac{\Gamma_{max}^2 - \mathrm{F}_{max}^2}{\sigma_b^2}\right) \tag{4-1}$$

Where $\sigma_b$ is the standard deviation of the background in the image.

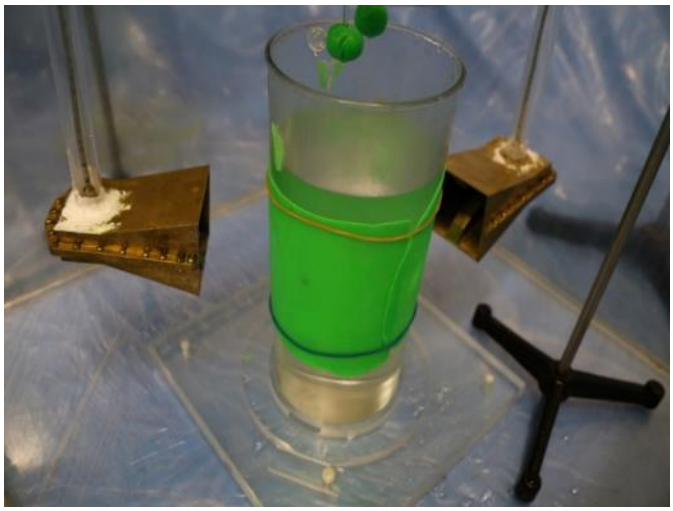

Figure 4.5-1 Cylindrical phantom covered with 1-mm-thick synthetic skin layer. The phantom is contained within the imaging tank of the first-generation BMI prototype from the University of Manitoba. A pair of double ridge horn antennas were used to probe the phantom. Suspended above the phantom are two fibroglandular inclusions created with a mixture of TX-151, and a saline-tumor inserted above the phantom.

Contrast metrics values are summarized in Figure 4.5-2 and Table 4.5-1. SCR and CNR consistently decrease with every layer of skin. After a 1-mm thick skin layer was added, SCR and

CNR values were significantly below the no-skin condition (unpaired one-tailed t-test, $p < 0.01$). The value of TFR remained within no-skin values until the 3 mm case. For the images with a 2-mm skin layer, SCR and TFR remain above the Rose criterion [14]. All metrics drop below the rose criterion in the presence of a 3-mm thick skin. It is worth noting that the drop in SCR and CNR between the 2 to 3 mm skin layer is greater than the drop after 1 mm or from 1 mm to 2 mm.

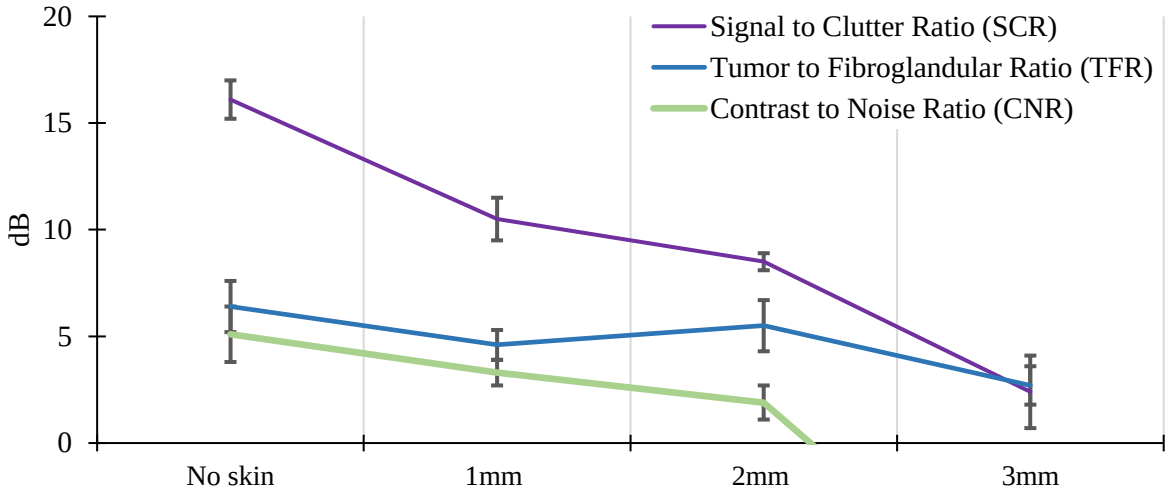


Figure 4.5-2 Plot of SCR, TFR, and CNR for reconstructed images with different of skin thickness. Error bars indicate SD for each metric ($n = 2$).

Table 4.5-1 SCR, TFR, and CNR for reconstructed images with 0 to 3 mm of skin thickness

| | **No skin** | **1 mm** | **2 mm** | **3 mm** |
|---|---|---|---|---|
| **SCR** | 16.1 ± 0.9 dB | 10.5 ± 1.0 dB | 8.5 ± 0.4 dB | 2.4 ± 1.7 dB |
| **TFR** | 6.4 ± 1.2 dB | 4.6 ± 0.7 dB | 5.5 ± 1.2 dB | 2.7 ± 0.9 dB |
| **CNR** | 5.1 ± 1.3 dB | 3.3 ± 0.6 dB | 1.9 ± 0.8 dB | −8.9 ± 3.2 dB |

## 4.6 Hemispherical CAB containers

Breast phantom containers provide support and shape to the synthetic materials used to emulate the dielectric properties of breast tissue. These containers are built with low-loss materials to reduce signal interference. Common materials for these containers include acrylic (Plexiglass) [35], [93], PVC [94], or low-loss ceramic shells [22]. The inflexibility of these materials results in phantoms with a crude approximation of the breast shape. For this reason, the use of a thermoformable plastic was investigated as a potential phantom container.

CAB (Cellulose acetate butyrate, commercially known as Uvex®) was investigated as a suitable material to generate the phantom containers due to its ease of thermoforming and low dielectric properties. In radiotherapy, CAB is widely used to produce patient-specific immobilization casts [95]. Table 4.6-1 shows that CAB dielectric properties are similar to acrylic, a material typically used for breast phantoms containers.

Table 4.6-1 Dielectric properties of CAB and acrylic at 3 GHz [96]

| **Material** | $\varepsilon_r$ | **σ (S/m)** |
|---|---|---|
| Acrylic | 2.6 | 0.001 |
| CAB | 2.9 | 0.001 |

An array of CT-informed hemispherical CAB containers was manufactured. First, CAD models were generated following the breast measurements reported in [43]. Next, the CAD models were 3D printed and later used to make resistant casts of plaster material. In the following step, each cast and a 2-mm thick CAB sheet were pressed using a vacuum forming machine. The resulting containers acquired the hemispherical form of the casts, with the dimension shown in Table 4.6-2.

Table 4.6-2 Dimensions of the hemispherical CAB container.

| **Phantom container** | **Maximum diameter (cm ± 0.2 cm)** | **Length (cm ± 0.2 cm)** |
|---|---|---|
| CAB-A | 14.0 | 8.4 |
| CAB-B | 16.0 | 10.4 |
| CAB-C | 15.0 | 11.9 |
| CAB-D | 15.6 | 14.4 |
| CAB-D+ | 15.8 | 15.6 |

The CAB containers were validated against acrylic containers. A 2-mm thick CAB sheet was thermoformed into a cylindrical container with a 10-cm radius and a 35-cm height. The container was filled with an adipose surrogate and contained two synthetic fibroglandular patches of 1.5 cm and a 1 cm tumor surrogate. The dielectric properties of these synthetic, materials are

detailed in Table 2.4-4. An identical phantom was manufactured within an acrylic container. Each phantom was scanned five times using the benchmark prototype and configuration previously detailed in Section 1.6.5. Datasets were reconstructed using the monostatic algorithm from [35]. For each reconstructed image, SCR, spatial error, and number of artifacts were calculated.

Reconstructed images for both acrylic and CAB phantom showed acceptable metrics of SCR, spatial error, and number of artifacts. The CAB material did not significantly affect the reconstructed image metrics (two-tailed t-test > 0.05). A summary of the results can be seen in Table 4.6-3. The phantom container CAB-D+ is shown in Figure 4.6-1.

Patient-specific CAB molds could be used to immobilize the breast during a scan. The idea was explored during the BIRR preclinical trial (see Section 2.4.3). However, the manufactured phantom containers were unable to provide the tight-fit required to constrict movement.

Table 4.6-3 Metrics for reconstructed images of acrylic and CAB phantoms ($n$ = 5)

| **Phantom** | **SCR ( ± SD)** | **Spatial error (± SD)** | **Number of artifacts** |
|---|---|---|---|
| Acrylic | 9.2 dB ± 0.4 dB | 1.5 cm ± 0.3 cm | 0 |
| CAB | 9.4 dB ± 0.1 dB | 1.2 cm ± 0.2 cm | 0 |
| Difference (two-tailed t-test > 0.05) | 0.2 dB ± 0.4 dB Not significant | 0.3 cm ± 0.4 cm Not significant | 0 Not significant |

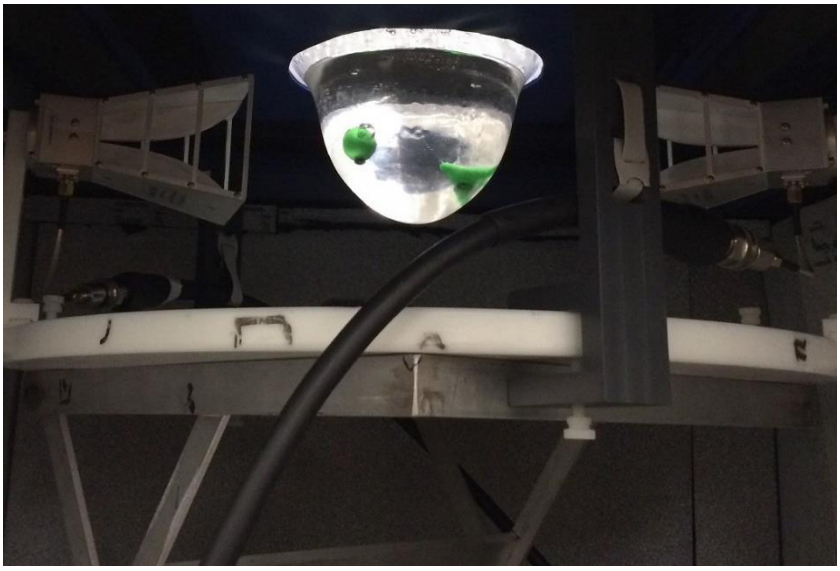

Figure 4.6-1 Photo of the CAB-D+ phantom container positioned in the imaging chamber of the BIRR. The dimensions of each container provided an approximate representation of the possible breast sizes during a clinical scan. During the BIRR pre-clinical trial (see section 2.6.3) the CAB containers served to adjust the radial position of the antennas before the patient examination. The transparency of CAB facilitates the setup of targets inside the phantom.

## 4.7 Anthropomorphic 3D-printed breast phantoms

Low-cost and complex shape structures can be obtained using 3D printing technologies with millimetric accuracy. However, previous attempts to improve breast phantoms using 3D printing technology have not truly reflected the anatomic complexity of the breast structure, or have lacked the flexibility to mimic the diversity breast densities, sizes, and tumor positions. The following experiment presents phantom containers that mimic the external and internal anatomy of the breast and that were manufactured using 3D printing technology. These phantoms were developed by a summer student, Tyson Reimer, under the author's supervision, during the summer of 2016.

Adipose and fibroglandular hollow containers for breast tissue surrogates were 3D printed following a process similar to [97]. Numerical phantoms for each BI-RAD classification were generated using MRI scan data (obtained from [98]). Binary fibroglandular and adipose models were extracted from each numerical phantom. The binary models were processed to generate hollow, smooth, and continuous surfaces for each tissue type. The surface models were exported to STL format. Using the CAD software MeshMixer (Autodesk Inc. CA, US), the surfaces were given

a 2-mm thickness and prepared for 3D printing. A 10 cm × 15 cm oval base was added to each model to provide support and ease of assembly. The hollow containers were 3D printed in polycarbonate using the fuse-deposition printer Fortus 400mc (Stratasys Inc, MN, US). Polycarbonate was selected due to its low-loss properties (i.e. $\tan\delta < 0.01$) [99]. In total, three adipose containers and five fibroglandular containers were printed. To prevent flow between shells, an oil-based polyurethane coating was applied as a sealant (Fast-Drying Polyurethane 350 V.O.C., MinWax Company, NJ, USA).

The containers can be mixed in a total of 16 different configurations to reproduce different breast sizes and all BI-RADS densities (see Figure 4.7-1). Each fibroglandular container was designed to be used with at least two adipose containers. The fibroglandular volume was adjusted to represent all breast densities. As mentioned previously, breast density classification is subjective to radiologist interpretation. However, Østerås et al. compared 537 mammography examinations to determine fibroglandular volumes in agreement with radiologists classifications [79]. Based on [79], fibroglandular volumes of 5%, 9%, and 21%, were set as a threshold between density I and II, II and III, and III and IV. The possible phantom configurations are summarized in Table 4.7-1

The 3D printed adipose and fibroglandular containers retained the volume of the original MRI breast density within 3%. The dimensional error of the final coated model was measured at $0.15 \pm 0.03$ mm. The phantoms retained liquids without diffusion between the layers for more than 24 hours.

Table 4.7-1 3D printed phantom configurations and corresponding BI-RADS classification.

| | Fibroglandular container | Fibroglandular volume | BI-RADS Classification |
|---|---|---|---|
| **Small adipose container** | *F-X2* | 4.4% | Class I |
| | *F-X3* | 19.9% | Class III |
| | *F-X4* | 37.2% | Class IV |
| **Medium adipose container** | *F-X1* | 1.8% | Class I |
| | *F-X2* | 4.1% | Class I |
| | *F-X4* | 15.0% | Class III |
| | *F-X5* | 38.2% | Class IV |
| **Large adipose container** | *F-X2* | 2.7% | Class I |
| | *F-X3* | 5.3% | Class II |
| | *F-X5* | 25.0% | Class IV |

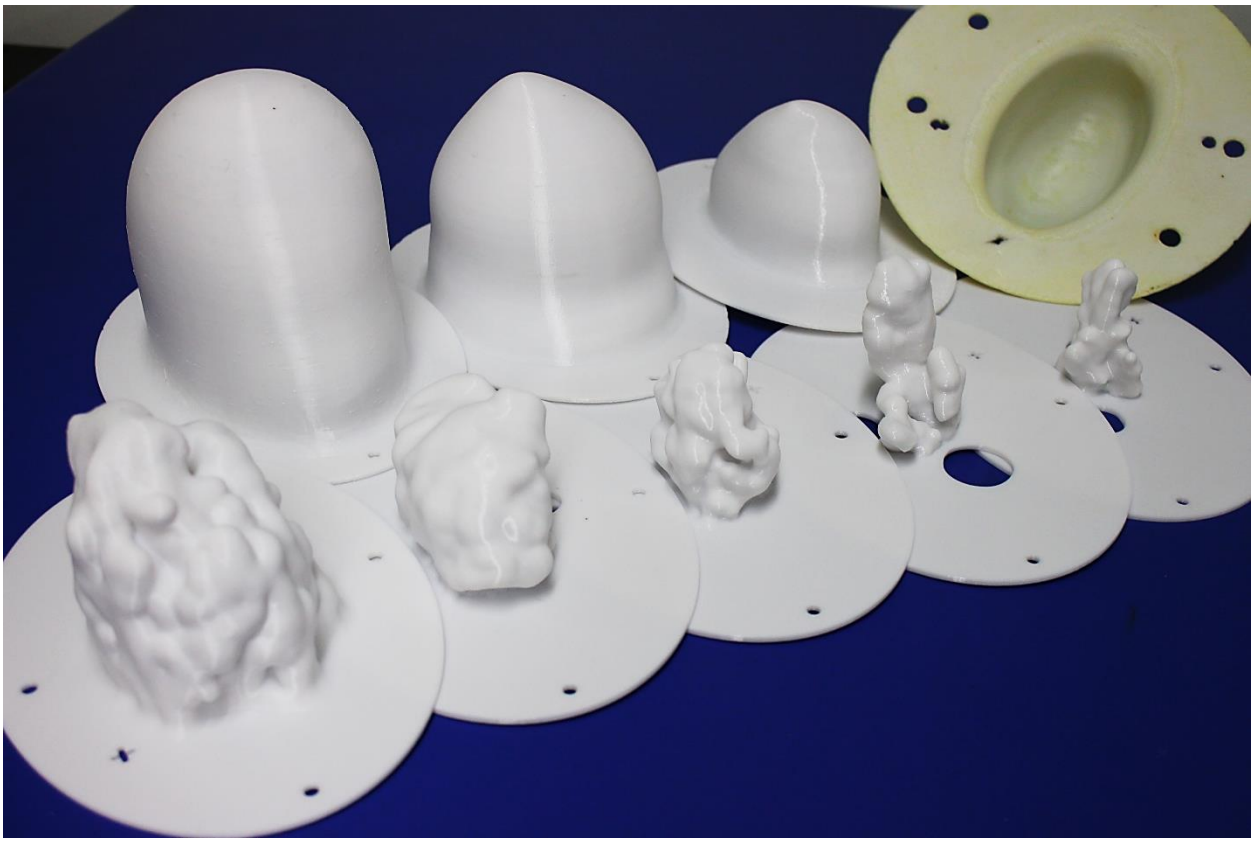

Figure 4.7-1 Array of 3D-printed phantoms. The three adipose containers (top row, white), combined with the five fibroglandular containers (bottom row) representing the diverse density and size of breasts. In the top right corner, a flipped prototype shows the inner side of an adipose container.

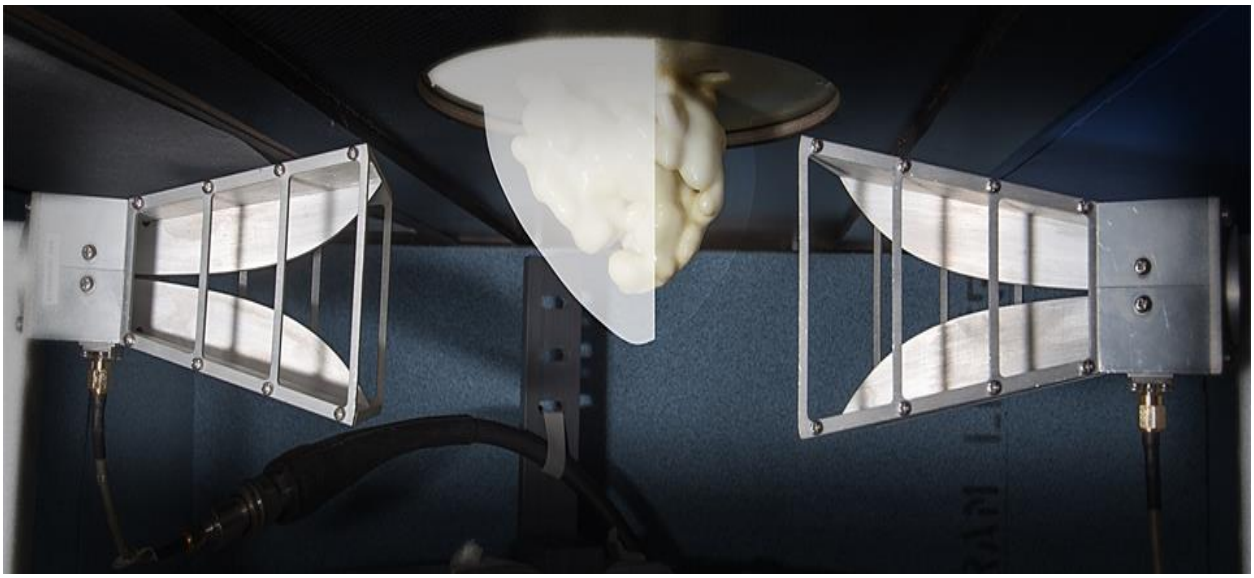

Figure 4.7-2 Class III 3D printed phantom in the BIRR imaging chamber. The photo shows half of an adipose container, with increased transparency, to show the fibroglandular insert. The opening on the base of the phantom allows for tumor inclusions to be placed close to the fibroglandular structure.

Following manufacture, a phantom Class I was scanned with the BIRR system described in Chapter 2. The medium adipose container and the fibroglandular container *F-2* were combined and filled with corresponding liquid tissue surrogates. As with the previous experiment, glycerin was used to match adipose tissue, and a 2-cm glass bulb was filled with saline solution (dielectric properties detailed in Table 2.4-4) As a fibroglandular surrogate, a mixture of Triton X-100 and distilled water (3:10) was used [100].

The configuration of the BIRR system was identical to the one detailed in Section 2.4.6. The phantom was scanned with three configurations. In the first configuration, the phantom was healthy, with no tumor inclusion and the fibroglandular insert. The second phantom configuration had a tumor inclusion, but no fibroglandular insert. The third configuration contained both the fibroglandular insert and the tumor inclusion.

Datasets were reconstructed using the monostatic algorithm detailed in [35]. In the reconstructed images, the location of the tumor and fibroglandular targets was determined based on a priori knowledge. SCR and TFR were calculated following Equations 2-4 and 2-5.

The reconstructed images for a Class I phantom are shown in Figure 4.7-3. In all images the, maximum intensity value corresponded to the tumor region. As shown in Figure 4.7-3b), the tumor had a higher energy when no fibroglandular insert was present. The reconstructed image of the configuration with tumor and fibroglandular inclusions (see Figure 4.7-3c)) has a SCR of 26.2 dB, and a TFR of 7.3 dB

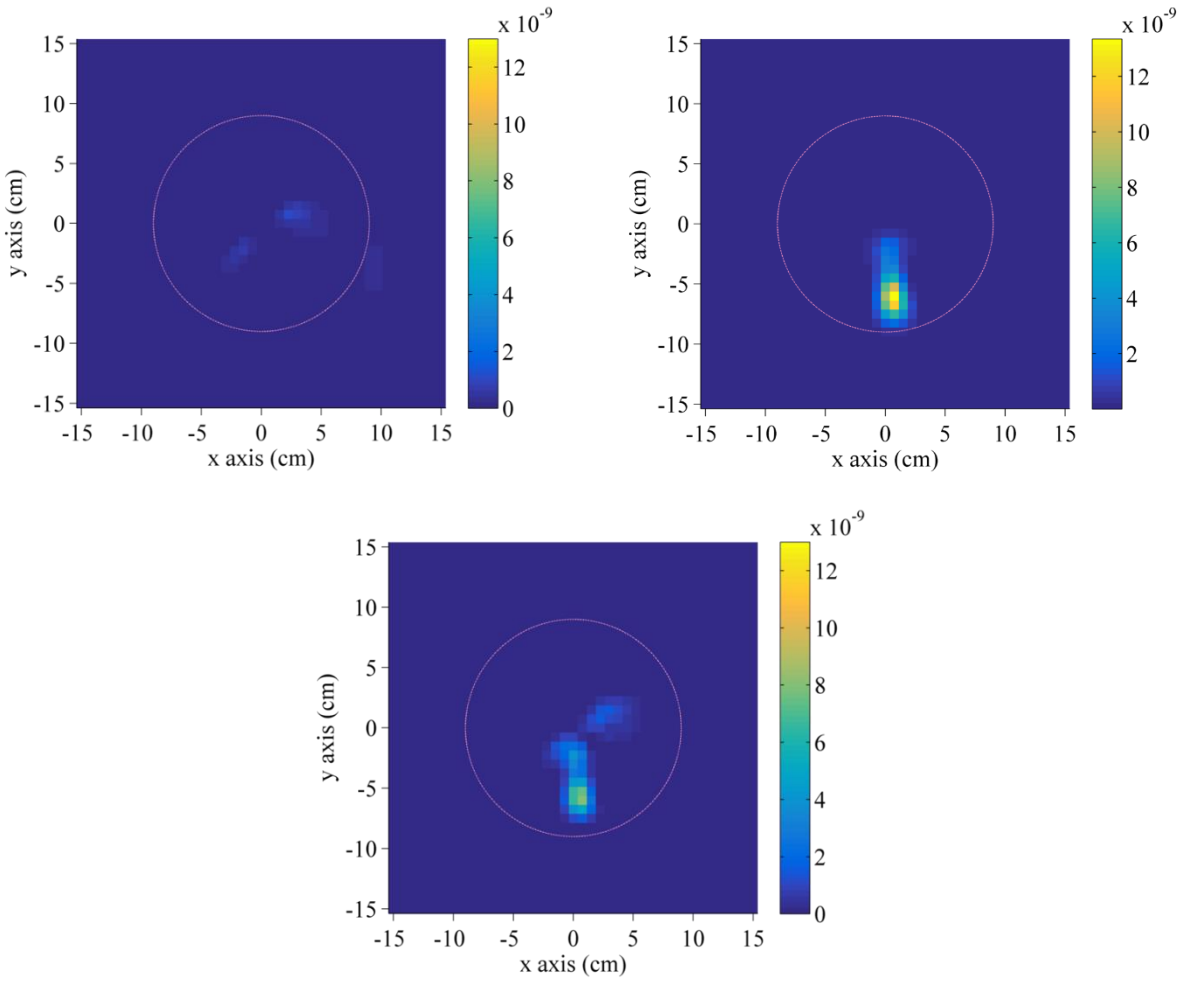


Figure 4.7-3 Reconstructed images of a 3D-printed Class I phantom scanned with the BIRR system. a) Healthy phantom configuration, b) Disease phantom configuration, with no fibroglandular insert. c) Disease phantom configuration with fibroglandular insert. Images are normalized to the maximum value in image b). The highest response in the all the images corresponds to the known tumor location.

## 4.8 Chapter conclusions

Breast phantoms are an essential tool for the validation of BMI systems. The usefulness of phantoms is dependent on their accuracy to match both the dielectric properties and the morphology of breast tissues in vivo. Previous phantoms have not been able to combine a solution to both requirements. This chapter presents the experiments that led to the creation of an array of breast phantoms with accurate dielectric and anatomical breast representation.

The first experiment presents the development of a skin surrogate applicable in layers. By scanning a cylindrical phantom with a BMI system, the effects of skin thickness were isolated and characterized. A non-linear decrease in signal intensity was associated with an increase in the skin thickness. Changes in skin thickness of only 1 mm significantly reduced the contrast between targets. SCR and a TFR remain above the rose criterion for skin thicknesses of up to 2 mm, indicating a successful detection of tumor lesions. This experiment was conducted with a pre-clinical system with an output power of 5 dBm. The BIRR system, which has an output power of 10 dBm and better SCR, is expected to overcome the effects of breast skin thickness.

Based on CT measurements, an array of five CAB breast phantom containers was created. The low dielectric profile, transparency and of malleability CAB make it a versatile material for microwave imaging applications. Scans of breast phantoms contained within a CAB container resulted in reconstructed images where the tumor lesion could easily be detected amidst the fatty background. The SCR and spatial errors in reconstructed images were identical to those obtained from a phantom contained in acrylic.

In the third experiment, MRI-informed, 3D-printed adipose and fibroglandular containers were combined with corresponding liquid tissue surrogates. The manufactured phantoms provide an accurate representation of the shape, electromagnetic behavior, and heterogeneity of the breast structure within the scope of microwave imaging applications.

The 3D printed phantoms presented in this chapter have several advantages over the phantoms available in the literature. Compared to hand-formed tissue surrogates (e.g. [21], [37], [101]), the rigid nature of the adipose and fibroglandular containers provide a repeatable radar cross section, increasing the reliability of measurements. The phantoms presented in this work exhibit a more complex morphology than the 3D printed phantom developed by Zastrow et al., while enabling the adjustment of the dielectric contrast between tissues, and using a more economical manufacturing process [102]. Compared to the prototype shown by Nadine et al., the phantom array presented in this work provides a complete representation of breast densities [97]. At the time of publication of this thesis, these phantoms provide the best representation of breast tissue in the microwave imaging literature.

Finally, a BI-RADS Class I phantom was scanned with the BIRR system. On the reconstructed images of phantom scans, a strong scattering response was consistent with the location of a 20-mm-wide in the phantom. The SCR and TFR values of 26.2 dB and 7.3 dB provide a very optimistic outlook for the diagnostic potential of the BIRR system

Breast phantoms are an essential tool to validate the diagnostic potential of BMI systems. The outcome of this work has been a reliable and dielectric-accurate array of breast phantoms that partially mimic the complex geometry of internal and external breast structures. The Phantoms were presented on March 2017 at the 11th European Conference on Antennas and Propagation [68], and in a collaborative effort, are currently being used by the Electromagnetic Imaging Laboratory at the University of Manitoba. These phantoms will undoubtedly improve the reliability of BMI systems and expedite the creation of sensitive and secure microwave technology for breast cancer detection.

# 5 SUMMARY

For the past three decades, the scientific community has sought to develop diagnostic tools that can exploit the significant electromagnetic contrast between benign and malignant tissue. Breast microwave imaging has the potential to become an adjutant imaging modality thanks to its low cost, high sensitivity, and non-ionizing characteristics. However, small-scale clinical trials have brought forward challenges previously unnoticed during simulations and laboratory experiments. Some of the recent obstacles include the underestimated diversity and complexity of breast tissues, patient movement during scans as well as image artifacts. An unexplored source of image degradation was the reliability of the mechanical systems used to irradiate the breast from different locations. The research conducted on this thesis represents the only literature on the effects of antenna positioning deviations during a BMI scans and the only published work on the positioning specifications for the motion-control components of radar-based BMI systems. Simultaneously, this document described the creation of a novel and clinically-ready BMI system along with the development of phantoms for its validation.

Chapter 2 contains the design and development of BIRR, a radar-based BMI system. Following a design for six-sigma philosophy, the requirements of the end-user and of the system were established, designs were refined to accommodate for 95% of the population, and the end-product was approved by a panel of experts, and it was considered safe and comfortable by eleven volunteers. The BIRR system can operate in monostatic and multistatic configurations. It features four degrees of freedom with elevation and rotation being motor-controlled and with tilt, radius and angular separation of antennas being manually adjustable. The novel system design replaces impedance-matching liquids with air-efficient antennas, and the modular nature of the system allows for easy replacement and adaption of components. Paired with a frequency-based

reconstruction algorithm, the system generates reconstructed images with a significant contrast between malignant and benign tissue. Phantom scans resulted in SCR as large as 25 dB and a TFR above 3 dB. The BIRR system was deemed as a safe and comfortable equipment, both through methodic testing as well as volunteer surveys, and has been approved as a Class III medical device by Health Canada's Medical Devices Bureau. The BIRR system, paired with an effective reconstruction algorithm, will soon commence clinical trials to validate its diagnostic capabilities,

In Chapter 3 the effects of positioning errors in the antenna positioning scheme of BMI systems was investigated. To conduct this research, the BIRR system was used to scan a breast phantom. Positioning errors were systematically induced in the azimuthal and vertical trajectories, during the antenna positioning scheme of phantom scans. The data collected was reconstructed into intensity-map images. Then, contrast metrics, spatial error, ROC curves and a set of diagnostic criteria were used to quantify the impact of positioning errors. The results indicate a tolerance for accuracy for errors as great as 2.5° and 0.20 cm. Precision errors, on the other hand, were highly detrimental, with artifacts and obscured targets at values of 1.25° and 0.05 cm. The results presented in this chapter show that BMI systems are sensitive to sub-millimetric positioning errors. This conclusion has further implications for clinical trials, where minimizing patient movement is considerably more challenging than improving the performance of a mechanical system. Future experiments will explore the effects of sub-millimetric precision errors to determine cost-effective specifications. To the best of the author's knowledge, this work represents the only attempt to establish antenna positioning specifications for BMI systems. This work provides a valuable reference for the development of new BMI systems and the maintenance of existing ones.

The development of a complex breast phantom solution is discussed in Chapter 4. A Synthetic breast skin-surrogate was developed using uniform, 1-mm thick sheets of TX-151. The thickness of the skin proved to be a significant factor for power loss with losses of up to 13.7 ± 1.9 dB. Next, transparent hemispherical breast phantom containers were developed using a thermoplastic

known as CAB. A phantom scan was performed to validate the use of the material. Reconstructed images prove that the material is virtually translucent to microwaves in the range of 1-6 GHz. Finally, an array of MRI-informed CAD models of adipose and fibroglandular structures were 3D printed to form high-fidelity breast phantom containers. Suitable liquid tissue surrogates were used to match the dielectric properties of breast tissue in the 1 to 8 GHz range. The phantoms were designed to match three different breast sizes and to cover the density ratios of the BI-RADS classification. A medium-sized Class I breast phantom was scanned with the BIRR system, resulting in SCR of 26.2 dB and TFR of 7.3 dB. These phantoms represent the most anatomically-accurate tool to validate breast microwave imaging systems. Future work will explore the creation of a transparent CAB shell using the 3D printed adipose containers as a cast. The use of a 3D printed shell to cast a layer of synthetic skin is currently being investigated. More research is required on creating liquid surrogates with time-invariant dielectric properties that can match the consistent cross-section of 3D printed phantoms.

This project has confronted many of the obstacles involved in the development of a medical device, while at the same time, expanded the knowledge of breast microwave imaging research. The project has concluded in an effective, comfortable, and safe system for breast cancer detection suitable for clinical use. The system includes an array of breast phantoms with an accurate representation of the dielectric and morphologic characteristics of the breast structure. Finally, this project has established the criteria for the selection, design, and maintenance of motion-control mechanisms in BMI systems. These criteria can be extrapolated to fixed-antenna arrays and in some cases, patient movement. This knowledge will serve to expedite the development of new breast microwave imaging technologies.

# 6 REFERENCES


[1] International Agency for Research on Cancer, "Estimated Incidence, Mortality and Prevalence Worldwide in 2012," *GLOBOCAN 2012*, 2012. [Online]. Available: http://globocan.iarc.fr/Pages/fact_sheets_cancer.aspx. [Accessed: 05-Sep-2016].

[2] Statistics Canada, "Canadian Cancer Statistics - Special topic: HPV -associated cancers," 2016.

[3] G. Lip, N. Zakharova, S. Duffy, M. Gillan, and F. Gilbert, "Breast density as a predictor of breast cancer risk," *Breast Cancer Res.*, vol. 12, no. Suppl 3, p. P1, 2010.

[4] C. Gilmore, A. Zakaria, S. Pistorius, and J. LoVetri, "Microwave Imaging of Human Forearms: Pilot Study and Image Enhancement," *Int. J. Biomed. Imaging*, vol. 2013, pp. 1–17, 2013.

[5] A. T. Mobashsher, K. S. Bialkowski, A. M. Abbosh, and S. Crozier, "Design and Experimental Evaluation of a Non-Invasive Microwave Head Imaging System for Intracranial Haemorrhage Detection," *PLoS One*, vol. 11, no. 4, p. e0152351, Apr. 2016.

[6] S. A. Rezaeieh, K. S. Bialkowski, and A. M. Abbosh, "Microwave System for the Early Stage Detection of Congestive Heart Failure," *IEEE Access*, vol. 2, pp. 921–929, 2014.

[7] F. Krewer, F. Morgan, and M. O'Halloran, "Incontinence management for the elderly: Development of a radar-based bladder volume monitor," in *2014 IEEE Antennas and Propagation Society International Symposium (APSURSI)*, 2014, vol. M, pp. 1137–1138.

[8] E. C. Fear, S. C. Hagness, P. M. Meaney, M. Okoniewski, and M. a. Stuchly, "Enhancing breast tumor detection with near-field imaging," *IEEE Microw. Mag.*, vol. 3, no. March, p. 48, 2002.

[9] N. K. Nikolova, "Microwave Imaging for Breast Cancer," *IEEE Microw. Mag.*, vol. 12, no. 7, pp. 78–94, Dec. 2011.

[10] R. Conceição, J. Mohr, and M. O'Halloran, *An Introduction to Microwave Imaging for Breast Cancer Detection*. Cham: Springer International Publishing, 2016.

[11] E. C. Fear, P. M. Meaney, and M. A. Stuchly, "Microwaves for breast cancer detection?," *IEEE Potentials*, vol. 22, no. 1, pp. 12–18, Feb. 2003.

[12] T. Sugitani *et al.*, "Complex permittivities of breast tumor tissues obtained from cancer surgeries," *Appl. Phys. Lett.*, vol. 104, no. 25, p. 253702, Jun. 2014.

[13] M. Lazebnik *et al.*, "A large-scale study of the ultrawideband microwave dielectric properties of normal, benign and malignant breast tissues obtained from cancer surgeries," *Phys. Med. Biol.*, vol. 52, no. 20, pp. 6093–6115, 2007.

[14] J. T. Bushberg, J. A. Seibert, E. M. Leidholdt, J. M. Boone, and E. J. Goldschmidt, *The*

*Essential Physics of Medical Imaging*, 2nd Ed. 2003.

[15] N. Bayat, "On the Role of Antennas in the Achievable Resolution and Accuracy from Near-Field Microwave Tomography," University of Manitoba., Winnipeg, Canada, 2014.

[16] M. Ostadrahimi *et al.*, "On the development of a clinical full-vectorial 3D microwave breast imaging system," in *2015 USNC-URSI Radio Science Meeting (Joint with AP-S Symposium)*, 2015, pp. 300–300.

[17] A. Baran, D. J. Kurrant, A. Zakaria, E. C. Fear, and J. LoVetri, "Breast Imaging Using Microwave Tomography with Radar-Based Tissue-Regions Estimation," *Prog. Electromagn. Res.*, vol. 149, no. August, pp. 161–171, 2014.

[18] J. H. Jacobi, "Microwave interrogation of dielectric targets. Part II: By microwave time delay spectroscopy," *Med. Phys.*, vol. 5, no. 6, p. 509, 1978.

[19] J. Bourqui and E. C. Fear, "Systems for ultra-wideband microwave sensing and imaging of biological tissues," in *Antennas and Propagation (EuCAP), 2013 7th European Conference on*, 2013, no. Eucap, pp. 834–835.

[20] T. Henriksson *et al.*, "Clinical trials of a multistatic UWB radar for breast imaging," in *2011 Loughborough Antennas & Propagation Conference*, 2011, no. November, pp. 1–4.

[21] D. Byrne, M. Sarafianou, and I. J. Craddock, "Compound Radar Approach for Breast Imaging," *IEEE Trans. Biomed. Eng.*, vol. 64, no. 1, pp. 40–51, 2017.

[22] M. Klemm, I. J. Craddock, J. A. Leendertz, A. Preece, and R. Benjamin, "Radar-Based Breast Cancer Detection Using a Hemispherical Antenna Array–Experimental Results," *IEEE Trans. Antennas Propag.*, vol. 57, no. 6, pp. 1692–1704, Jun. 2009.

[23] M. Klemm, J. A. Leendertz, D. Gibbins, I. J. Craddock, A. Preece, and R. Benjamin, "Microwave Radar-Based Differential Breast Cancer Imaging: Imaging in Homogeneous Breast Phantoms and Low Contrast Scenarios," *IEEE Trans. Antennas Propag.*, vol. 58, no. 7, pp. 2337–2344, Jul. 2010.

[24] E. Porter, M. Coates, and M. Popovic, "An Early Clinical Study of Time-Domain Microwave Radar for Breast Health Monitoring," *IEEE Trans. Biomed. Eng.*, vol. 63, no. 3, pp. 530–539, Mar. 2016.

[25] P. M. Meaney, M. W. Fanning, D. Li, S. P. Poplack, and K. D. Paulsen, "A clinical prototype for active microwave imaging of the breast," *IEEE Trans. Microw. Theory Tech.*, vol. 48, no. 11, pp. 1841–1853, 2000.

[26] S. P. Poplack *et al.*, "Electromagnetic breast imaging: results of a pilot study in women with abnormal mammograms.," *Radiology*, vol. 243, no. 2, pp. 350–359, 2007.

[27] P. M. Meaney *et al.*, "Microwave imaging for neoadjuvant chemotherapy monitoring: initial clinical experience.," *Breast Cancer Res.*, vol. 15, no. 2, p. R35, 2013.

[28] N. R. Epstein, P. M. Meaney, and K. D. Paulsen, "3D parallel-detection microwave

tomography for clinical breast imaging," *Rev. Sci. Instrum.*, vol. 85, no. 12, 2014.

[29] Parker Hannifin Corporation, "ET Series Electric Cylinders," Wadsworth,Ohio USA.

[30] J. Bourqui, J. M. Sill, and E. C. Fear, "A prototype system for measuring microwave frequency reflections from the breast," *Int. J. Biomed. Imaging*, vol. 2012, 2012.

[31] E. C. Fear, J. Bourqui, C. Curtis, D. Mew, B. Docktor, and C. Romano, "Microwave breast imaging with a monostatic radar-based system: A study of application to patients," *IEEE Trans. Microw. Theory Tech.*, vol. 61, no. 5, pp. 2119–2128, 2013.

[32] E. C. Fear, J. Bourqui, M. A. Campbell, and T. C. Williams, "Antenna evaluation for ultra-wideband microwave imaging," *Int. J. Antennas Propag.*, vol. 2010, 2010.

[33] E. C. Fear, X. Li, S. C. Hagness, and M. A. Stuchly, "Confocal microwave imaging for breast cancer detection: localization of tumors in three dimensions," *IEEE Trans. Biomed. Eng.*, vol. 49, no. 8, pp. 812–822, 2002.

[34] E. Porter, A. Santorelli, M. Coates, and M. Popovic, "Time-Domain Microwave Breast Cancer Detection: Extensive System Testing with Phantoms," *Technol. Cancer Res. Treat.*, vol. 12, no. 2, 2012.

[35] D. Flores-Tapia and S. Pistorius, "Real time breast microwave radar image reconstruction using circular holography: A study of experimental feasibility," *Med. Phys.*, vol. 38, no. 10, p. 5420, 2011.

[36] M. Solis Nepote, D. Rodriguez Herrera, D. Flores-Tapia, S. Latif, and S. Pistorius, "A comparison study between Horn and Vivaldi antennas for 1.5-6 GHz Breast Microwave Radar Imaging," in *The 8th European Conference on Antennas and Propagation (EuCAP 2014)*, 2014, vol. 5, no. EuCAP, pp. 59–62.

[37] D. Flores-Tapia *et al.*, "Experimental feasibility of multistatic holography for breast microwave radar image reconstruction," *Med. Phys.*, vol. 43, no. 8, pp. 4674–4686, Aug. 2016.

[38] Newport Corporation, "Motion Control Metrology Primer," 2010. [Online]. Available: https://www.newport.com/n/motion-control-metrology-primer. [Accessed: 05-May-2017].

[39] A. Mital, *Product Development: A Structured Approach to Design and Manufacture*. Amsterdam: Butterworth-Heinemann, 2008.

[40] B. El-Haik and K. S. Mekki, *Medical Device Design for Six Sigma: A Road Map for Safety and Effectiveness*. Wiley, 2008.

[41] A. J. Krul, H. A. M. Daanen, and H. Choi, "Self-reported and measured weight, height and body mass index (BMI) in Italy, the Netherlands and North America," *Eur. J. Public Health*, vol. 21, no. 4, pp. 414–419, Aug. 2011.

[42] M. Shields, S. Connor Gorber, I. Janssen, and M. S. Tremblay, "Bias in self-reported estimates of obesity in Canadian health surveys: an update on correction equations for adults.," *Heal. reports*, vol. 22, no. 3, pp. 35–45, Sep. 2011.

[43] S.-Y. Huang *et al.*, "The characterization of breast anatomical metrics using dedicated breast CT," *Med. Phys.*, vol. 38, no. 4, pp. 2180–2191, Mar. 2011.

[44] V. Y. Sohn, Z. M. Arthurs, J. A. Sebesta, and T. A. Brown, "Primary tumor location impacts breast cancer survival," *Am. J. Surg.*, vol. 195, no. 5, pp. 641–644, May 2008.

[45] S. Rummel, M. T. Hueman, N. Costantino, C. D. Shriver, and R. E. Ellsworth, "Tumour location within the breast: Does tumour site have prognostic ability?," *Ecancermedicalscience*, vol. 9, p. 552, Jul. 2015.

[46] M. Klemm *et al.*, "Development and Testing of a 60-Element UWB Conformal Array for Breast Cancer Imaging," in *Antennas and Propagation (EUCAP), Proceedings of the 5th European Conference on*, 2011, pp. 3077–3079.

[47] D. Flores-Tapia, O. Maizlish, and S. Pistorius, "Spatial sampling requirements for multistatic Breast Microwave Radar imaging," *Proc. 2012 Int. Conf. Electromagn. Adv. Appl. ICEAA'12*, no. 204, pp. 420–423, 2012.

[48] J. J. Carr, *Microwaves & Wireless Communications Technology*, 1st ed. Woburn, MA: Newnes, 1997.

[49] M. Pastorino, *Microwave Imaging*. Hoboken, NJ, USA: John Wiley & Sons, Inc., 2010.

[50] D. F. Tapia, D. Rodriguez Herrera, M. Solis Nepote, S. Latif, and S. Pistorius, "An experimental study on the effects of the antenna - breast surface separation in microwave radar imaging," in *2014 IEEE Conference on Antenna Measurements & Applications (CAMA)*, 2014, pp. 1–4.

[51] S. I. Latif, D. Flores-Tapia, S. Pistorius, and L. Shafai, "Design and performance analysis of the miniaturised water-filled double-ridged horn antenna for active microwave imaging applications," *IET Microwaves, Antennas Propag.*, vol. 9, no. 11, pp. 1173–1178, 2015.

[52] D. Rodriguez Herrera, "Antenna Characterisation and Optimal Sampling Constraints for Breast Microwave Imaging Systems with a Novel Wave Speed Propagation Algorithm.," University of Manitoba, 2016.

[53] J. C. Lin, "Frequency optimization for microwave imaging of biological tissues," *Proc. IEEE*, vol. 73, no. 2, pp. 374–375, 1985.

[54] I. R. Walker, *Reliability in scientific research : improving the dependability of measurements, calculations, equipment, and software*, 1st Ed. Cambridge, UK: Cambridge University Press, 2011.

[55] (CSA) Canadian Standards Association, "Medical Electrical Equipment. Part 1: General requirements for basic safety. CAN/CSA-C22.2 No. 601.1 -M90," Ontario, Canada, 1990.

[56] Mattressizez.info, "Mattress Size :: USA & Canada," 2009. [Online]. Available: http://www.mattresssizes.info/. [Accessed: 22-Mar-2017].

[57] Item America, "Profile Technical Data," 2010. [Online]. Available:

http://www.itemwest.com/products/product-catalog/products/profiles-8.html. [Accessed: 20-May-2006].

[58] (ISO) International Organization for Standardization, "Test code for machine tools - Part 2: Determination of accuracy and repeatability of positioning of numerically controlled axes. ISO 230-2:2006(E)," Geneva, Switzerland, 2006.

[59] (ISO) International Organization for Standardization, "Test code for machine tools - Part 9: Estimation of measurement uncertainty for machine tool tests according to series ISO 230, basic equations. ISO/TR 230-9:2005," Geneva, Switzerland, Mar. 2005.

[60] Zolix Co Ltd, "Motorized stage catalog - RAK: High precision motorized stage," Beijing, China, 2013.

[61] National Instruments, "Vector Network Analyzer Calibration," 2013. [Online]. Available: http://www.ni.com/tutorial/14114/en/. [Accessed: 24-Jun-2017].

[62] S. I. Latif, D. Flores-Tapia, D. Rodriguez Herrera, M. Solis Nepote, S. Pistorius, and L. Shafai, "A Directional Antenna in a Matching Liquid for Microwave Radar Imaging," *Int. J. Antennas Propag.*, vol. 2015, pp. 1–8, 2015.

[63] (IEC) International Electrotechnical Commission, "IEC 60601-1:2005 Medical electrical equipment - Part 1: General requirements for basic safety and essential performance.," 2005.

[64] Consumer and Clinical Radiation Protection Bureau - Health Canada., "Limits of Human Exposure to Radiofrequency Electromagnetic Energy in the Frequency Range from 3 kHz to 300 GHz.," Ottowa, Ontario, Canada, 2009.

[65] G. J. A. Bird, *Radar precision and resolution*. Pentech Press, 1974.

[66] S. A. Narod, "Tumour size predicts long-term survival among women with lymph node-positive breast cancer," *Curr. Oncol.*, vol. 19, no. 5, pp. 249–253, 2012.

[67] M. Solis Nepote, D. Rodriguez Herrera, D. Flores-Tapia, and S. Pistorius, "Initial results on cellulose acetate butyrate vessels for breast microwave radar imaging," in *Canadian-American-Mexican Graduate Student Physics Conference*, 2013, pp. 32–33.

[68] D. Rodriguez Herrera, T. Reimer, M. Solis Nepote, and S. Pistorius, "Manufacture and testing of anthropomorphic 3D-printed breast phantoms using a microwave radar algorithm optimized for propagation speed," in *2017 11th European Conference on Antennas and Propagation (EUCAP)*, 2017, pp. 3480–3484.

[69] D. Kurrant, J. Bourqui, C. Curtis, and E. C. Fear, "Evaluation of 3-D Acquisition Surfaces for Radar-Based Microwave Breast Imaging," *IEEE Trans. Antennas Propag.*, vol. 63, no. 11, pp. 4910–4920, 2015.

[70] D. Flores-Tapia and S. Pistorius, "Spatial sampling constraints on Breast Microwave Radar scan acquired along circular scan geometries," in *2011 IEEE International Symposium on Biomedical Imaging: From Nano to Macro*, 2011, pp. 496–499.

[71] J. J. McCombe and N. K. Nikolova, "SNR assessment of microwave imaging systems," *IEEE Antennas Propag. Soc. AP-S Int. Symp.*, pp. 149–150, 2014.

[72] J. A. Hanley and B. J. McNeil, "The Meaning and Use of the Area under a Receiver Operating Characteristic (ROC) Curve," *Radiology*, vol. 143, no. 1, pp. 29–36, 1982.

[73] M. Gönen, *Analyzing Receiver Operating Characteristic Curves with SAS*. Cary, NC: SAS Institute Inc, 2007.

[74] M. Solis Nepote, D. Rodriguez Herrera, J. Sacristan, D. Flores-Tapia, and S. Pistorius, "Evaluation of the skin thickness effects in Breast Microwave Radar images," in *2014 IEEE Antennas and Propagation Society International Symposium (APSURSI)*, 2014, pp. 516–517.

[75] S. A. Love and K. Lindsey, *Dr. Susan Love's Breast Book*, 4th ed. Da Capo Press, 2005.

[76] G. J. Tortora and B. Derrickson, *Principles of Anatomy and Physiology*, 13th ed. Wiley, 2012.

[77] A. M. R. Agur and A. F. Dalley, *Grant's Atlas of Anatomy*, 13th ed. Lippincott Williams & Wilkins, 2012.

[78] A. Sutradhar and M. J. Miller, "In vivo measurement of breast skin elasticity and breast skin thickness," *Ski. Res. Technol.*, vol. 19, no. 1, pp. 191–199, 2013.

[79] B. H. Østerås *et al.*, "BI-RADS density classification from areometric and volumetric automatic breast density measurements," *Acad. Radiol.*, vol. 23, no. 4, pp. 468–478, 2016.

[80] E. R. Price *et al.*, "The California Breast Density Information Group: A Collaborative Response to the Issues of Breast Density, Breast Cancer Risk, and Breast Density Notification Legislation," *Radiology*, vol. 269, no. 3, pp. 887–892, Dec. 2013.

[81] C. D'Orsi, E. Sickles, E. Mendelson, and E. Morris, *Breast imaging reporting and data system: ACR BI-RADS—breast imaging atlas (Quick reference chart)*, 5th ed. Reston, VA: American College of Radiology, 2013.

[82] G. M. Cooper, "The Development and Causes of Cancer," in *The Cell: A Molecular Approach.*, 2nd ed., Sunderland (MA): Sinauer Associates, 2000.

[83] American Cancer Society, "Types of Breast Cancer." [Online]. Available: https://www.cancer.org/cancer/breast-cancer/understanding-a-breast-cancer-diagnosis/types-of-breast-cancer.html. [Accessed: 11-Oct-2017].

[84] E. Honrado, J. Benítez, and J. Palacios, "The Pathology of Hereditary Breast Cancer," *Hered. Cancer Clin. Pract.*, vol. 2, no. 3, p. 131, Jul. 2004.

[85] Breast Cancer Org, "ILC — Invasive Lobular Carcinoma," 2017. [Online]. Available: http://www.breastcancer.org/symptoms/types/ilc. [Accessed: 06-Dec-2017].

[86] Keysight Technologies, "Basics of Measuring the Dielectric Properties of Materials," *Keysight Lit. number 5989-2589En*, pp. 1–32, 2015.

[87] Kaye & Laby Online, "Tables of Physical & Chemical Constants (16th edition 1995). 2.6.5 Dielectric properties of materials," *Version 1.0*, 2005. [Online]. Available: http://www.kayelaby.npl.co.uk/general_physics/2_6/2_6_5.html. [Accessed: 11-Oct-2017].

[88] M. Lazebnik *et al.*, "A large-scale study of the ultrawideband microwave dielectric properties of normal breast tissue obtained from reduction surgeries," *Phys. Med. Biol.*, vol. 52, no. 10, pp. 2637–2656, 2007.

[89] T. Sugitani *et al.*, "Erratum: 'Complex permittivities of breast tumor tissues obtained from cancer surgeries' [Appl. Phys. Lett. 104 , 253702 (2014)]," *Appl. Phys. Lett.*, vol. 107, no. 1, p. 19902, Jul. 2015.

[90] R. J. Halter *et al.*, "The correlation of in vivo and ex vivo tissue dielectric properties to validate electromagnetic breast imaging: initial clinical experience," *Physiol. Meas.*, vol. 30, no. 6, pp. S121–S136, Jun. 2009.

[91] T. C. Williams, J. Bourqui, T. R. Cameron, M. Okoniewski, and E. C. Fear, "Laser surface estimation for microwave breast imaging systems," *IEEE Trans. Biomed. Eng.*, vol. 58, no. 5, pp. 1193–1199, 2011.

[92] J. Garrett and E. C. Fear, "A New Breast Phantom With a Durable Skin Layer for Microwave Breast Imaging," *IEEE Trans. Antennas Propag.*, vol. 63, no. 4, pp. 1693–1700, 2015.

[93] P. M. Meaney, K. D. Paulsen, A. Hartov, and R. K. Crane, "Microwave imaging for tissue assessment: initial evaluation in multitarget tissue-equivalent phantoms," *IEEE Trans. Biomed. Eng.*, vol. 43, no. 9, pp. 878–890, 1996.

[94] J. M. Sill and E. C. Fear, "Tissue sensing adaptive radar for breast cancer detection: preliminary experimental results," in *IEEE MTT-S International Microwave Symposium Digest, 2005.*, 2005, vol. 2005, no. C, pp. 1789–1792.

[95] A. Kneebone, V. Gebski, N. Hogendoorn, and S. Turner, "A randomized trial evaluating rigid immobilization for pelvic irradiation," *Int. J. Radiat. Oncol. Biol. Phys.*, vol. 56, no. 4, pp. 1105–1111, 2003.

[96] T. Ishii, Ed., *Handbook of Microwave Technology, Volume 2*, 1st ed. Academic Press, 1995.

[97] N. Joachimowicz, B. Duchêne, C. Conessa, and O. Meyer, "Easy-to-produce adjustable realistic breast phantoms for microwave imaging," *2016 10th Eur. Conf. Antennas Propagation, EuCAP 2016*, pp. 3–6, 2016.

[98] M. J. Burfeindt *et al.*, "MRI-derived 3-D-printed breast phantom for microwave breast imaging validation," *IEEE Antennas Wirel. Propag. Lett.*, vol. 11, pp. 1610–1613, 2012.

[99] Emerson & Cuming, "Dielectric Materials Chart - Eccostock® Low Loss Dielectrics & Other Common Materials." [Online]. Available: http://www.eccosorb.eu/sites/default/files/files/dielectric-chart.pdf. [Accessed: 15-Oct-2017].

[100] N. Joachimowicz, C. Conessa, T. Henriksson, and B. Duchêne, "Breast phantoms for

microwave imaging," *IEEE Antennas Wirel. Propag. Lett.*, vol. 13, pp. 1333–1336, 2014.

[101] E. Porter, J. Fakhoury, R. Oprisor, M. Coates, and M. Popovic, "Improved tissue phantoms for experimental validation of microwave breast cancer detection," *Antennas Propag. (EuCAP), 2010 Proc. Fourth Eur. Conf.*, pp. 4–8, 2010.

[102] E. Zastrow, S. K. Davis, M. Lazebnik, F. Kelcz, B. D. Van Veen, and S. C. Hagness, "Development of Anatomically Realistic Numerical Breast Phantoms With Accurate Dielectric Properties for Modeling Microwave Interactions With the Human Breast," *IEEE Trans. Biomed. Eng.*, vol. 55, no. 12, pp. 2792–2800, 2008.

[103] Lin Engineering, "Silverpak 23CE." [Online]. Available: https://www.linengineering.com/products/integrated_motors/silverpak-23ce-2/. [Accessed: 01-Dec-2017].

# 7 APPENDIX

## 7.1 Equations for accuracy and repeatability of motion-control systems.

The following definitions and equations are adapted from ISO 230-2(E):2006 [58]

A.1. Target position:
Position to which the moving part is programmed to move, where $\boldsymbol{i}$ is the targeted position.

$$P_i \ (i = 1 \ to \ m) \tag{A.1}$$

A.2. Actual position:
Measured position of the moving part at the $\boldsymbol{i}^{\text{th}}$ target position on the $\boldsymbol{j}^{\text{th}}$ approach.

$$P_{ij} \ (i = 1 \text{ to } m; j = 1 \text{ to } n) \tag{A.2}$$

A.3. Positional deviation:

$$x_{ij} = P_{ij} - P_i \tag{A.3}$$

A.4. Mean unidirectional positional deviation at a position:

$$\bar{x}_i \uparrow = \frac{1}{n}\sum_{j=1}^{n} x_{ij} \uparrow \quad \text{and} \quad \bar{x}_i \downarrow = \frac{1}{n}\sum_{j=1}^{n} x_{ij} \downarrow \tag{A.4}$$

A.5. Mean bidirectional positional deviation at a position:

$$\bar{X}_i = \frac{\bar{x}_i \uparrow \ + \bar{x}_i \downarrow}{2} \tag{A.5}$$

A.6. Reversal value at a position:

$$B_i = \bar{x}_i \uparrow \ - \bar{x}_i \downarrow \tag{A.6}$$

A.7. Reversal value of an axis:

$$B = |B_i|_{max} \tag{A.7}$$

A.8. Mean reversal value of an axis:

$$\bar{B} = \frac{1}{m}\sum_{i=1}^{m} B_i \tag{A.8}$$

A.9. Standard uncertainty for the positional deviations at a position:

$$s_i \uparrow = \sqrt{\frac{1}{n-1}\sum_{j=1}^{n}(x_{ij} \uparrow - \bar{x} \uparrow)^2} \qquad s_i \downarrow = \sqrt{\frac{1}{n-1}\sum_{j=1}^{n}(x_{ij} \downarrow - \bar{x} \downarrow)^2} \tag{A.9}$$

A.10. Unidirectional repeatability of positioning at a position:

$$r_i \uparrow = 4s_i \uparrow \quad \text{and} \quad r_i \downarrow = 4s_i \downarrow \tag{A.10}$$

A.11. Unidirectional repeatability of positioning of an axis:

$$r \uparrow = [r_i \uparrow]_{max} \quad \text{and} \quad r \downarrow = [r_i \downarrow]_{max} \tag{A.11}$$

A.12. Bidirectional repeatability of positioning at a position:

$$R_i = [2s_i \uparrow + 2s_i \downarrow + |B_i| \; ; \; r_i \uparrow ; r_i \downarrow]_{max} \tag{A.12}$$

A.13. Bidirectional repeatability of positioning of an axis:

$$R = [R_i]_{max} \tag{A.13}$$

A.14. Unidirectional systematic positional deviation of an axis:

$$e \uparrow = [\bar{x}_i \uparrow]_{max} - [\bar{x}_i \uparrow]_{min} \quad \text{and} \quad e \downarrow = [\bar{x}_i \downarrow]_{max} - [\bar{x}_i \downarrow]_{min} \tag{A.14}$$

A.15. Bidirectional systematic positional deviation of an axis:

$$E = [\bar{x}_i \uparrow ; \bar{x}_i \downarrow]_{max} - [\bar{x}_i \uparrow ; \bar{x}_i \downarrow]_{min} \tag{A.15}$$

A.16. Mean bidirectional systematic positional deviation of an axis:

$$M = [\bar{X}_i]_{max} - [\bar{X}_i]_{min} \tag{A.16}$$

A.17. Unidirectional accuracy of positioning of an axis:

$$a \uparrow = [\bar{x}_i \uparrow + 2s_i \uparrow]_{max} - [\bar{x}_i \uparrow - 2s_i \uparrow]_{min}$$

and (A.17)

$$a \downarrow = [\bar{x}_i \downarrow + 2s_i \downarrow]_{max} - [\bar{x}_i \downarrow - 2s_i \downarrow]_{min}$$

A.18. Bidirectional accuracy of positioning of an axis:

$$A = [\bar{x}_i \uparrow + 2s_i \uparrow ; \; \bar{x}_i \downarrow + 2s_i \downarrow]_{max} - [\bar{x}_i \downarrow - 2s_i \downarrow ; \; \bar{x}_i \downarrow - 2s_i \downarrow]_{min} \tag{A.18}$$

A.19. Mean offset of an axis:

$$\bar{\bar{X}}_{off} = \frac{1}{m} \sum_{i=1}^{m} \bar{x}_i \tag{A.19}$$

## 7.2 Equations for uncertainty estimations

The following uncertainties estimations follow ISO/TR 230-9: 2005 regulations for measurements performed with a coverage factor of $\boldsymbol{k} = 2$ [59]. Uncertainties due to the temperature compensation were omitted. Although measurements were performed at uncontrolled temperatures, the effects of thermal expansion for the length of the axes measured was small (i.e., less than 0.01 mm) and can be neglected.

A.20. Uncertainty due to the measuring device:

$$U_{device} = U_{calibration}$$

or (A.20)

$$U_{device} = U_{calibration} \times L$$

Where $U_{calibration}$ is the error stated by the calibration certificate of the device in millimeters or degrees (mm or °). $L$ is the measurement length in millimeters (mm).

A.21. Uncertainty due to misalignment:

$$U_{\text{misalignment}} = 0.3 \times \frac{R^2_{\text{misalignment}}}{L} \quad \text{(A.21)}$$

Where $R_{\text{misalignment}}$ is the value of misalignment of measuring device to machine axis under test in millimeters (mm);

A.22. Uncertainty due to the environmental variation error:

$$U_{EVE} = 0.3 \times E_{VE} \quad \text{(A.22)}$$

Where $E_{VE}$ is the range of values from a drift test in millimeters (mm).

A.23. Uncertainty for unidirectional repeatability:

$$U(r\uparrow, r\downarrow) = 2 \times U_{EVE} \quad \text{(A.23)}$$

A.24. Uncertainty for reversal value

$$U(B) = 2 \times U_{EVE} \quad \text{(A.24)}$$

A.25. Uncertainty of bidirectional repeatability

$$U(R) = 2.2 \times U_{EVE} \tag{A.25}$$

A.26. Uncertainty of systematic deviations:

$$U(E, e\uparrow, e\downarrow) = \sqrt{U_{device}^2 + U_{\text{misalignment}}^2 + \frac{1}{5} \times U_{EVE}^2} \tag{A.26}$$

A.27. Uncertainty of mean systematic deviation:

$$U(M) = \sqrt{U_{device}^2 + U_{\text{misalignment}}^2 + \frac{1}{10} \times U_{EVE}^2} \tag{A.27}$$

A.28. Uncertainty of accuracy of positioning

$$U(A, a\uparrow, a\downarrow) = \sqrt{U(E)^2 + U(r\uparrow, r\downarrow)^2} \tag{A.28}$$

## 7.3 Volunteer experience questionnaire

Study: "Performance assessment of a first-generation breast microwave imaging system: Study of human imaging feasibility".

Principal investigators: Dr. Stephen Pistorius and Dr. Joseph LoVetri

Study coordinator: Dr. Daniel Flores Tapia
Research Assistant: Mr. Mario Solis Nepote,
Clinical Assistant: Ms. Tiffany Dupont

---

**Demographics**

Age:_____ Breast Cup Size:_____

**Imaging procedure**

1. While on the bed, did you experience any discomfort during the imaging procedure?

   Yes No

2a. If you answered **Yes** to Q1 please rate the discomfort or pain caused by:

The inspection bed

| 1 | 2 | 3 | 4 |
|---|---|---|---|
| Minor discomfort | Very slight pain | Minor pain, like pinching the fold of skin | Noticeable pain on the same degree as an injection |

Please describe the source of pain or discomfort identified above, or if there was another source of discomfort or pain that was not associated with the bed or how your body lied on it.

2b. Would you be able to remain in the same position for another 30 minutes?

Yes No

3. Now that the procedure has been completed, please indicate if you are still experiencing any pain or discomfort.

| 1 | 2 | 3 | 4 |
|---|---|---|---|
| No pain or discomfort | Very slight pain or minor discomfort/ache | Minor pain, like pinching the fold of skin | Noticeable pain on the same degree as an injection |

If you experienced any discomfort or pain after the procedure, please describe the source of it.

**Patient care**

4. Was the imaging equipment clean?

Yes No

5. Was the imaging room clean?

Yes No

6. Was the research assistant who helped you respectful?

Yes No

7. Was the procedure explained to you adequately?

Yes No

If not, please describe which aspects of the procedure were not adequately explained:

**Safety**

8. Do you have any concerns about the radiation safety of this process?

Yes No

If so, please state your concerns:

9. Did you have any concerns about your physical safety during this process?

Yes No

If so, please state your concerns:

**Overall Impression**

10. Have you ever been imaged using an X-ray mammogram procedure?

Yes No

If so, how would you rate the comfort of the breast microwave imaging procedure in comparison to X-ray mammography?

| 1 | 2 | 3 | 4 | 5 |
|---|---|---|---|---|
| Much more comfortable | More comfortable | Equally comfortable | More uncomfortable | Much more uncomfortable |

11. Have you ever been imaged using a Magnetic Resonance Imaging (MRI) procedure?

Yes No

If so, how would you rate the comfort of breast microwave imaging procedure compared to MRI?

| 1 | 2 | 3 | 4 | 5 |
|---|---|---|---|---|
| Much more comfortable | More comfortable | Equally comfortable | More uncomfortable | Much more uncomfortable |

12. If this was a standard clinical procedure, how often would you be willing to be imaged using this technology:

| 1 | 2 | 3 |
|---|---|---|
| Twice a year | Once a year | I would not be willing to be imaged using this technology again |

Overall Comments and suggestions:

## 7.4 Volunteer experience results

Eleven women were scanned with the BIRR system during a phase 0 clinical trial. Volunteers were women between the ages of 42 to 52, with no history of breast cancer. The results of a post-scan survey are disclosed below.

| | | Rate of discomfort or pain caused by the inspection bed. | Source of pain or discomfort. | Rate of discomfort or lingering pain after the procedure. | Source of lingering discomfort or pain. | Would you be able to remain in the same position for another 30 minutes? |
|---|---|---|---|---|---|---|
| Volunteers | v1 | – | – | – | – | Yes |
| | v2 | Very slight pain | Neck and abdomen | Very slight pain or minor discomfort | Neck | Yes |
| | v3* | Minor discomfort | Body in general | – | – | Yes |
| | v4 | Minor pain, like pinching the fold of skin | Neck | – | – | Yes |
| | v5 | Minor discomfort | Neck and abdomen | Very slight pain or minor discomfort | Neck | Yes |
| | v6* | Minor discomfort | Neck and shoulder | – | – | Yes |
| | v7 | – | – | – | – | Yes |
| | v8 | Minor discomfort | – | Very slight pain or minor discomfort | Body in general | Yes |
| | v9 | Very slight pain | Abdomen | – | – | Yes |
| | v10* | Minor discomfort | Neck and am | Very slight pain or minor discomfort | Shoulder or arm | Yes* |
| | v11 | – | – | Very slight pain or minor discomfort | Abdomen | No* |

*Volunteers 3, 6 and 10 were not scanned with the BIRR system, their evaluation reflects only comfort and safety of the inspection bed.
§Volunteers 10 and 11 were scanned twice. Their procedure took more than 50 minutes.

| | | Do you have any concerns about the radiation safety of this process? | Did you have any concerns about your physical safety during this process? | Comfort of the breast microwave imaging procedure in comparison to X-ray mammography. | Comfort of the breast microwave imaging procedure compared to MRI. | If this was a standard clinical procedure, how often would you be willing to be imaged using this technology? |
|---|---|---|---|---|---|---|
| Volunteers | v1 | No | No | Much more comfortable | Much more comfortable | Twice a year |
| | v2 | No | No | More uncomfortable | – | – |
| | v3 | No | No | More comfortable | – | Once a year |
| | v4 | *Yes, Microwave side effects, exposure.* | No | Much more comfortable | Much more comfortable | Twice a year |
| | v5 | No | No | More comfortable | – | Twice a year |
| | v6 | No | Yes (no comments) | Much more comfortable | More uncomfortable | Once a year |
| | v7 | No | No | Much more comfortable | – | Once a year |
| | v8 | No | No | More comfortable | – | Twice a year |
| | v9 | No | No | Much more comfortable | – | Once a year |
| | v10 | No | No | Much more comfortable | More uncomfortable | Twice a year |
| | v11 | No | No | Much more comfortable | More comfortable | Twice a year |

| | | Was the imaging equipment clean? | Was the imaging room clean? | Was the research assistant who helped you, respectful? | Was the procedure explained to you adequately? | If not, please describe which aspects of the procedure were not adequately explained: |
|---|---|---|---|---|---|---|
| Volunteers | v1 | Yes | Yes | Yes | Yes | – |
| | v2 | Yes | Yes | Yes | Yes | – |
| | v3 | Yes | Yes | Yes | Yes | – |
| | v4 | Yes | Yes | Yes | Yes | *"All information was clear but would have preferred to have information and consent forms in advance"* |
| | v5 | Yes | Yes | Yes | Yes | – |
| | v6 | Yes | Yes | Yes | Yes | – |
| | v7 | Yes | Yes | Yes | Yes | – |
| | v8 | Yes | Yes | Yes | Yes | – |
| | v9 | Yes | Yes | Yes | Yes | – |
| | v10 | Yes | No | Yes | Yes | – |
| | v11 | Yes | Yes | Yes | Yes | – |

| | | Overall comments and suggestions* |
|---|---|---|
| Volunteers | v1 | *She really enjoyed having someone in the room with her throughout the entirety of the procedure. It helped her feel comfortable and relaxed, as opposed to other procedures where you may be left alone in the room. Also mentioned that some other procedures have made her feel claustrophobic and confined whereas this procedure was more open and airy, and the music in the background was very enjoyable* |
| | v2 | *I would [be] more able to be willing to be imaged this way if the table was more like a massage table with a head/neck support sticking on the end. Music was nice, but radio would also be ok.* |
| | v3 | – |
| | v4 | *If there are further clinical studies, I would be willing to participate. Thank you for the opportunity.* |
| | v5 | *Very positive experience. In general, would suggest that the couch be more like a massage table and that a padded face rest (like a massage or chiropractic table). Lower table so a step would not need to be used. Radar opening more comfortable.* |
| | v6 | *Head straight would eliminate two things for me: 1) strained neck 2) strained shoulder* |
| | v7 | *Preferably, I wouldn't want to take to long for overall process* |
| | v8 | – |
| | v9 | – |
| | v10 | *I feel asleep. I recommend working with an expert in body movement and support to build a bed, i.e., an occupational therapist or physiotherapist. In particular, Dr. Michael Moncini has experience in 3D motion of bodies, research in hospital settings, and has graduated in both chiropractic and physiotherapy.* |
| | v11 | *Much more comfortable in comparison to a mammogram, less compression, and pain of the breast. Volunteer and her friends never look forward to mammograms because of the pain – this procedure is much more tolerable. Volunteer had a knee and hip reconstruction surgery, and a back metal plate.* |

**Original comments as recorded in the questionnaire. The assisting volunteer transcribed some comments in behalf of volunteers.*

## 7.5 Lift stage characterization

Once the lift stage was manufactured, a functionality test was carried out. Further experiments were performed to guarantee reliable movement of the lift stage. These evaluations included range of movement, load capacity, movement speed, and positioning performance (see Section 2.3.2.1.1).

### 7.5.1 Range and calibration

Goal: Determine the maximum range of the lift stage and define a conversion table for microsteps to lift stage positions.

Motivation: The design requirements for the lift stage demanded a travel distance of at least 110 mm to cover different breast sizes.

Method: The lift stage was placed below the bed frame. The scissor lift was extended using the stepper motor on 5-mm-increments. The process continued until the antennas contacted the chest support, sitting directly above the antennas. A digital caliper with an uncertainty of 0.02 mm was used to measure the height of the stage after every movement.

Results: From the collapsed position to the full extension, the stage traveled 166.2 ± 0.02 mm. To prevent damage to the equipment, the operational range of the stage is limited to 160 mm. The stepper motor value and corresponding lift stage height are summarized

Table 7.5-1 Motor position to lift stage position conversion table

| Motor (microsteps) | Lift stage (mm ± 0.02 mm) | Motor (microsteps) | Lift stage (mm ± 0.02 mm) |
|---|---|---|---|
| 0 | 0 | 859000 | 85 |
| 34000 | 5 | 930500 | 90 |
| 70000 | 10 | 1006000 | 95 |
| 107000 | 15 | 1085000 | 100 |
| 147000 | 20 | 1168000 | 105 |
| 190000 | 25 | 1254000 | 110 |
| 232000 | 30 | 1345000 | 115 |
| 277000 | 35 | 1439000 | 120 |
| 325000 | 40 | 1536000 | 125 |
| 375000 | 45 | 1641000 | 130 |
| 427000 | 50 | 1746000 | 135 |
| 480500 | 55 | 1856000 | 140 |
| 537000 | 60 | 1972000 | 145 |
| 596500 | 65 | 2090000 | 150 |
| 658000 | 70 | 2230000 | 155 |
| 722000 | 75 | 2370000 | 160 |
| 790000 | 80 | 2485000 | 165 |

### 7.5.2 Load capacity

Goal: Determine the speed vs. load capacity of the scissor lift.

Motivation: The system design requires the lift stage to support a load equal to the weight of the antenna array and supporting structures (6.5 kg with a safety factor of 3). However, the load capacity of the lift stage is limited by the intrinsic torque curve of the stepper motor (Figure 7.5-1). The desired condition is the fastest movement at the maximum load.

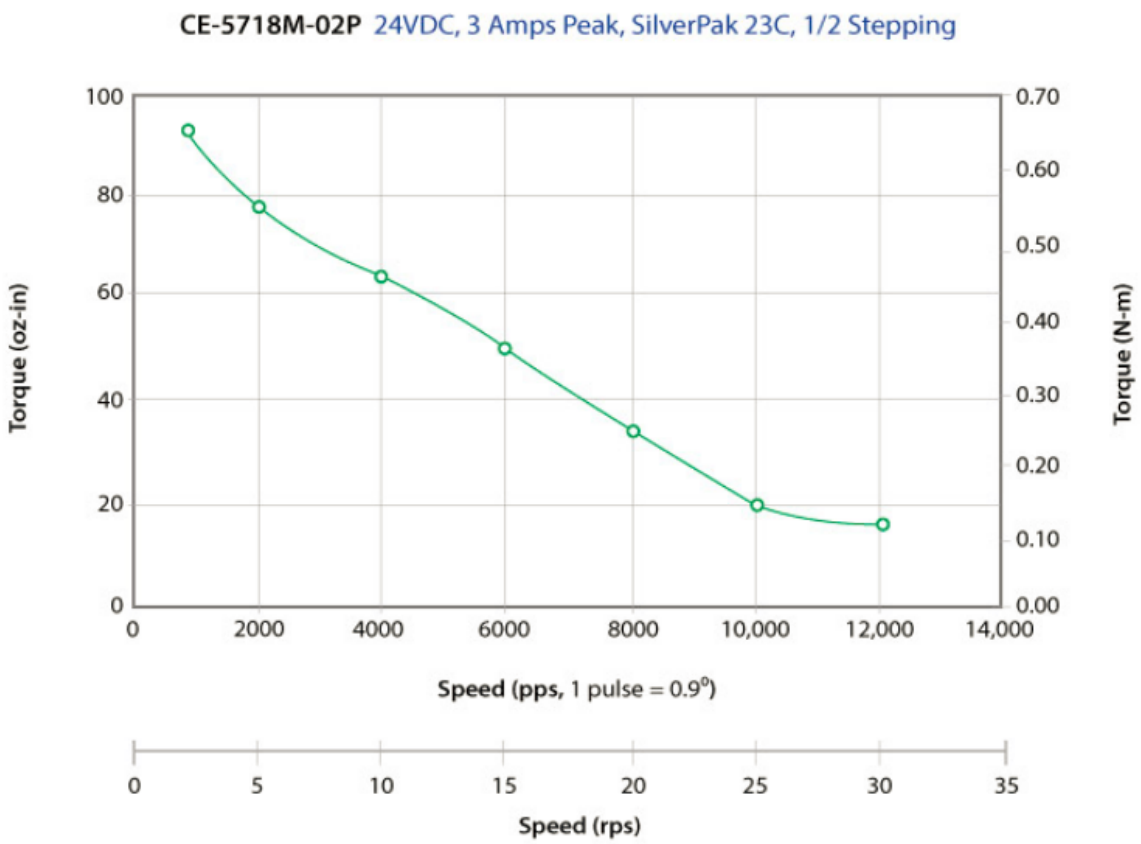


Figure 7.5-1 Torque curve for the stepper motor driving the lift stage [103]. Greater loads can be moved at the cost of speed

Methods: The lift stage was programmed to move in 60 mm increments. The motor speeds tested were 100,000, 80,000, 60,000, 40,000 and 20,000 pulses per second (pps). Weights were added to the stage until a motion error was detected. An error greater than 0.5 mm represented a stalling condition. Lack of movement or an error greater than 1 mm represented a failing condition. The experiment was performed with along of the full range of motion of the scissor lift.

Results: The lift stage was able to raise up to 11.1 kg at the higher positions. Stalling was only observed at 100,000 pps (Table 7.5-2). At higher positions, the speed of the stepper motor can be increased up to 100,000 pps to move the desired weight.

At lower positions, stalling was more frequent, and greater torque is required to move the stage. Table 7.5-3 shows that the maximum load capacity is 8.8 kg at 20,000 pps. To move the desired weight of 6.5 kg, the speed of the stepper motor had to be decreased to 40,000 pps.

Table 7.5-2 Load capacity during movement at **higher** lift stage positions (70 mm to 150 mm)

| | | Weight (kg ± 0.1 kg) | | | | | | |
|---|---|---|---|---|---|---|---|---|
| | | 4.7 | 5.5 | 6.0 | 7.2 | **8.8** | 9.9 | 11.1 |
| Motor speed (pps) | 100,000 | Pass | Pass | Pass | Pass | **Pass** | Pass | Stall |
| | 80,000 | Pass | Pass | Pass | Pass | **Pass** | Pass | Pass |
| | 60,000 | Pass | Pass | Pass | Pass | **Pass** | Pass | Pass |
| | 40,000 | Pass | Pass | Pass | Pass | **Pass** | Pass | Pass |
| | 20,000 | Pass | Pass | Pass | Pass | **Pass** | Pass | Pass |

Table 7.5-3 Load capacity during movement at **lower** lift stage positions (10 mm to 70 mm)

| | | Weight (kg ± 0.1 kg) | | | | | | |
|---|---|---|---|---|---|---|---|---|
| | | 4.7 | 5.5 | 6.0 | 7.2 | **8.8** | 9.9 | 11.1 |
| Motor speed (pps) | 100,000 | Pass | Pass | Stall | Fail | **Fail** | Fail | Fail |
| | 80,000 | Pass | Pass | Stall | Fail | **Fail** | Fail | Fail |
| | 60,000 | Pass | Pass | Stall | Stall | **Fail** | Fail | Fail |
| | 40,000 | Pass | Pass | Pass | Pass | **Stall** | Fail | Fail |
| | 20,000 | Pass | Pass | Pass | Pass | **Pass** | Stall | Fail |

### 7.5.3 Speed curve

Goal: Determine the speed of the lift stage at different positions.

Motivation: Scissor lift mechanisms do not have a constant movement velocity.

Methods: The lift stage was programmed to move in 10 mm increments using a motor velocity of 20,000 pps and an acceleration of 1000 pps². A LabView program was created to sequentially move the stage and report the time taken to reach each position.

Results: Table 7.5-4 shows the velocity of the lift stage from 0 to 160 mm. Velocities of up to 2.8 mm/s can be achieved. It takes 121 ± 0.2 seconds to for the lift stage to cover its operational range. Figure 7.5-2 shows the velocity curve for the lift stage. If the velocity of the stepper motor is kept constant, the lift stage will have a slower movement at higher positions (closer to the subject).

Table 7.5-4 Velocity of the lift stage along its travel range (motor speed of 20,000 pps)

| Absolute position (mm ± 2 mm) | Time (s ± 0.2 s) | Velocity (mm/s) |
|---|---|---|
| 0 | – | – |
| 10 | 3.6 | 2.8 ± 0.6 |
| 20 | 4.0 | 2.5 ± 0.5 |
| 30 | 4.2 | 2.4 ± 0.5 |
| 40 | 4.8 | 2.1 ± 0.4 |
| 50 | 5.2 | 1.9 ± 0.4 |
| 60 | 5.6 | 1.8 ± 0.4 |
| 70 | 6.2 | 1.6 ± 0.3 |
| 80 | 6.8 | 1.5 ± 0.3 |
| 90 | 7.2 | 1.4 ± 0.3 |
| 100 | 8.0 | 1.3 ± 0.3 |
| 110 | 8.6 | 1.2 ± 0.2 |
| 120 | 9.4 | 1.1 ± 0.2 |
| 130 | 10.6 | 0.9 ± 0.2 |
| 140 | 11.0 | 0.9 ± 0.2 |
| 150 | 11.8 | 0.8 ± 0.2 |
| 160 | 14.0 | 0.7 ± 0.1 |
| **Total time** | 121 | |

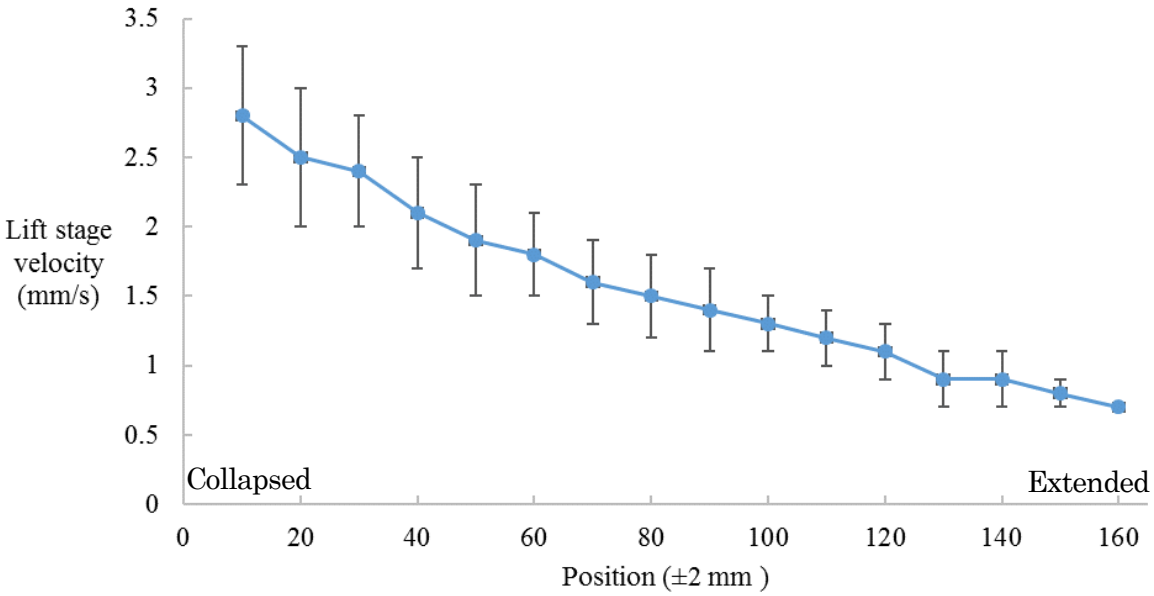


Figure 7.5-2 Velocity curve for the lift stage at a constant motor speed of 20,000 pps. Error bars indicate one standard deviation.

## 7.6 Technical drawings

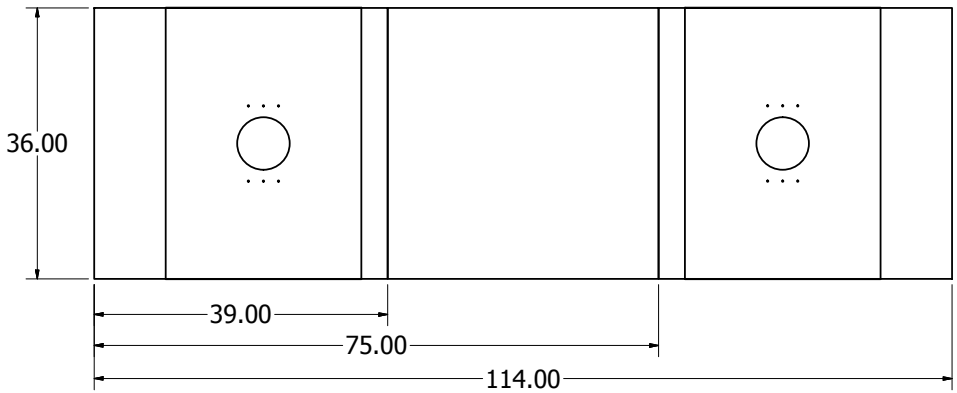


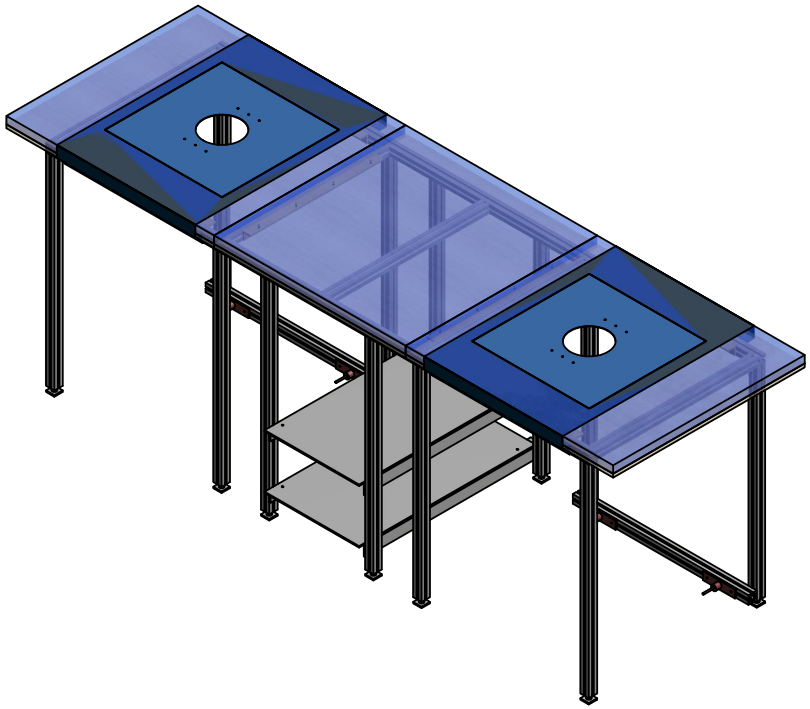

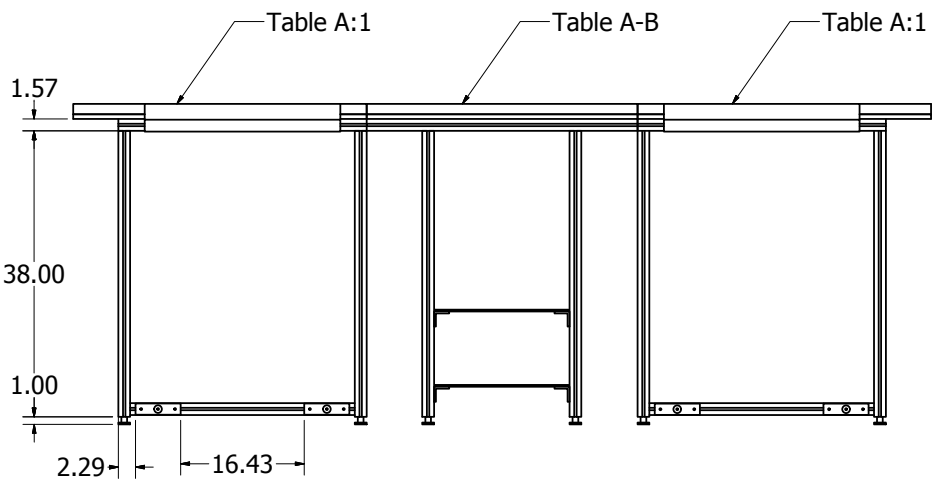


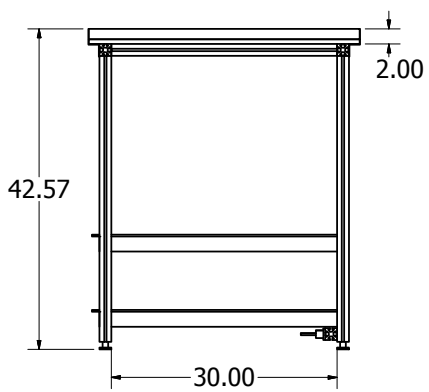


| | | | |
|---|---|---|---|
| DRAWN Mario Solis | 2014-04-21 | Cover | |
| CHECKED | | TITLE | |
| QA | | Breast Microwave Radar Bed | |
| MFG | | | |
| APPROVED | | | |
| UNLESS OTHERWISE SPECIFIED DIMENSIONS ARE IN INCHES ANGLES ±X.X° 2 PL ±X.XX 3 PL ±X.XXX | | SIZE A2 / DWG NO BMRS BedRevB / REV B | |
| | | SCALE | SHEET 1 OF 10 |

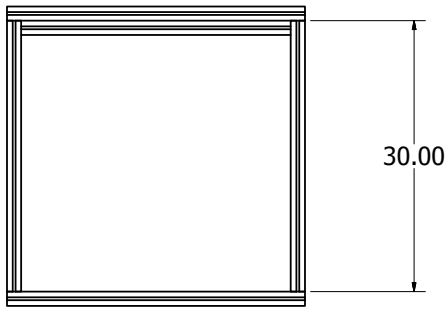


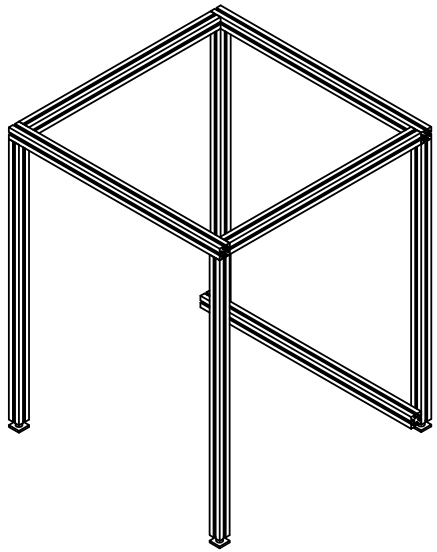

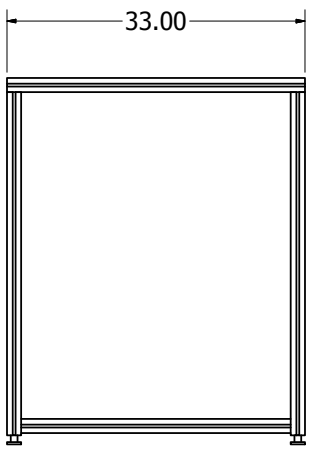


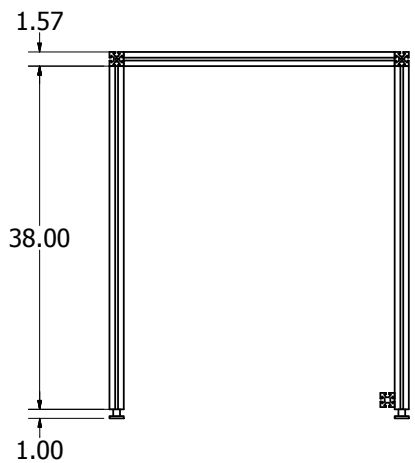


| | | |
|---|---|---|
| DRAWN Mario Solis | 2014-04-21 | Table A:1 |
| CHECKED | | |
| QA | | TITLE: Breast Microwave Radar Bed |
| MFG | | |
| APPROVED | | |
| UNLESS OTHERWISE SPECIFIED DIMENSIONS ARE IN INCHES ANGLES ±X.X° 2 PL ±X.XX 3 PL ±X.XXX | | SIZE A2 / DWG NO BMRS BedRevB / REV B |
| | | SCALE / SHEET 2 OF 10 |

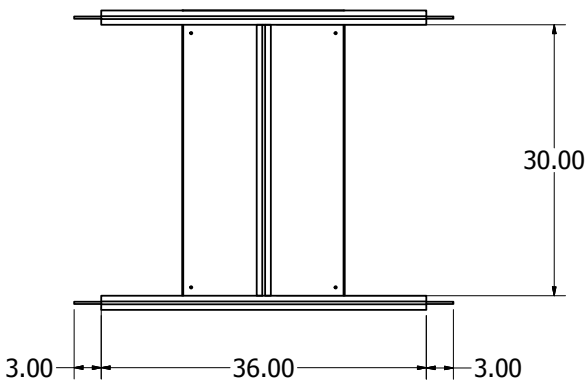


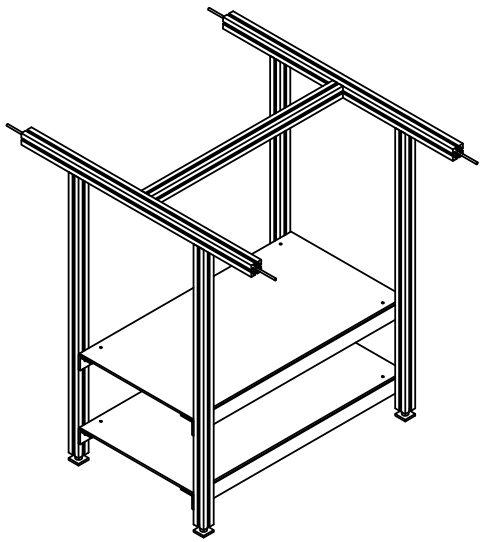

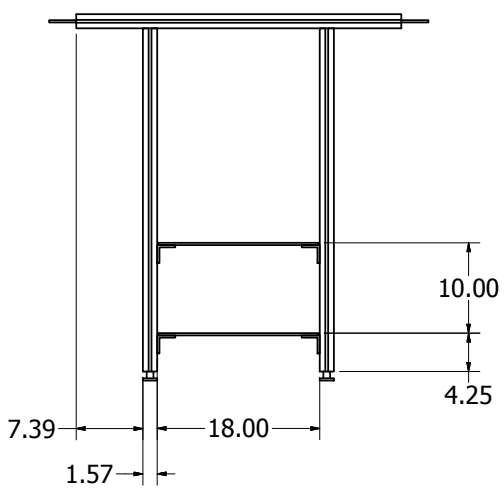


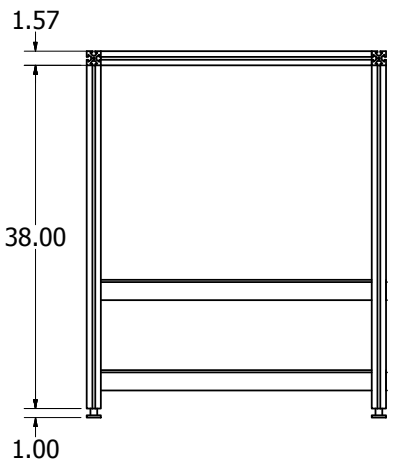


| | | |
|---|---|---|
| DRAWN Mario Solis | 2014-04-21 | Table A-B |
| CHECKED | | |
| QA | | TITLE: Breast Microwave Radar Bed |
| MFG | | |
| APPROVED | | |
| UNLESS OTHERWISE SPECIFIED DIMENSIONS ARE IN INCHES ANGLES ±X.X° 2 PL ±X.XX 3 PL ±X.XXX | SIZE A2 | DWG NO BMRS BedRevB — REV B |
| | SCALE | SHEET 3 OF 10 |

item profile 8
40x40, natural

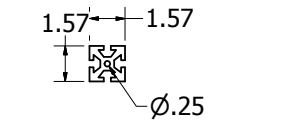


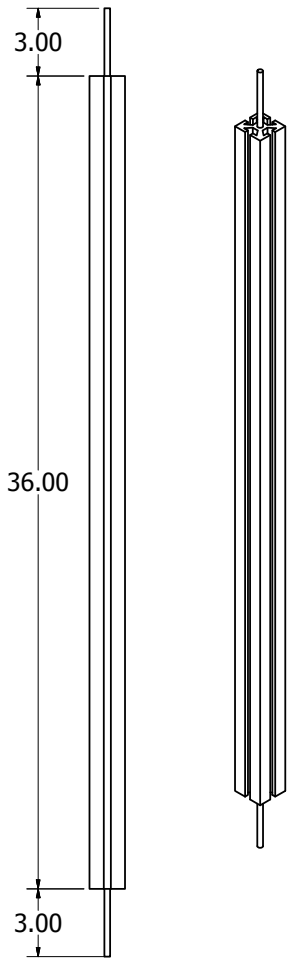


2 pcs required for Table A-B

item profile 8
40x40, natural

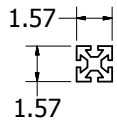


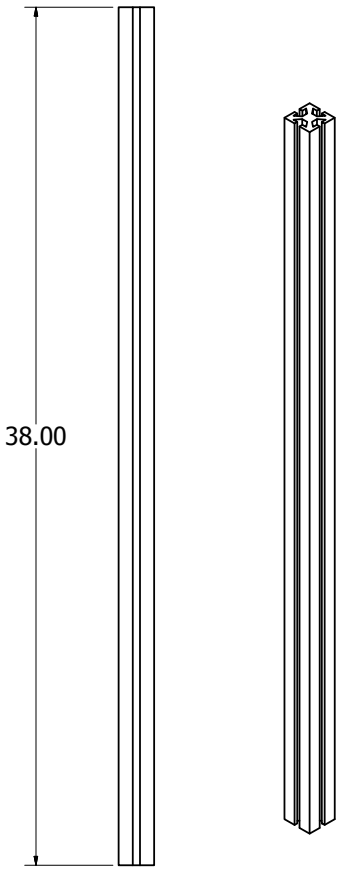


4 pcs required for Table A
4 pcs required for Table A-B

item profile 8
40x40, natural

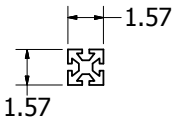


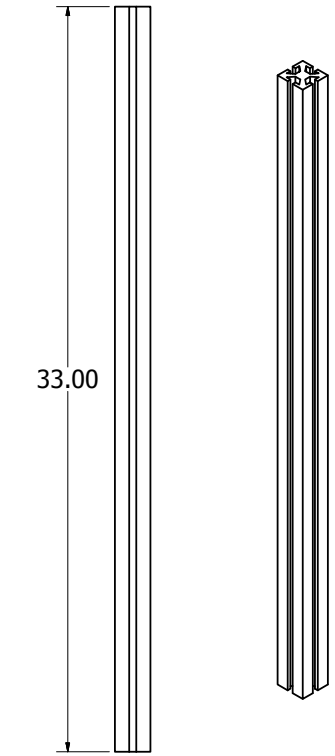


3 pcs required for Table A

item profile 8
40x40, natural

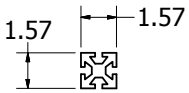


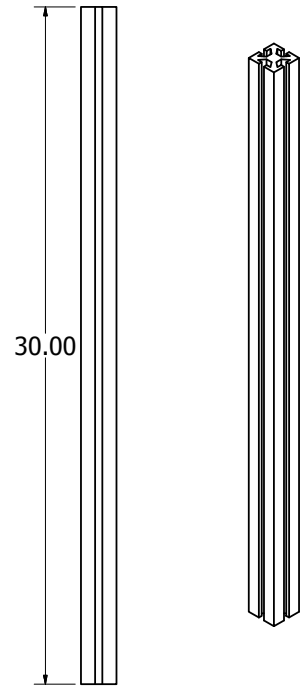


2 pcs required for Table A
1 pc required for Table A

| | | | |
|---|---|---|---|
| DRAWN Mario Solis | 2014-04-21 | Item Profiles | |
| CHECKED | | TITLE | |
| QA | | Breast Microwave Radar Bed | |
| MFG | | | |
| APPROVED | | | |
| UNLESS OTHERWISE SPECIFIED DIMENSIONS ARE IN INCHES ANGLES ±X.X° 2 PL ±X.XX 3 PL ±X.XXX | | SIZE A2 / DWG NO BMRS BedRevB / REV B | |
| | | SCALE / SHEET 4 OF 10 | |

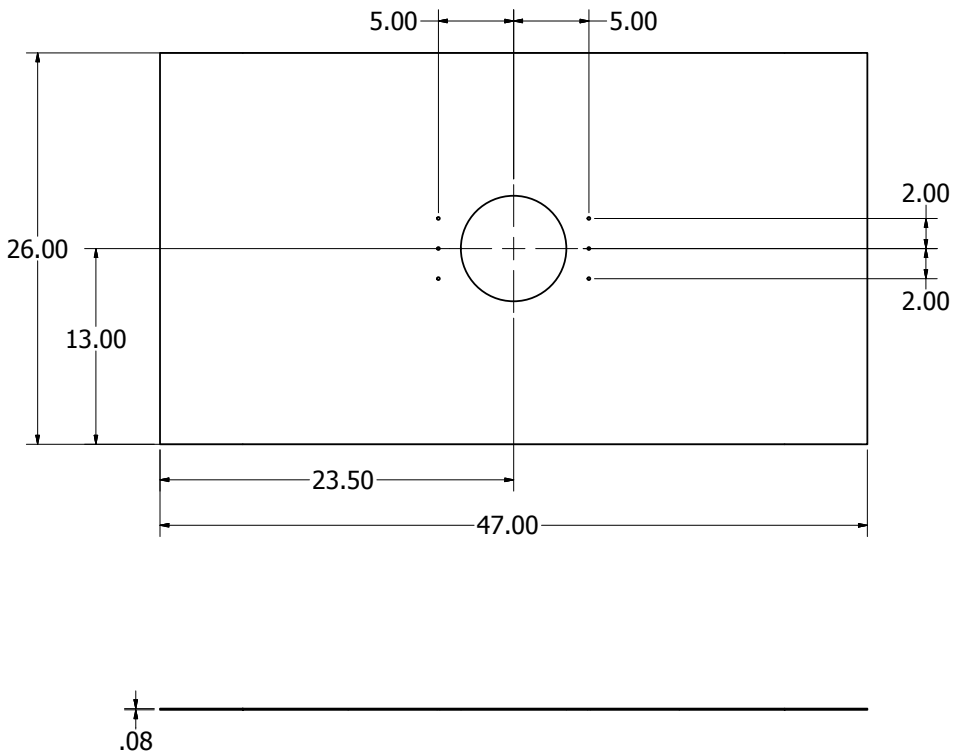


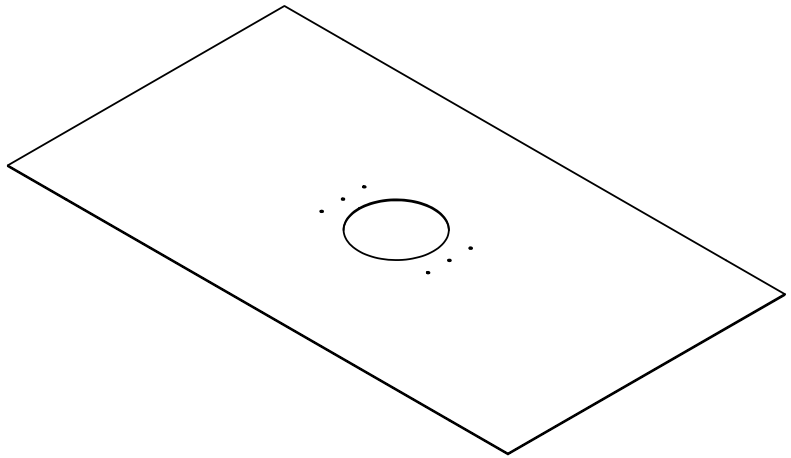

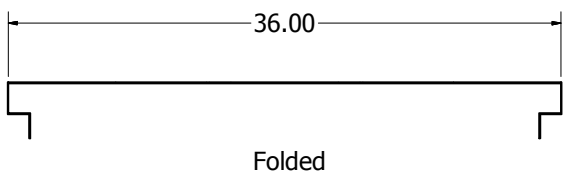


Folded

| | | |
|---|---|---|
| DRAWN Mario Solis | 2014-04-21 | Bed Canvas Ext |
| CHECKED | | TITLE: Breast Microwave Radar Bed |
| QA | | |
| MFG | | |
| APPROVED | | |

UNLESS OTHERWISE SPECIFIED DIMENSIONS ARE IN INCHES
ANGLES ±X.X°
2 PL ±X.XX 3 PL ±X.XXX

| SIZE | DWG NO | REV |
|---|---|---|
| A2 | BMRS BedRevB | B |

SCALE | SHEET 5 OF 10

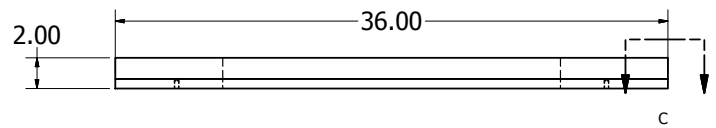


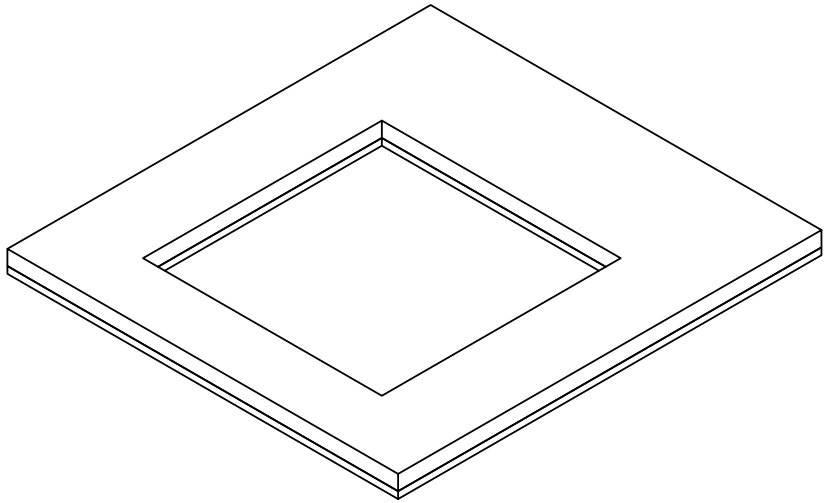

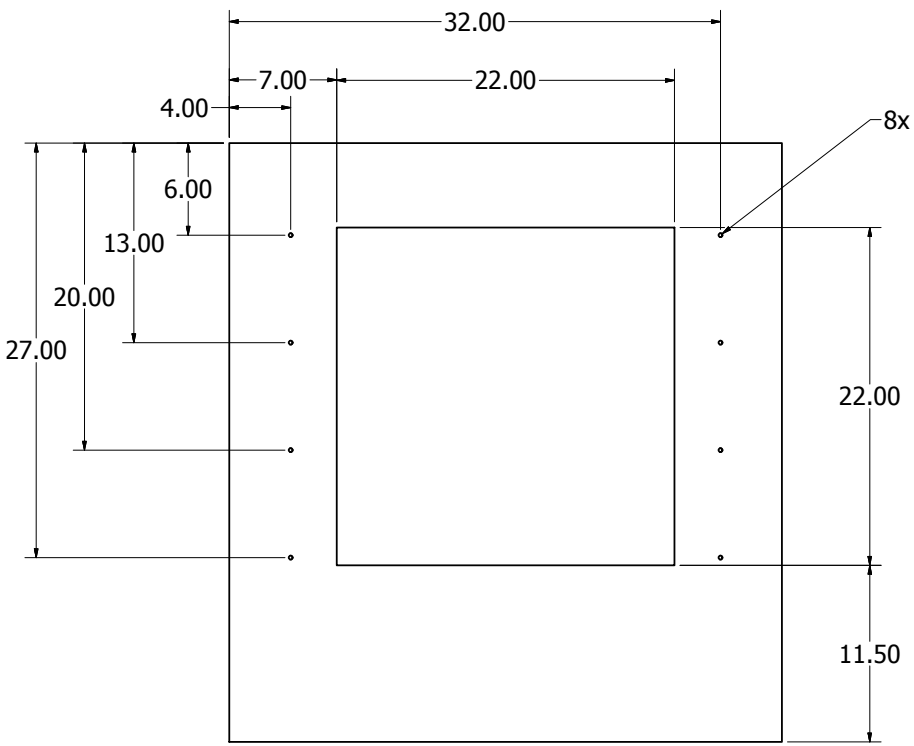


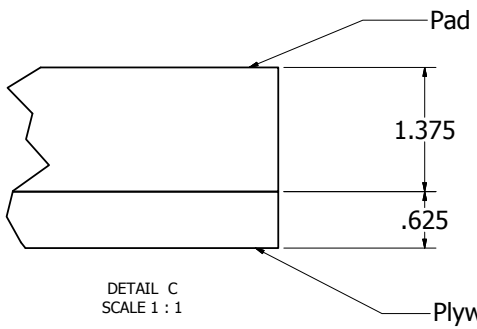


DETAIL C
SCALE 1 : 1

1 pcs required for Table A

| | | |
|---|---|---|
| DRAWN Mario Solis | 2014-04-21 | Plywood Lid A |
| CHECKED | | TITLE: Breast Microwave Radar Bed |
| QA | | |
| MFG | | |
| APPROVED | | |
| UNLESS OTHERWISE SPECIFIED DIMENSIONS ARE IN INCHES ANGLES ±X.X° 2 PL ±X.XX 3 PL ±X.XXX | | SIZE A2 / DWG NO BMRS BedRevB / REV B |
| | | SCALE / SHEET 6 OF 10 |

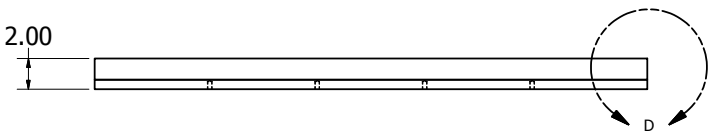


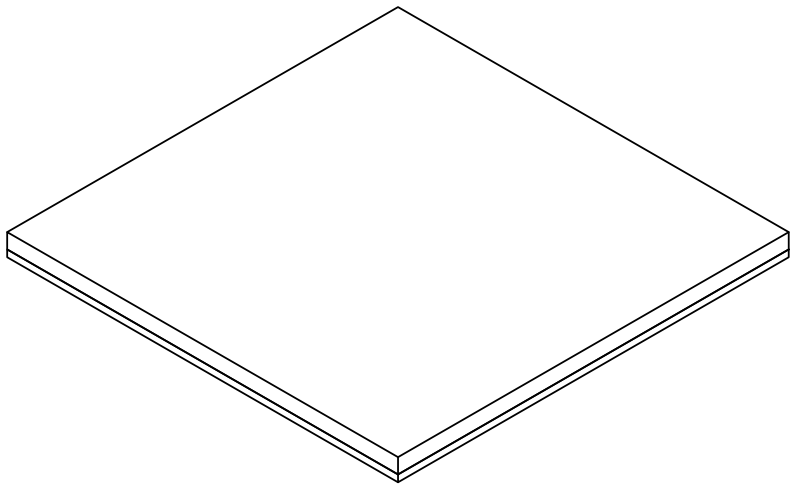

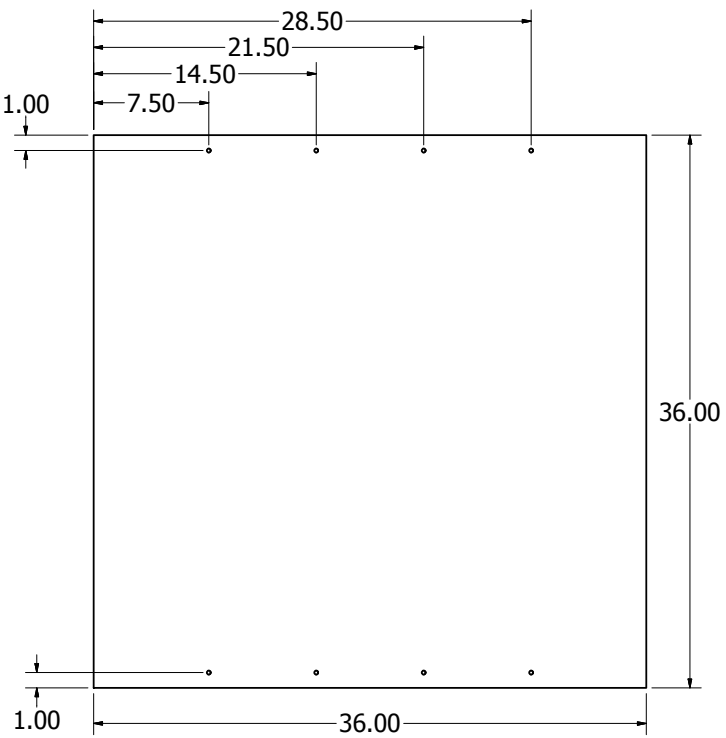


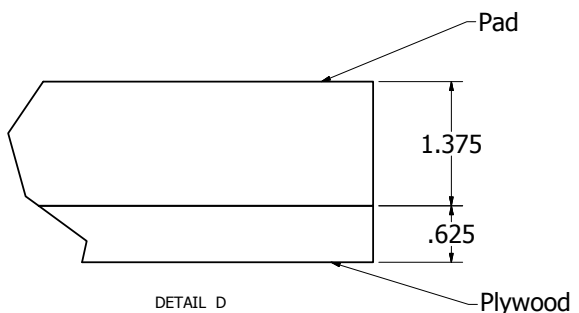


DETAIL D
SCALE 1 : 1

1 pc required for Table A-B

| | | |
|---|---|---|
| DRAWN Mario Solis | 2014-04-21 | Plywood Lid Middle Section |
| CHECKED | | TITLE: Breast Microwave Radar Bed |
| QA | | |
| MFG | | |
| APPROVED | | |

UNLESS OTHERWISE SPECIFIED DIMENSIONS ARE IN INCHES
ANGLES ±X.X°
2 PL ±X.XX 3 PL ±X.XXX

| SIZE | DWG NO | REV |
|---|---|---|
| A2 | BMRS BedRevB | B |
| SCALE | SHEET 7 OF 10 | |

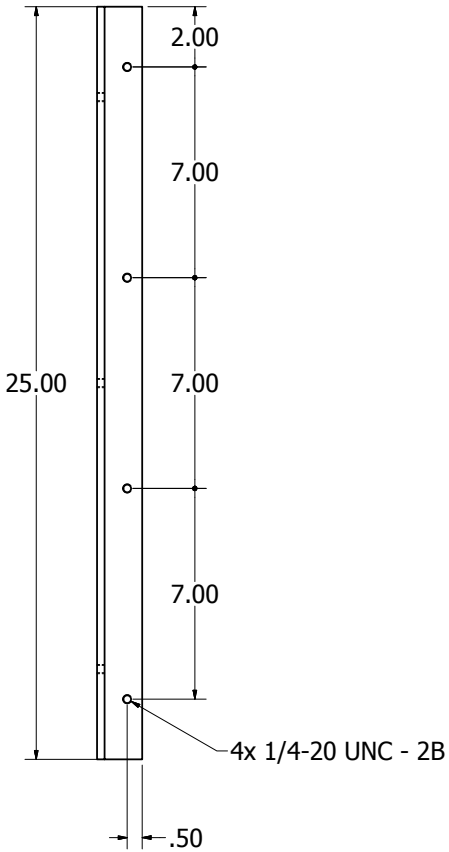


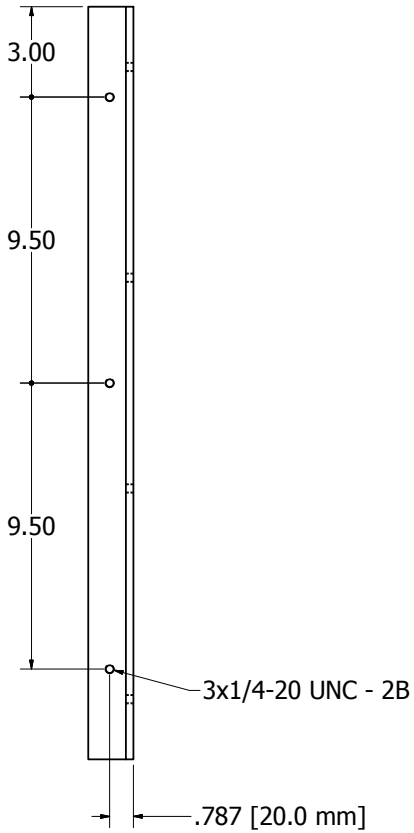


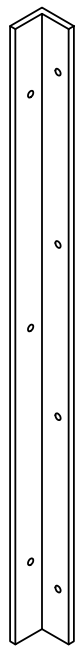

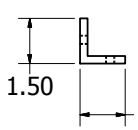


2 pcs required for Table A
2 pcs required for Table A-B

| | | |
|---|---|---|
| DRAWN Mario Solis | 2014-04-21 | Angle for Plywood Lids |
| CHECKED | | TITLE: Breast Microwave Radar Bed |
| QA | | |
| MFG | | |
| APPROVED | | |

UNLESS OTHERWISE SPECIFIED DIMENSIONS ARE IN INCHES ANGLES ±X.X° 2 PL ±X.XX 3 PL ±X.XXX

| SIZE | DWG NO | REV |
|---|---|---|
| A2 | BMRS BedRevB | B |
| SCALE | SHEET 8 OF 10 | |

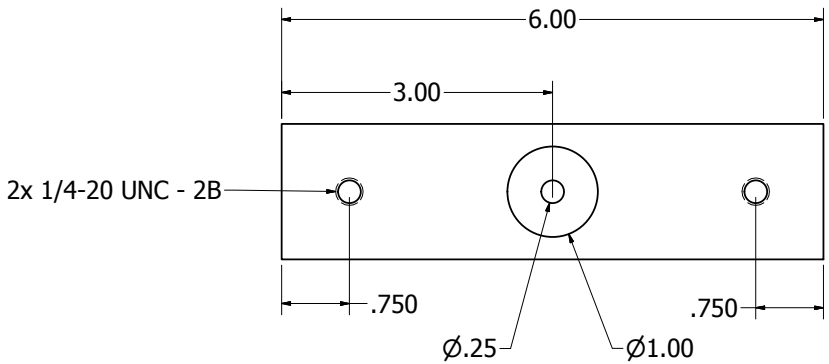


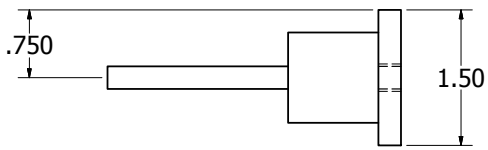


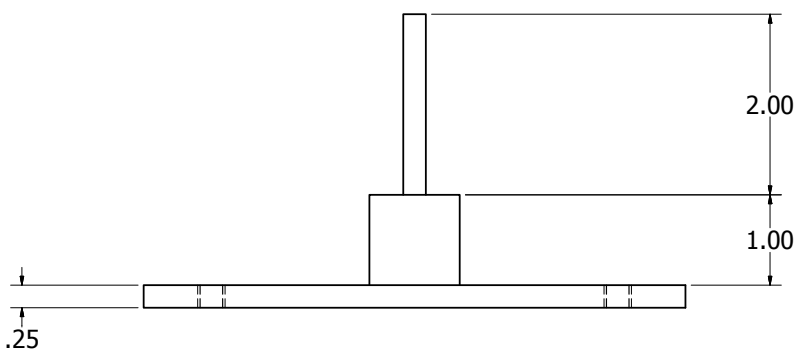


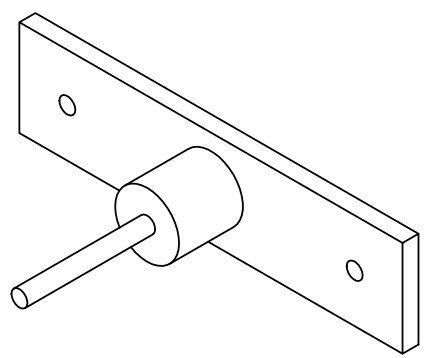

2 pcs required for Table A

| | | |
|---|---|---|
| DRAWN Mario Solis | 2014-04-21 | Docking Male |
| CHECKED | | TITLE |
| QA | | Breast Microwave Radar Bed |
| MFG | | |
| APPROVED | | |
| UNLESS OTHERWISE SPECIFIED DIMENSIONS ARE IN INCHES ANGLES ±X.X° 2 PL ±X.XX 3 PL ±X.XXX | | SIZE A2 / DWG NO BMRS BedRevB / REV B |
| | | SCALE / SHEET 9 OF 10 |

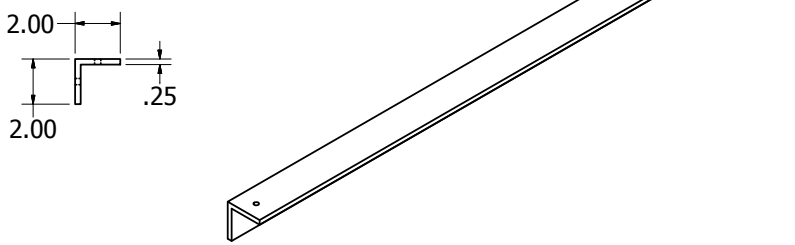




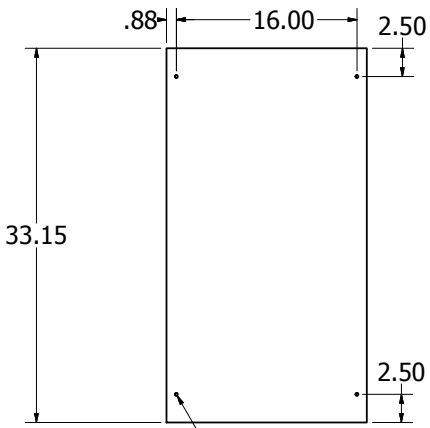


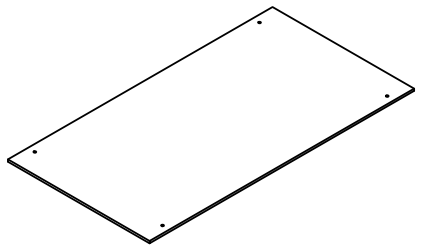

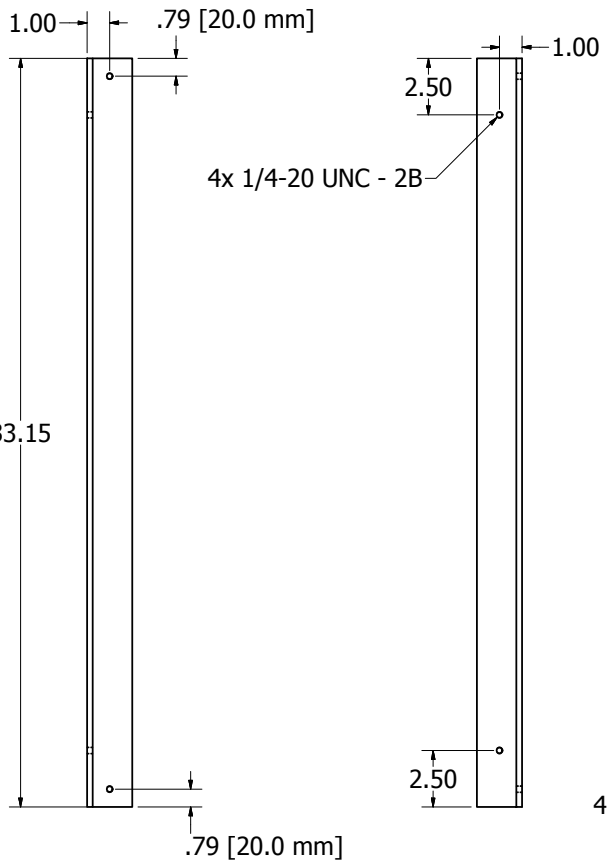


4 pcs required

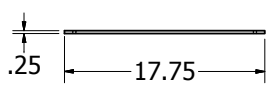


2 pcs required

| | | |
|---|---|---|
| DRAWN Mario Solis | 2014-04-21 | Shelves Table A-B |
| CHECKED | | TITLE: Breast Microwave Radar Bed |
| QA | | |
| MFG | | |
| APPROVED | | |

UNLESS OTHERWISE SPECIFIED DIMENSIONS ARE IN INCHES
ANGLES ±X.X°
2 PL ±X.XX 3 PL ±X.XXX

| SIZE | DWG NO | REV |
|---|---|---|
| A2 | BMRS BedRevB | B |

SCALE | SHEET 10 OF 10

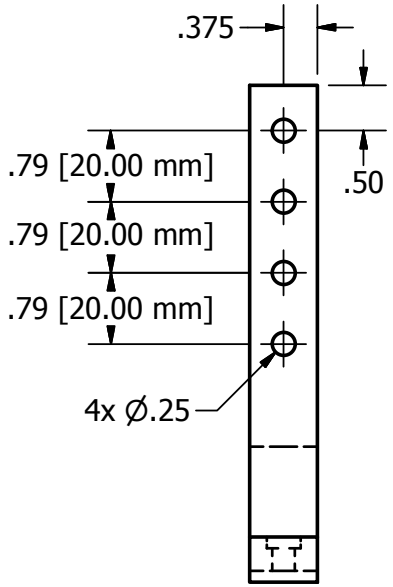


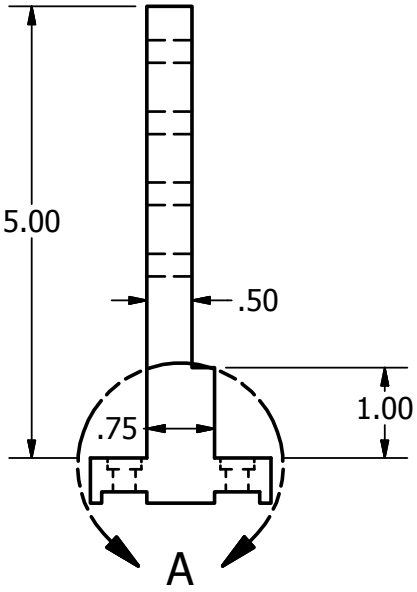


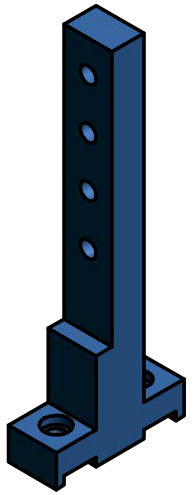

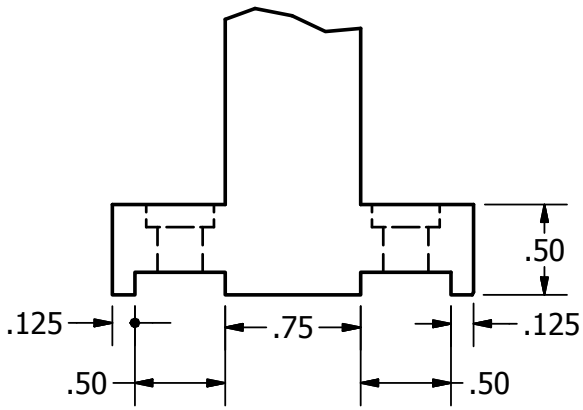


DETAIL A
SCALE 1 : 1

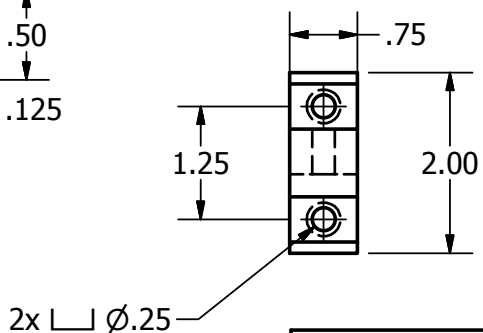


| | | | |
|---|---|---|---|
| DRAWN Mario Solis | 2015-05-07 | TITLE Simple Antenna Holder | |
| CHECKED | | | |
| TOLERANCES 2 PL +/- X.XX 3 PL +/- X.XXX | | | |
| UNITS INCHES UNLESS OTHERWISE SPECIFIED | | | |
| MATERIAL HDPE | | SIZE A4 / DWG NO AntennaHolderSimple-1 / REV 1 | |
| | | SCALE 1:2 | SHEET 1 OF 1 |

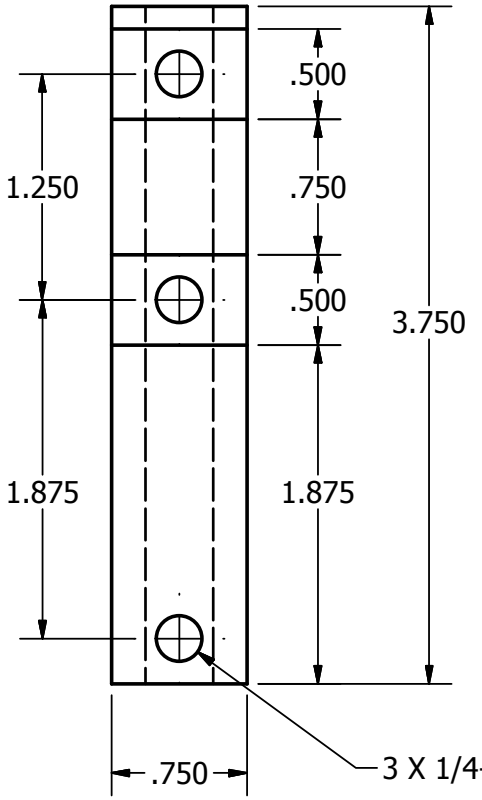


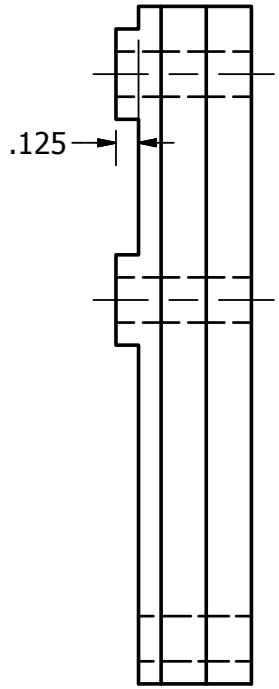


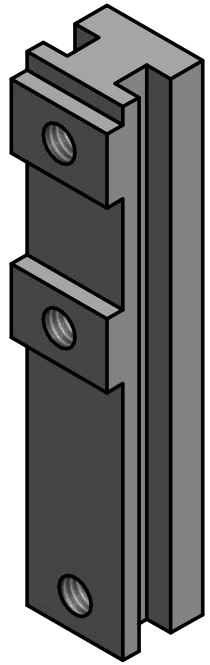

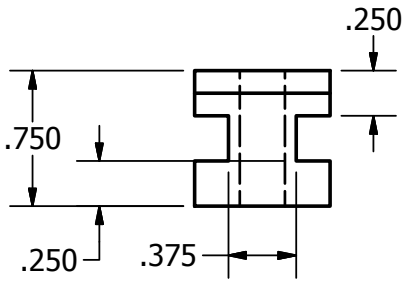


| | | |
|---|---|---|
| DRAWN Calene Treichel | 06/05/2015 | |
| CHECKED | | |
| QA | | |
| MFG | | |
| APPROVED | | |
| TOLERANCES 2 PL +/- X.XX 3 PL +/- X.XXX | | TITLE Solid Edge |
| UNITS INCHES UNLESS OTHERWISE SPECIFIED | | SIZE A4 / DWG NO BaseHolderEdit2 / REV 1 |
| MATERIAL HDPE | | SCALE 1:1 / SHEET 1 OF 1 |

| REVISION HISTORY | | | |
|---|---|---|---|
| REV | DESCRIPTION | DATE | APPROVED |
| | | | |

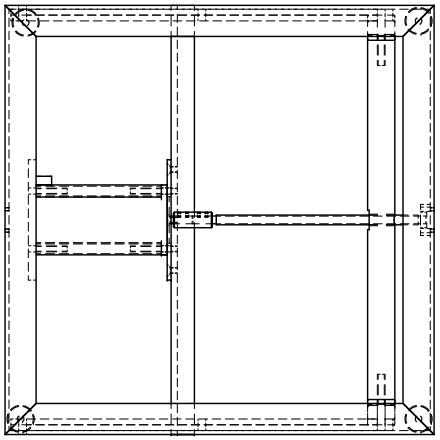

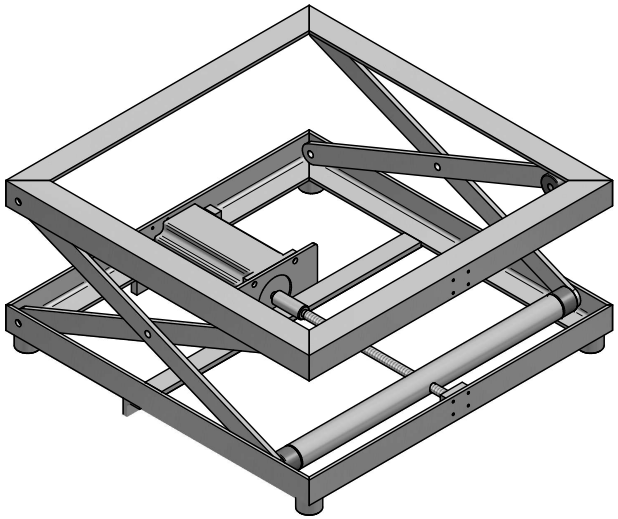

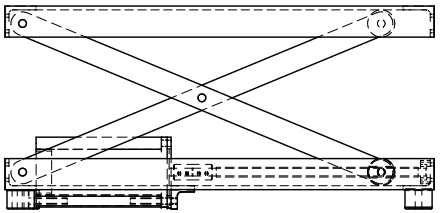

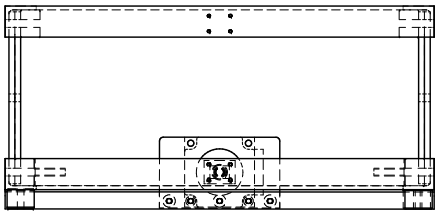

| | NAME | DATE |
|---|---|---|
| DRAWN | aegtbert | 01/30/14 |
| CHECKED | | |
| ENG APPR. | | |
| MGR APPR. | | |

UNLESS OTHERWISE SPECIFIED
DIMENSIONS ARE IN INCHES
ANGLES ±XX°
2 PL ±XXX 3 PL ±XXXX

Solid Edge

TITLE

| SIZE | DWG NO | REV |
|---|---|---|
| D | | |

FILE NAME: scissor lift.dft

SCALE: | WEIGHT: | SHEET 1 OF 8

| REVISION HISTORY | | | |
|---|---|---|---|
| REV | DESCRIPTION | DATE | APPROVED |
| | | | |

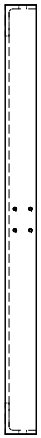

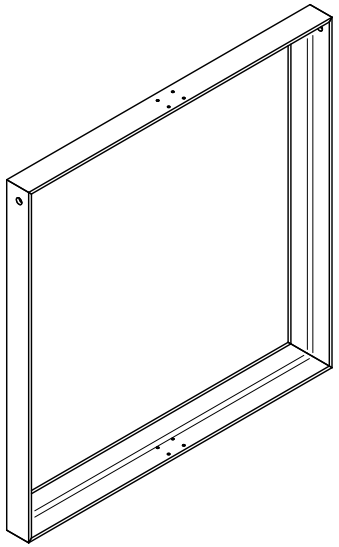

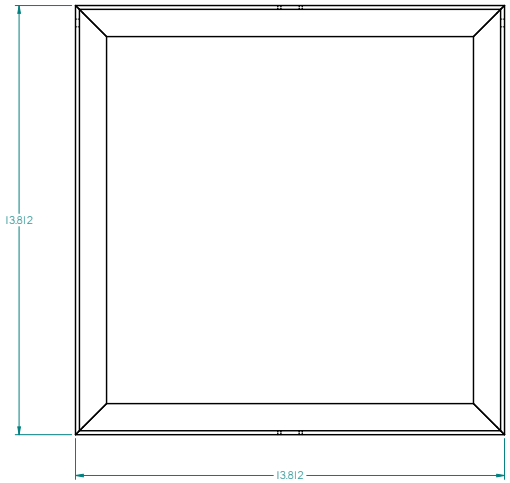


| | NAME | DATE |
|---|---|---|
| DRAWN | aegtbert | 01/30/14 |
| CHECKED | | |
| ENG APPR. | | |
| MGR APPR. | | |

UNLESS OTHERWISE SPECIFIED
DIMENSIONS ARE IN INCHES
ANGLES ±XX°
2 PL ±XXX 3 PL ±XXXX

Solid Edge

TITLE

| SIZE | DWG NO | REV |
|---|---|---|
| D | | |

FILE NAME: scissor lift.dft

| SCALE: | WEIGHT: | SHEET 2 OF 8 |
|---|---|---|

| REVISION HISTORY | | | |
|---|---|---|---|
| REV | DESCRIPTION | DATE | APPROVED |

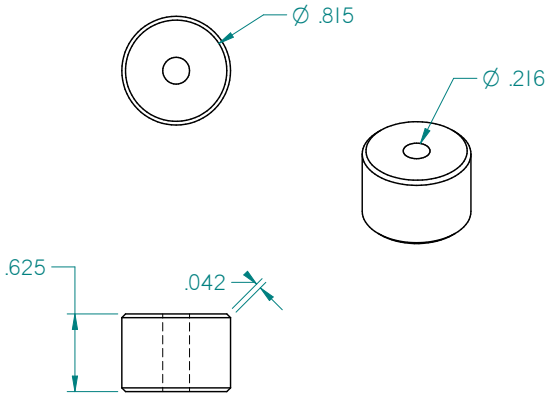


4 pc required

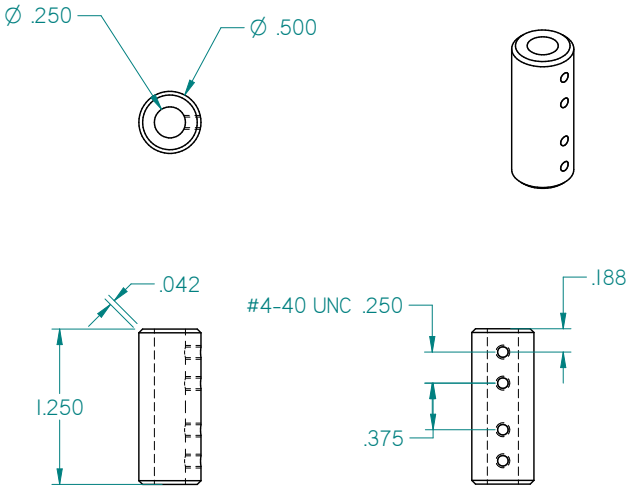


1 pc required

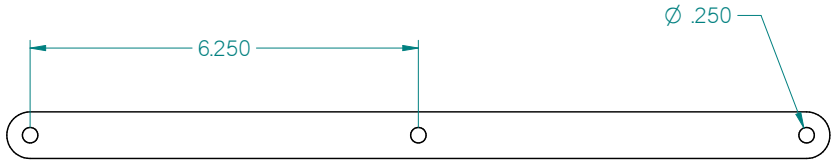


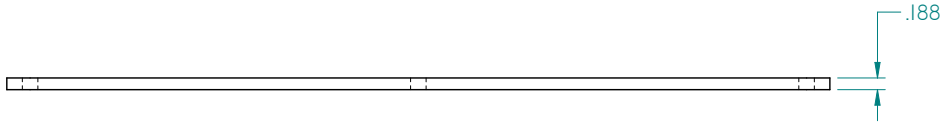


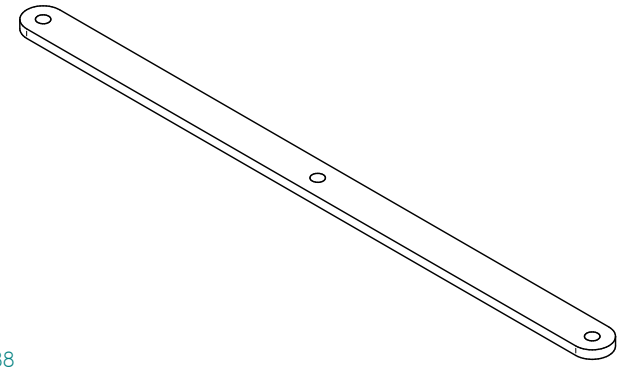

4 pcs required

| | NAME | DATE |
|---|---|---|
| DRAWN | aegtbert | 01/30/14 |
| CHECKED | | |
| ENG APPR | | |
| MGR APPR | | |

UNLESS OTHERWISE SPECIFIED
DIMENSIONS ARE IN INCHES
ANGLES ±XX°
2 PL ±XXX 3 PL ±XXXX

Solid Edge

TITLE

SIZE D | DWG NO | REV

FILE NAME: scissor lift.dft

SCALE: | WEIGHT: | SHEET 3 OF 8

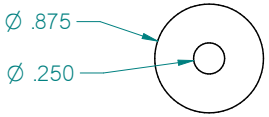


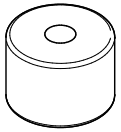

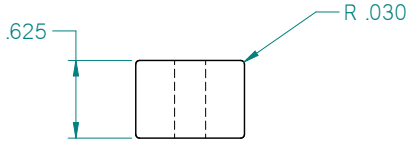


4 pc required
purchasedd item

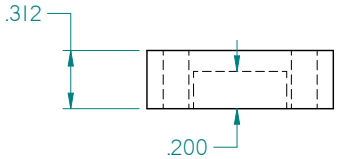


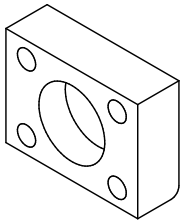

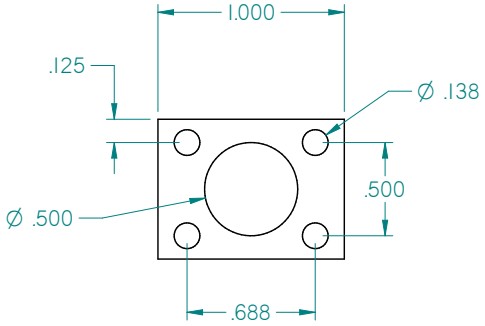


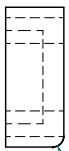


1 pc required

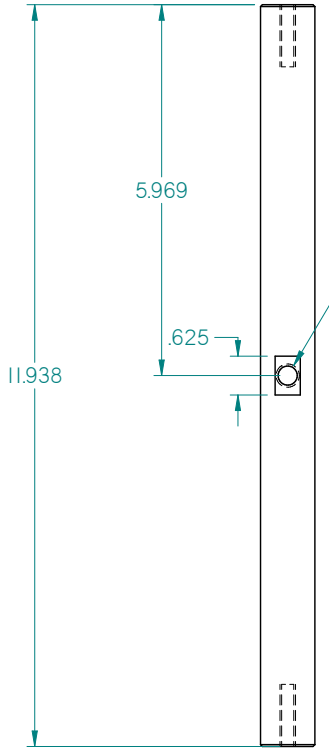


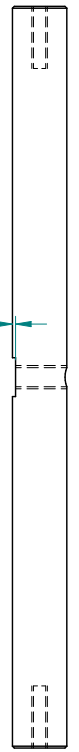


1 pc required

REVISION HISTORY

| REV | DESCRIPTION | DATE | APPROVED |
|---|---|---|---|

| | NAME | DATE |
|---|---|---|
| DRAWN | aegtbert | 01/30/14 |
| CHECKED | | |
| ENG APPR. | | |
| MGR APPR. | | |

UNLESS OTHERWISE SPECIFIED
DIMENSIONS ARE IN INCHES
ANGLES ±XX°
2 PL ±XXX 3 PL ±XXXX

Solid Edge

TITLE

SIZE D | DWG NO | REV

FILE NAME: scissor lift.dft

SCALE: | WEIGHT: | SHEET 4 OF 8

| REVISION HISTORY | | | |
|---|---|---|---|
| REV | DESCRIPTION | DATE | APPROVED |

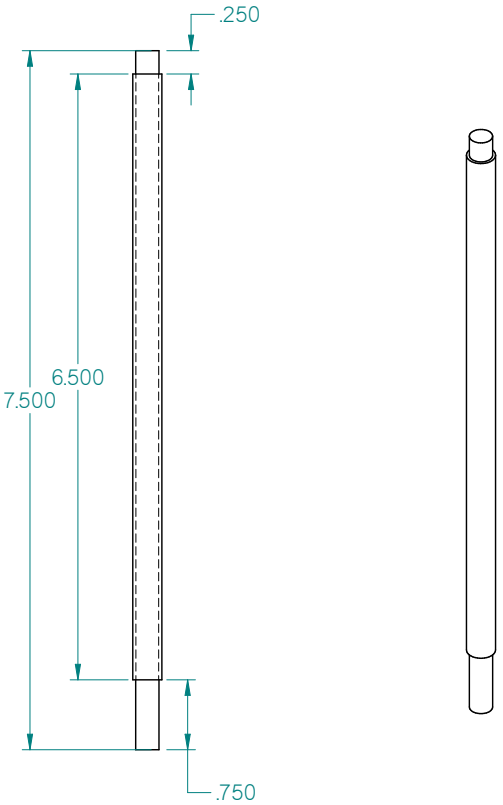


DETAIL B

1 pc required

material $\frac{5}{16}$ ms

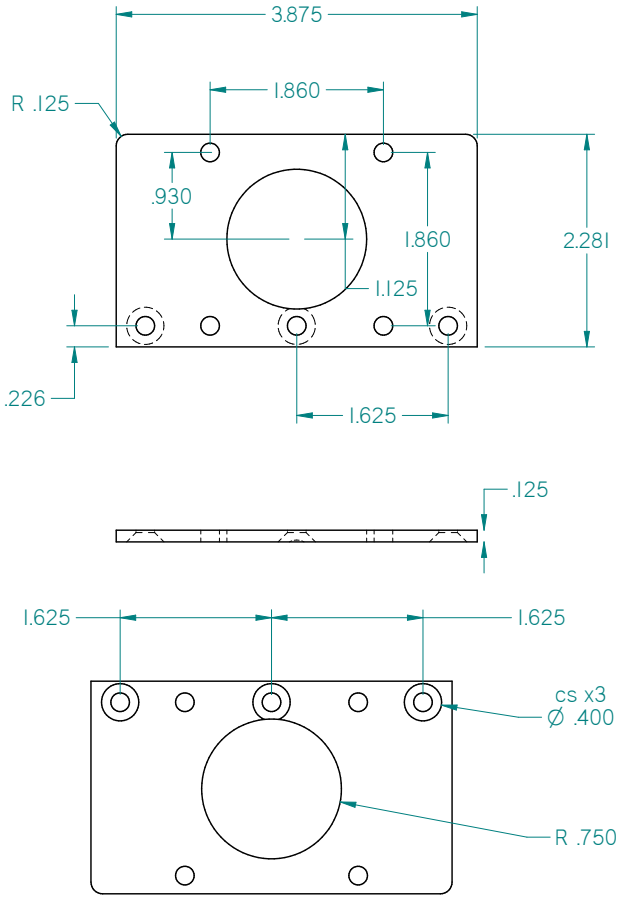


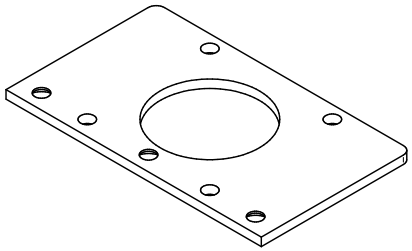

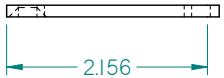


1 pc required

| | NAME | DATE |
|---|---|---|
| DRAWN | aegtbert | 01/30/14 |
| CHECKED | | |
| ENG APPR | | |
| MGR APPR | | |

UNLESS OTHERWISE SPECIFIED
DIMENSIONS ARE IN INCHES
ANGLES ±XX°
2 PL ±XXX 3 PL ±XXXX

Solid Edge

TITLE

SIZE D | DWG NO | REV

FILE NAME: scissor lift.dft

SCALE: | WEIGHT: | SHEET 5 OF 8

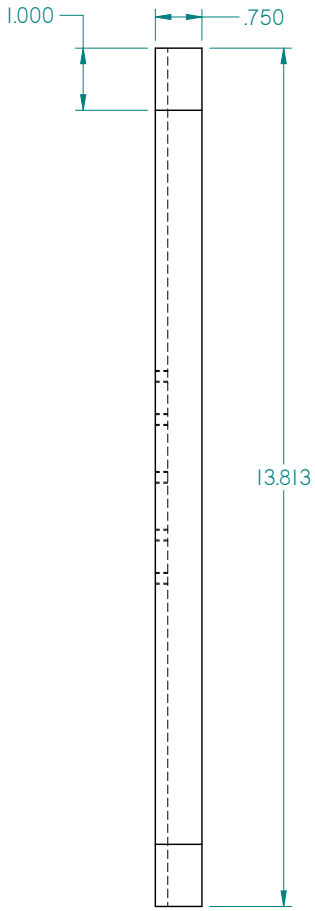


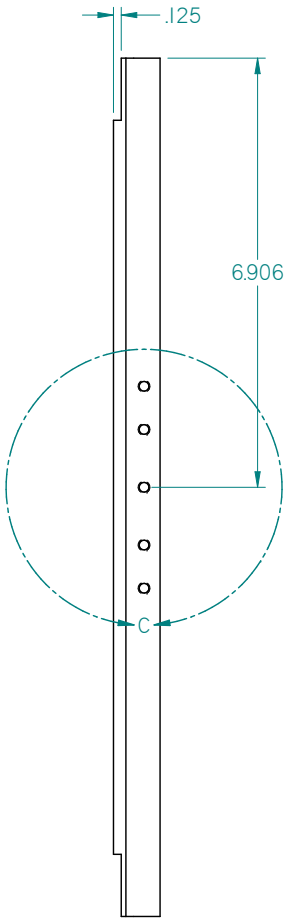


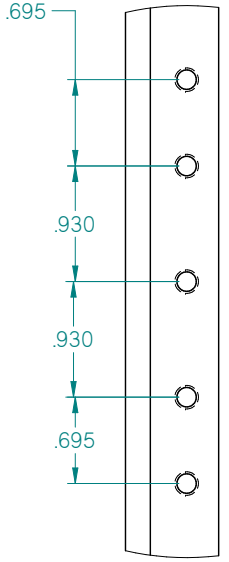


DETAIL C

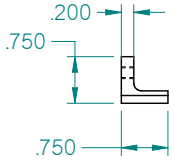


1 pc required

| REVISION HISTORY | | | |
|---|---|---|---|
| REV | DESCRIPTION | DATE | APPROVED |

| | NAME | DATE |
|---|---|---|
| DRAWN | aegtbert | 01/30/14 |
| CHECKED | | |
| ENG APPR | | |
| MGR APPR | | |

UNLESS OTHERWISE SPECIFIED
DIMENSIONS ARE IN INCHES
ANGLES ±XX°
2 PL ±XXX 3 PL ±XXXX

Solid Edge

TITLE

SIZE D | DWG NO | REV

FILE NAME: scissor lift.dft

SCALE: | WEIGHT: | SHEET 6 OF 8

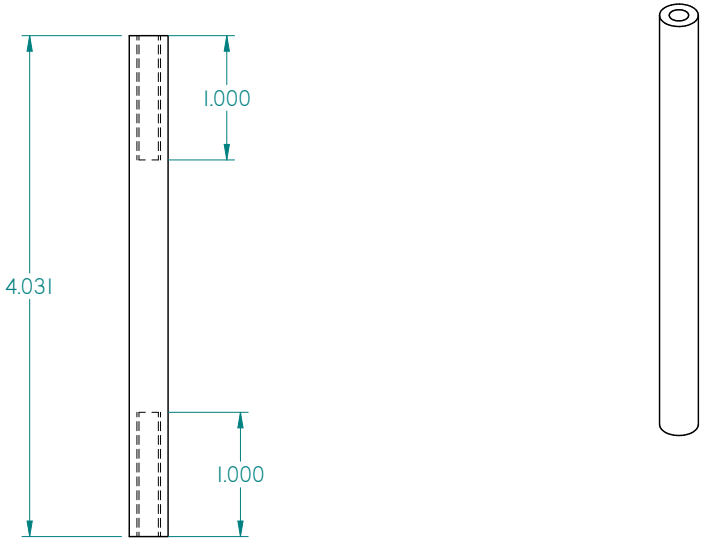


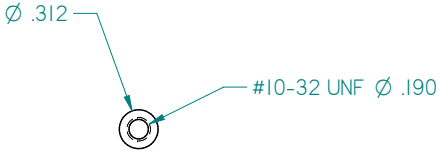


2 pc required

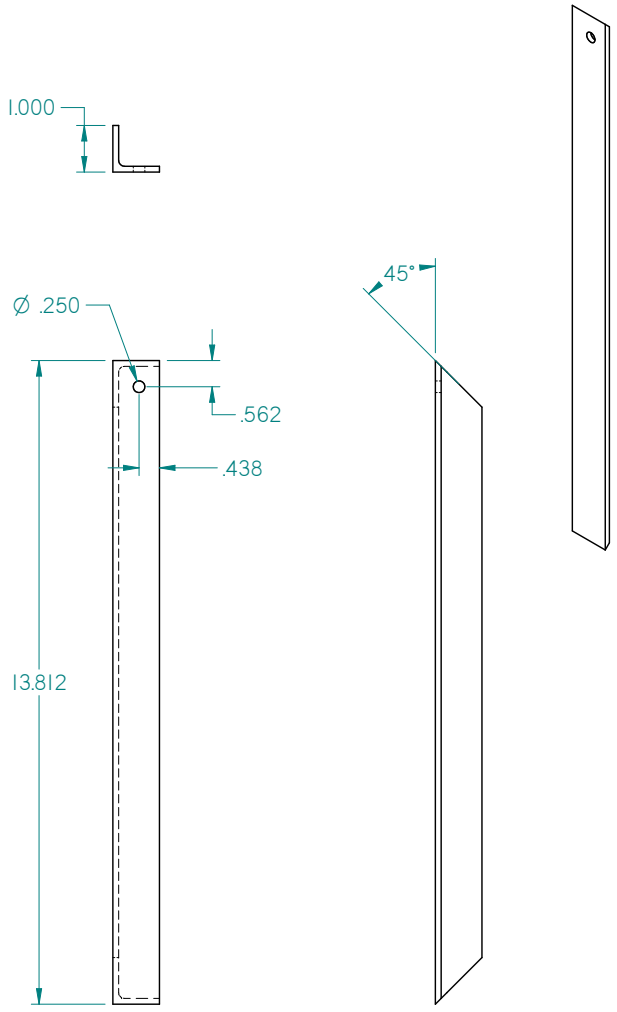


2 pc required

REVISION HISTORY

| REV | DESCRIPTION | DATE | APPROVED |
|---|---|---|---|

| | NAME | DATE |
|---|---|---|
| DRAWN | aegtbert | 01/30/14 |
| CHECKED | | |
| ENG APPR | | |
| MGR APPR | | |

UNLESS OTHERWISE SPECIFIED
DIMENSIONS ARE IN INCHES
ANGLES ±XX°
2 PL ±XXX 3 PL ±XXXX

Solid Edge

TITLE

SIZE D | DWG NO | REV

FILE NAME: scissor lift.dft

SCALE: | WEIGHT: | SHEET 7 OF 8

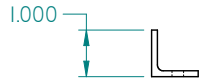


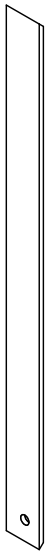

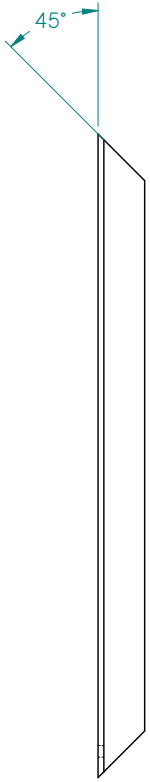


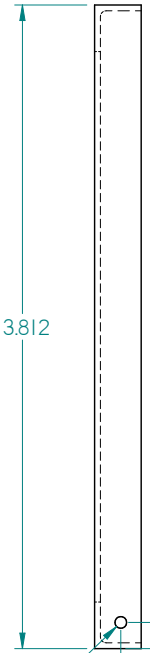


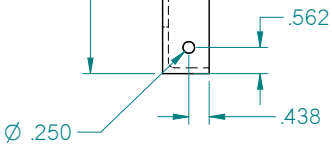


2pcs requied

| REVISION HISTORY | | | |
|---|---|---|---|
| REV | DESCRIPTION | DATE | APPROVED |

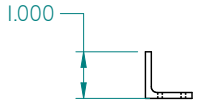


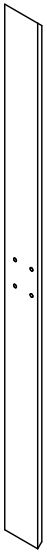

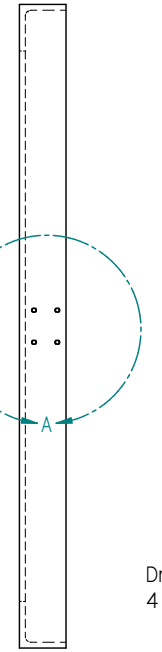


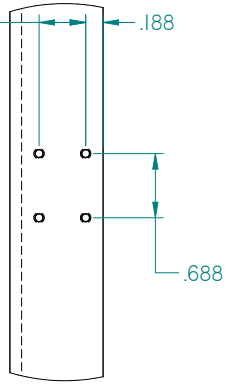


DETAIL A

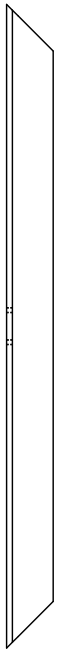

Drill and tap 1 pc only
4 pcs required

| | NAME | DATE |
|---|---|---|
| DRAWN | aegtbert | 01/30/14 |
| CHECKED | | |
| ENG APPR. | | |
| MGR APPR. | | |

UNLESS OTHERWISE SPECIFIED
DIMENSIONS ARE IN INCHES
ANGLES ±XX°
2 PL ±XXX 3 PL ±XXXX

Solid Edge

TITLE

SIZE D | DWG NO | REV

FILE NAME: scissor lift.dft

SCALE: | WEIGHT: | SHEET 8 OF 8

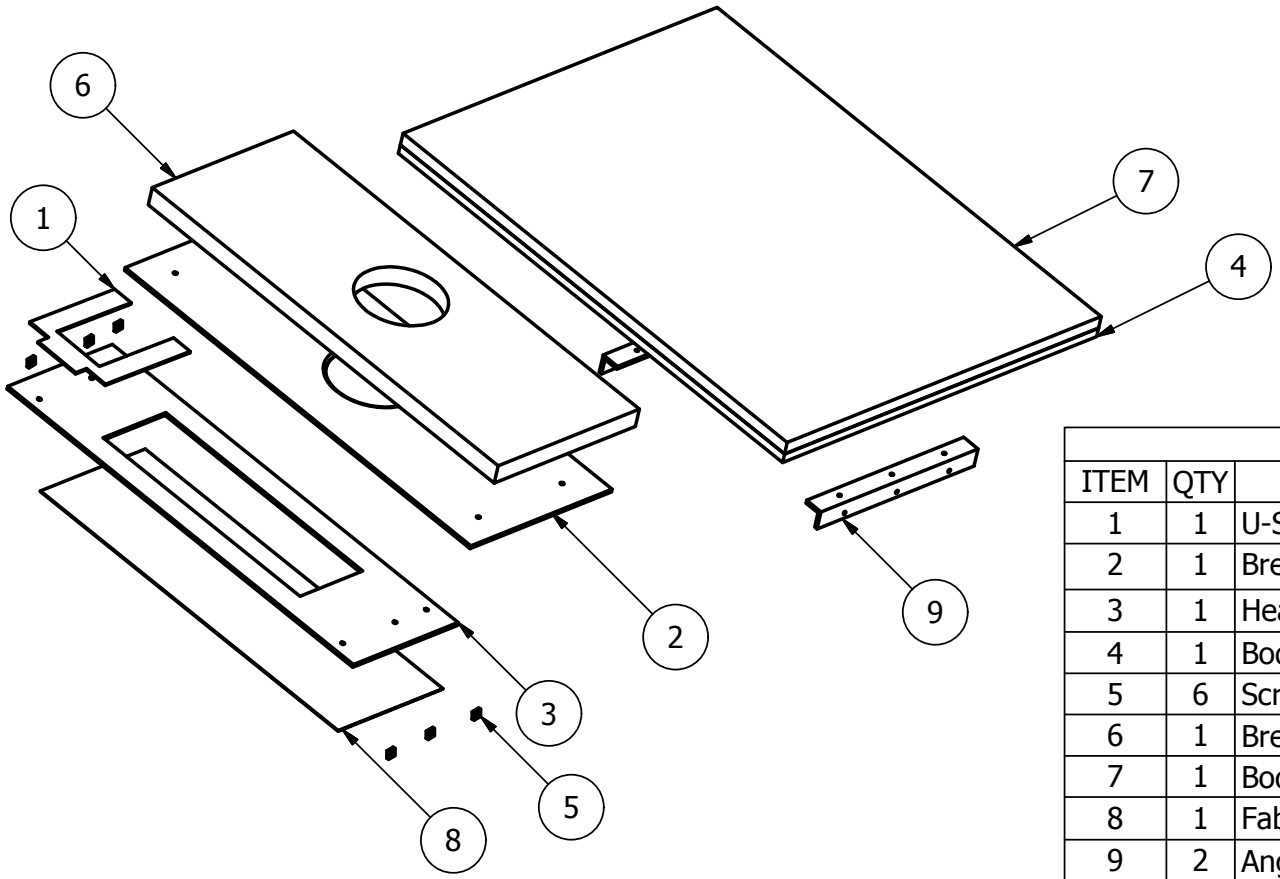


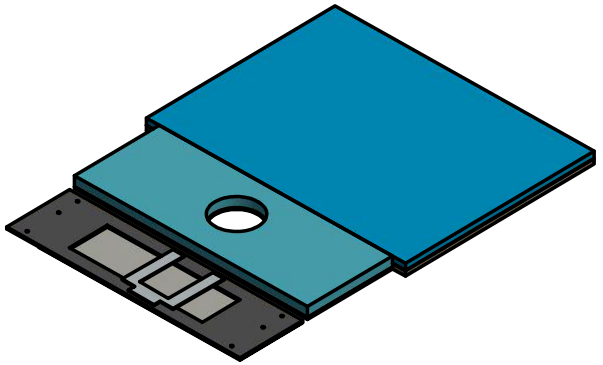

| PARTS LIST | | | |
|---|---|---|---|
| ITEM | QTY | PART NUMBER | DESCRIPTION |
| 1 | 1 | U-Shaped Head Support | ABS |
| 2 | 1 | Breast Support | Carbon Fiber |
| 3 | 1 | Head Support Frame | Carbon Fiber |
| 4 | 1 | Body Support | 3/4in Plywood |
| 5 | 6 | Screw Fastener | |
| 6 | 1 | Breast Support Upholstery (1.5in) | |
| 7 | 1 | Body Support Upholstery (1in) | |
| 8 | 1 | Fabric Below Head Frame | |
| 9 | 2 | Angle Iron Support | 1/4in Angle Iron |
| 10 | 18 | Screws (1/4-28) | |
| 11 | 6 | Knob Screw (1/4-28) | |

| | | |
|---|---|---|
| DRAWN Calene Treichel | 13/05/2015 | Cover |
| CHECKED | | TITLE: Breast Microwave Radar Body Supports |
| QA | | |
| MFG | | |
| APPROVED Mario Solis | 19/05/2015 | |
| TOLERANCES: 2 PL +/- X.XX 3 PL +/- X.XXX | | SIZE A4 \| DWG NO tabletop and headrest2 \| REV 1 |
| UNITS: INCHES UNLESS OTHERWISE SPECIFIED | | SCALE 0.08:1 \| SHEET 1 OF 8 |

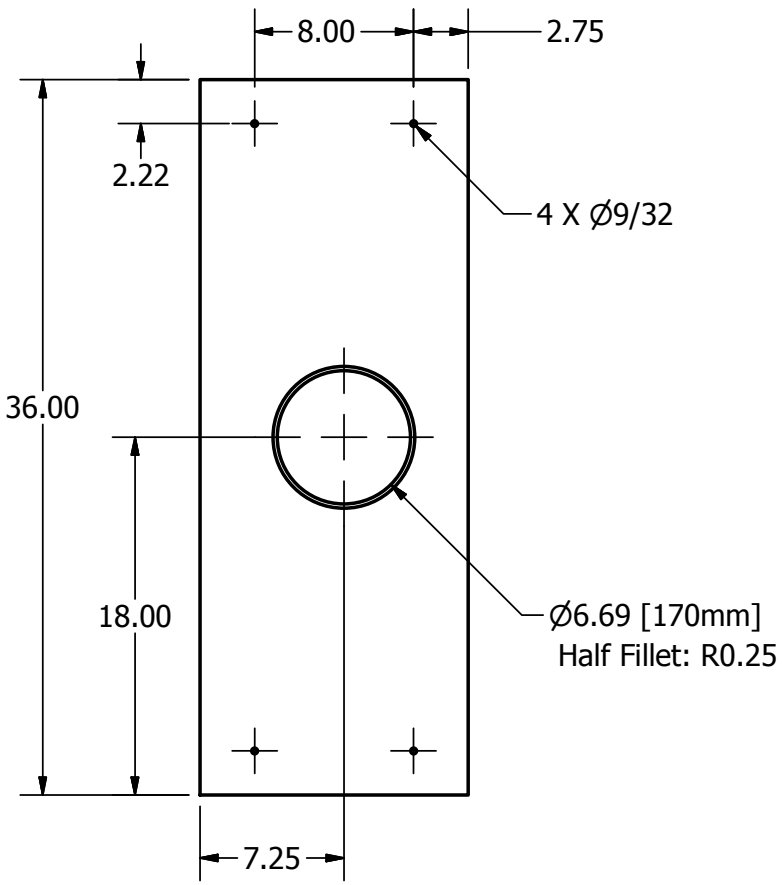


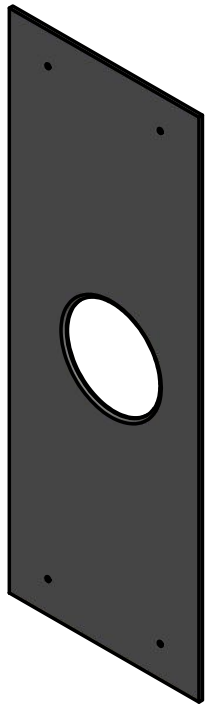

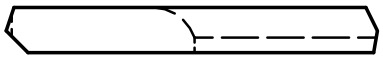

DETAIL A
SCALE 1 : 1

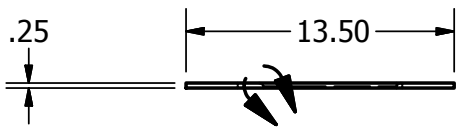


A

| | | |
|---|---|---|
| DRAWN Calene Treichel | 13/05/2015 | Breast Support |
| CHECKED | | TITLE |
| QA | | Breast Microwave Radar Body Supports |
| MFG | | |
| APPROVED Mario Solis | 19/05/2015 | |
| TOLERANCES 2 PL +/- X.XX 3 PL +/- X.XXX | | SIZE A4 / DWG NO tabletop and headrest2 / REV 1 |
| UNITS INCHES UNLESS OTHERWISE SPECIFIED | | |
| Material: Carbon Fiber | | SCALE 0.11:1 / SHEET 2 OF 8 |

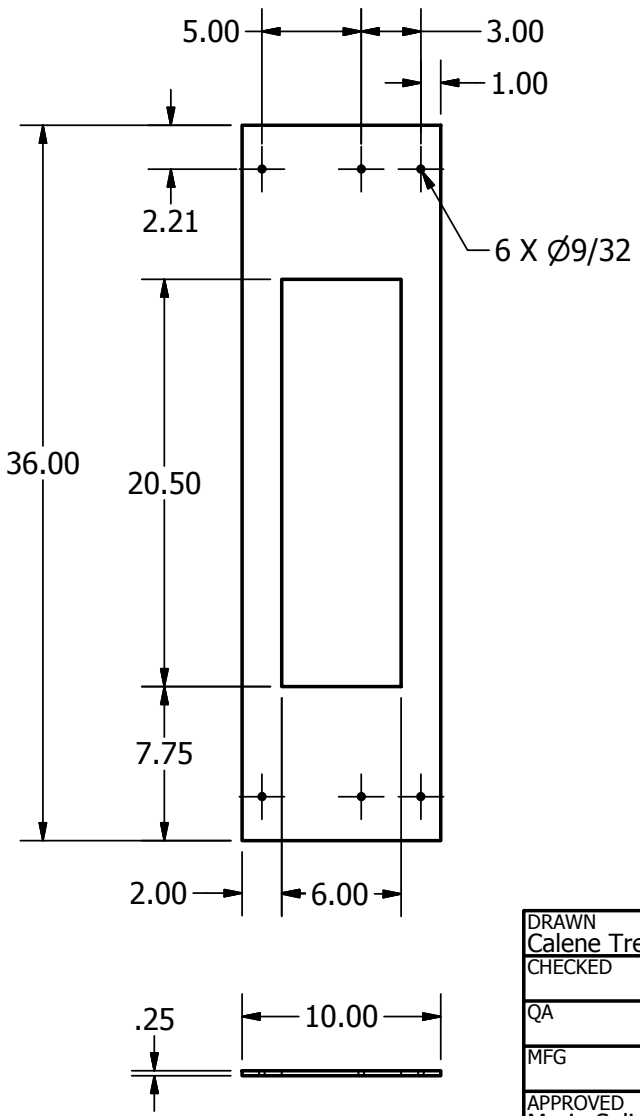


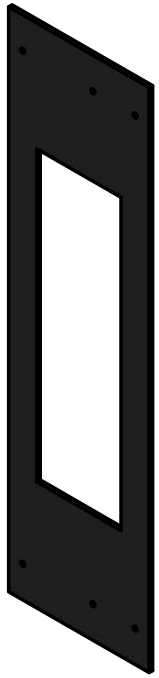

| | | |
|---|---|---|
| DRAWN Calene Treichel | 13/05/2015 | Head Support Frame |
| CHECKED | | TITLE: Breast Microwave Radar Body Supports |
| QA | | |
| MFG | | |
| APPROVED Mario Solis | 19/05/2015 | |
| TOLERANCES: 2 PL +/- X.XX 3 PL +/- X.XXX | | SIZE A4 / DWG NO tabletop and headrest2 / REV 1 |
| UNITS: INCHES UNLESS OTHERWISE SPECIFIED | | |
| Material: Carbon Fiber | | SCALE 0.11:1 / SHEET 3 OF 8 |

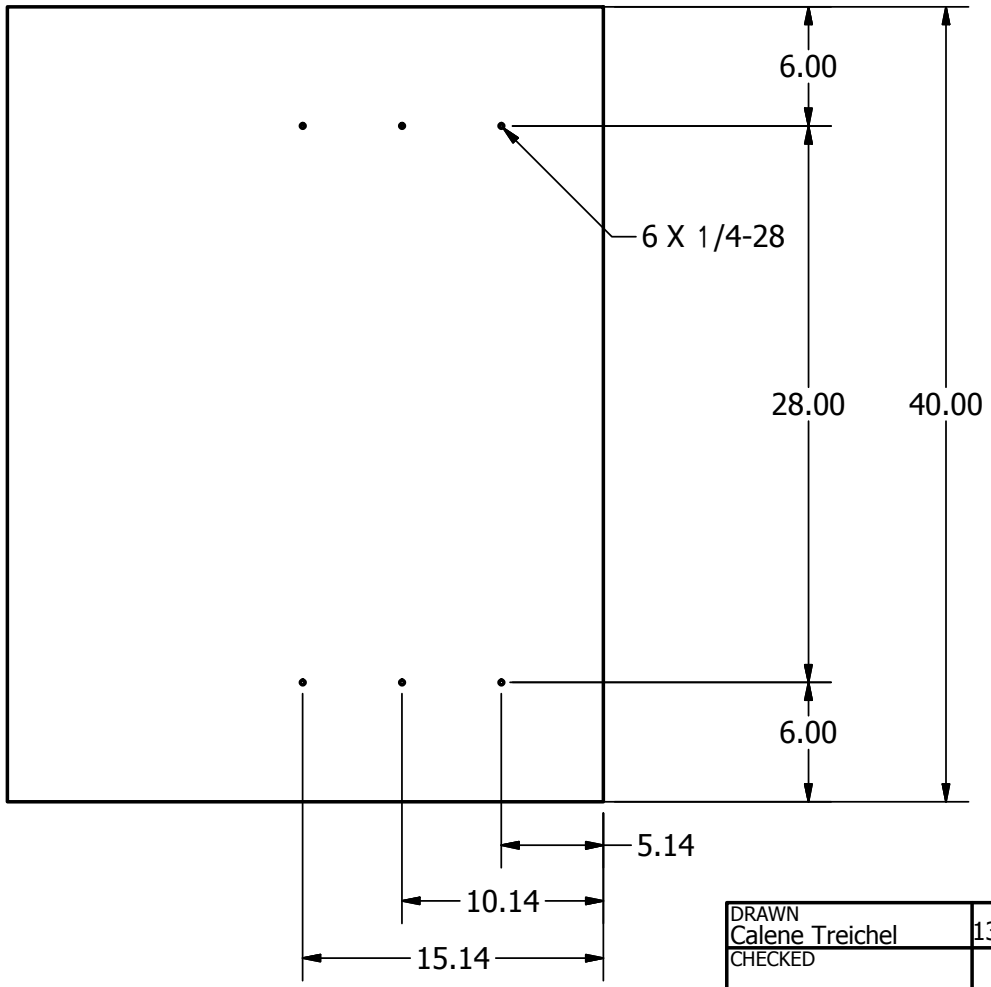


| | | |
|---|---|---|
| DRAWN Calene Treichel | 13/05/2015 | Body Support |
| CHECKED | | TITLE |
| QA | | Breast Microwave Radar Body Supports |
| MFG | | |
| APPROVED Mario Solis | 19/05/2015 | |
| TOLERANCES 2 PL +/- X.XX 3 PL +/- X.XXX | | SIZE A4 / DWG NO tabletop and headrest2 / REV 1 |
| UNITS INCHES UNLESS OTHERWISE SPECIFIED | | |
| Material: 3/4in Plywood | | SCALE 0.1:1 / SHEET 4 OF 8 |

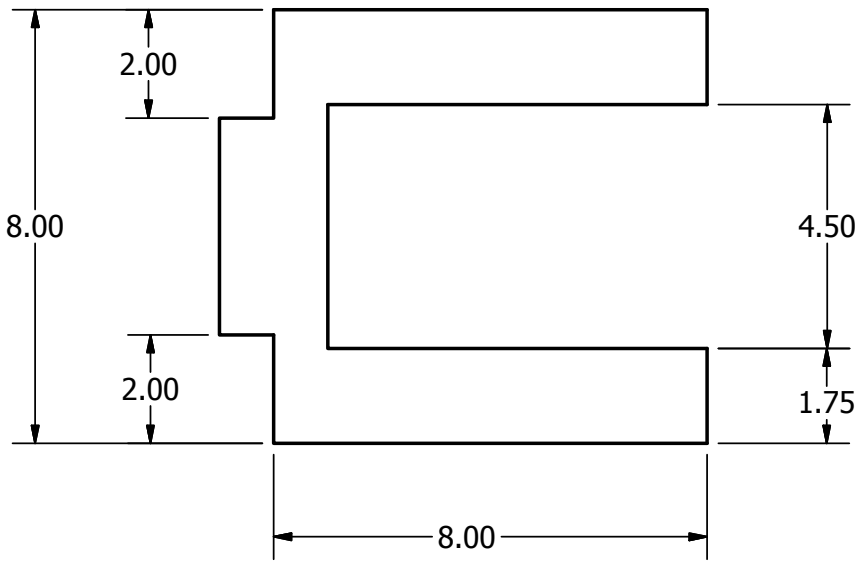


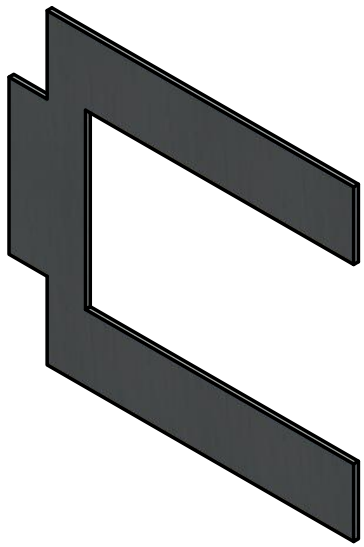

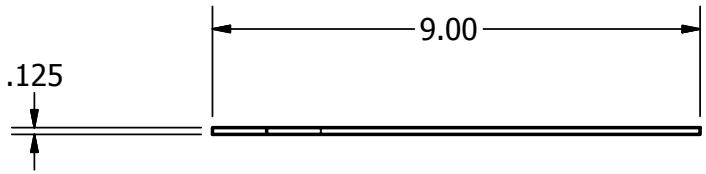


| | | |
|---|---|---|
| DRAWN Calene Treichel | 13/05/2015 | U-Shaped Head Support |
| CHECKED | | TITLE |
| QA | | Breast Microwave Radar Body Supports |
| MFG | | |
| APPROVED Mario Solis | 19/05/2015 | |
| TOLERANCES 2 PL +/- X.XX 3 PL +/- X.XXX | | SIZE A4 / DWG NO tabletop and headrest2 / REV 1 |
| UNITS INCHES UNLESS OTHERWISE SPECIFIED | | |
| Material: ABS | | SCALE 0.3:1 / SHEET 5 OF 8 |

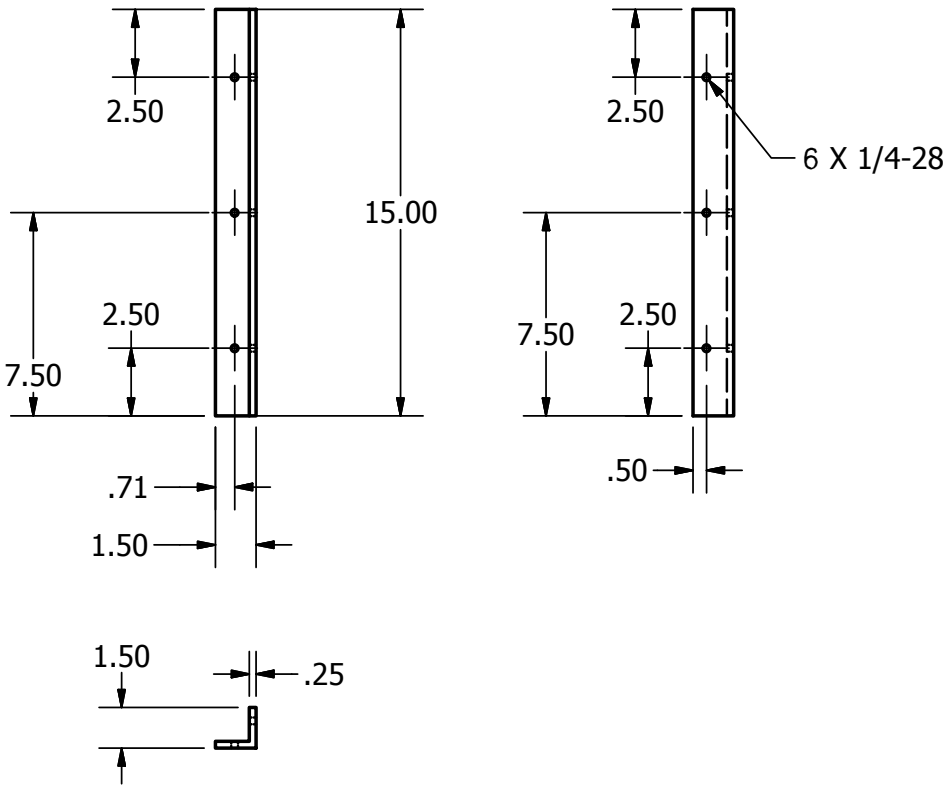


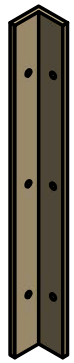

| | | | |
|---|---|---|---|
| DRAWN Calene Treichel | 13/05/2015 | Angle Iron Support | |
| CHECKED | | TITLE | |
| QA | | Breast Microwave Radar Body Supports | |
| MFG | | | |
| APPROVED Mario Solis | 19/05/2015 | | |
| TOLERANCES 2 PL +/- X.XX 3 PL +/- X.XXX | | SIZE A4 | DWG NO tabletop and headrest2 / REV 1 |
| UNITS INCHES UNLESS OTHERWISE SPECIFIED | | | |
| Material: 1 /4 in Angle Iron | | SCALE 0.15:1 | SHEET 6 OF 8 |

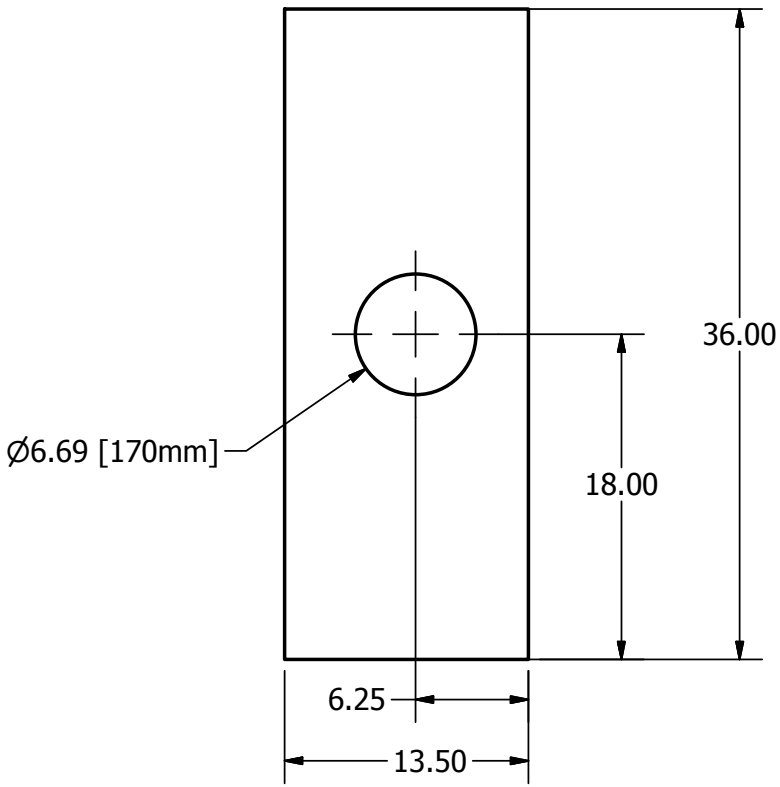


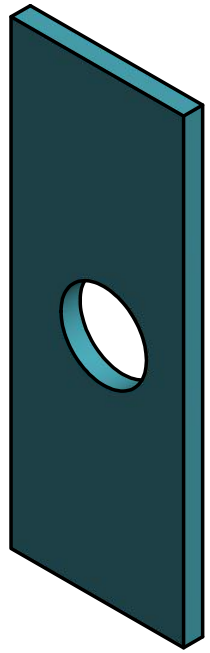

| | | | |
|---|---|---|---|
| DRAWN Calene Treichel | 13/05/2015 | Breast Support Upholstery | |
| CHECKED | | TITLE | |
| QA | | Breast Microwave Radar Body Supports | |
| MFG | | | |
| APPROVED Mario Solis | 19/05/2015 | | |
| TOLERANCES 2 PL +/- X.XX 3 PL +/- X.XXX | | SIZE A4 | DWG NO tabletop and headrest2 REV 1 |
| UNITS INCHES UNLESS OTHERWISE SPECIFIED | | SCALE 0.1:1 | SHEET 7 OF 8 |

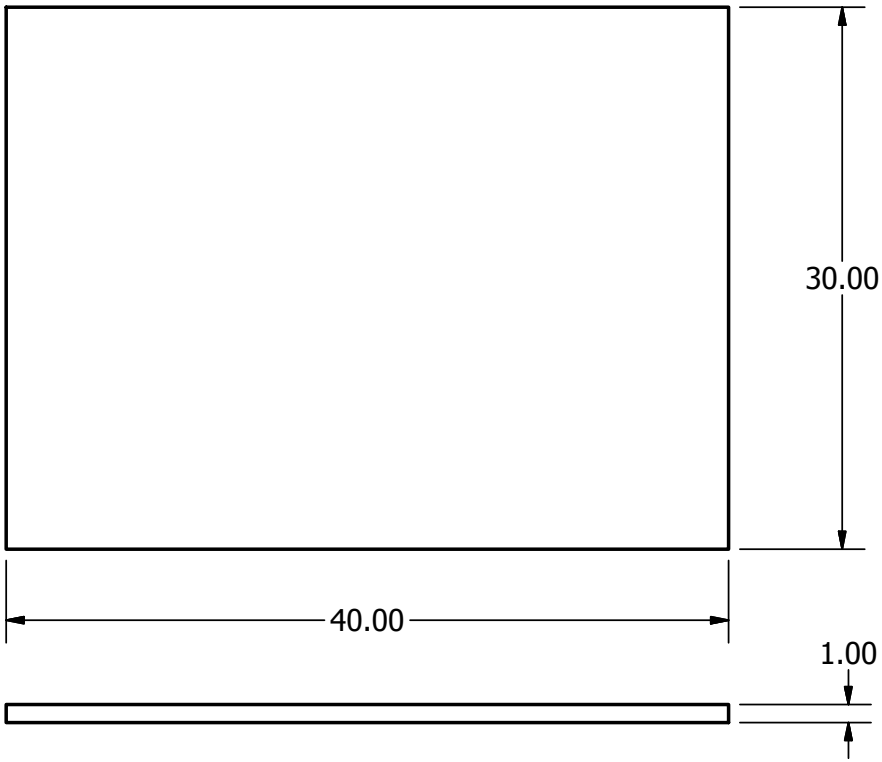


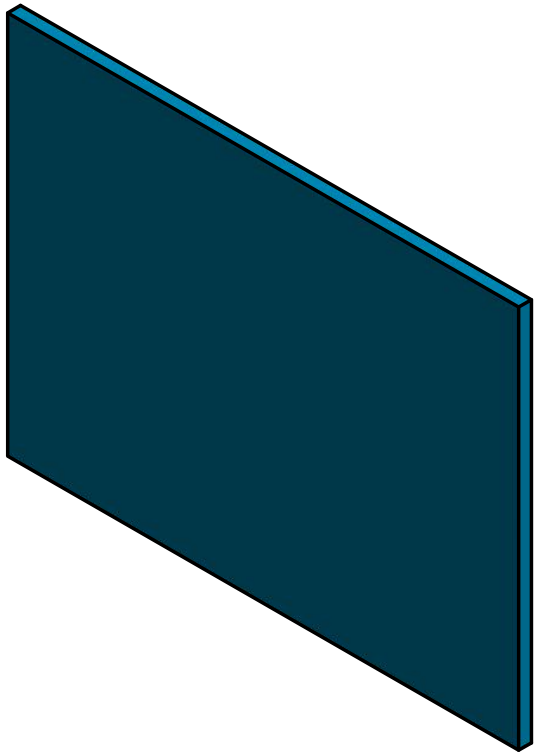

| | | | |
|---|---|---|---|
| DRAWN Calene Treichel | 13/05/2015 | Body Support Upholstery | |
| CHECKED | | TITLE | |
| QA | | Breast Microwave Radar Body Supports | |
| MFG | | | |
| APPROVED Mario Solis | 19/05/2015 | | |
| TOLERANCES 2 PL +/- X.XX 3 PL +/- X.XXX | | SIZE A4 | DWG NO tabletop and headrest2 / REV 1 |
| UNITS INCHES UNLESS OTHERWISE SPECIFIED | | SCALE 0.1:1 | SHEET 8 OF 8 |